SAN DIEGO STATE UNIVERSITY

and

UNIVERSITY OF CALIFORNIA, IRVINE

Design of Novel Phased Array Antennas with Integrated Beamforming Network and Dual Band Shared Aperture Feed Source for Reflector Antenna for Satellite Communication Applications

DISSERTATION

submitted in partial satisfaction of the requirements
for the degree of

DOCTOR OF PHILOSOPHY

in Computational Science

by

Rudraishwarya Banerjee

Dissertation Committee:
Professor Satish K. Sharma, Chair
Professor Filippo Capolino
Professor Franco de Flaviis
Professor Gustaaf Jacobs
Professor Faryar Jabbari

DEDICATION

To

my parents (Mr. Pradip Banerjee and Mrs. Rita Banerjee)

for always loving me and supporting me.

TABLE OF CONTENTS

LIST OF FIGURES

LIST OF TABLES

ACKNOWLEDGEMENTS

I would like to sincerely thank my advisor, Professor Satish K. Sharma for giving me the opportunity to pursue a doctoral program under his guidance. I am grateful for his advice, time, support and help during my Ph.D. journey since Fall 2018. I also thank him for offering me unlimited opportunity to gain hands-on experience using the research resources available in the Antenna and Microwave Laboratory (AML). I am grateful to Professor Sharma for connecting me with his collaborators, namely NIWC, Pacific and NASA, Glenn Research Center (GRC), and giving me the opportunity to work on exciting projects with them. I am thankful to him for the financial supports I received as a Research Assistant in the projects funded by NIWC, Pacific and NASA, GRC. I am also thankful to Professor Sharma for nominating me for the University Graduate Fellowship that I received during my doctoral studies.

I would like to sincerely thank Professor Filippo Capolino for being my co-advisor, and giving me the opportunity to work under his guidance (particularly during my quarters in UC, Irvine and during my third project as well). I would like to sincerely thank Professor Franco de Flaviis, Professor Gustaaf Jacobs, and Professor Faryar Jabbari for their time and efforts as a part of my doctoral committee members. I would like to thank Professor Jose Castillo, the program director of the Computational Science Research Center at SDSU, for his all the support during my Ph.D. program. I would also like to thank the computational science joint doctoral program JDP staff, Ms. Parisa Plant from SDSU, and Ms. Jean Bennett from University of California, Irvine (UCI) for their continuous assistance.

I would like to sincerely thank the funding agencies, namely, NIWC, Pacific and NASA Glenn Research Center (GRC) for their financial support. I would like to thank Jia-Chi Samuel Chieh and Raif Farkough from NIWC, Pacific, and Seth W. Waldstein, James M. Downey, Bryan L. Shoenholz, Sarah M. Dever, James A. Nessel from NASA, GRC for their and valuable technical help. I would like to thank Mr. Mark Bruno of SDSU for assisting me in the fabrication of antenna and mount during my research. I would like to thank my former and present

colleagues in the research group, namely, Mr. Connor Laffey, Dr. Sanghamitro Das, and Dr. Kaushik Debbarma for their help and suggestions.

Chapter 3 of this dissertation is a partial reprint of the material as it appears in R. Banerjee, S. K. Sharma, J. -C. S. Chieh and R. Farkouh, "Investigations of Heat Sink Property of a Novel Dual Linear Polarized Low Cross-Polarization X-Band Phased Array Antenna Employing Silicon RFICs-Based Beamforming Network," in *IEEE Open Journal of Antennas and Propagation*, vol. 3, pp. 523-537, 2022, doi: 10.1109/OJAP.2022.3170791, and R. Banerjee, S. K. Sharma and J. S. Chieh, "An Innovative 3D Metal Printed Dual Linear Polarized Dual Beam Tx/Rx Phased Array Heat Sink Antenna with Silicon RFIC Beamformers," *2022 IEEE International Symposium on Phased Array Systems & Technology (PAST)*, Waltham, MA, USA, 2022, pp. 01-07, doi: 10.1109/PAST49659.2022.9975042.

Chapter 4 of this dissertation is a partial reprint of the material as it appears in Rudraishwarya Banerjee, Satish K. Sharma, Seth W. Waldstein, James M. Downey, Bryan L. Shoenholz, Sarah M. Dever, James A. Nessel, and Sanghamitro Das, "A 22 -28 GHz Polarization Reconfigurable Flat Panel 8x8 Tx/Rx Phased Array Antenna with Uniquely Arranged Novel Radiating Elements for CubeSat Communication," in *IEEE Transactions on Antennas and Propagation*, and Rudraishwarya Banerjee, Satish K. Sharma, Seth W. Waldstein, James M. Downey, Bryan L. Shoenholz, Sarah M. Dever, James A. Nessel, and Sanghamitro Das, "A Wideband Dual Linear/Circular Polarized 64-Element Phased Array Antenna for SATCOM Applications," *2023 United States National Committee of URSI National Radio Science Meeting (USNC-URSI NRSM)*, Boulder, CO, USA, 2023, pp. 60-61.

Chapter 5 of this dissertation is a partial reprint of R. Banerjee, S. K. Sharma and F. Capolino, "A Shared Aperture Ku-/Ka-Band Feed Source for a High Gain Fixed Beam Offset Reflector Antenna," *2022 IEEE Conference on Antenna Measurements and Applications (CAMA)*, Guangzhou, China, 2022, pp. 1-3, doi: 10.1109/CAMA56352.2022.10002441. This work will be submitted soon and may appear as R. Banerjee, S. K. Sharma and F. Capolino, “Dual Circular Polarized (RHCP/LHCP) Dual (Ku/K-) Band Shared Aperture Feed Source with Common Phase Center for an Offset Reflector Antenna”, *IEEE Antenna and Wireless Propagation Letters.*

The co-authors listed in all my publications are in the advisory role during my doctoral research.

VITA

Rudraishwarya Banerjee

June, 2013	Bachelor of Technology in Radio Physics and Electronics (equivalent to B.S in Electrical Engineering), University of Calcutta, India
June, 2015	Master of Technology in Radio Physics and Electronics (equivalent to M.S in Electrical Engineering), University of Calcutta, India (specialization in 'Space Science and Microwaves')
Sept, 2015 -June, 2018	Research Fellow in the Department of Electronics and Telecommunication of the Indian Institute of Engineering Science and Technology (IIEST), India
Aug,2018- June, 2023	PhD of Computational Science, San Diego State University and University of California, Irvine, California, USA

FIELD OF STUDY

Computational Science (with research field focused on Electrical Engineering, precisely Microwave Engineering and Antennas)

REFERRED PUBLICATIONS (2018-2023)

1. **Rudraishwarya Banerjee**, Satish K. Sharma, Seth W. Waldstein, James M. Downey, Bryan L. Shoenholz, Sarah M. Dever, James A. Nessel, and Sanghamitro Das, "A 22 GHz to 28 GHz Polarization Reconfigurable Flat Panel 8x8 Tx/Rx Phased Array Antenna with Uniquely Arranged Novel Radiating Elements for CubeSat Communication," in *IEEE Transactions on Antennas and Propagation,* vol. 71, no. 5, pp. 4138-4152, May 2023, doi: 10.1109/TAP.2023.3249820.
2. **R. Banerjee**, S. K. Sharma, J. -C. S. Chieh and R. Farkouh, "*Investigations of Heat Sink Property of a Novel Dual Linear Polarized Low Cross-Polarization X-Band Phased Array*

Antenna Employing Silicon RFICs-Based Beamforming Network," in *IEEE Open Journal of Antennas and Propagation*, vol. 3, pp. 523-537, 2022.

3. **R. Banerjee**, S. K. Sharma and F. Capolino, "Dual Circularly Polarized (RHCP/LHCP) Dual-Band (Ku/K-) Shared Aperture Arrays as Feed Source with Common Phase Center for an Offset Parabolic Reflector Antenna", *IEEE Antenna and Propagation Wireless Letters (under preparation)*.
4. **R. Banerjee**, S. K. Sharma and J. S. Chieh, "An Innovative 3D Metal Printed Dual Linear Polarized Dual Beam Tx/Rx Phased Array Heat Sink Antenna with Silicon RFIC Beamformers," *2022 IEEE International Symposium on Phased Array Systems & Technology (PAST)*, Waltham, MA, USA, 2022, pp. 01-07.
5. **Rudraishwarya Banerjee**, Satish K. Sharma, Seth W. Waldstein, James M. Downey, Bryan L. Shoenholz, Sarah M. Dever, James A. Nessel, and Sanghamitro Das, "A Wideband Dual Linear/Circular Polarized 64-Element Phased Array Antenna for SATCOM Applications," *2023 United States National Committee of URSI National Radio Science Meeting (USNC-URSI NRSM)*, Boulder, CO, USA, 2023, pp. 60-61.
6. **R. Banerjee**, S. K. Sharma and F. Capolino, "A Shared Aperture Ku-/Ka-Band Feed Source for a High Gain Fixed Beam Offset Reflector Antenna," *2022 IEEE Conference on Antenna Measurements and Applications (CAMA)*, Guangzhou, China, 2022, pp. 1-3.
7. **Rudraishwarya Banerjee**, Satish K. Sharma, Philip Nguyen, Jia-Chi S. Chieh, and Randall Olsen, "*Investigations of All Metal Heat Sink Dual Linear Polarized Phased Array Antenna for Ku-Band Applications*", *2020 International Applied Computational Electromagnetics Society Symposium (ACES)*, Virtual, July 2020.
8. **R. Banerjee**, S. K. Sharma and S. Das, "*Design of Dual Circular Polarized Wideband Stacked Patch Flat Panel Phased Array Antenna using Ka-band 5G Silicon RFICs in Beamforming Network*," *2021 IEEE 19th International Symposium on Antenna Technology and Applied Electromagnetics (ANTEM)*, 2021, pp. 1-2.

Awards and Honors

1. Received student travel grant in National Radio Science Meeting (NRSM, URSI), 2023
2. Finalist in Student Paper competition in International Symposium on Phased Array Systems and Technology (PAST), 2022.
3. Received Hewlett-Packard Award in ACSESS, SDSU, 2021
4. Received University Graduate Fellowship in SDSU in Fall, 2019.
5. First Rank Holder and Gold Medalist in Master of Technology in Radio Physics and Electronics, University of Calcutta, 2015; Received the offer of a prestigious fellowship entitled 'Innovation in Science Pursuit for Inspired Research (INSPIRE)' Department of Science and Technology (DST), Ministry of Science and Technology, Govt. of India.
6. Received AICTE GATE scholarship during Masters (2013-2015) in India.

ABSTRACT OF THE DISSERTATION

Design of Novel Phased Array Antennas with Integrated Beamforming Network and Dual Band Shared Aperture Feed Source for Reflector Antenna for Satellite Communication Applications

by

Rudraishwarya Banerjee

Doctor of Philosophy in Computational Science

San Diego State University and University of California, Irvine, 2023

Professor Satish K. Sharma, Chair

The phased array antennas (PAAs) are indispensable for satellite communications (SATCOM), battlefield applications, 5G communications and different other developing technological applications. The recent advances of commercial silicon beamforming chipsets have aided the pervasive employment of phased array antennas for commercial applications. This research work is focused on the design and development of phased array antennas that fulfill the growing demands of high-gain beam steering antennas in satellite and wireless communications.

In the first project of this thesis, investigations on the heat sink property of a 4x2 wideband dual linear polarized phased array antenna comprised of 3D metal printed all metallic radiators, serving also as a heat sink, is presented for X-band frequency. This radiating element resembles heat fins, and is designed to cover 8.5-11.5 GHz impedance bandwidth. Excellent radiation pattern with low cross-polarization is obtained over the entire bandwidth, while the peak broadside gain is varying between 11-14 dBi. Beam scans are viable ±50° in $\varphi=0^0$ plane and ±30° in $\varphi=90^0$ plane. The beamforming network (BFN) is comprised of commercial silicon Radio Frequency Integrated Circuit (RFIC) chips which have been integrated with the antenna aperture. The temperature reduction of 60°C is achieved with the heat sink structure when the temperature distribution of BFN with and without heat sink are compared for the 4x2 array.

In the second project, a wideband (22-28 GHz), polarization reconfigurable (horizontal (X-), vertical (Y-), left-hand circular and right-hand circular polarizations), flat panel, 8x8 transmit (Tx)/receive (Rx) phased array antenna (PAA), with RFIC based integrated BFN, is proposed. The array offers a realized gain of 22-23 dBi/dBic in the broadside direction and scans to approximately ±50° while maintaining 3dB gain drop/scan loss, low cross-polarized fields, and axial ratio (AR) below 3dB (in case of circular polarization (CP)) over the entire bandwidth within the given scan range. The array is comprised of novel radiating elements, arranged in a unique way in the array such that the benefit of element mirroring is achieved during the dual linear cases, whereas the benefit of sequential rotation of elements is achieved in dual CP cases. The simulated results are validated through the measurement results for a fabricated PAA prototype for the scanned radiation patterns for all four polarizations in receive mode, antenna gain-to-noise temperature (G/T) in receive mode, and effective isotropic radiated power (EIRP) in transmit mode.

SATCOM employs reflector antennas with circularly polarized feed sources at their terminals for high directivity and relatively low cost. In the third project, an innovative design technique of a dual circularly polarized feed source suitable for a parabolic reflector working in two far-off bands with *1:1.8* ratio is proposed, which can find applications in satellite communications (SATCOM). The proposed design covers an impedance bandwidth of 500 MHz in Ku-band (14.2-14.8 GHz), and 1 GHz in K-band (25-26 GHz), with a peak directivity of almost 15 dBic and axial ratio below 3dB over the entire bandwidth for both bands. This feed source assures that the half-edge-illumination beamwidths are the same for both the bands for an offset parabolic reflector of focal-length-to-diameter (f/d) ratio of 1.5. The feed prototype is built, and simulation results are experimentally validated.

Chapter 1

Introduction and Motivation

1.1 Objective

For satellite communications (SATCOM), battlefield applications, 5G communications and different other developing technological applications, the demand for phased array antennas (PAAs) and high gain reflector antennas are pervasive. The recent developments of commercial silicon beamforming chipsets have increased the flexibility of phased array antennas. This research work is a pursuit of novel high gain antenna technologies that comply with the growing demands of innovative antenna design in satellite and wireless communications.

As part of the doctoral research, the first significant antenna research contribution is the investigations of heat sink property of a novel dual linear polarized low cross-polarization X-Band phased array antenna employing silicon RFICs based beamforming network. Here, a wideband, dual linear polarized phased array antenna, comprised of intuitively shaped all metallic radiators is proposed for X-band applications. The antenna aperture is 3D metal printed, and the beamforming network, consisting of Anokiwave radio frequency integrated chips (RFICs), is integrated with the antenna aperture. The antenna aperture works as a heat sink in addition to radiation, which in turn helps to dissipate the heat generated by the RFICs. This work is already completed and published in a peer reviewed journal of IEEE.

In the next phase of research, a polarization reconfigurable wideband flat panel transmit (Tx)/receive (Rx) phased array antenna with uniquely arranged novel radiating elements for satellite communication is proposed. This work is based on requirements derived from a National Aeronautics and Space Administration (NASA) Glenn Research Center (GRC) mission concept for an orbiting lunar relay providing persistent connectivity to the lunar south pole. A flat panel phased array with RFIC based beamforming network is proposed. The array consists of novel radiating elements arranged exclusively in sub-array level,

thereby improving cross-polarized fields and axial ratio. The gain to noise temperature (G/T) in receiving mode and effective isotropic power (EIRP) in transmit mode are also studied in addition to beam scan performance in receive and transmit modes. This work is already completed and published in a peer reviewed journal of IEEE.

In the next step, a Fabry-Perot cavity based shared aperture Ku-/Ka-band dual circular polarized array, both having same phase center, is designed as a feed source of an offset parabolic reflector antenna intended for SATCOM application. The dual band feed source facilitates Tx and Rx purpose at two far off bands in SATCOM applications. This work is already completed and has been submitted in a peer reviewed journal of IEEE.

1.2 Motivation and background

1.2.1 Investigations of Heat Sink Property of a Novel Dual Linear Polarized Low Cross-Polarization X-Band Phased Array Antenna Employing Silicon RFICs Based Beamforming Network

For satellite communications (SATCOM), battlefield applications, 5G communications and different other developing technological applications, the phased array antennas (PAAs) are preferred over mechanical scanning antennas as the PAA can radiate ample amount of microwave power in an intended direction to accomplish system link requirements and the beam can be electronically scanned instantaneously, [1], [2]. The recent developments of commercial silicon beamforming chipsets have increased the flexibility of phased array antennas. The fully integrated chipset discards the need for discrete transceiver blocks and employs a transmit/receive (T/R) switch, low noise amplifier, power amplifier, phase shifters, and variable attenuators. Moreover, the fully integrated chipset reduces overall size, cost, and RF losses.

On the other side, with the advancement of 3-D system in package (SiP) technology, multiple radio frequency (RF) components including antennas are highly integrated in a single package with very limited space. Thus, the heat generated by the chips become severe problem since excessive thermal energy may affect the performance and even destroy

sensitive devices. For the purpose of improving thermal management and maintain performance of compact RF devices, extra heatsink structures are required.

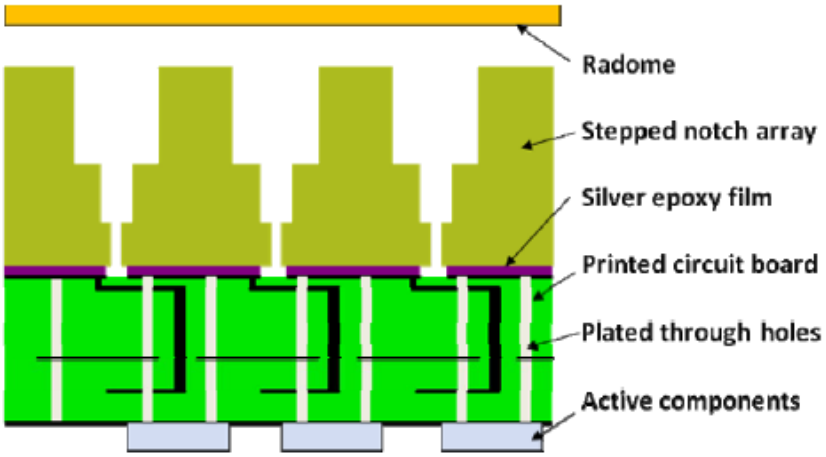

(a)

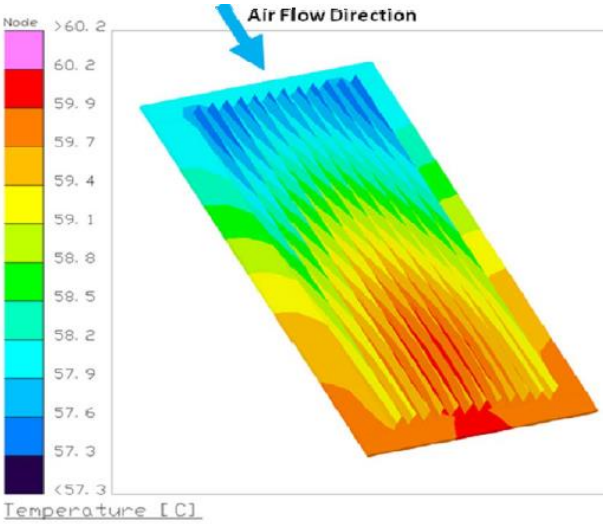

(b)

Fig. 1.1: (a) Cross-sectional view of notch antenna array with radome and a printed circuit board, and (b) Calculated temperature of a notch array with 50 Watt load with 40oC inlet air with 0.425 m3/s. [3].

In [3], a single polarized stepped notch antenna attached to a flat multi-layered printed circuit board (PCB), working at Ku-band, is explored, where the antenna aperture, along with serving as a radiator, provides a thermal heat sink for active arrays as well. The heat generated by the active devices, such as amplifiers (HPA or LNA), passes through the PCB, into the antenna aperture through plated holes which provide the principal heat path, as shown in Fig. 1.1(a). A thin radome is placed above the 26 x 11 notch array, and a maximum temperature of 60°C is noted with 40° C inlet air flow of 0.425 m^3/s, and a heat load of 50 WA, as shown in Fig. 1.1(b).

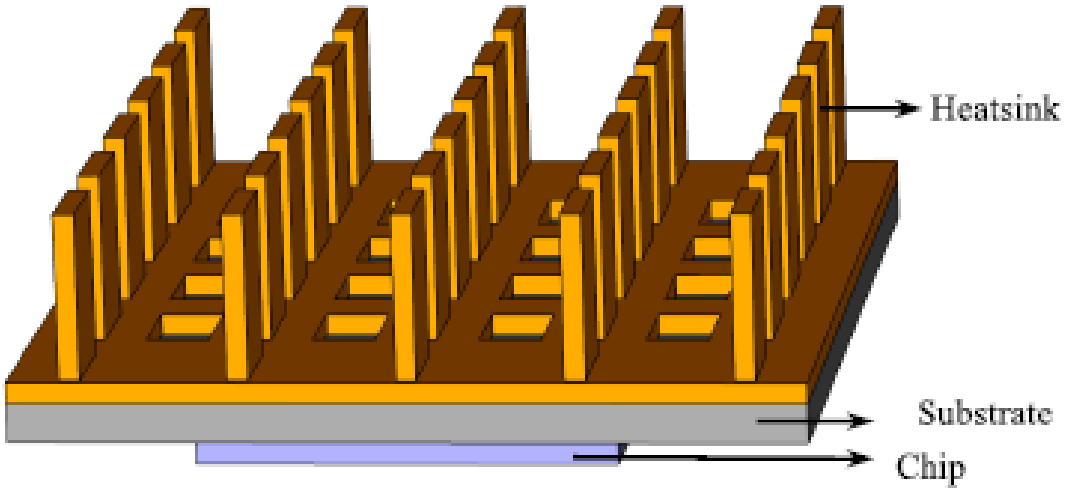

(a)

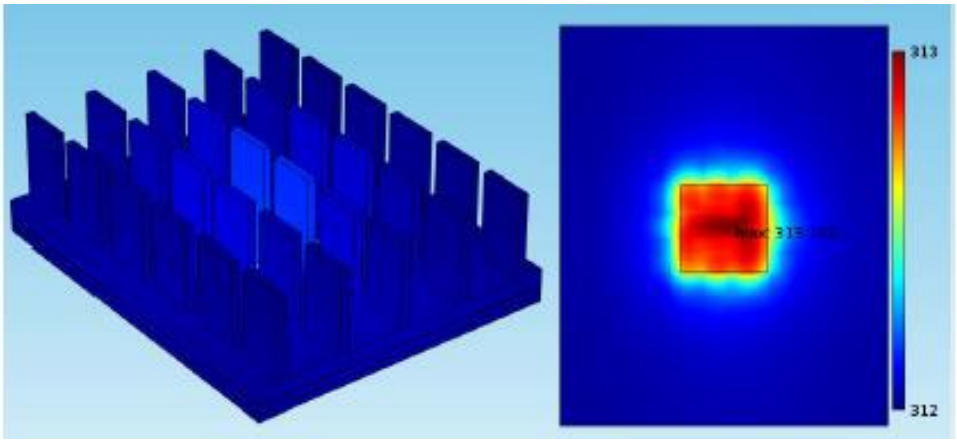

(b)

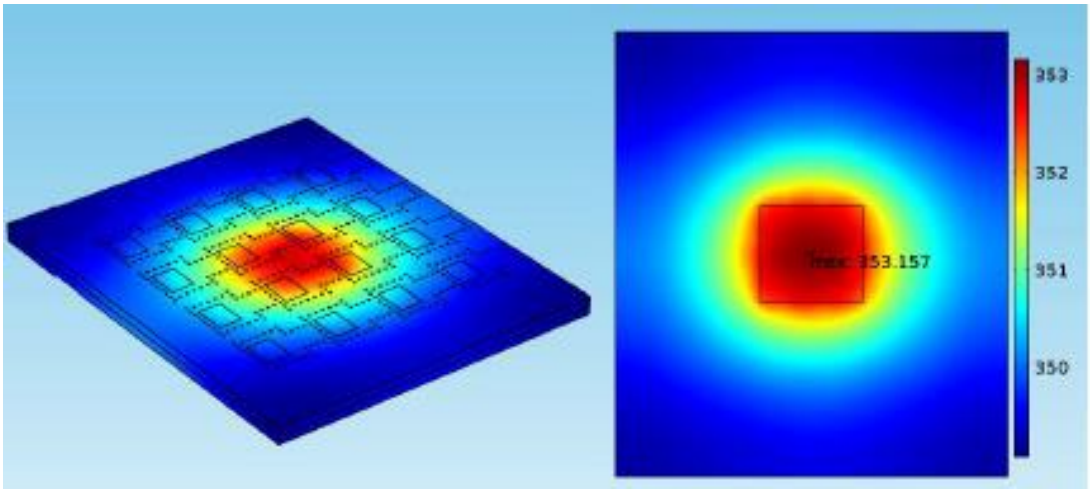

(c)

Fig. 1.2. (a) Schematic of the proposed heatsink antenna, Simulated temperature distributions: (b) with heatsink and (c) without heatsink [4].

In [4], a single polarized 4x4 fixed beam heat sink antenna array on low-temperature cofired ceramic (LTCC) substrate is proposed [Fig. 1.2 (a)], where the antenna element is a horn-like structure that consists of an open-ended waveguide and two vertical metallic fins, and the feeding network is comprised of the substrate integrated waveguides (SIWs) with numerous metallic vias. Metallic vias help to transfer the heat from chips to the heatsink, and temperature reduction of 40.1°C is achieved, as seen in Fig. 1.2 (b).

The first project of this doctoral research is a Navy-funded project where an X-band phased array antenna comprised of anall-metall radiating element with dual linear polarization in a 4x2 array that also serves as a heat sink for dissipating the heat generated by the chipsets in the integrated beam forming network (BFN) is designed.

1.2.2. A Polarization Reconfigurable Wideband Flat Panel Tx/Rx Phased Array Antenna with Uniquely Arranged Novel Radiating Elements for Satellite Communication

National Aeronautics and Space Administration (NASA) is exploring the use of 5G as a key component of the future lunar surface communications architecture. A relay satellite capable of interoperability with the lunar surface 5G network is highly desired. The second project of this doctoral research is based on requirements of the NASA, Glenn Research Center (GRC) mission concept for an orbiting lunar relay providing constant connectivity to the lunar south pole. Fig. 1.3 shows the schematic of the NASA flight test, which has the following two objectives, firstly to demonstrate the capabilities of phased array technologies to provide relay services to future lunar surface missions, and to demonstrate the use of 5G protocols in a relay architecture to interoperate with 5G cells on the lunar surface.

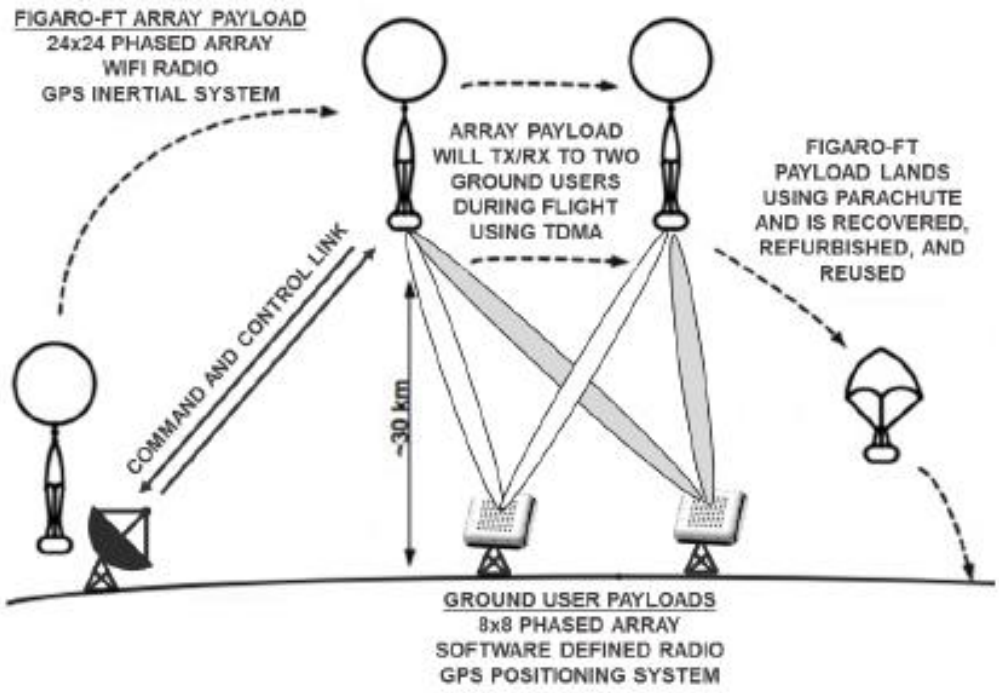

Fig. 1.3. Schematic for NASA flight test to demonstrate the capabilities of phased array technologies.

In [5] and [6] an RFIC based 256 elements polarization agile Ku-band phased-array working in receive mode and transmit modes, respectively, are presented for SATCOM applications. Extensive measurement results, including beam scan performance and gain to noise temperature (G/T) in receive case [5] and effective isotropic radiated power (EIRP) in case of transmit case [6] is presented, which explains the versatility of the RFIC based phased array. Fig. 1.4 (a) shows the Ku-band phased-array terminal, whereas Fig. 1.4(b) shows the 256-element phased-array architecture [5].

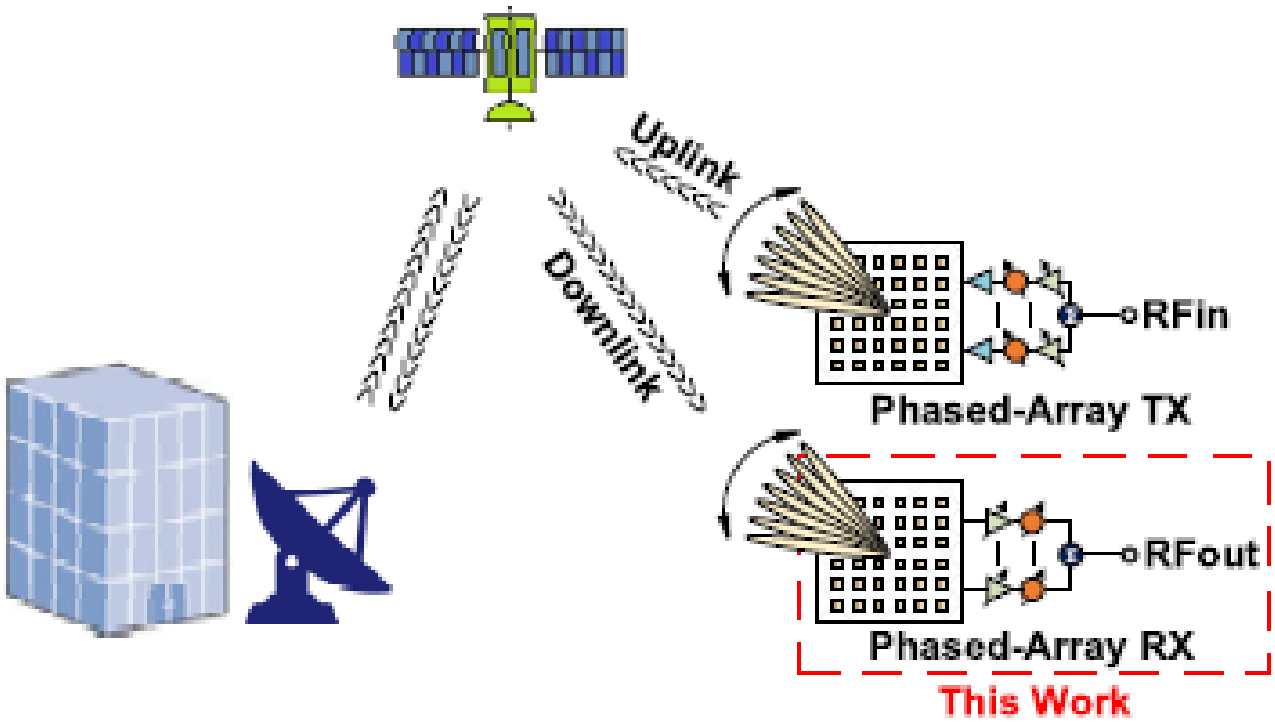

(a)

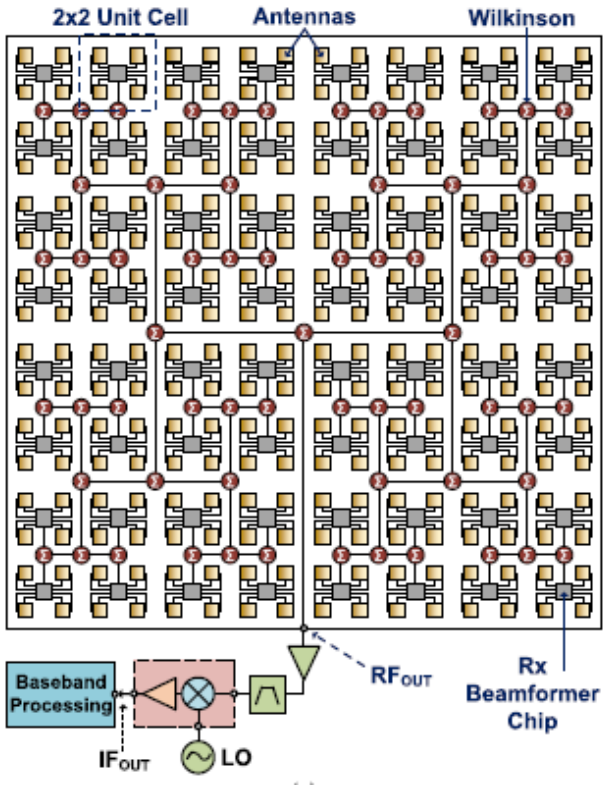

(b)

Fig. 1.4. (a) Ku-band phased-array terminal (RF-front end) and (b) The 256-element phased-array SATCOM receiver based on 64 quad beamformer chips [5].

In the second project of this doctoral research, an RFIC based Tx/Rx, wideband, flat panel, polarization reconfigurable (dual linear as well as dual circular polarized) phased array antenna working in K-/Ka-band (22-28 GHz) frequency range with very low cross-polarized fields and an axial ratio below 3dB over entire scan volume and entire bandwidth is explored. Though the phased array is designed to meet the requirements of the NASA project, but this array is scalable, versatile, and highly applicable to advanced communication systems.

1.2.3. Dual Circular Polarized (RHCP/LHCP) Dual (Ku/K-) Band Shared Aperture Feed Source with Common Phase Center for an Offset Reflector Antenna

A dual linear polarized array antenna with a large distance between the radiating elements is designed in a Fabry–Perot cavity (FPC) between a ground plane and a partially reflective surface (PRS) [7]. The configuration offers the following advantages, like higher directivity with a lesser number of radiating elements, large interelement spacing which, leads to small coupling and easy feeding network development, and so forth.

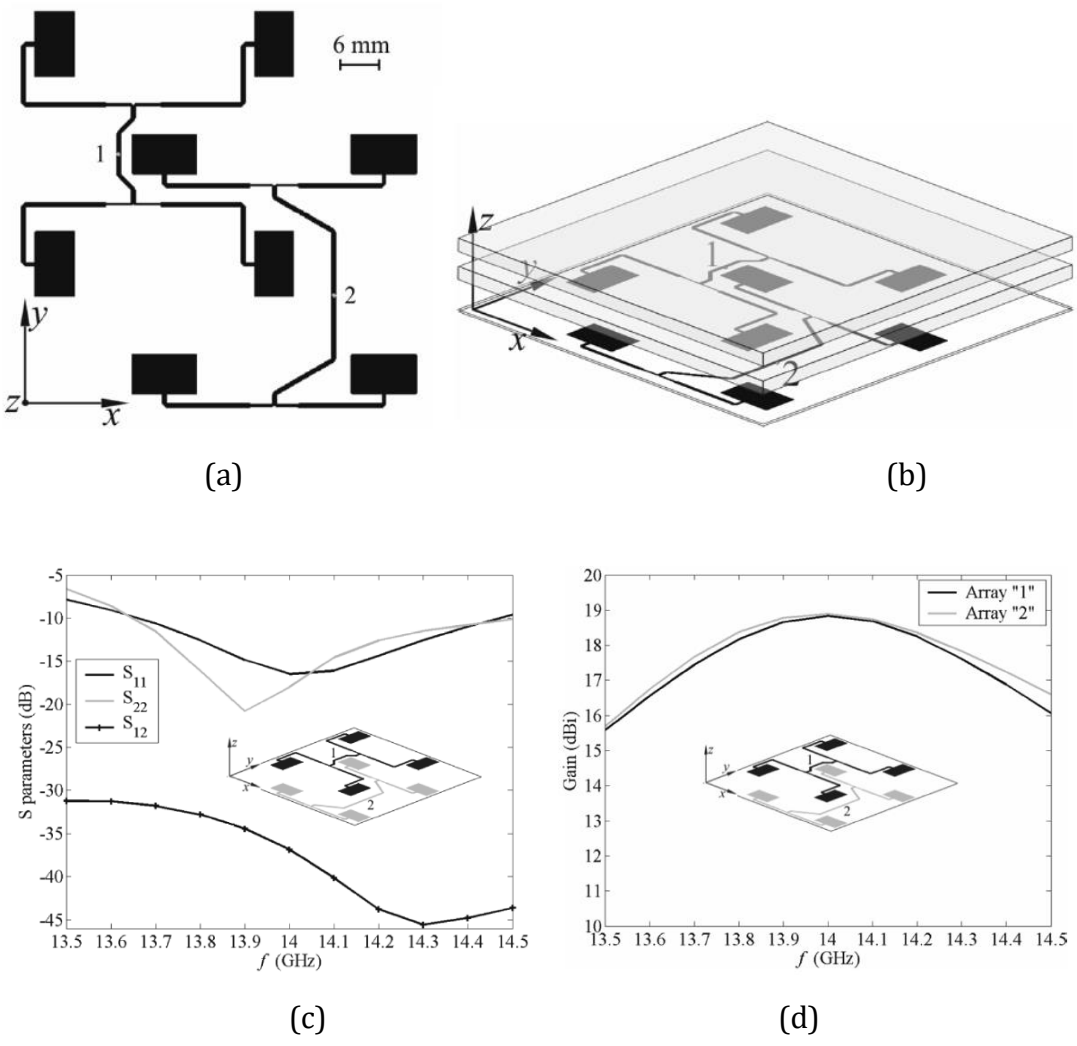

Fig. 1.5. Dual polarized antenna layout (a) 2-D view, (b) 3-D view, (c) Scattering parameters at the two ports of the dual-polarized antenna, and (d) Gain of the two interleaved arrays forming the dual-polarized antenna [7].

SATCOM employs reflector antennas with circularly polarized feed sources at their terminals for high directivity and relatively low cost. SATCOM requires two independent widely separated bands for the transmit (Tx) and receive (Rx) applications. In [8], a linear polarized dual-band EBG antenna has been designed as a feed source of an offset parabolic reflector antenna. The same phase center has been obtained at 5 GHz and 7.5 GHz, and the antenna is suitable to feed a reflector antenna with a focal-length-to-diameter (f/d) ratio of 1.2.

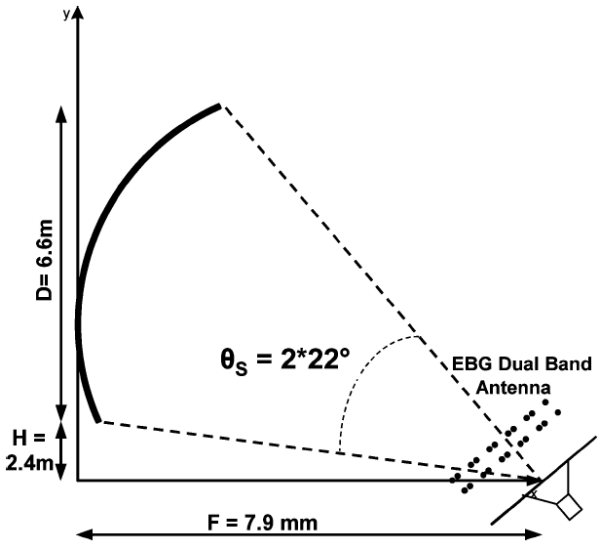

(a)

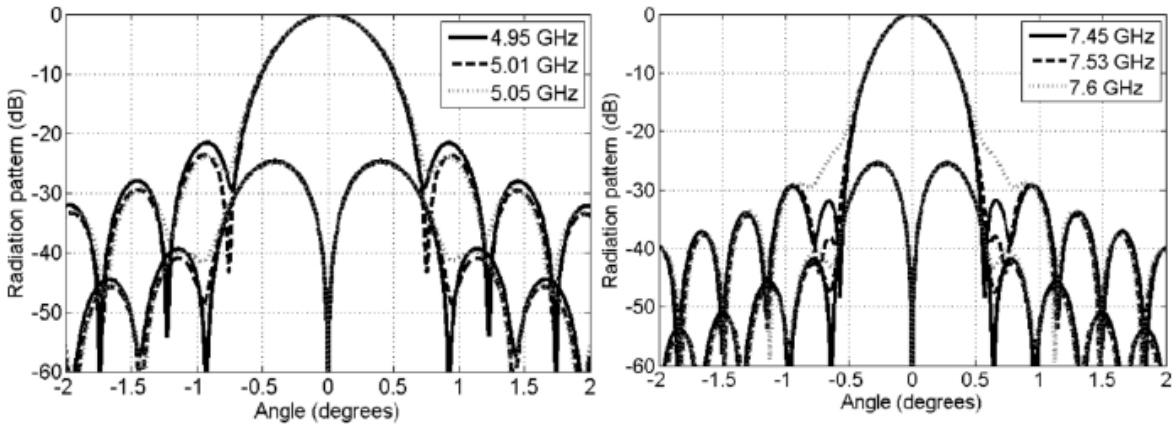

(b)

Fig. 1.6. (a) Reflector antenna geometry, and (b) Reflector antenna radiation patterns with the dual-band.

Based on the concept of array thinning proposed in [11], in the third project of this doctoral research, a right-hand circular polarized (RHCP) sparse array is designed inside a Fabry-Perot cavity (FPC) for Ku-band with a single layer PRS as a superstrate. A conventional left-hand circular polarized (LHCP) K- band array is designed on the same substrate layer with the same phase center as the Ku-band array. This shared aperture array is employed as a dual-band feed source for an offset parabolic reflector.

1.3 Simulation, Fabrication and Measurement Resources

The initial research begins with a concept supported by electromagnetic analysis and mathematical equations. Immediately after the concept is perceived, the simulation in electromagnetic software is to be done. High-Frequency Structure Simulator (HFSS), which is based on the Finite element Method, is the primary software tool for this doctoral research. Other supporting Electromagnetic software are Computer Simulation Technology (CST) Microwave Studio, Altair FEKO, TICRA Grasp, Keysight Advanced Design System (ADS), and Cadence AWR Microwave Office. Along with electromagnetic simulation, we need an analytical study to see whether the simulated results agree with the mathematical solution. MATLAB is employed as the programming software for analytical analysis. The Antenna and Microwave Laboratory (AML) at San Diego State University is equipped with almost all the resources to accomplish the electromagnetic simulation and mathematical study.

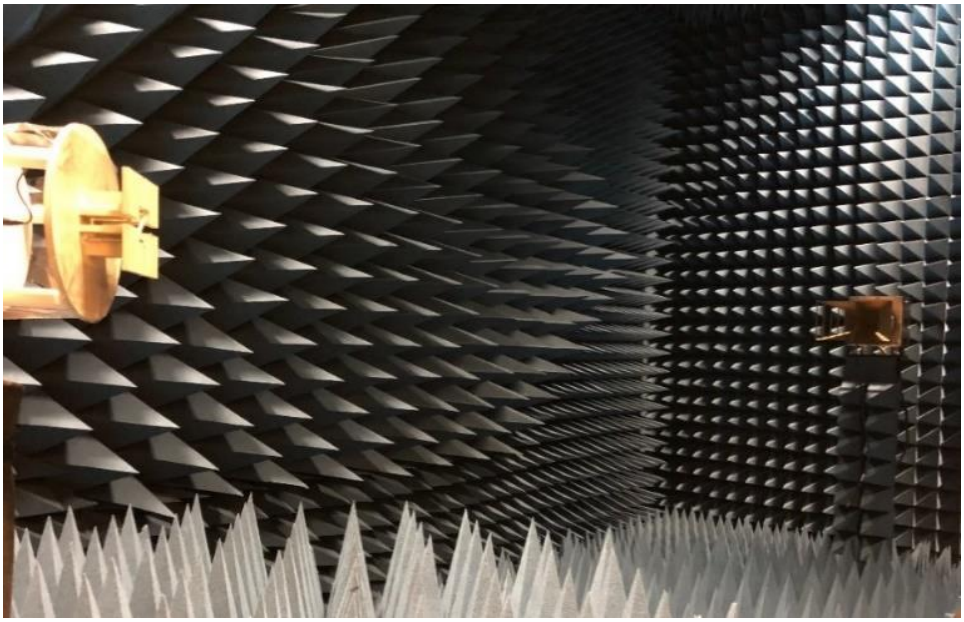

(a)

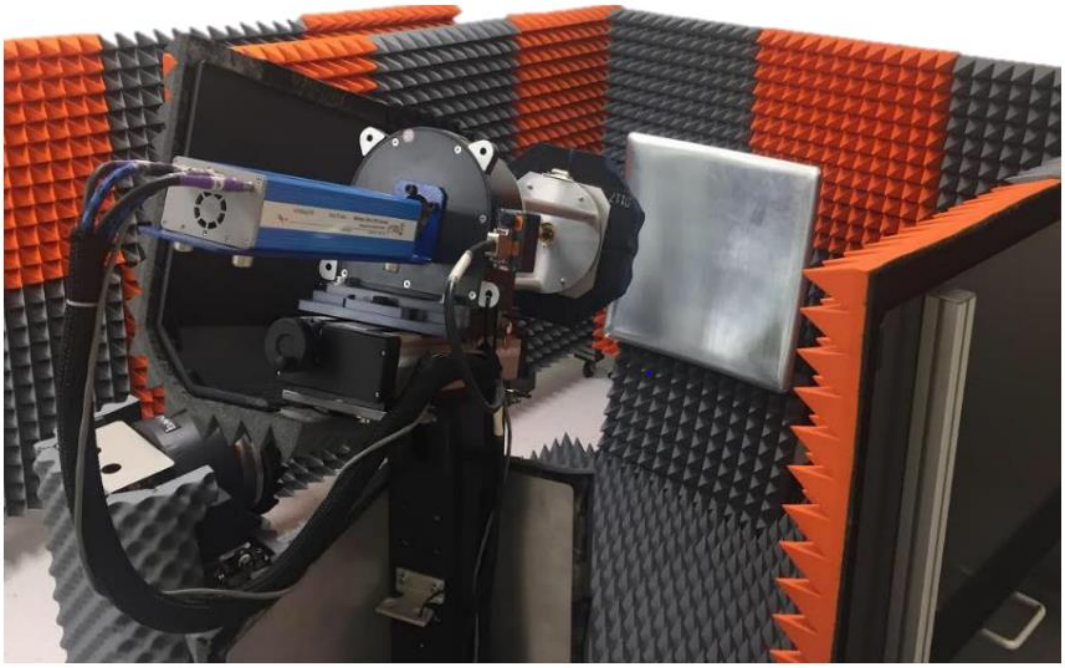

(b)

Fig. 1.8. Photograph of the (a) Anechoic Chamber (800 MHz-40 GHz), and (b) Mini-Compact Antenna Test Range (M-CATR) system at the Antenna and Microwave Laboratory, San Diego State University.

When desired results are obtained through a thorough parametric study in electromagnetic simulation, the prototype has to be fabricated and measured for impedance matching and radiation pattern to validate the simulation results. The first two projects of this doctoral research include complicated printed circuit boards and RFICs. Therefore, the all-metal 3D metal-printed phased array antenna prototype for the first project and the flat panel phased array antenna for the second project are fabricated by local fab-houses.

The Fabry Perot Cavity-based shared aperture array for the third project is fabricated in the Antenna and Microwave Laboratory (AML) in SDSU. The PCB milling machine, soldering station, and 3D printing machine are also available in the AML, SDSU.

The scattering parameters of the fabricated prototypes are measured using the Anritsu 37269D vector network analyzer (VNA) covering 40 MHz to 40 GHz and Keysight E5063A covering 100 kHz to 18 GHz available in AML, SDSU. The anechoic chamber in AML, SDSU, shown in Fig.1.8(a), is capable far-field radiation measurements in the frequency range from 800 MHz to 40 GHz with the ORBIT/FR 959 acquisition measurement software and provides measurement results for 2D/3D radiation pattern, realized gain, and polarization with a sense of rotation. Therefore, fabricated prototypes are measured for impedance matching and radiation patterns in the AML, SDSU. Apart from the first anechoic chamber shown in Fig. 1.18(a), the second anechoic chamber, shown in Fig. 1.18 (b), is a Mini-Compact Antenna Test Range (M-CATR) from Microwave Vision Group (MVG) for millimeter-wave antenna measurements up to 110 GHz, which has helped me to get a hands-on experience in mm-wave antenna measurement.

1.4. Conclusion

The theory of computational electromagnetics and relevant antenna technology is discussed in the following chapter. Chapter 3 is about the innovative 3D metal printed all-metal heat sink phased array antenna for Ku-band application. The novel flat panel transmit/receive phased array developed for NASA-funded project is elaborately described in Chapter 4.

Chapter 5 presents the design technique of a novel dual-band feed for a reflector antenna intended for SATCOM application. Chapter 7 is the conclusion and discussion about future possibilities.

Chapter 2

Computational Electromagnetics and Related Antenna Theory

2.1 Review of Computational Methods

Finite Element Method (FEM) is a computational tool for engineers and physicists, utilizing quick computations to solve large problems insoluble by analytical, closed-form expressions. The "Finite Element Method" is a procedure where a structure is subdivided into a large number of simple constituent units called finite elements, which are each solved using direct analytical methods, and then re-assemble the solution for the entire problem space as a matrix of simultaneous equations. Here, Ansys HFSS (High Frequency Structure Simulator) simulation tool is used to set up the FEM problem for the proposed research problems. A brief overview of the FEM method employed in HFSS is discussed in this section [10].

The model is subdivided into tetrahedral elements and a basis function, W_n is defined per tetrahedral. W_n is constructed on the basis of problem inputs and define conditions between nodal locations in the overall mesh of tetrahedra. The functions are simple and nonzero only within the tetrahedra. These basis functions are then multiplied by field equation. HFSS solves field equation derived from Maxwell's equations. Following are the steps in the HFSS FEM solution process.

The model is subdivided into tetrahedral elements and basis function, W_n is defined per tetrahedral. W_n defines conditions between nodal locations in the overall mesh of tetrahedra, based on the problem inputs. The functions are simple and nonzero only within the tetrahedra. These basis functions are then multiplied by field equation. Following are the steps in the HFSS FEM solution process.

HFSS solves field equation derived from Maxwell's equations:

$$\nabla \times \left(\frac{1}{\mu_r} \nabla \times \vec{E}\right) - k_0^2 \varepsilon_r \vec{E} = 0 \tag{2.1}$$

Integrating the result over volume, we get:

$$\int_v \left[W_n . \nabla \times \left(\frac{1}{\mu_r}\nabla \times \vec{E}\right) - k_0^2 \varepsilon_r W_n \vec{E}\right] dv = 0 \qquad (2.2)$$

Integration is replicated in thousands of equations for n=1, 2 ...N. Intent is to obtain N equations with N unknowns for solution. The equation is rewritten, using Green's and Divergence theorems:

$$\int_v \left[(\nabla \times W_n) . \nabla \times \left(\frac{1}{\mu_r}\nabla \times \vec{E}\right) - k_0^2 \varepsilon_r W_n \vec{E}\right] dv = \int_s (boundary\ term) ds \qquad (2.3)$$

The E-field is written as summation of unknowns, x_m, times same basis functions used in generating the initial series of equations:

$$\vec{E} = \sum_{m=1}^{N} x_m W_m \qquad (2.4)$$

Resulting equations allow solution of unknowns, x_m, to find E:

$$\sum_{m=1}^{N} x_m . \left(\int_v \left[(\nabla \times W_n) . \nabla \times \left(\frac{1}{\mu_r}\nabla \times \vec{E}\right) - k_0^2 \varepsilon_r W_n \vec{E}\right] dv\right) = \int_s (boundary\ term) ds \qquad (2.5)$$

Equation has the basic form $Ax=B$, where A is the basis functions and field equation, in a known N x N matrix 'x' is the unknowns to be solved for B is the excitation. In the matrix equation, A is a known NxN matrix that includes any applied boundary condition terms, B contains the port excitations which is voltage and current sources and incident waves. Once you have solved for x, we can find E.

The Finite-Element solution matrix has a number of known properties such as:

- Matrix is generally large, N on the order of tens of thousands.
- Matrix is generally sparse (matrix in which most of the elements are zero) matrix
- Only basis functions in the same tetrahedra result in nonzero element.
- Intelligent ordering of the mesh results in nonzero elements being gathered along the diagonal.
- Lossless problems will have only real nonzero elements.
- Lossy problems will have complex nonzero elements.
- Problems with standard excitations will have symmetric matrices.

• Problems with certain boundary conditions may have asymmetric matrices.

Due to its sparse and banded (diagonal band) nature, the matrix can be solved using different matrix decomposition techniques. HFSS uses an iterative process. HFSS uses the above process repeatedly, changing the mesh in a very deliberate manner, until the correct field solution is found. Matrix equations are thus formulated to solve for electromagnetic field behavior. The flowchart of the general design process in Ansys HFSS is illustrated in Fig. 4.1.

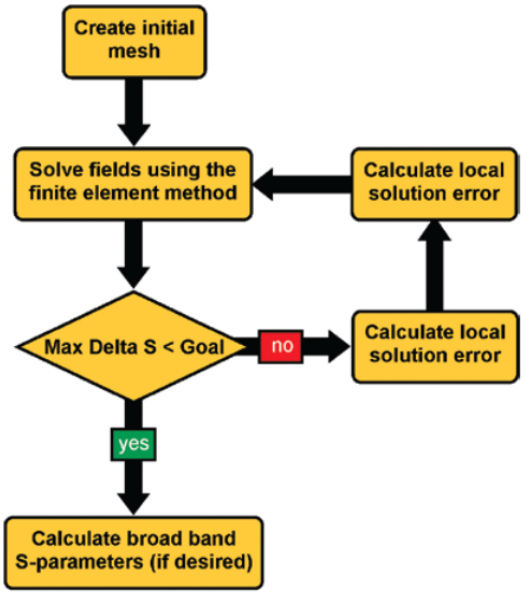

Fig. 2.1: Flowchart of the general design process in Ansys HFSS [10].

2.2. Phased Array Antenna (PAA)

2.2.1. Concept of PAA

The basic principle of electronic scanning phased array operation is that, by controlling the progressive phase difference between the radiating elements in an antenna array, the maximum radiation can be steered in any desired direction to form a scanning array. In phased array technology, the scanning must be continuous, and hence the system should be

capable of continuously varying the progressive phase between the elements, and phase shifters are employed to achieve this. The progressive phase can be obtained using analog or digital phase shifters to achieve continuous or discrete beam steering/scanning. Fig. 2.2 schematically describes the beam steering mechanism of a one-dimensional phased array antenna by application of a particular progressive phase shift $\Delta\varphi$.

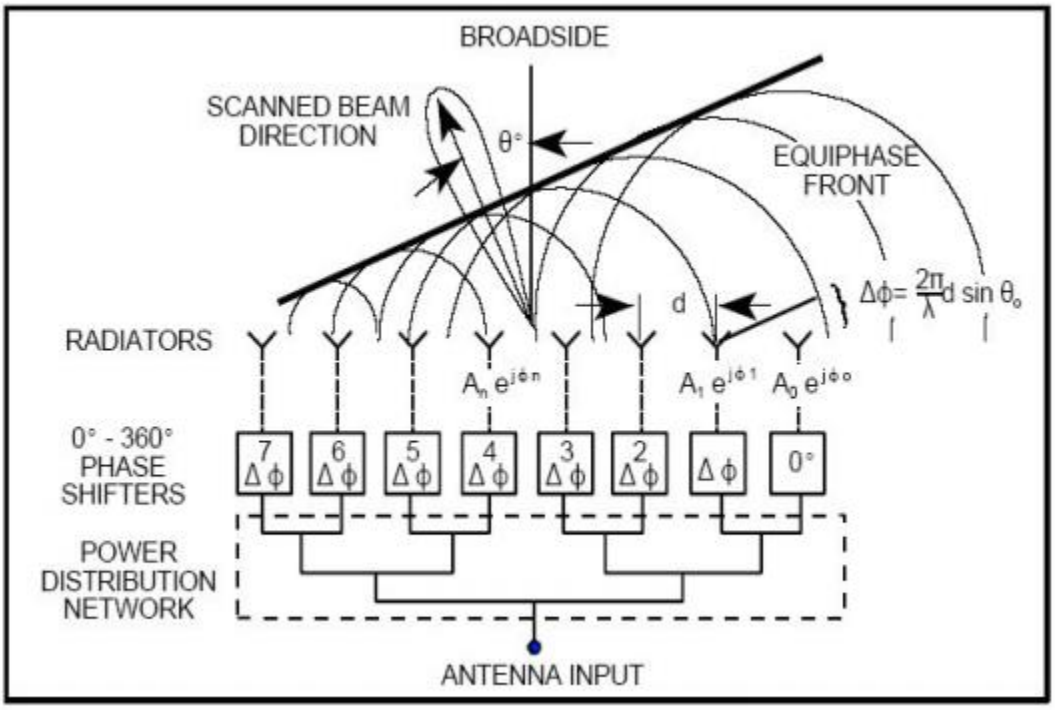

Fig. 2.2: Beam steering mechanism in one dimensional Phased Array Antenna [https://www.rfcafe.com/references/electrical/ew-radar-handbook/frequency-phase-effects-antennas.htm]

2.2.2. *N* Elements Linear Array with Uniform Amplitude and Spacing

A uniform array is an array of identical elements, with identical amplitude and each with a progressive phase shift. Let us consider a one-dimensional linear array, as shown in Fig. 5.2, where all the elements have identical amplitudes but each succeeding element has a β progressive phase lead current excitation relative to the preceding one. The array factor is evaluated by considering the elements as point sources [1].

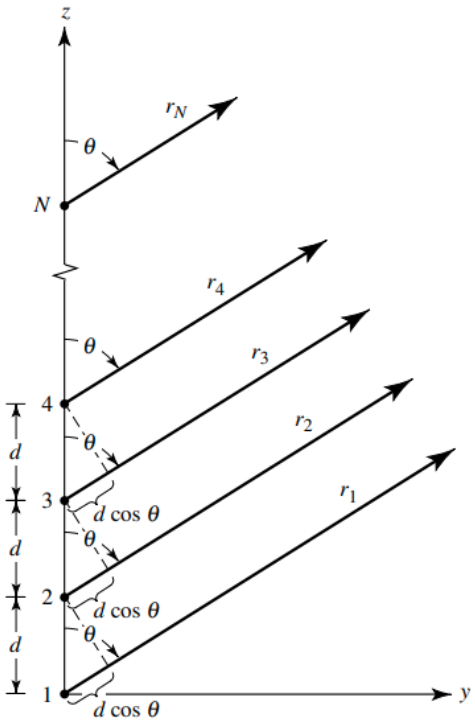

Fig. 2.3: Far-field geometry of *N*-element array of isotropic sources positioned along the *Z*-axis [1].

The array factor is given by

$$AF = \sum_{n=1}^{N} e^{j(n-1)(kdcos\theta+\beta)} \tag{2.6}$$

This can be simplified as

$$AF = \frac{\sin\left(\frac{N\psi}{2}\right)}{sin\left(\frac{\psi}{2}\right)} \tag{2.7}$$

where, $$\psi = kdcos\theta + \beta \tag{2.8}$$

or, assuming small ψ and normalizing we get,

$$AF = \frac{\sin\left(\frac{N\psi}{2}\right)}{\left(\frac{N\psi}{2}\right)} \tag{2.9}$$

For nulls in the array,

$$\sin\left(\frac{N\psi}{2}\right) = 0 \qquad where, n = 1,2,3 \ldots, N \neq N, 2N, 3N \ldots \tag{2.10}$$

For maximum of the array,

$$\frac{\psi}{2} = \pm m\pi \qquad where, m = 0,1,2, \ldots \tag{2.11}$$

2.2.3. Broadside Array and End-fire Array

To obtain the maximum radiation of an array directed normal to the axis of the array or in broadside direction, i.e., at θ=90°,

$$\psi = kdcos\theta + \beta|_{\theta=90^\circ} = kdcos90^\circ + \beta = 0 \tag{2.12}$$

Therefore,

$$\beta = 0^\circ \tag{2.13}$$

Thus, for the array factor to be directed in the broadside of the axis of the uniform linear array, all the elements must have the same phase excitation along with the same amplitude excitation. To avoid any grating lobes, the largest spacing between the elements should be less than one wavelength.

To obtain maximum radiation along the axis of the array (end-fire)

Either

$$\psi = kdcos\theta + \beta|_{\theta=0^\circ} = kdcos0^\circ + \beta = 0 \tag{2.14}$$

Therefore,

$$\beta = -kd \tag{2.15}$$

Or

$$\psi = kdcos\theta + \beta|_{\theta=180^\circ} = kdcos180^\circ + \beta = 0 \tag{2.16}$$

Therefore,

$$\beta = kd \tag{2.17}$$

If the spacing between two elements is half wavelength, end-fire exists in both directions simultaneously. Therefore, to generate only one end-fire maximum and to avoid any grating lobes, the maximum spacing between the elements should be less than half wavelength.

2.2.4. Phased Array

If the maximum radiation of the array is required to be oriented at any arbitrary angle θ_0 ($0^\circ \leq \theta_0 \leq 180^o$), the phase excitation β between the elements must be adjusted so that

$$\psi = kdcos\theta_0 + \beta = 0 \tag{2.18}$$

Therefore,

$$\beta = -kd\ cos\theta_0 \tag{2.19}$$

Thus, by controlling the progressive phase difference between the elements, the maximum radiation can be steered in any desired direction to form a scanning array. Since in phased array technology the scanning must be continuous, the system should be capable of continuously varying the progressive phase between the elements. In practice, this is accomplished electronically by the use of ferrite or diode phase shifters.

2.2.5. *N*-Elements Along *X*-, *Y*-, and *Z*-Axis

Let us assume a linear array of *N* isotropic elements are positioned along the either *X*- or *Y*- or *Z*-axis and are separated by a distance *d*. Fig. 5.3 shows the arrangement: Linear array of *N* isotropic elements along *X*-axis.

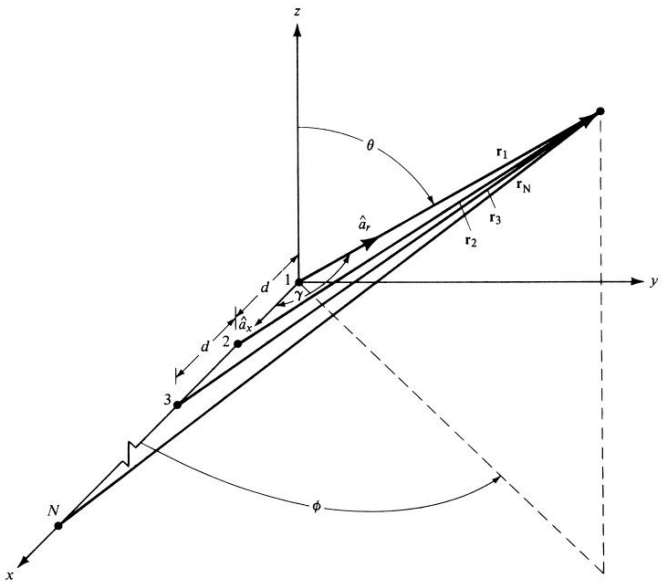

Fig. 2.4: Linear array of *N* isotropic elements along *X*-axis [1].

The amplitude excitation of each element is a_n, and there is a progressive phase excitation β between the elements. For far-field observations, the array factor can be written as:

$$AF = \sum_{n=1}^{N} a_n e^{j(n-1)(kdcos\gamma+\beta)} \quad = \quad \sum_{n=1}^{N} a_n e^{j(n-1)\psi} \tag{2.20}$$

where,

$$\psi = kdcos\gamma + \beta \tag{2.21}$$

In general, the angle γ can be obtained from the dot product of a unit vector along the axis of the array with a unit vector directed toward the observation point.

When the array is along *Z*- axis,

$$cos\gamma = \widehat{a_z}.\widehat{a_r} = cos\theta \tag{2.22}$$

When the array is along *X*- axis,

$$cos\gamma = \widehat{a_x}.\widehat{a_r} = cos\phi\ sin\theta \tag{2.23}$$

When the array is along *Y*- axis,

$$cos\gamma = \widehat{a_y}.\widehat{a_r} = cos\theta\ sin\phi \tag{2.24}$$

2.2.6. A Rectangular Planar Array

Fig. 5.4 shows a rectangular array, where *M* elements are equispaced at a distance of *dx* along *X*-axis and *N* elements are equispaced at a distance of *dy* along *Y*-axis, and there is a progressive phase shift of βx in each row along *X*-axthe is and βy in each column along *Y*-axis.

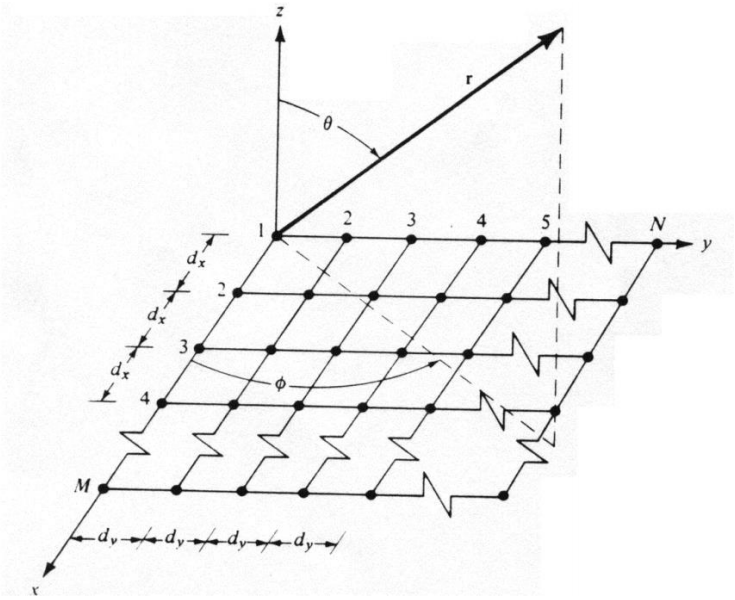

Fig 2.5: Planer rectangular antenna array of isotropic elements [1].

The array factor is given by

$$AF = \left\{\frac{1}{M}\ \frac{\sin\left(\frac{M\psi_x}{2}\right)}{\left(\frac{M\psi_x}{2}\right)}\right\}\left\{\frac{1}{N}\ \frac{\sin\left(\frac{N\psi_y}{2}\right)}{\left(\frac{N\psi_y}{2}\right)}\right\} \tag{2.25}$$

where,

$$\psi_x = kd_x sin\theta cos\phi + \beta_x \tag{2.26}$$

$$\psi_y = kd_y sin\theta sin\phi + \beta_y \tag{2.27}$$

If the principal maximum is specified by (θ_0, ϕ_0), then the progressive phases βx and βy must satisfy:

$$\beta_x = -kd_x sin\theta_0 cos\phi_0 \tag{2.28}$$

$$\beta_y = -kd_y sin\theta_0 sin\phi_0 \tag{2.29}$$

2.2.7. Beamwidth and Directivity of Phased Array

The beamwidth and sidelobe level of an array antenna are depend on the chosen aperture taper of the array. Antenna sidelobes are reduced by applying tapered excitation so that elements at the array center are excited more strongly than those near the edge. However, tapering reduces directivity, and hence broadens the array beamwidth. The half-power beamwidth of the radiation pattern in the principal planes of a rectangular array at broadside is given by the following [2]:

$$\theta_{BMW} = 0.886\, B_b\, \lambda/L \tag{2.30}$$

Where, B_b is the beam broadening factor which is unity for the uniformly illuminated array, and L is the length of rectangular array in the plane of scan.

For a large array, the beamwidth calculated from the above expression increases approximately as $(1/\cos\theta)$ with scanning.

The maximum directivity of a planer array is given by the following:

$$D_{max} = 4\pi A_{cell}/\lambda^2 \tag{2.31}$$

Where, $A_{cell}=L_xL_y$, is the area of each unit cell.

Therefore, the directivity for a large scanned array is given by the following:

$$D = D_{max} \cos\theta \tag{2.32}$$

However, the array gain and directivity are related by the following equation:

$$G = \epsilon_L (1 - |\Gamma|^2) D \tag{2.33}$$

The reflection coefficient Γ varies as a complex function of the scan angle because of the impedance mismatch due to interelement coupling. However, it is often convenient to combine both factors into one and assume scan loss in the form of some power of the cosine $(\cos\theta)^n$, where *n* is usually approximately $3/2$.

2.2.8. Active Element Pattern

The isolated elements are analyzed to predict the parameters of an element like resonant frequency, impedance bandwidth, polarization, general pattern shape, and so forth. But elements generally behave very differently in an array than when isolated. The active element pattern (AEP) is defined as the element pattern of the center element when only the center element is excited but all other array elements are matched terminated. The array scan behavior can be characterized by using the active element pattern (AEP).

2.2.9. Maximum Element Spacing of Phased Array

A criterion for determining the maximum element spacing for planar array, with element spacing *dx=dy=d,* scanned to a given scan angle θ_0 at frequency *f* is to set the element spacing in such a way that the nearest grating lobe is at the horizon. The condition is given by the following [see Fig. 2.5 for coordinate system and assume array along X-axis]:

$$\frac{d}{\lambda} \leq \frac{1}{1+|sin\theta|} \tag{2.34}$$

The condition requires spacing not much greater than one-half wavelength for wide angles of scan.

2.2.10. EIRP and G/T of an Active Phased Array

The effective isotropic radiated power (EIRP) of an active array per polarization is given by [2]:

$$EIRP_{perPol,P1dB} = 20log_{10}^{(N)} + G_{element} + P_{element,P1dB} \tag{2.35}$$

Where $P_{element,P1dB}$ is the input power for each radiating element per polarization.

The EIRP of the array for circular polarization is given by:

$$EIRP_{LHCP,P1dB} = 20log_{10}^{(N)} + G_{element} + P_{element,P1dB} + 3dB \tag{2.36}$$

The brief calculation for the gain over noise temperature of the active array (G/T) is as follows:

The system noise temperature of the array is calculated as:

$$T_{system} = T_s + T_{a'} \tag{2.37}$$

$$T_{a'} = \eta_{ant} T_a + T_0(1 - \eta_{ant}) \tag{2.38}$$

T_a is the scene temperature, and T_0 is the room temperature.

$$\eta_{ant} = 10^{\frac{-L_{ant}}{10}} \tag{2.39}$$

Where, L_{ant} is Antenna loss that can be found from simulation

$$T_s = T_0(F_s - 1) \tag{2.40}$$

Where F_s is the Noise Figure of the receiver/transmitter/RFIC (when RFIC are employed).

The gain over noise in is given as:

$$\frac{G}{T} = G_{ant} - 10\, log_{10}^{(T_{system})} \tag{2.41}$$

2.2.11. Beamforming Technology

It is becoming more common to use solid-state transmit/receive (T/R) modules at some subarray level or at each element, as shown in Fig. 2.6. Here, separate feeds are used for transmit and receive because and each port is routed to a T/R module, where it passes through a power amplifier on transmit or low-noise amplifier on receive path accompanied by a phase shifter and variable gain attenuator. The solid-state module usually includes a circulator for separating the two channels.

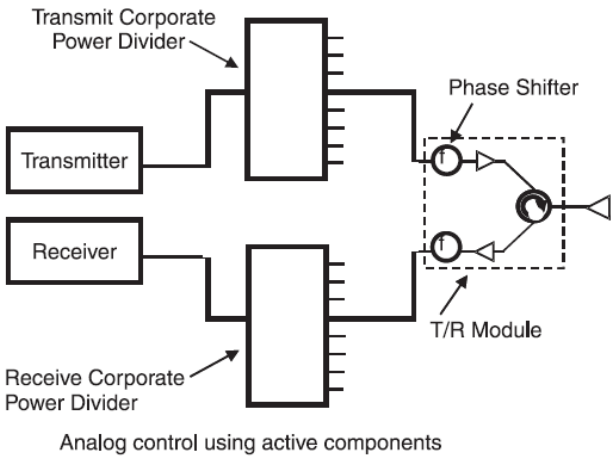

Fig. 2.6: Array control technology with analog control using active components [2].

2.3 Fabry Perot Cavity (FPC) Antenna

The Fabry-Perot Cavity (FPC) resonator can also be used in the design of high-gain antennas [11], where a partially reflection surfaces (PRS) is placed over a primary radiator at a predetermined height, and the electromagnetic wave emanating from the primary radiator experiences multiple reflections and transmissions between the PRS and the ground plane, as shown in Fig. 2.7. One part of the electromagnetic wave is transmitted through the PRS and the other part is reflected back to the ground plane by the PRS. The reflected wave is totally reflected by the ground plane and is incident to the PRS with the same angle, and therefore the secondary wave is again partially transmitted and reflected. Forward radiation can be enhanced remarkably by means of in-phase bouncing when the spacing between these two plates is about integer times of half wavelength.

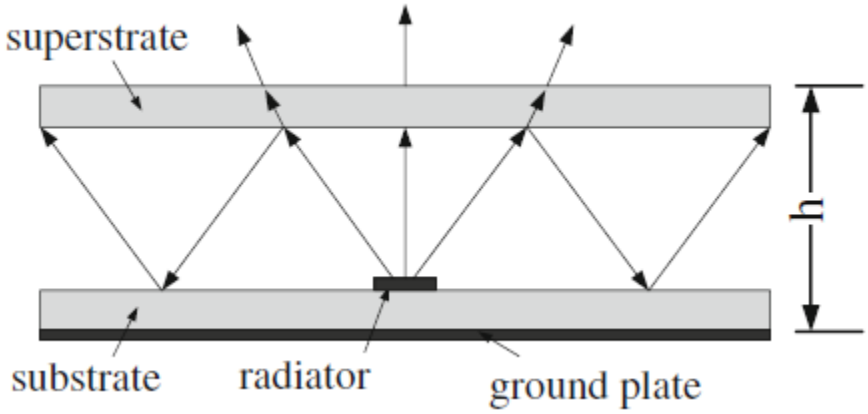

Fig. 2.7. The schematic model of the FPC antenna [13].

2.4. Reflector Antenna Theory

2.4.1. Physical Optics (P.O.) for Reflector Analysis

Physical optics assumes that a surface current of J_s is excited on the reflector surface by the incident field from the feed source, and the incident field is a known quantity. The surface current is given by the following equation [1]:

$$J_s = \hat{n} \times H^{incident} \tag{2.42}$$

If the surface current can be calculated, the far field can be calculated as follows:

$$E^{farfield} = -j\omega\mu \frac{e^{-j\beta r}}{4\pi r} \iint_{S_r} [J_s - (J_s.\hat{r})\hat{r}]\, e^{j\beta \hat{r}.r'} ds' \tag{2.43}$$

HFSS employs P.O. based technique to evaluate the far field pattern of the reflector.

2.4.2. Offset Parabolic Reflector Antenna

Parabolic reflector can take two different shapes, parabolic right cylinder and paraboloid, as shown in Fig.2.8 (a) and (b), respectively.

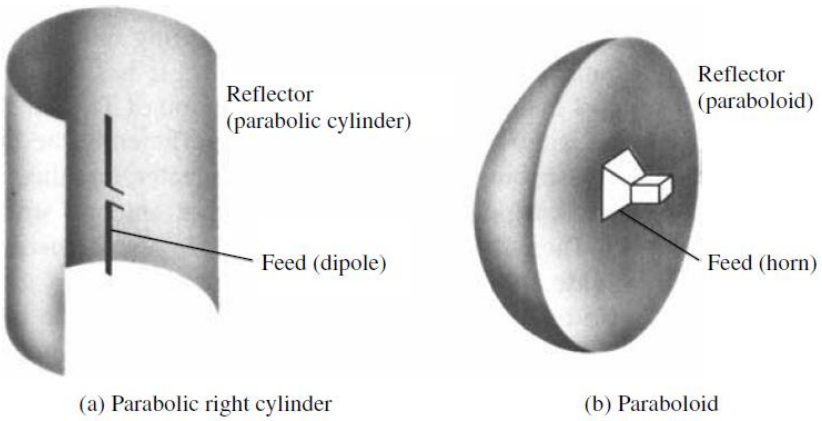

Fig. 2.9. Parabolic right cylinder and paraboloid [1].

In parabolic right cylinder, shown in Fig. 2.9(a), energy is collimated at a line that is parallel to the axis of the cylinder through the focal point of the reflector. The reflector configuration, shown in Fig. 2.9(b), is formed by rotating the parabola around its axis, and it is referred to as a paraboloid.

Offset-reflector designs reduce aperture blocking in addition to supporting a larger focal length to diameter ratios while providing acceptable structural rigidity. However, offset-reflector configurations generate cross-polarized fields in case of linearly polarized feed, and squinting of the main beam from boresight in case of Circularly polarized feeds.

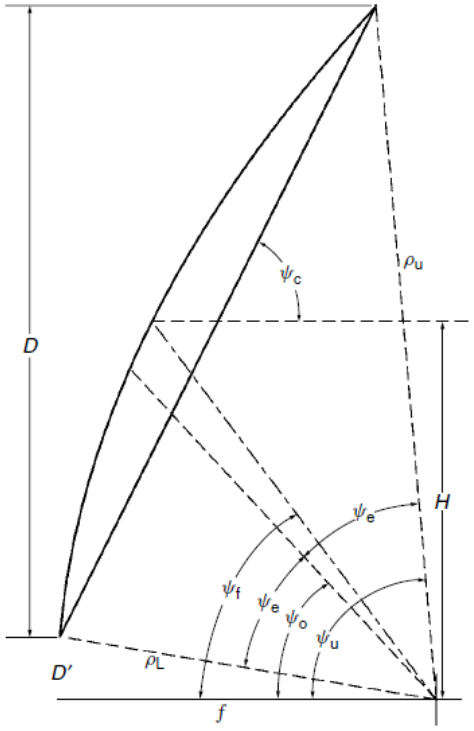

Fig. 2.8. An offset-fed parabolic reflector geometry [12].

Fig. 2.8 shows an offset-fed parabolic reflector geometry [12]. The aperture plane projects to a circle, whereas the rim shape is an ellipse. The angle from the axis of the parabola to the center of the cone of the reflector is given by φ_0, and the angle subtended by the reflector about this centerline is given by $2\varphi_e$. The aperture plane diameter is D, the height of the center is H, and the lower rim offset $D' = H - D/2$. The reflector parameters are given by the following equations:

$$\varphi_0 = \tan^{-1} \frac{16fH}{16f^2 + D^2 - 4H^2} \tag{2.44}$$

$$\varphi_e = \tan^{-1} \frac{8fD}{16f^2+D^2-4H^2} \tag{2.45}$$

The feed is directed at an angle φ_f from the z-axis to the center of the projected diameter.

$$\varphi_f = 2 \tan^{-1} \frac{H}{2f} \tag{2.46}$$

The rim lies in a plane at an angle φ_c with respect to the z-axis

$$\varphi_c = \tan^{-1} \frac{2f}{H} \tag{2.47}$$

The parabolic cylindrical reflector provides of a wide-angle beam steering along the cylindrical axis and therefore, the phased array can be used as a feed of a cylindrical parabolic reflector to achieve one dimensional scanning.

2.5 Conclusion

A brief review of the relevant antenna theory is presented in this chapter. The thesis is focused on design and development of innovative phased array antennas for SATCOM and 5G applications, and Fabry-Perot Cavity (FPC) based circularly polarized feed design for reflector antenna intended for SATCOM application, and finally a hybrid phased array and reflector system. Therefore, the basic theory of phased array antenna, FPC antenna and reflector antenna is presented in a nut shell in this chapter. The remaining part of the thesis is comprised of the theory, analysis, design, simulation and measurement results for innovative phased array antennas and feed for reflector antenna.

Chapter 3

Investigations of Heat Sink Property of a Novel Dual Linear Polarized Low Cross-Polarization X-Band Phased Array Antenna Employing Silicon RFICs Based Beamforming Network

3.1. Introduction

Naval ships require high-speed wireless communications to improve their image sharing, multimedia data sharing, and accelerate better coordination in battlefield operations. The antennas that support high data rate wireless network require a wide impedance bandwidth, stable radiation patterns, high gain, and beam steering properties. Electronic scanning phased array antenna radiates huge amount of microwave power in an intended direction, as well as provides instantaneous beam steering [1], [2]. Recently phased array antennas with integrated beamforming networks comprised of silicon RFICs have gained major attention.

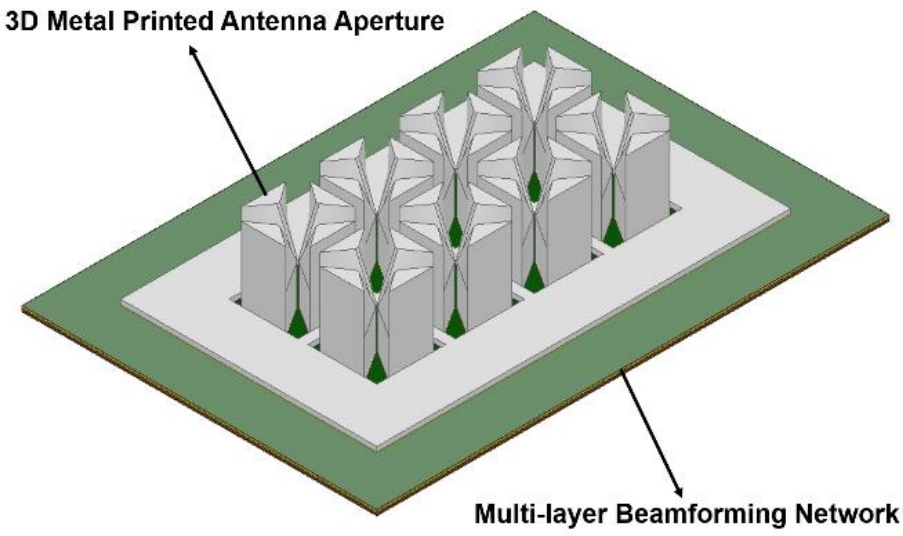

Fig. 3.1. All metal 3D metal printed dual linear polarized 4x2 phased array heat sink antenna with integrated beamforming.

Beam steering performance of phased arrays working at Ku- and Ka- bands using Anokiwave RFICs are proposed in [13] and [14]. In [9], a RFIC based 8 × 4 dual linear polarized stacked patch phased array antenna is employed as a feed source for a reflector antenna. The temperature measured on the antenna aperture side of the patch array using the infrared (IR) camera is 58.4ºC. The measured peak power consumption of this antenna was 6.3W (3.5A, 1.8V). The coplanar waveguide (CPW) transmission lines along with ground via fencing is employed to excite the driven patch, where the ground vias help in impedance matching as well as in heat spreading. In [15], effect of temperature on the electromagnetic performance of active phased array antennas is discussed.

With the recent advancement of the commercial silicon beamforming chipsets, the heat generated by the chips in the beamforming network (BFN) attached with the antenna aperture can become a problem, and hence cooling arrangement should be included to solve this. Again, heat sinks are made of metal materials, and if heat sink dimensions are comparable to the wavelength at operating frequency, it can cause unwanted electromagnetic interference [16]-[18]. As radiation from heatsinks is usually undesirable, bonding posts are employed to ground the heatsink structure to a nearby printed circuit board (PCB) to mitigate heatsink radiation in [19] and [20].

An antenna structure that can serve as radiator as well as heat sink, can be proposed as a solution for the phased array antennas that employ RFICs based BFN. A radiator working as heat sink as well, was proposed in [21], where a heat sink loaded patch with improved radiation efficiency was explored. In [22], a 3-D fractal heatsink antenna is proposed, with improved radiation efficiency and gain and lower thermal resistance in comparison to a conventional fin shaped heat sinks. However, these proposed configurations consist of a single antenna working at low frequencies. In [23], and [24], antenna working as heat sink is studied for mm-wave applications.

One important aspect for the heat sink antenna is the choice and placement of thermal spreader between the heat source and heatsink. The metallic thermal via is a widely used structure as in [3] and [4]. In [3], a single polarized stepped notch antenna attached to a flat multi-layered printed circuit board (PCB), working at Ku-band, is proposed which, along

with serving as a radiator, provide a thermal heat sink for active arrays as well. The heat generated by the active devices, such as high power amplifiers (HPA) or low noise amplifiers, passes through the PCB, into the antenna aperture through plated holes which provide the principal heat path. A thin radome is placed above the 26 x 11 notch array, and a maximum temperature of 60°C is noted with 40° C inlet air flow of 0.425 m^3/s, and a heat load of 50 W. In [4], a single polarized 4x4 heat sink antenna array on low-temperature cofired ceramic (LTCC) substrate is proposed, where the antenna element is a horn-like structure that consists of an open-ended waveguide and two vertical metallic fins, and the feeding network is comprised of the substrate integrated waveguides (SIWs) with numerous metallic vias, which in turn, helps to transfer the heat from chips to the heatsink, and temperature reduction of 40.1°C is achieved.

In [25], preliminary study on a 4 ×8 dual linear polarized phased array antenna, comprised of all metallic radiators, serving also as heat sink as well, is presented for Ku-band wireless communication applications.

In this research project, a 4x2 dual linear polarized phased array antenna, as shown in Fig. 3.1, with all metal 3D printed radiating elements, is thoroughly investigated for heat sink property. Considering the fact that we will be using X-band Anokiwave chips (AWMF-0101) for the beamforming network, the radiator is designed to cover 8.5-11.5 GHz and shaped intuitively in such a way that the antenna array aperture can serve as a heat sink as well. A design principle of this new wideband metallic radiator is provided in the following sections. The antenna aperture is integrated with a multilayered BFN employing Anokiwave RFICs. The scanning performance and thermal analysis of the structure is presented here which is discussed in the later sections.

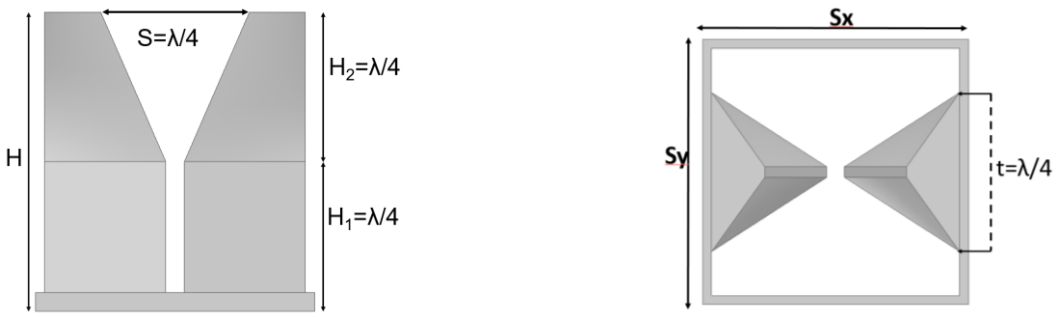

(a) (b)

Fig. 3.2. The single polarized standalone antenna (a) side view, and (b) top view.

3.2. Study of the standalone radiating element

Initially, a two-armed unique radiator surrounded by a metal ring, is intuitively designed for X-band applications in such a way that it will be working as a heat sink as well as a wideband radiator. The top view and side view of the proposed standalone radiator is shown in Figs. 3.2(a) and 3.2(b) with specified dimensions where λ corresponds to the center frequency (9.50 GHz). The standalone radiator is fed by a lumped port. The radiator has two parts: two shaped flared vertical arms and one metal ring around the two arms. The two-armed structure is combined with the outer metal ring which in turn radiates like a rectangular large loop antenna of $\lambda/2$ x $\lambda/2$ cross-section, thereby improving the gain of the antenna. This metal ring helps in the fabrication of the array aperture and its integration with the beamforming board in addition to improving radiation performance. The peak accepted gain versus frequency for a radiator with and without metal ring is shown in Fig. 3.3(a). From Fig. 3.3(a), it is clear that the proposed radiator is wideband subject to impedance matching can be achieved. Also, we can see that the peak accepted gain improves by approximately 1.5 dB towards the lower end and to approximately 1 dB towards the higher end of the bandwidth when the ring is employed. To further clarify the contribution of the ring, the radiation pattern of the only rectangular ring (without the two-armed structure) atop BFN stack up (described in section III) at 9.50 GHz is shown in Fig. 3.3(b), which shows that the ring is radiating in broadside direction. Here the ring is not fed like a

conventional loop antenna and therefore, it is not properly matched for the operating band. However, it is getting induced excitation through the trapezium shaped metal plate (shown later in Fig. 3.8(b)) where the two-armed radiating element is attached with BFN, hence it works as an inefficient loop radiator.

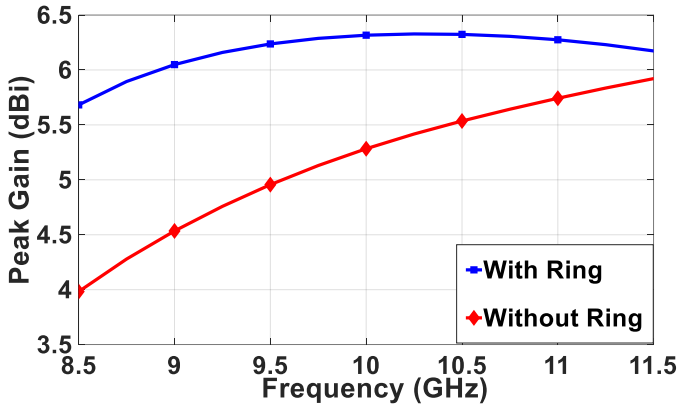

(a)

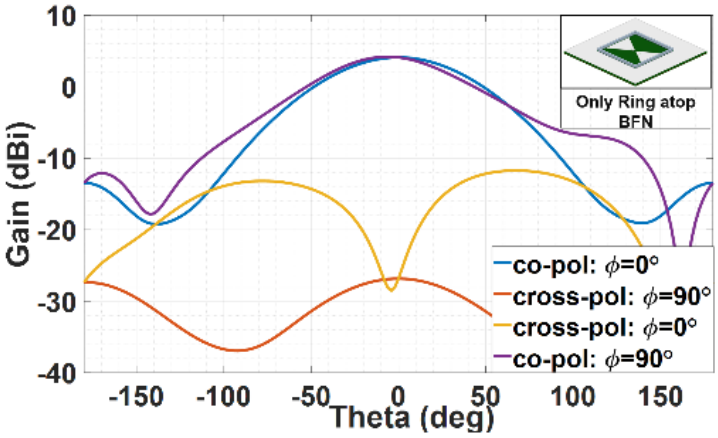

(b)

Fig. 3.3. (a) Peak gain versus frequency for the single polarized standalone radiator with and without metal ring, and (b) Radiation pattern of the only metal ring atop BFN at 9.50 GHz (without two-armed radiator).

The radiator is designed with a target to cover 8.5-11.5 GHz impedance bandwidth which includes the bandwidth offered by RFICs employed for the BFN. The radiator dimensions are optimized for X-band through thorough parametric study. It is clear from the peak gain versus frequency curves in Fig. 3.4 that the overall radiator height, $H = H_1 + H_2$, should be $\lambda/2$ corresponding to 9.50 GHz to get the best performance. After a thorough parametric study, it is observed that optimum combination of the flared and non-flared heights of the radiator is $H_1=H_2$ = 8 mm, whereas the width is t = 8mm and flare of the radiator, S=8mm, which is $\lambda/4$ at 9.50 GHz. The radiator is surrounded by a square metal ring of overall dimensions $\lambda/2\times\lambda/2$ corresponding to 9.50 GHz. The radiation pattern of the single polarized radiator at 9.50 GHz is shown in Fig. 5. The radiation pattern shows a peak realized gain of 5.4 dBi, in addition to the co- to cross-polarization separation of 17 dB.

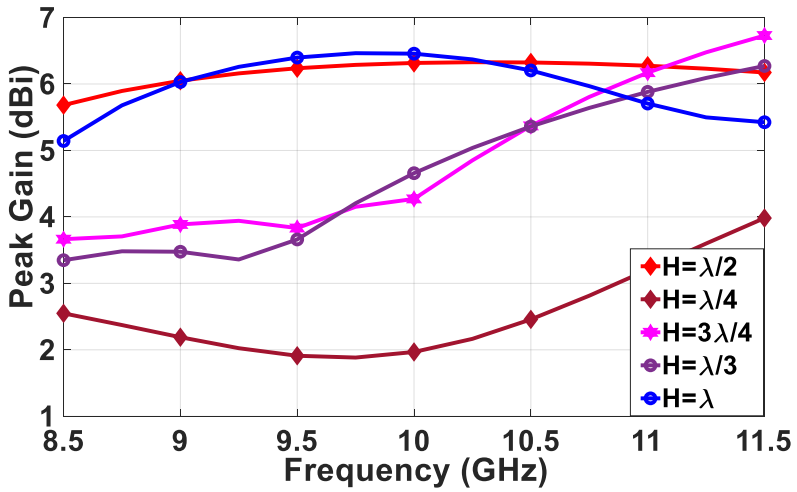

Fig. 3.4. Peak gain versus frequency for the single polarized standalone radiator for different heights.

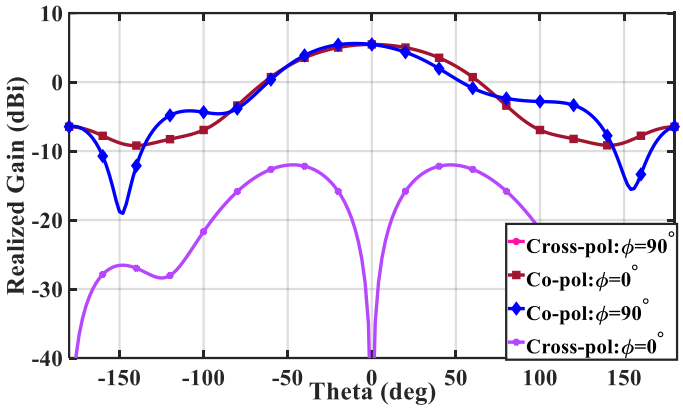

Fig. 3.5. Radiation pattern of the single polarized standalone radiator at 9.50 GHz.

3.3. Heat sink property of the radiating element

We have employed Ansys Icepak for the heat sink study. Ansys Icepak is based on Navier-Stoke's equations [26]. Navier-Stoke's equations of fluid mechanics involves partial differential equation that describes the flow of incompressible fluids. Ansys Icepak solves the Navier-Stokes equations for transport of mass, momentum, and energy. The governing equations for Ansys Icepak are as follows [26]:

(i) The Mass Conservation Equation:

$$\frac{\partial \rho}{\partial t} + \nabla.(\rho.\overrightarrow{v}) = 0 \tag{3.1}$$

(ii) Momentum Equation:

$$\frac{\partial(\rho\vec{v})}{\partial t} + \nabla.(\rho.\vec{v}\vec{v}) = -\nabla p + \nabla.(\bar{\bar{\tau}}) + p\vec{g} + \vec{F} \tag{3.2}$$

where, stress tensor is given by,

$$\bar{\bar{\tau}} = \mu\left[(\nabla\vec{v} + \nabla\vec{v}^T) - \frac{2}{3}\nabla.\vec{v}.I\right] \quad (3.3)$$

Here, p is the static pressure, $p\vec{g}$ is the gravitational body force, and $\vec{F}$ contains other source terms. And μ is the molecular viscosity, I is the unit tensor, and the second term on the right-hand side is the consequence of volume dilation.

(iii) Energy Conservation:

$$\frac{\partial}{\partial t}(\rho h) + \nabla.(\rho h\vec{v}) = \nabla.[(k + k_t)\nabla T] + S_h \quad (3.4)$$

where, sensible enthalpy is given by

$$h = \int_{T_{ref}}^{T} c_P dT \quad (3.5)$$

where, T is the temperature, T_{ref} is 298.15˚K and ρ is the density. Here, k is the molecular conductivity and k_t is the conductivity due to turbulent transport.

$$k_t = c_p\mu_t/Pr_t \quad (3.6)$$

The source term S_h takes into account any volumetric heat sources defined by the user.

$$\frac{\partial}{\partial t}(\rho h) = \nabla.(k\nabla T) + S_h \tag{3.7}$$

A conduction equation, that contains the heat flux due to conduction and volumetric heat sources within the solid, is solved by Icepak in conducting solid regions.

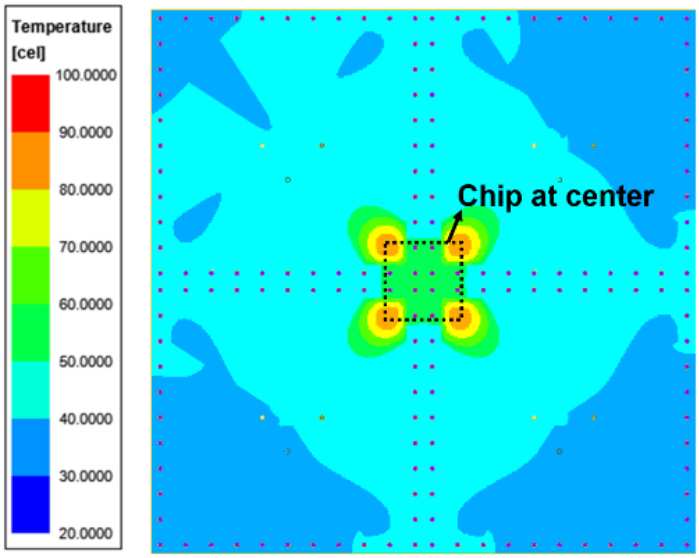

Fig. 3.6. Temperature distribution of the BFN stack-up without antenna aperture (heat sink) with a RFIC of measured peak power consumption of 1.35 Watts below it.

The Anokiwave RFIC (AWMF-0101) employed in our BFN design has measured peak power consumption of 1.35 Watts which is dissipated as heat. Each chip feeds four dual polarized radiating elements simultaneously. Thus, each 2x2 subarray is fed by one RFIC source which in turn shares heat dissipation resulting from the measured peak power consumption of 1.35 Watts. The radiators are realized using the 3D metal printed process and hence we

considered solid aluminum alloy (*AlSi10Mg*, conductivity 600000 S/m) for all the radiating element simulations. For thermal analysis, no forced air flow or no forced cooling arrangement is considered, and there is opening all around the antenna with air at room temperature i.e. 26.85°C (300˚K) and a velocity of 0.1m/sec against gravity (indoor air flow can be assumed as 0.1m/sec).

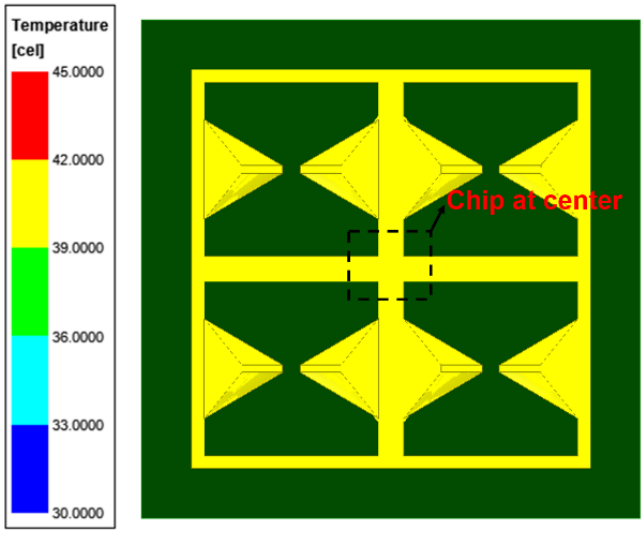

(a)

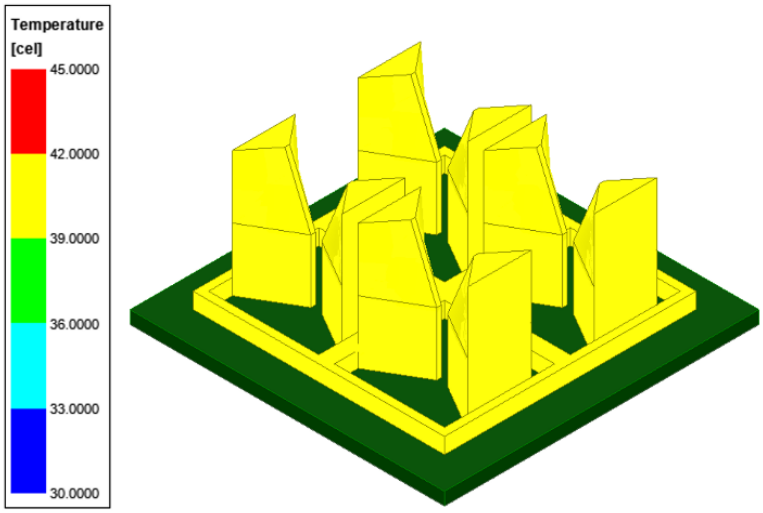

(b)

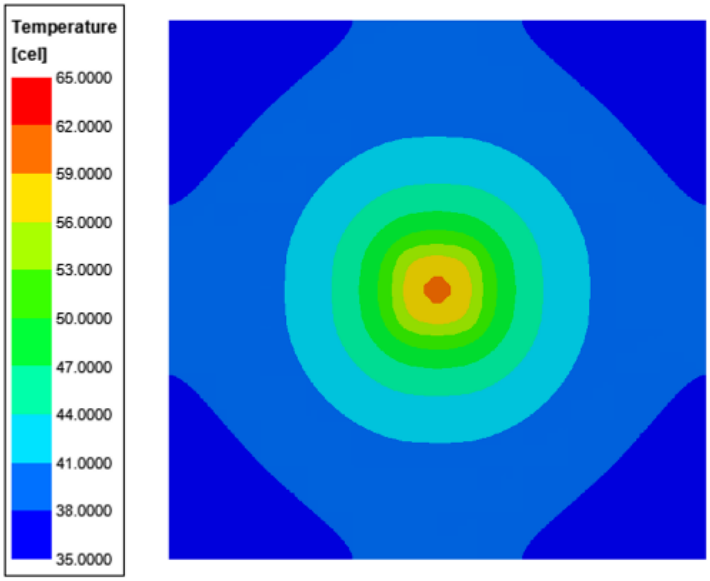

(c)

Fig. 3.7. Temperature distribution of 2x2 all metal heat sink antenna atop a RFIC with the peak power consumption of 1.35 Watts (a) top view, (b) isometric view, and (c) bottom view.

Before describing thermal analysis of the proposed 2x2 subarray, we present the thermal analysis of the BFN stack-up of this subarray (Fig. 3.6) without the proposed antenna structure atop it, assuming the chip at center below BFN has power consumption of 1.35 Watts. We noted that the maximum temperature, without heat sink, ranges up to 90°C. Here, it should be noted that the temperature distribution has four peaks at four corners of the chip, whereas temperature at the center position of the chip is lower than the maximum temperature. This is due to the presence of metal vias at the center of the stack up (as shown in Fig. 3.6) which work as thermal spreaders.

Now, a single polarized 2x2 subarray antenna atop BFN is simulated with the same 1.35 Watts at the center below the BFN stack-up. We can notice, in the 2x2 subarray, each radiator is connected with the adjacent radiator, thereby creating a continuous metal structure. This helps in realizing the array antenna aperture using 3D metal printing in addition to improved

heat sink property. Fig. 3.7(a) shows the top view of the antenna and the isometric view is shown in Fig. 3.7(b). We can observe that the temperature varies between 39-42°C which is evenly distributed across the antenna aperture. If we compare this with the temperature distribution of the BFN without heat sink, we can observe that the proposed heat sink antenna aperture helps to reduce the temperature by approximately 50°C compared to a structure without the heat sink. Fig. 3.7(c) shows the temperature distribution of the bottom view, where we observe that the maximum temperature is 60°C. The reduction in temperature happens because of the periodic arrangement of conducting copper vias underneath each radiator (shown in Fig. 3.8) helps in spreading the heat from the source at the bottom surface of the PCB to the antenna atop BFN, and the heat sink antenna in turn further reduces temperature by spreading out the heat to the surrounding air. Heat sink employs the principle of thermal diffusion and air convection, where heat sink continuously diffuses heat in surrounding air and the heated air become lighter and moves upward and reduced temperature is maintained in this way.

In view of the above, while designing the proposed heat sink antenna structure, the target is to maximize the surface area of the structure to enhance the interaction of the structure with air, whereas the thermal spreaders transport the heat from the chips to the heat sink and distribute the heat over entire structure evenly. On the other hand, our aim is to design a dual linear polarized antenna array. Hence in this case, we have to consider the heat sink performance as well as the coupling between the X- and Y-polarized radiators. In the next section, we discuss additional details about this aspect of the design and analysis.

3.4. Stack-up description of the PCB

As mentioned earlier, while discussing Fig. 3.7., Fig. 3.8 (a) shows the PCB stack up and feed structure used for the array implementation. Rogers 4350B (ε_r = 3.48 and $tan\ \delta$ = 0.004) is used throughout the board as a core material. The total thickness of the PCB is approximately 45 mils. Two sets of blind vias are used in this design to route RF signal to the dual polarized element. A set of blind vias are present underneath each metal ring for shorting the ground planes. These blind vias in turn helps in suppressing the surface waves generated due to multi-layered substrate as well as helps in heat transfer.

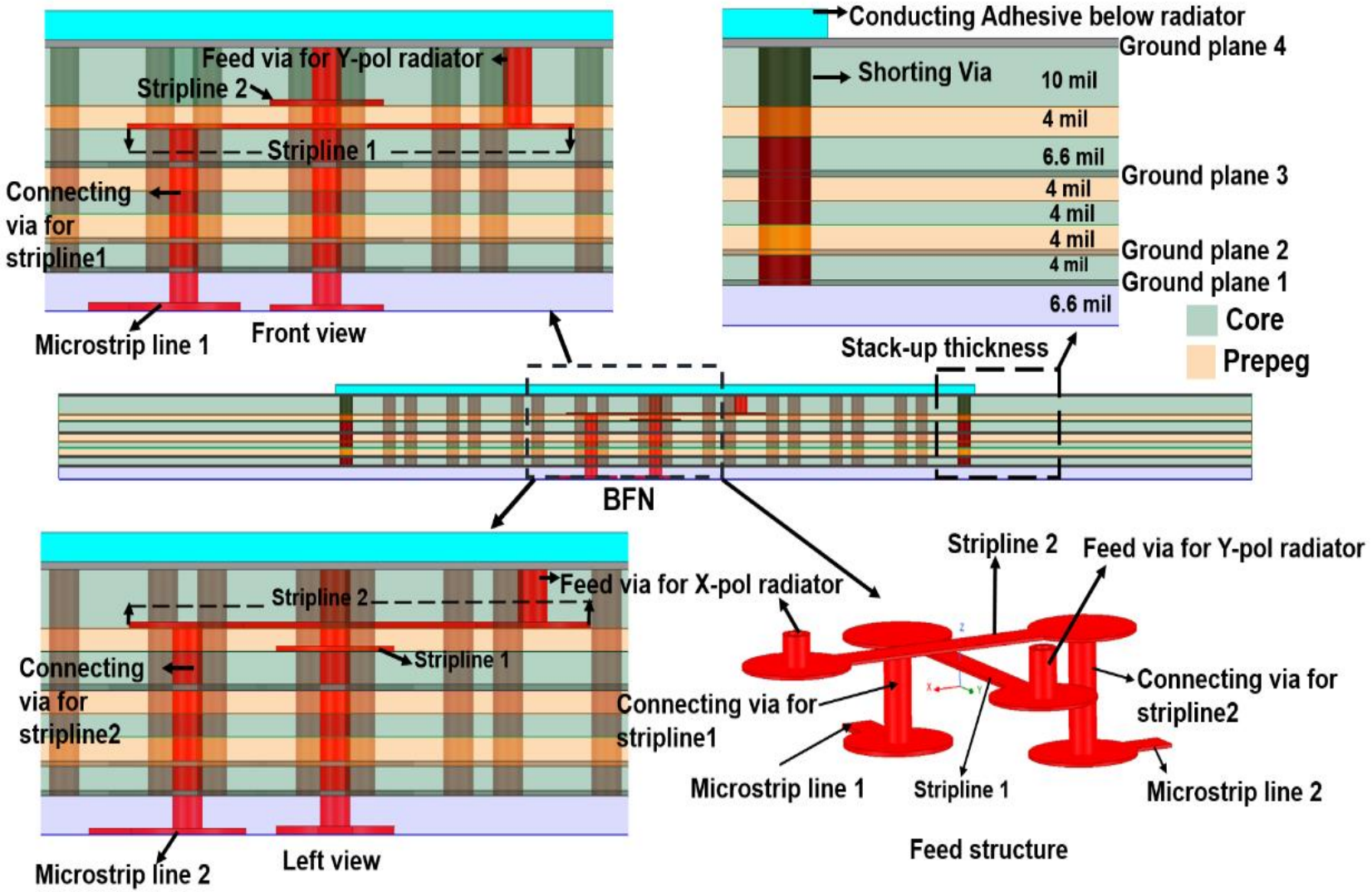
Feed via for Y-pol radiator
Stripline 2
Stripline 1
Connecting via for stripline1
Microstrip line 1
Front view
Conducting Adhesive below radiator
Ground plane 4
Shorting Via
10 mil
4 mil
6.6 mil
Ground plane 3
4 mil
4 mil
4 mil
Ground plane 2
4 mil
Ground plane 1
6.6 mil
Core
Prepeg
Stack-up thickness
BFN
Stripline 2
Feed via for X-pol radiator
Stripline 1
Connecting via for stripline2
Microstrip line 2
Left view
Stripline 2
Feed via for Y-pol radiator
Connecting via for stripline2
Connecting via for stripline1
Microstrip line 1
Stripline 1
Microstrip line 2
Feed structure

(a)

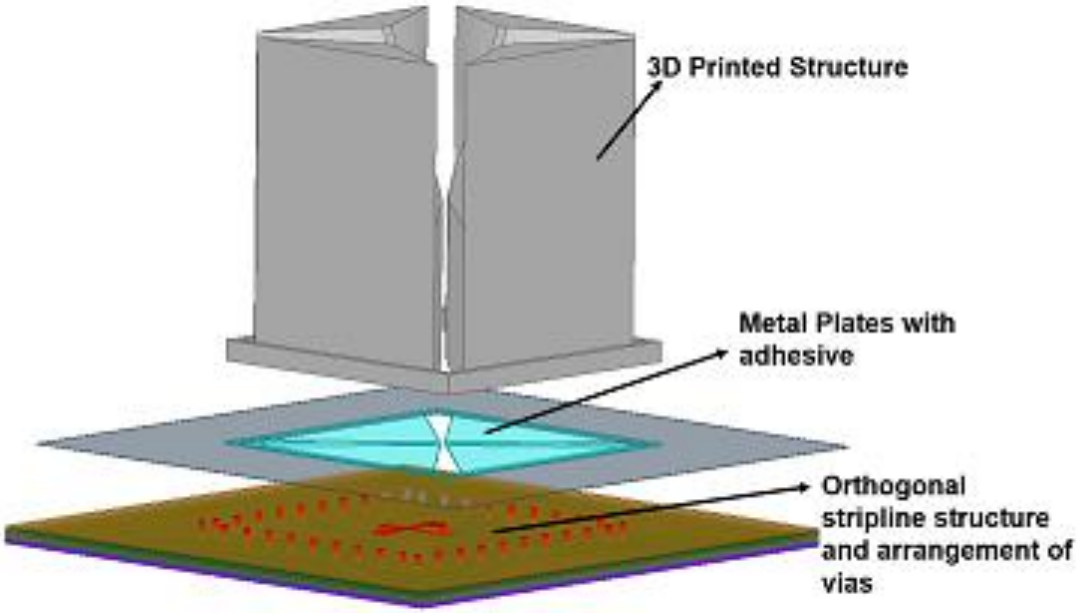
3D Printed Structure
Metal Plates with adhesive
Orthogonal stripline structure and arrangement of vias

(b)

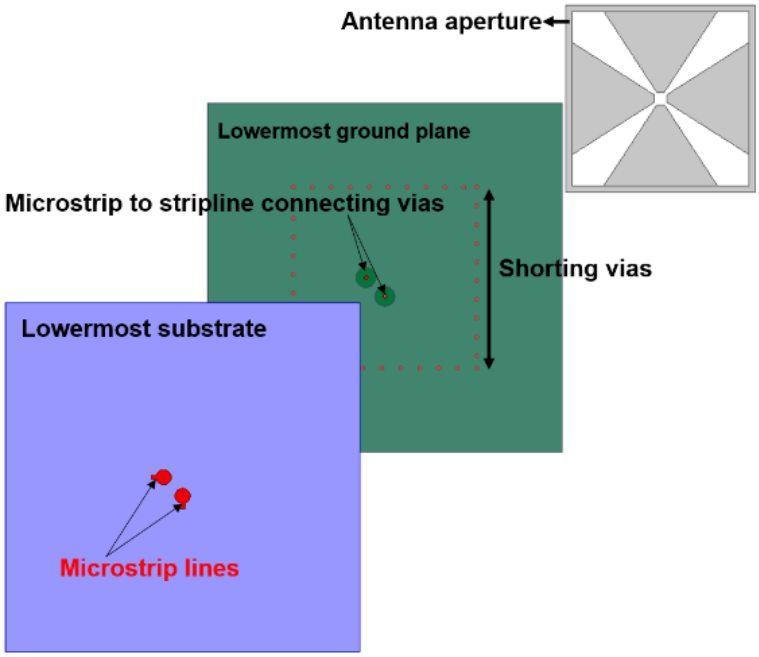
Antenna aperture
Lowermost ground plane
Microstrip to stripline connecting vias
Shorting vias
Lowermost substrate
Microstrip lines

(c)

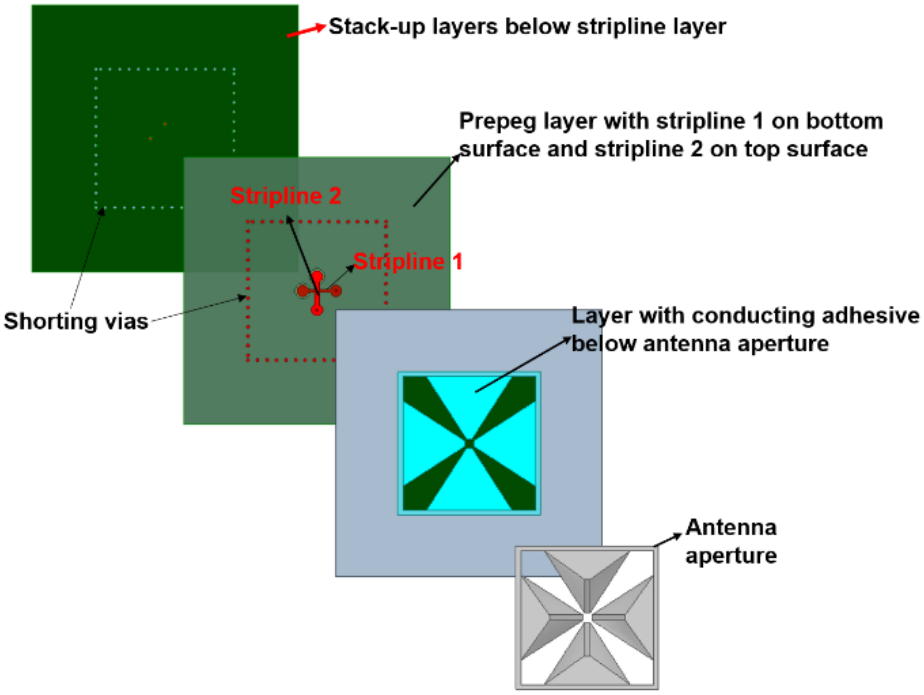
Stack-up layers below stripline layer
Prepeg layer with stripline 1 on bottom surface and stripline 2 on top surface
Stripline 2
Stripline 1
Shorting vias
Layer with conducting adhesive below antenna aperture
Antenna aperture

(d)

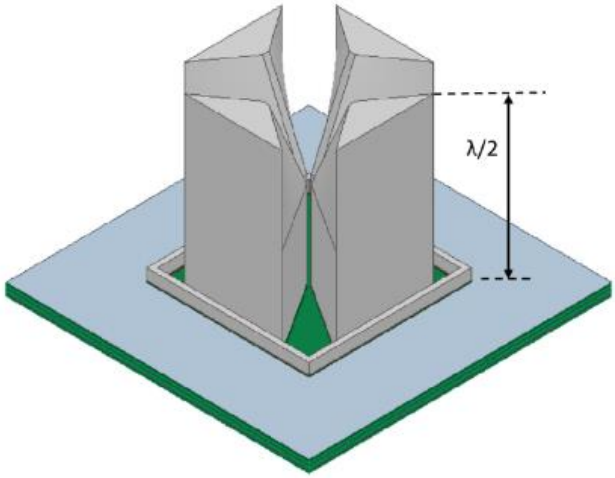
λ/2

(e)

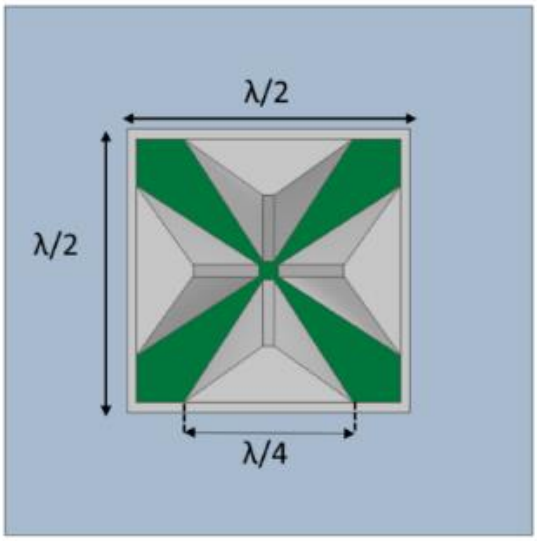

(f)

Fig. 3.8. (a) Side view of the PCB stack up of the multi-layered feed structure with zoomed in feed structure, (b) Exploded isometric view of the antenna structure and feed structure, (c) Exploded bottom view of the stack-up and antenna aperture, (d) Exploded top view of the stack-up and antenna aperture, (e) Isometric view of the antenna structure and (f) Top view of the antenna structure.

The thermal expansion coefficient of RO4350B material is comparable to that of copper [27]. The coefficient of thermal expansion (CTE) of copper is 16 ppm/°C, whereas that for R4350B is 10 ppm/°C along X-axis and 12 ppm/°C along Y-axis. So, the material shows excellent dimensional stability which makes it good for mixed dielectric multi-layer boards construction. The PCB has eleven metal layers, with different power, ground, and digital routing planes underneath the stripline feed layer to bias and control the Anokiwave chipsets. Two orthogonal striplines (Fig. 3.8. (a)), employed to feed two orthogonal two-armed antenna structures, are perpendicular to each other and placed asymmetrically between the two same ground planes, which provides dual-linear polarization as discussed in the next subsection. The power splitter network that feed the chips is simulated in Ansys

HFSS and the BFN layout is developed in Altium software. There is a square shaped copper ring with trapezium shaped plates of the same dimension as antenna footprint with an adhesive layer of bulk conductivity of 263160 S/m atop it on the top surface of the stack-up as shown in Fig. 3.8.(b). This conducting adhesive helps to adhere the antenna aperture with the BFN. The exploded bottom view and top view of the antenna and BFN stack-up are shown in Fig. 3.8(c) and Fig. 3.8.(d), which explains arrangement of the stripline, microstrip line and vias underneath each metal ring around the two orthogonal two-armed antenna structures.

3.5. Dual linear polarized single element atop PCB stack-up

In the dual polarized radiating element another two-armed flared structure is placed perpendicular to the first one within the same metal ring. The single polarized radiator is a two-armed balanced radiator, and hence, balanced feed technique should be applied. Here stripline1 and stripline2 are employed to feed Y-polarized and X-polarized radiators, respectively. These striplines are placed perpendicular to each other, on both sides of a prepreg layer, and are placed asymmetrically between ground planes 3 and 4, as shown in in Figs. 3.8(a) and 3.8(b). The Figs. 3.8(e) and 3.8(f) show the isometric and top view of the structure of the dual polarized single radiating element, respectively.

It is observed from the gain versus frequency graph (Fig. 3.4) of the single polarized radiator that the best performance is obtained when overall height of the radiator is $\lambda/2$ corresponding to 9.5 GHz. Fig. 3.9(a) shows the parametric study for the magnitude of reflection coefficient for X-polarized radiator for different combinations of H_1 and H_2. It is observed that optimum bandwidth is obtained for $H_1=H_2=\lambda/4$ corresponding to 9.5 GHz. Fig. 3.9(b) shows the parametric study for the magnitude of reflection coefficient for X-polarized radiator for different values of the thickness, *t* of each arm of the radiator. It is observed that optimum bandwidth is obtained for $t= \lambda/4$ corresponding to 9.5 GHz. Fig. 3.9(c) shows the parametric study for the magnitude of reflection coefficient for X-polarized radiator for different flare values '*S*' of the radiators. Satisfactory impedance matching is obtained for $S= \lambda/4$ corresponding to 9.5 GHz. Identical performances are observed for the Y-polarized radiator, hence not shown for the sake of brevity.

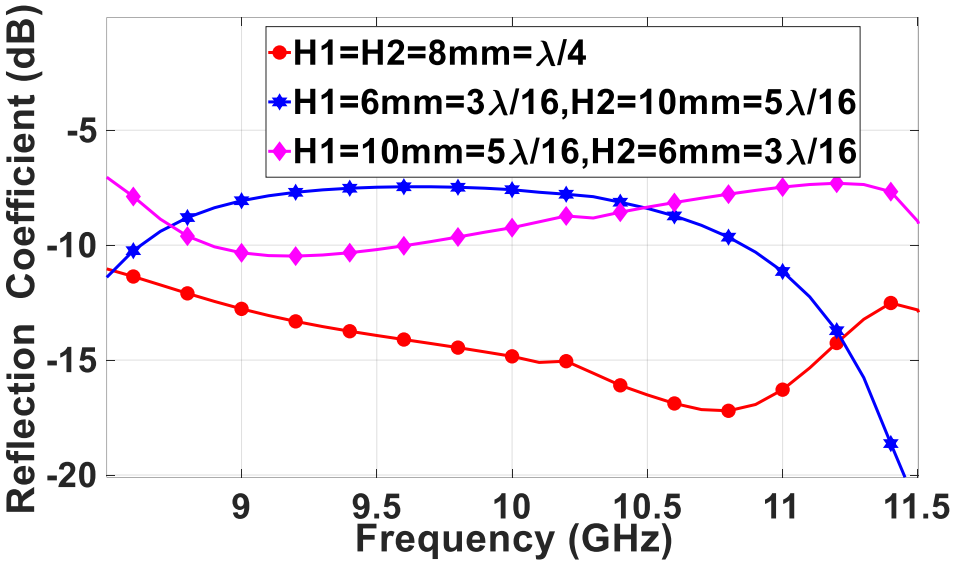
H1=H2=8mm=λ/4
H1=6mm=3λ/16,H2=10mm=5λ/16
H1=10mm=5λ/16,H2=6mm=3λ/16
Reflection Coefficient (dB)
-5
-10
-15
-20
9
9.5
10
10.5
11
11.5
Frequency (GHz)

(a)

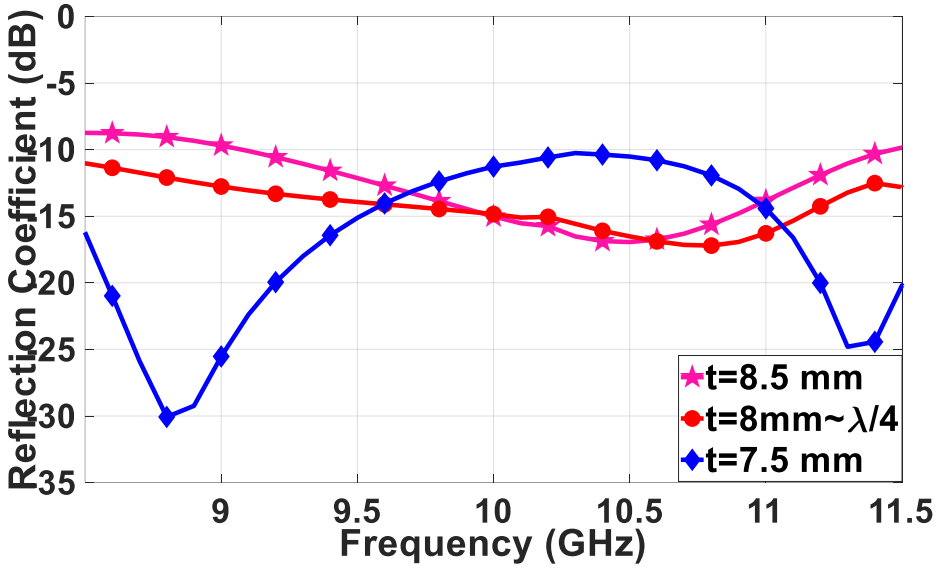
Reflection Coefficient (dB)
0
-5
-10
-15
-20
-25
-30
-35
9
9.5
10
10.5
11
11.5
Frequency (GHz)
t=8.5 mm
t=8mm~λ/4
t=7.5 mm

(b)

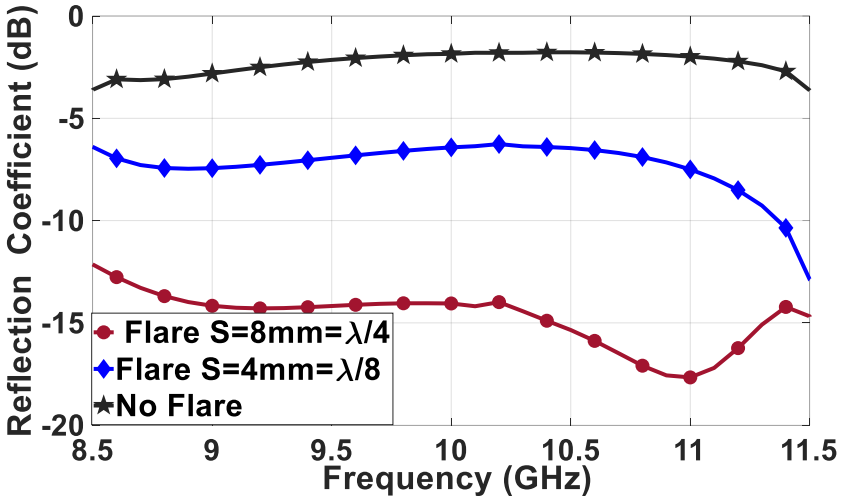

(c)

Fig. 3.9. The magnitude of reflection coefficient for (a) different combinations of H_1 and H_2, (b) different values of '*t*', and (c) different flare value '*S*' for X-polarized array.

Fig. 3.10(a) shows the magnitude of reflection coefficient for both polarizations and isolation between two ports and Figs. 3.10(b) and 3.10(c) show the radiation patterns at 9.50 GHz for X- and Y-polarized radiators for the optimum dimensions. It can be observed that the single dual-polarized element provides wideband performance with respect to S_{11} of -10dB between 8-11.5 GHz and port to port isolation (S_{21}) of around -20 dB, along with acceptable radiation pattern. But the separation between peak co- and cross-polarized fields is not more than 15dB, which may become worse for the array implementation. This non-satisfactory co-cross separation is resolved in the next section while designing the 4x2 array.

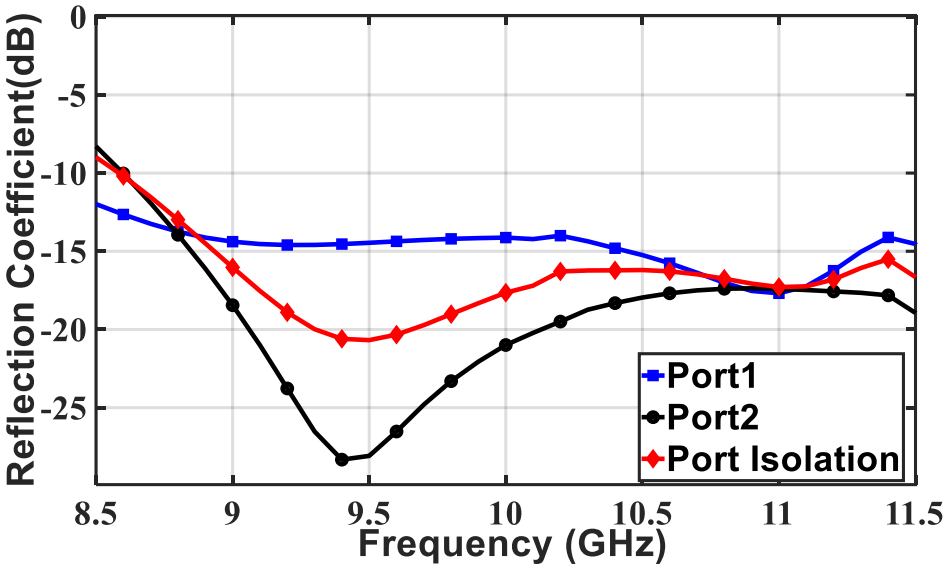
Reflection Coefficient(dB)
0
-5
-10
-15
-20
-25
8.5
9
9.5
10
10.5
11
11.5
Frequency (GHz)
Port1
Port2
Port Isolation

(a)

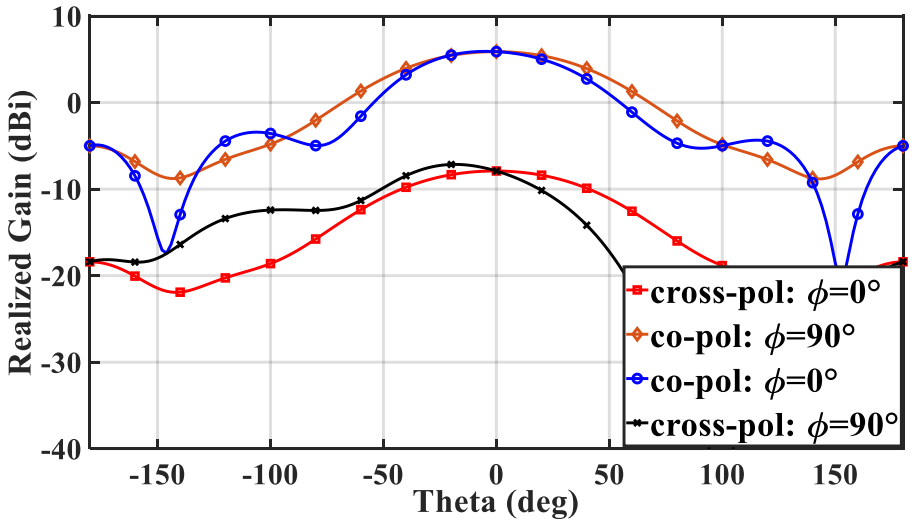
Realized Gain (dBi)
10
0
-10
-20
-30
-40
-150
-100
-50
0
50
100
150
Theta (deg)
cross-pol: ϕ=0°
co-pol: ϕ=90°
co-pol: ϕ=0°
cross-pol: ϕ=90°

(b)

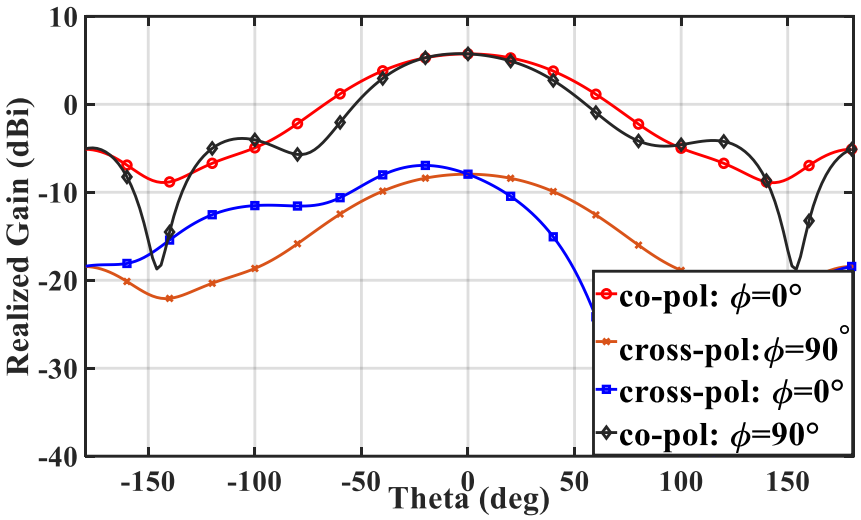

(c)

Fig.3.10. (a) The magnitude of reflection coefficient for both polarizations and isolation between the two ports, and Radiation patterns at 9.50 GHz for (b) X-polarized radiator, and (c) Y-polarized radiator.

Brief design guidelines for this wideband dual linear polarized radiator can be developed from the above observations:

1. The height of each arm of the radiator is nearly $H = \lambda/2$ at the center frequency

2. The height of the flared and non-flared sections should be $(H1+H2) = (\lambda/4+\lambda/4) = \lambda/2$

3. The thickness (t) of each arm is nearly $\lambda/4$

4. The width of the flare should be $S= \lambda/4$

5. The dimension of the metal ring is $Sx = Sy = \lambda/2$

The peak realized gain and total efficiency (Factoring mismatch and dielectric and Ohmic losses) for the both X- and Y-polarizations is shown in Fig. 3.11. Peak realized gain varies from 5 – 6 dBi for both polarizations, whereas the efficiency is above 85% over the entire

bandwidth. Considering the 3D metal printing using the aluminum alloy, the total efficiency is quite good.

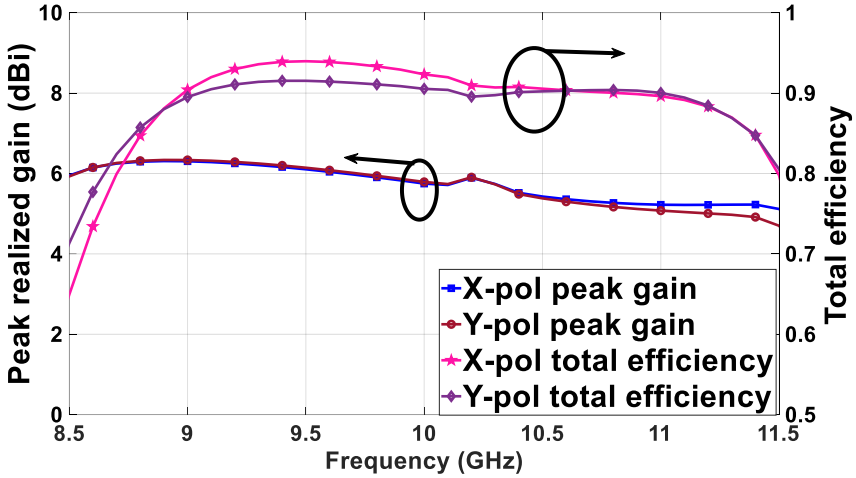

Fig.3.11. Peak gain versus frequency and Total efficiency versus frequency for both X-polarized and Y-polarized radiators.

3.6. 2x2 Subarray with dual linear polarized elements

3.6.1. 2x2 Subarray configuration

The top view of a 2x2 all metal heat sink subarray is shown in Fig. 3.12(a). Here, the inter-element spacing is half of the free space wavelength ($\lambda/2$) corresponding to 9.50 GHz, i.e., 16mm. In Figs. 3.10(b) and 3.10(c), it is observed that the peak cross-polarization level is quite high. With an aim to reduce peak cross-polarization level, two different feed configurations of 2x2 subarray are studied. Bottom view of the configurations I, and II are shown in Figs. 3.12(b), and 3.12(c), respectively. Configuration I employs the conventional feed structure of a 2x2 subarray. In configuration II, the upper right and the lower left elements are mirrored with respect to a vertical plane [28]. The mirror ports must be excited with a 180° phase to achieve in phase or broadside radiation, as shown in Fig. 3.12(c). The radiation pattern for both polarizations of configuration I are shown in in Figs. 3.13(a) and 3.13(b) and configuration II are shown in Figs. 3.13(c) and 3.13(d), respectively. We can

observe that configuration II causes notable cross-polarization improvement as compared to conventional array, which makes it a better choice for the bigger array. Configuration II provide more than 30dB co- to cross-polarization separation whereas only 15 dB separation is obtained for the conventional array.

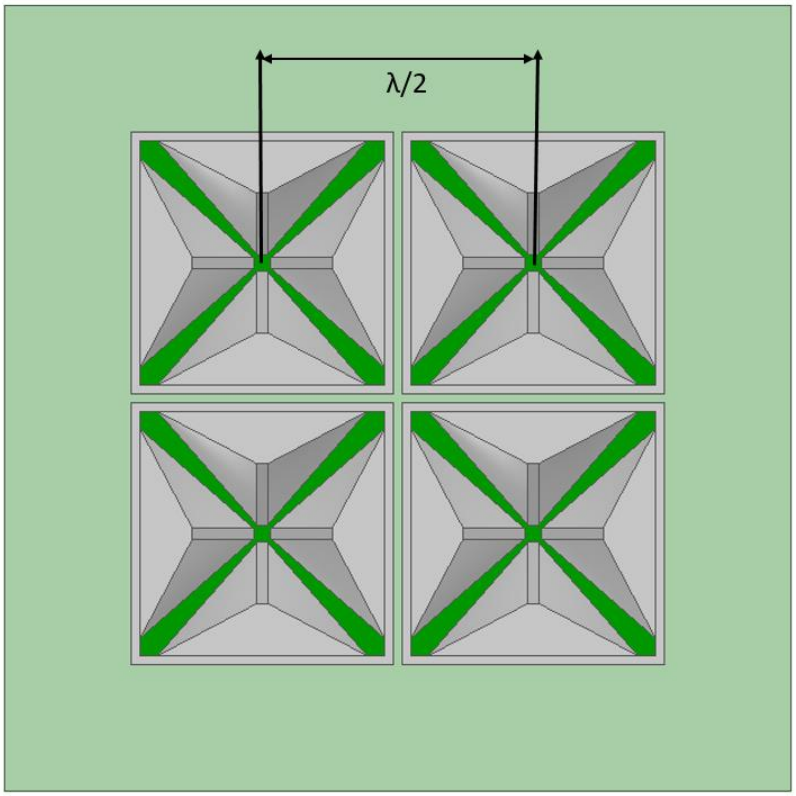

(a)

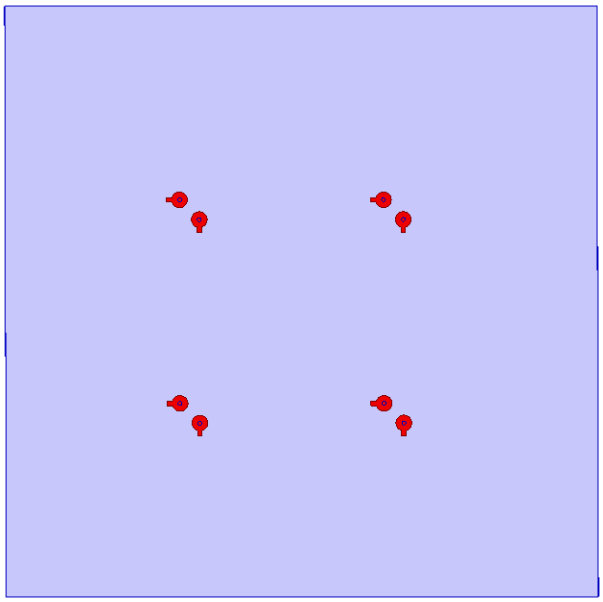

(b)

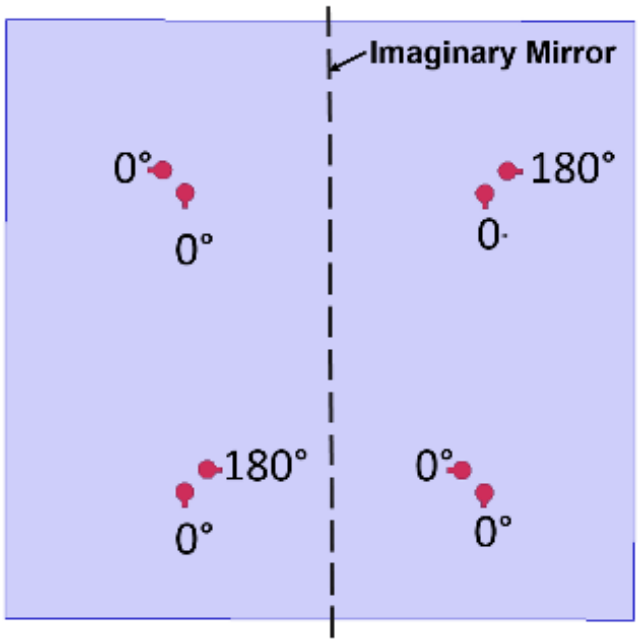

(c)

Fig. 3.12. Top view of a 2x2 all metal heat sink array (same for configurations I, and II), (b) Bottom view of configurations I, and (c) Bottom view of mirror feed configurations II showing feed orientations and phase values.

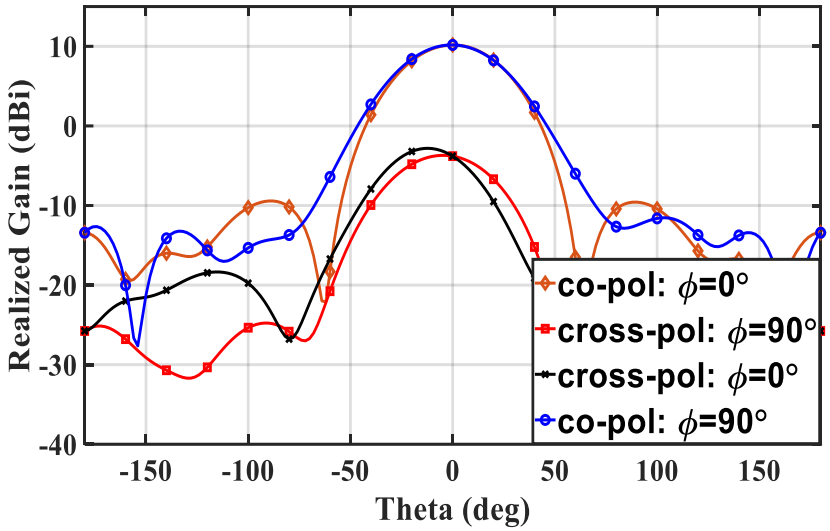
Realized Gain (dBi)
10
0
-10
-20
-30
-40
-150
-100
-50
0
50
100
150
Theta (deg)
co-pol: ϕ=0°
cross-pol: ϕ=90°
cross-pol: ϕ=0°
co-pol: ϕ=90°

(a)

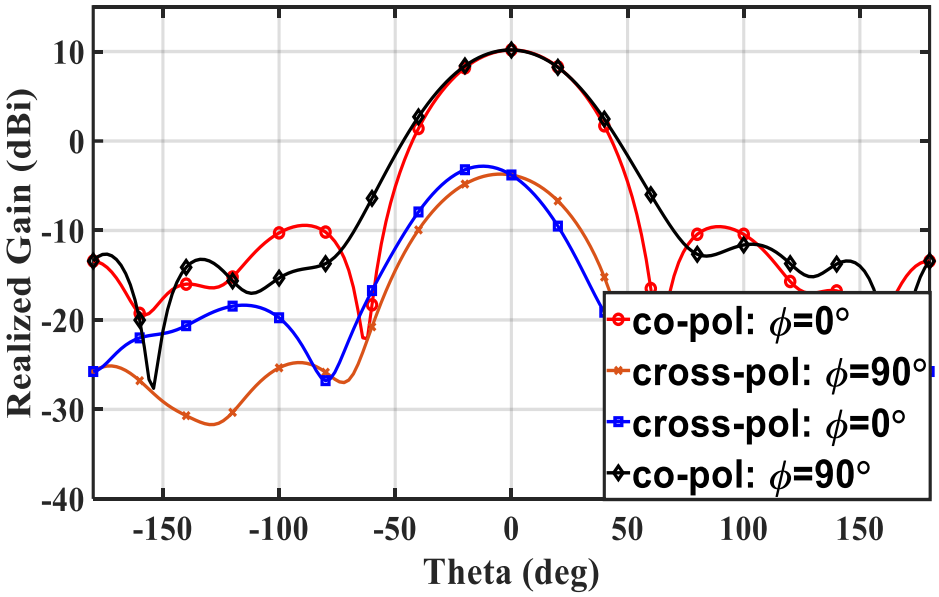
Realized Gain (dBi)
10
0
-10
-20
-30
-40
-150
-100
-50
0
50
100
150
Theta (deg)
co-pol: ϕ=0°
cross-pol: ϕ=90°
cross-pol: ϕ=0°
co-pol: ϕ=90°

(b)

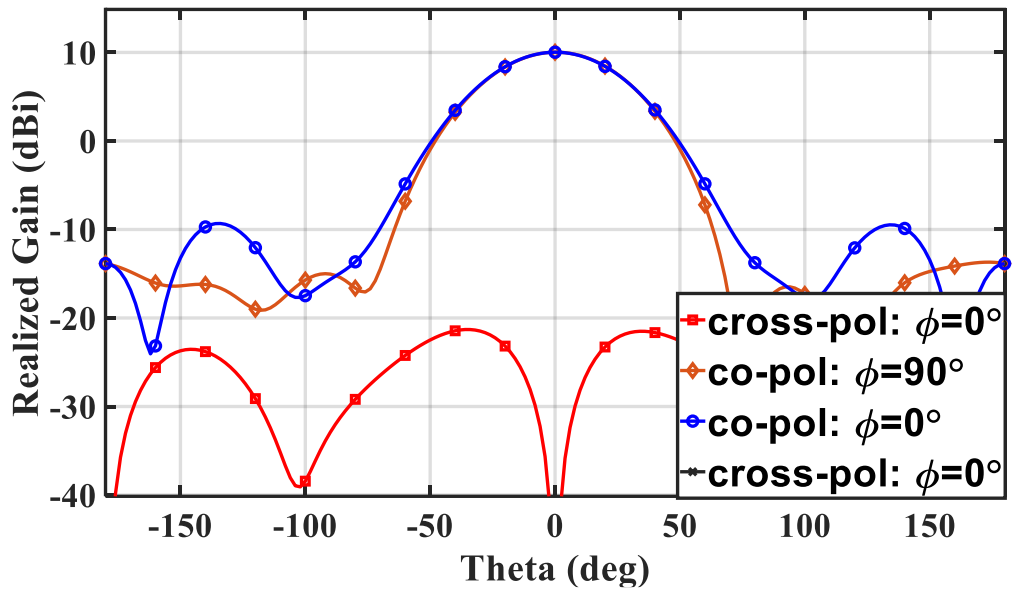

(c)

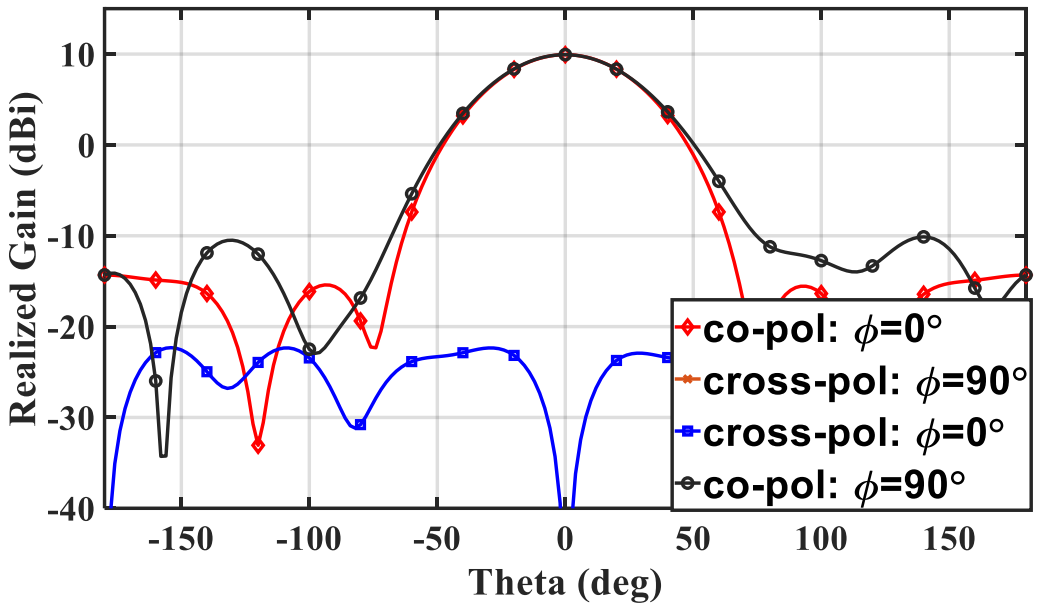

(d)

Fig. 3.13. Radiation Patterns at 9.5 GHz, (a) X-polarized array for Configuration I, (b) Y-polarized array for Configuration I, (c) X-polarized array for Configuration II, and (d) Y-polarized array for Configuration II.

3.6.2. Heat sink properties

Figs. 3.14(a) and 3.14(b) show the top view and isometric view of the thermal analysis (Simulation setup as in single polarized 2x2 subarray)) of a dual polarized 2x2 subarray assuming a RFIC of 1.35 Watts of power consumption at center dissipating as heat. It is observed that the temperature ranges from 36-39°C. Fig. 3.14(c) shows the bottom view of the array where we can see the maximum temperature is nearly 59°C which is similar to Fig. 3.7(c) with the same source.

In heat sink study, usually cooling fluid passes across the surface of the warm heat sink and heat sink diffuses the heat in air. So, if we assume air flow in one particular direction over heat sink, we observe the temperature of the outlet air is much higher than the inlet air. Here, we have assumed that the whole antenna is in air box with a velocity of 0.1m/sec against gravity (indoor air flow). Although dual polarized antenna offers more metal surface area to diffuse more heat, the dual polarized structure is offering hindrance in normal air flow due to the presence of antenna elements in both X- and Y- directions, therefore, we have observed little difference in the temperature distribution between the single polarized (39-42°C) and dual polarized (36-39°C) sub-arrays.

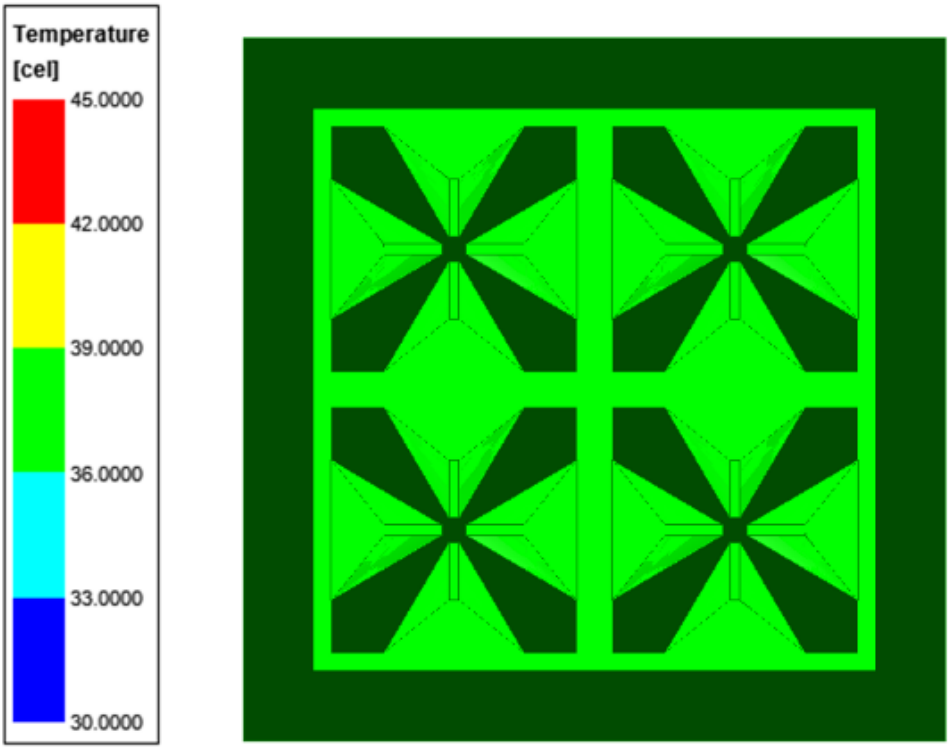
Temperature
[cel]
45.0000
42.0000
39.0000
36.0000
33.0000
30.0000

(a)

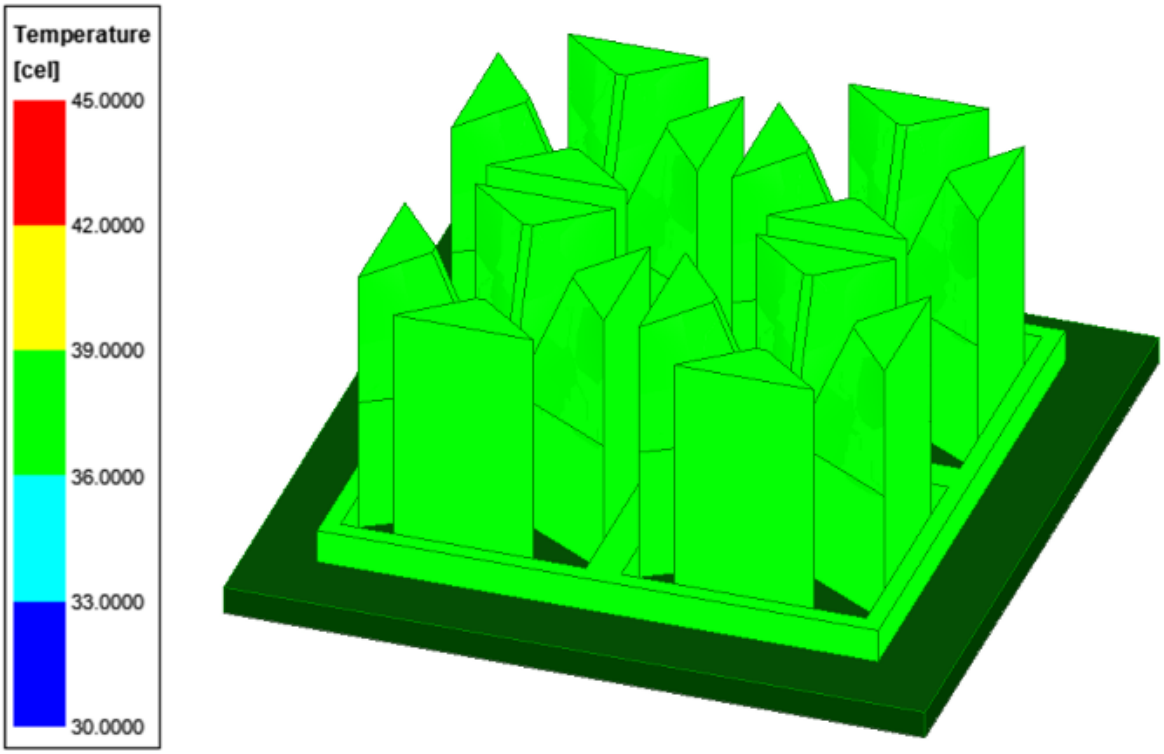
Temperature
[cel]
45.0000
42.0000
39.0000
36.0000
33.0000
30.0000

(b)

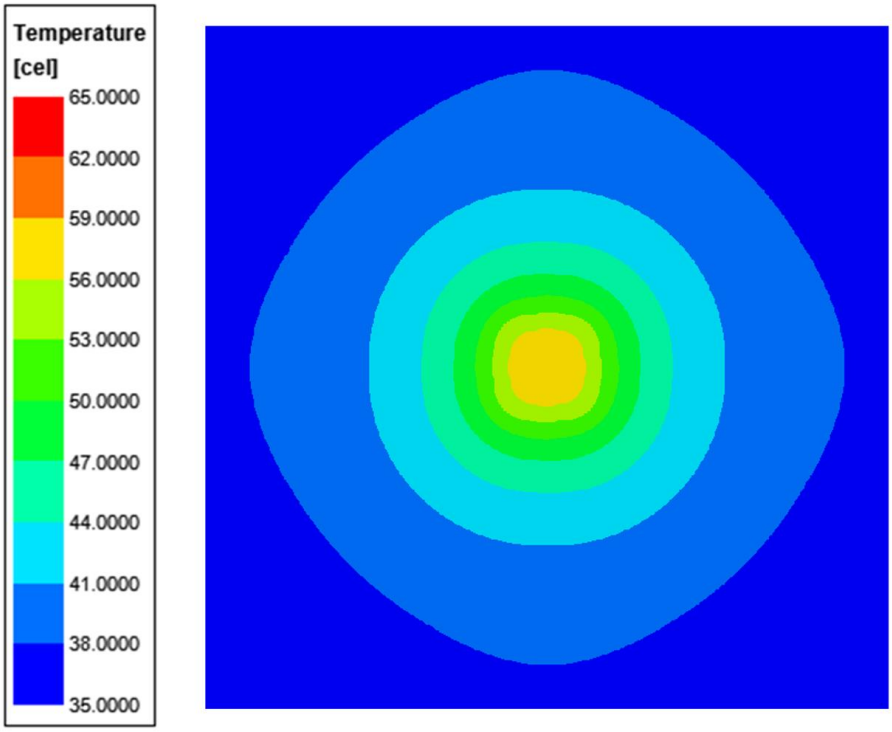

(c)

Fig. 3.14. Temperature distribution of 2x2 dual polarized antenna aperture atop a RFIC of power consumption of 1.35 Watts (a) Top view, (b) Isometric view, and (c) Bottom view.

3.7. 4x2 Antenna Array Configuration

3.7.1. The 4x2 dual polarized array with mirror feed structure

The 4x2 dual polarized array is designed using the subarray discussed in Figs. 3.12(a) and 3.12(c) with mirror configuration. The array has overall dimension of 104 mm x 84 mm, with 8 radiating elements and total 16 ports. Fig. 3.15 shows the top view of the 4x2 antenna aperture. Here, the inter-element spacing is designated as $Dx = Dy = 16$ mm ($\lambda/2$ *at* 9.50 GHz), and width *W1*=2x16=32 mm, Length *L1*= 4x16=64 mm, *W2*= 52 mm, *W3*= 72 mm, *L2*=84

mm, *L3* = 104 mm. It is to be noted that each single element structure is connected with the adjacent structure. Also, there is metal extension around the 4x2 radiating aperture, which in turn helps in 3D metal fabrication of a continuous metallic antenna aperture, and in addition helps in enhancing the heat sinking property.

Magnitude of the reflection coefficients for all the ports for X- and Y-polarized array elements are shown in Figs. 3.16(a) and 3.16(b), respectively. The broadside radiation pattern of the X-polarized array and Y-polarized array at 9.50 GHz are shown in Figs. 3.16(c) and 3.16(d), respectively. It is observed that the array offers good impedance matching over 8.5-11.5 GHz with excellent broadside radiation pattern, the peak co- to cross-polarization separation being more than 20 dB over entire bandwidth. Fig. 3.16(e) shows the peak realized gain and the total efficiency. We can observe that the total efficiency is nearly 80% which is acceptable considering that we are using aluminium alloy with a conductivity of 600000S/m. The peak realized gain varies between 11 dBi to 14 dBi over the entire bandwidth.

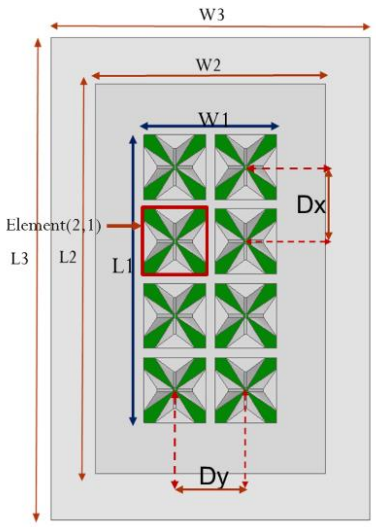

Fig.3.15. Top view of the 4x2 all metal heat sink antenna array.

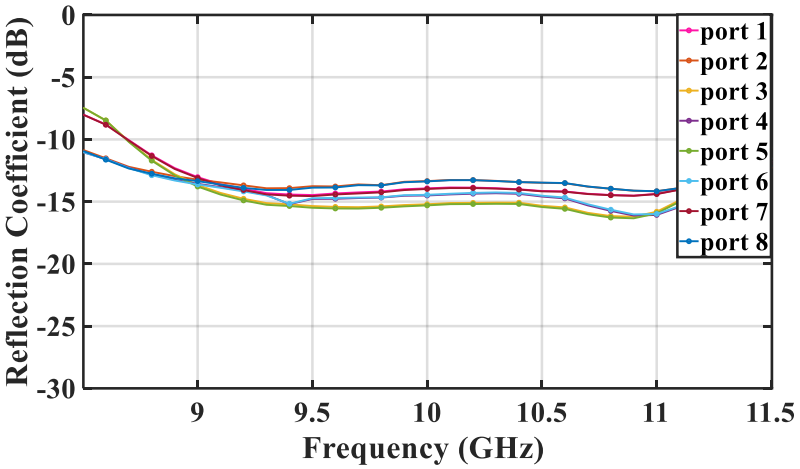
Reflection Coefficient (dB)
0
-5
-10
-15
-20
-25
-30
9
9.5
10
10.5
11
11.5
Frequency (GHz)
port 1
port 2
port 3
port 4
port 5
port 6
port 7
port 8

(a)

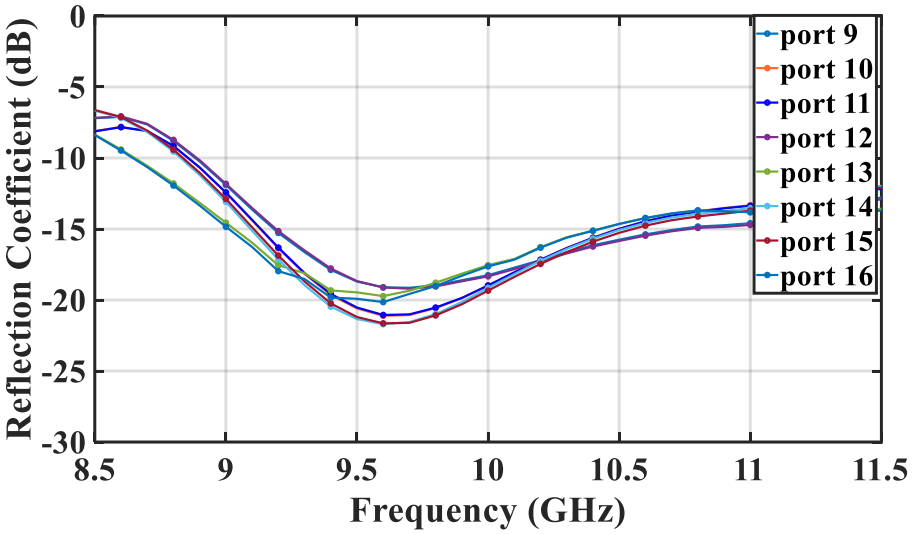
Reflection Coefficient (dB)
0
-5
-10
-15
-20
-25
-30
8.5
9
9.5
10
10.5
11
11.5
Frequency (GHz)
port 9
port 10
port 11
port 12
port 13
port 14
port 15
port 16

(b)

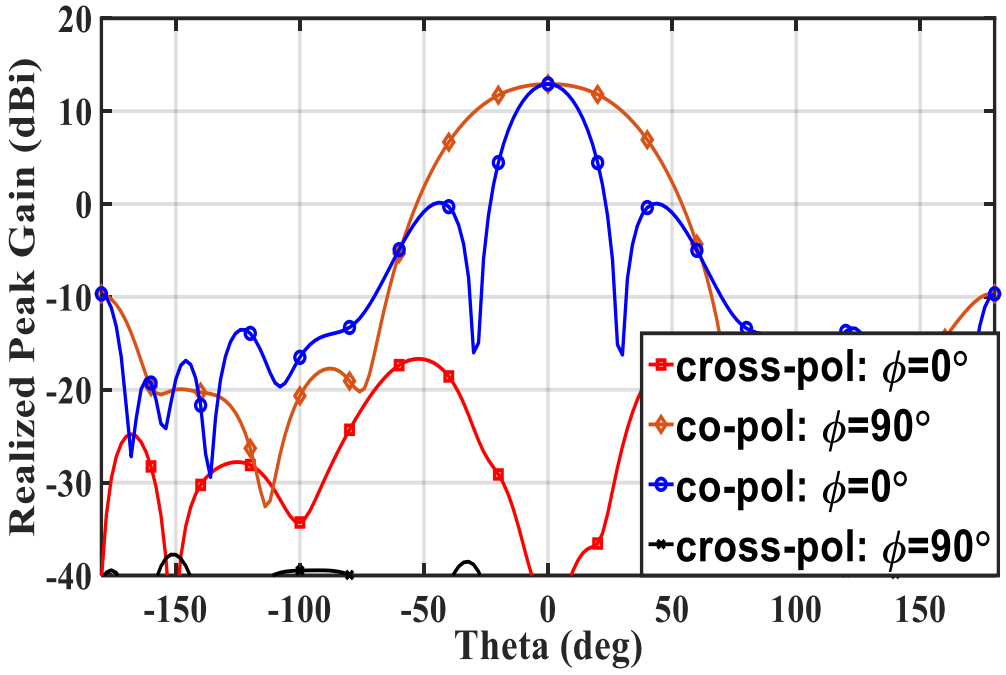
Realized Peak Gain (dBi)
20
10
0
-10
-20
-30
-40
-150
-100
-50
0
50
100
150
Theta (deg)
cross-pol: ϕ=0°
co-pol: ϕ=90°
co-pol: ϕ=0°
cross-pol: ϕ=90°

(c)

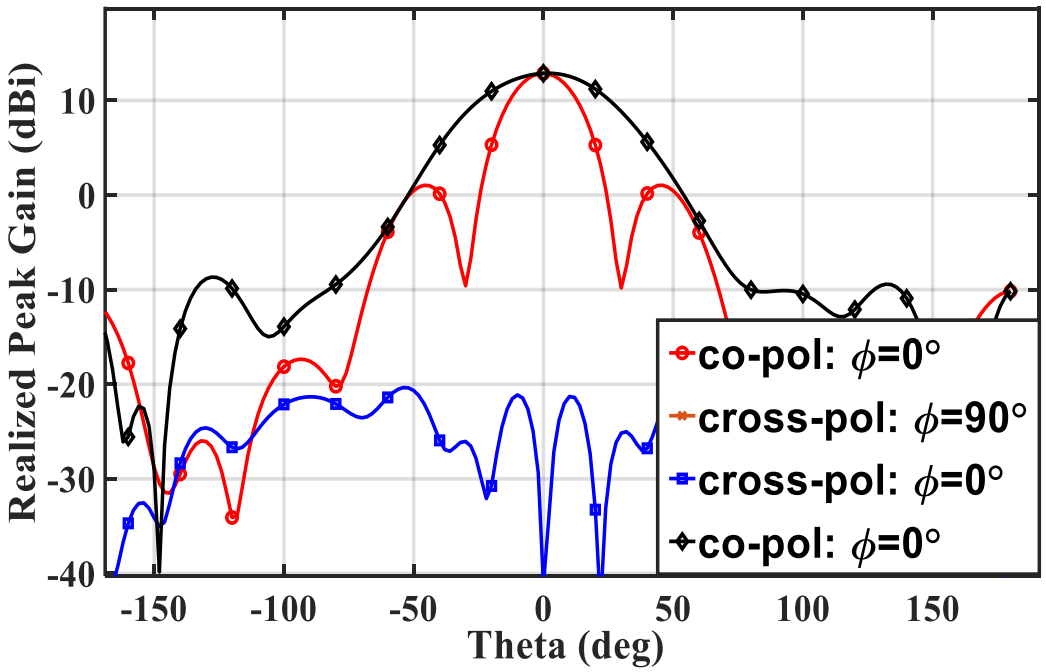
Realized Peak Gain (dBi)
10
0
-10
-20
-30
-40
-150
-100
-50
0
50
100
150
Theta (deg)
co-pol: ϕ=0°
cross-pol: ϕ=90°
cross-pol: ϕ=0°
co-pol: ϕ=0°

(d)

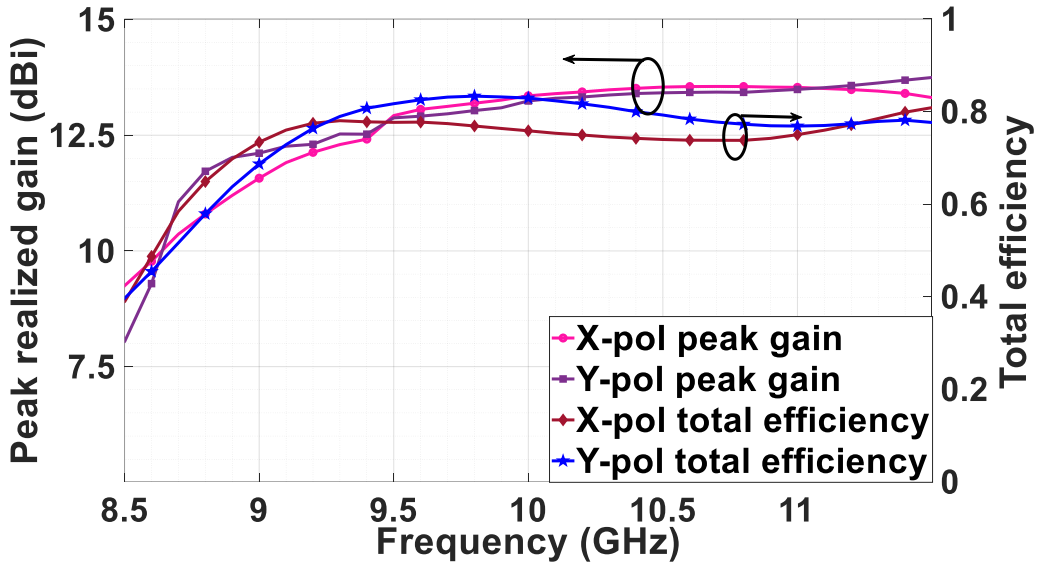

(e)

Fig.3.16. (a) The magnitude of reflection coefficient for X-polarized array for all ports, (b) The magnitude of reflection coefficient for Y-polarized array for all ports, (c) Radiation pattern at 9.5 GHz for X-polarized array, (d) Radiation pattern at 9.5 GHz for Y-polarized array, and (e) Broadside peak realized gain and total efficiency for both polarizations.

Figs. 3.17(a) and 3.17(b) show the scanning performance of both X-polarized and Y-polarized cases in $\varphi=0^0$ plane At 9.5 GHz and Figs. 3.17(a) and 3.17(b) shows that at 11 GHz. In Fig. 3.17(a) and 3.17(b), it can be seen that gain drops from 12.8 dBi to 12.5 dBi as beam scans till ±50° for X-polarized case and ±45° for Y-polarized case in $\varphi=0^0$ plane. In Fig. 3.17(c) and 3.17(d), it is observed that gain drops from 13.8 dBi to 12.2 dBi as beam scans till ±30° for X-polarized case and 13.8 dBi to 13.1 dBi as beam scans till ±34° for Y-polarized case in $\varphi=0^0$ plane. Figs. 3.17(e) and 3.17(f) show the active S-parameter of the Element (2, 1) for the broadside and ±50° beam scan in $\varphi=0^0$ plane for the both X-polarized and Y-polarized cases. It is observed that active S-parameter is below -10dB almost over entire bandwidth for maximum scan as well.

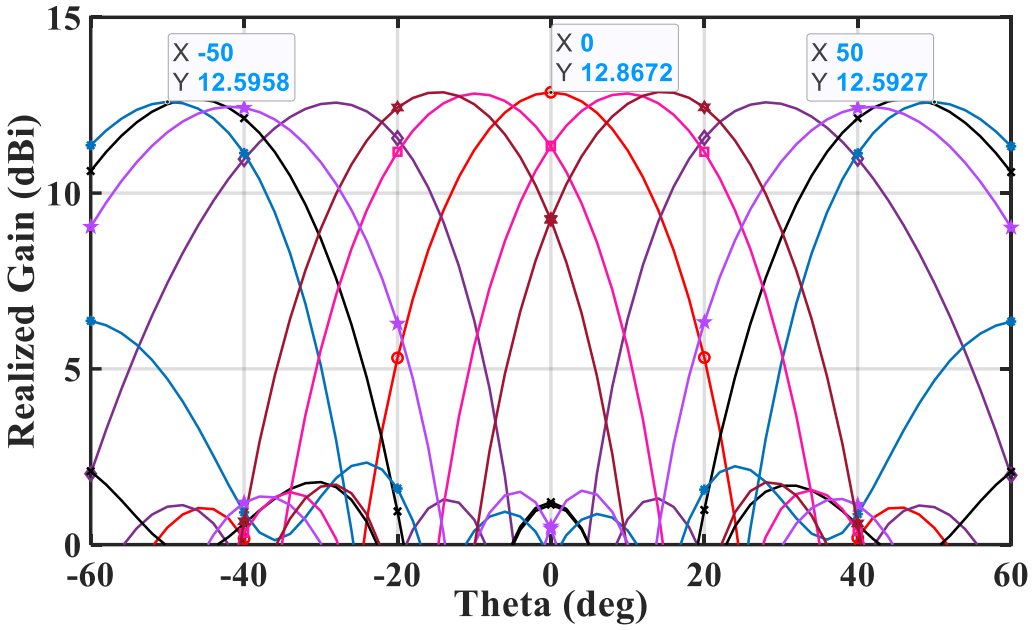
X -50
Y 12.5958
X 0
Y 12.8672
X 50
Y 12.5927
Realized Gain (dBi)
Theta (deg)
15
10
5
0
-60
-40
-20
0
20
40
60

(a)

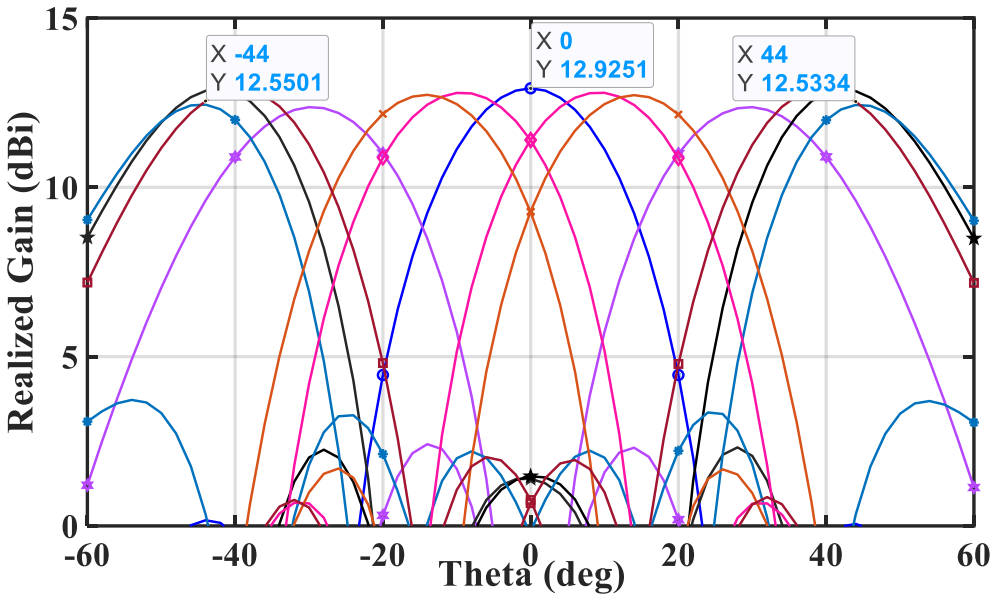
X -44
Y 12.5501
X 0
Y 12.9251
X 44
Y 12.5334
Realized Gain (dBi)
Theta (deg)
15
10
5
0
-60
-40
-20
0
20
40
60

(b)

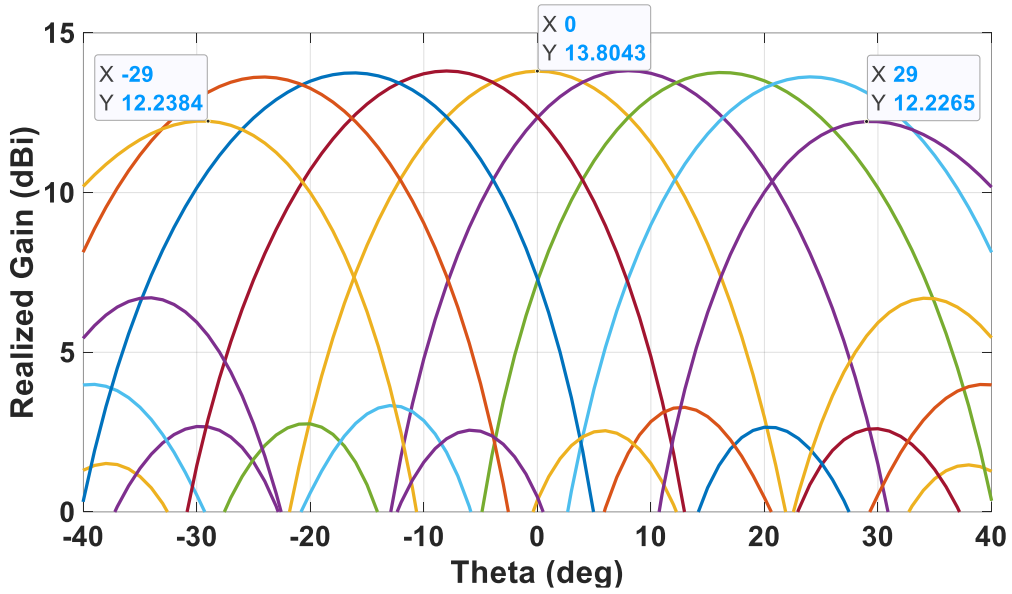
X 0
Y 13.8043
X -29
Y 12.2384
X 29
Y 12.2265
Realized Gain (dBi)
Theta (deg)
15
10
5
0
-40
-30
-20
-10
0
10
20
30
40

(c)

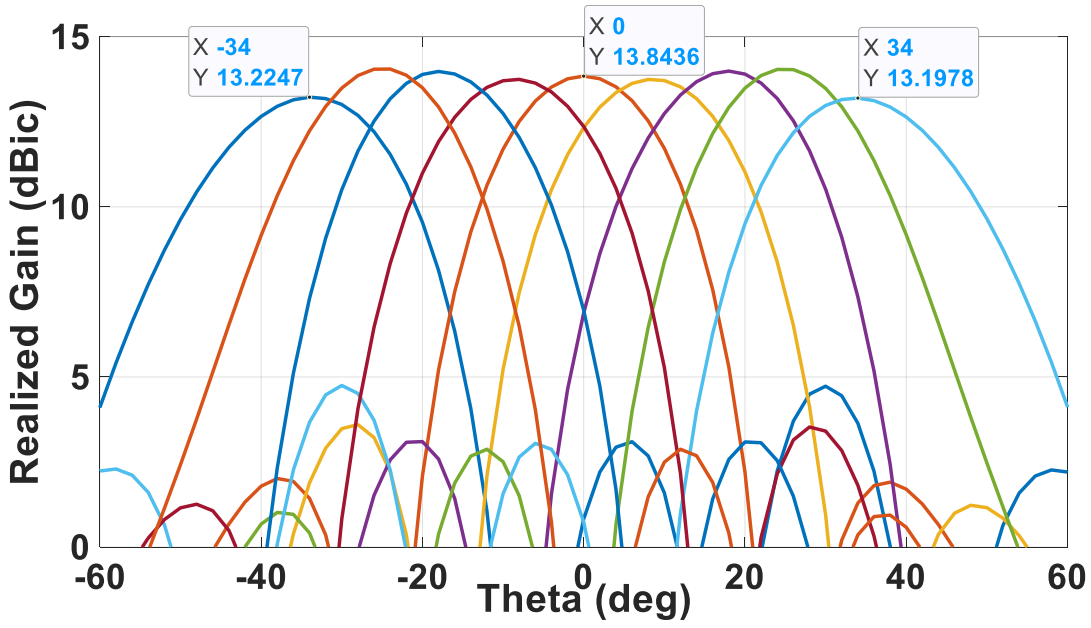
X 0
Y 13.8436
X -34
Y 13.2247
X 34
Y 13.1978
Realized Gain (dBic)
Theta (deg)
15
10
5
0
-60
-40
-20
0
20
40
60

(d)

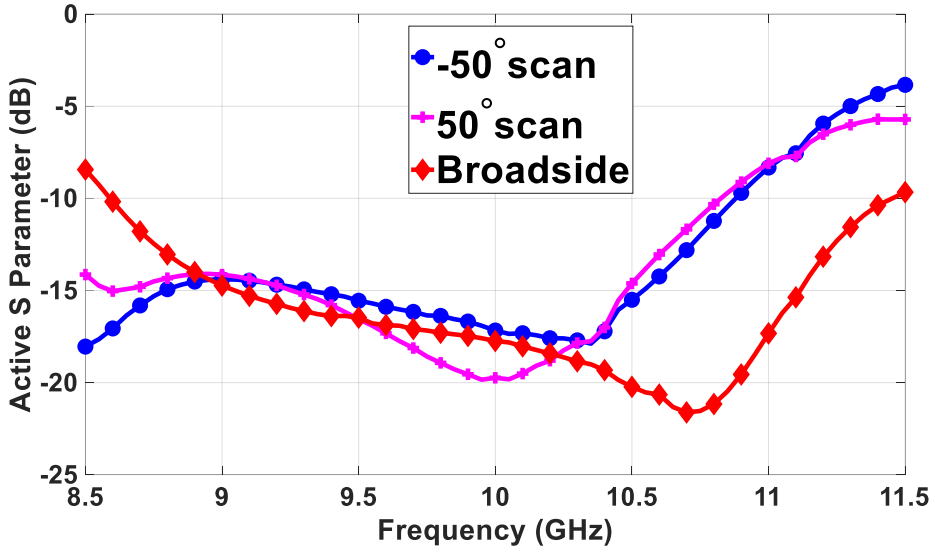

(e)

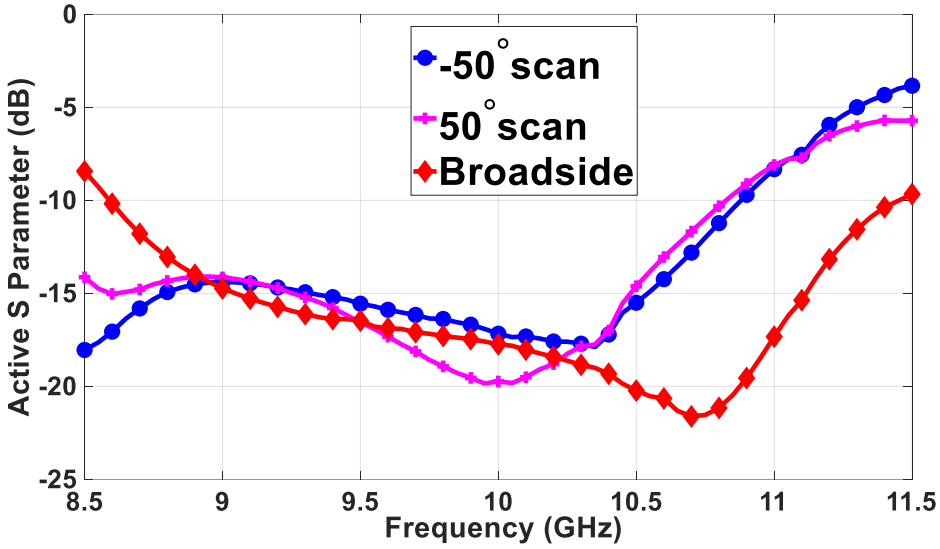

(f)

Fig. 3.17. Scanning performance of the 4x2 array in $\varphi=0^0$ plane for (a) X-polarized array, and (b) Y-polarized array at 9.5 GHz, and (c) X-polarized array, and (d) Y-polarized array at 11 GHz. Active S-parameter for the broadside and maximum scan angle for (e) Element (2, 1) for X-polarized radiator, and (f) Element (2, 1) for Y-polarized radiator.

3.7.2. Thermal analysis of the 4x2 dual polarized array

For thermal analysis included here, there is no forced air flow or no forced cooling arrangement. One Anokiwave X-band chip is feeding four dual polarized radiators, as discussed earlier. Each chip has a RF power consumption of 1.35 Watts which dissipates as heat. Here, two chips are present underneath the 4x2 antenna array aperture. There is opening all around the aperture with air at room temperature i.e. 26.85°C (300°K) with a velocity of 0.1m/sec against gravity.

The temperature distribution of the BFN without the heat sink (antenna aperture) is shown in Fig. 3.18. It shows that the maximum temperature of the BFN is approximately 100°C without the heat sink structure. Here also we can notice the peak of temperature distribution is located at the positions of four corners of the chip (as observed in Fig. 3.6 as well).

The results for thermal analysis of the antenna aperture atop BFN is shown in Fig. 3.19. From Figs. 3.19(a) and 3.19(b), we see the maximum temperature of the antenna aperture ranges from 40°-41°C. Since we know that each chip feeds four radiators simultaneously, and located at the center of each 2x2 sub array, which implies two chips are separated by 32mm and each chip individually dissipates 1.35 Watts of the consumed power into heat. Therefore, the overall combined temperature of the backside of the PCB ranges from 40°C to 62°C, as shown in Fig. 3.20(c). So, we can see there is more than 20°C temperature difference between the temperature of the heatsink and the backside of the BFN board.

With the same simulation setup, the temperature of same antenna structure with different input power is studied, which is shown in Figs. 3.20(a-e). The input power versus maximum temperature curve is shown in Fig. 3.20(f), where it is observed that temperature rise is not perfectly linear with the input power, however the rise in power by 1 Watt causes approximately 4-5 °C rise in temperature for the same heat sink structure. It can be noted that when each chip is assumed to be causing power consumptions of 0.5 Watt (total 1 Watt), 1 Watt (total 2 Watt), 1.35 Watt (total 2.7 Watt), 1.5 Watt (total 3 Watt) and 2 Watt (total 4 Watt), the temperature ranges from 27°-32°C, 25°-37°C, 35°-40°C,35°-42°C and 39°-47°C, respectively.

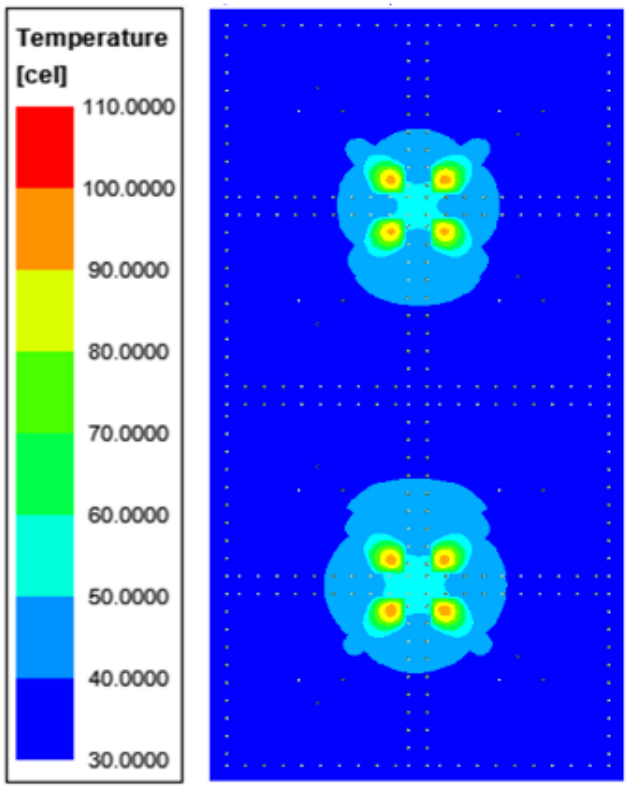

Fig. 3.18. Temperature distribution of the BFN without the 4x2 heat sink radiator antenna with the two chips where each chip has power consumption of 1.35 Watts.

Figs. 3.21(a) and 3.21(b) shows the comparison of the 4x2 antenna aperture simulated with the same simulation setup assuming each chip with power consumption of 1.35 Watts dissipating as heat, where Fig. 3.21(a) is considering aluminum alloy (already used for other simulations) and Fig. 3.21(b) is considering copper as material. Since copper is much better heat conductor than aluminum alloy, therefore, we see that temperature ranges from 25 °-31°C for copper (Fig. 3.21(b)) whereas it ranges from 36 °-42°C for aluminum alloy (Fig. 3.21(a)). So, if the same heat sink antenna structure with same dimensions can be built using copper, further temperature reduction of 11°C can be achieved.

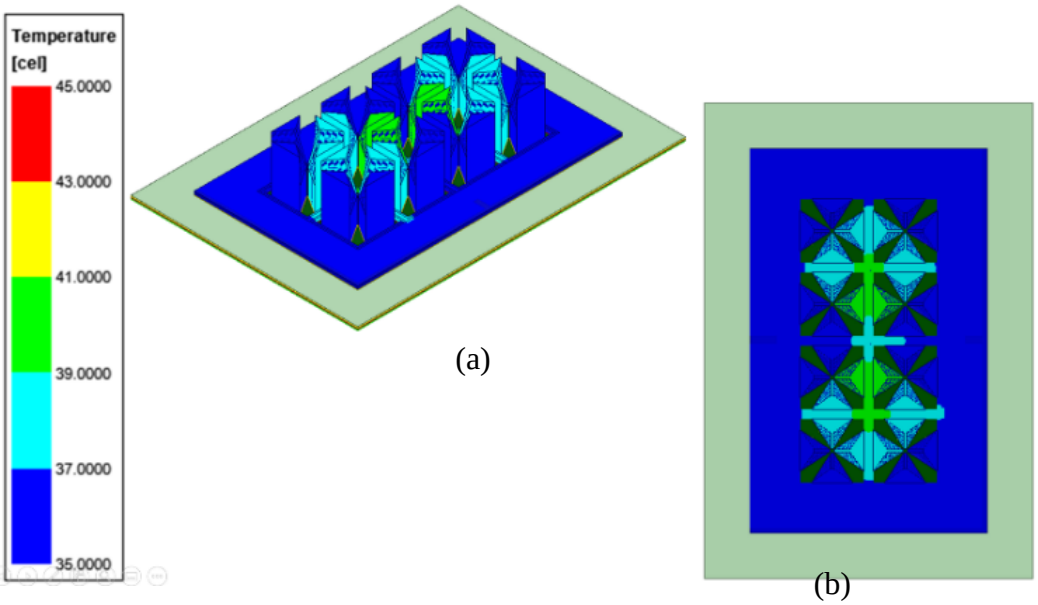

(a)

(b)

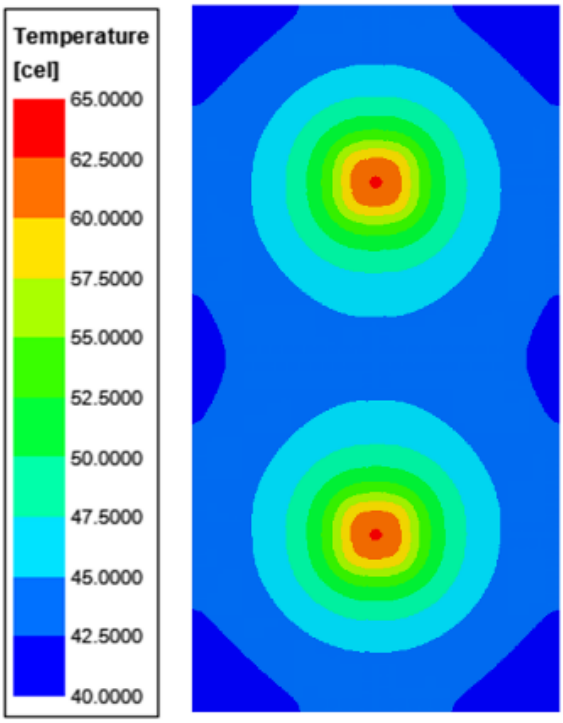

(c)

Fig.3.19. Temperature distribution of 4x2 array antenna with the two chips each having power consumption of 1.35 Watts: (a) isometric view, (b) top view, and (c) bottom view.

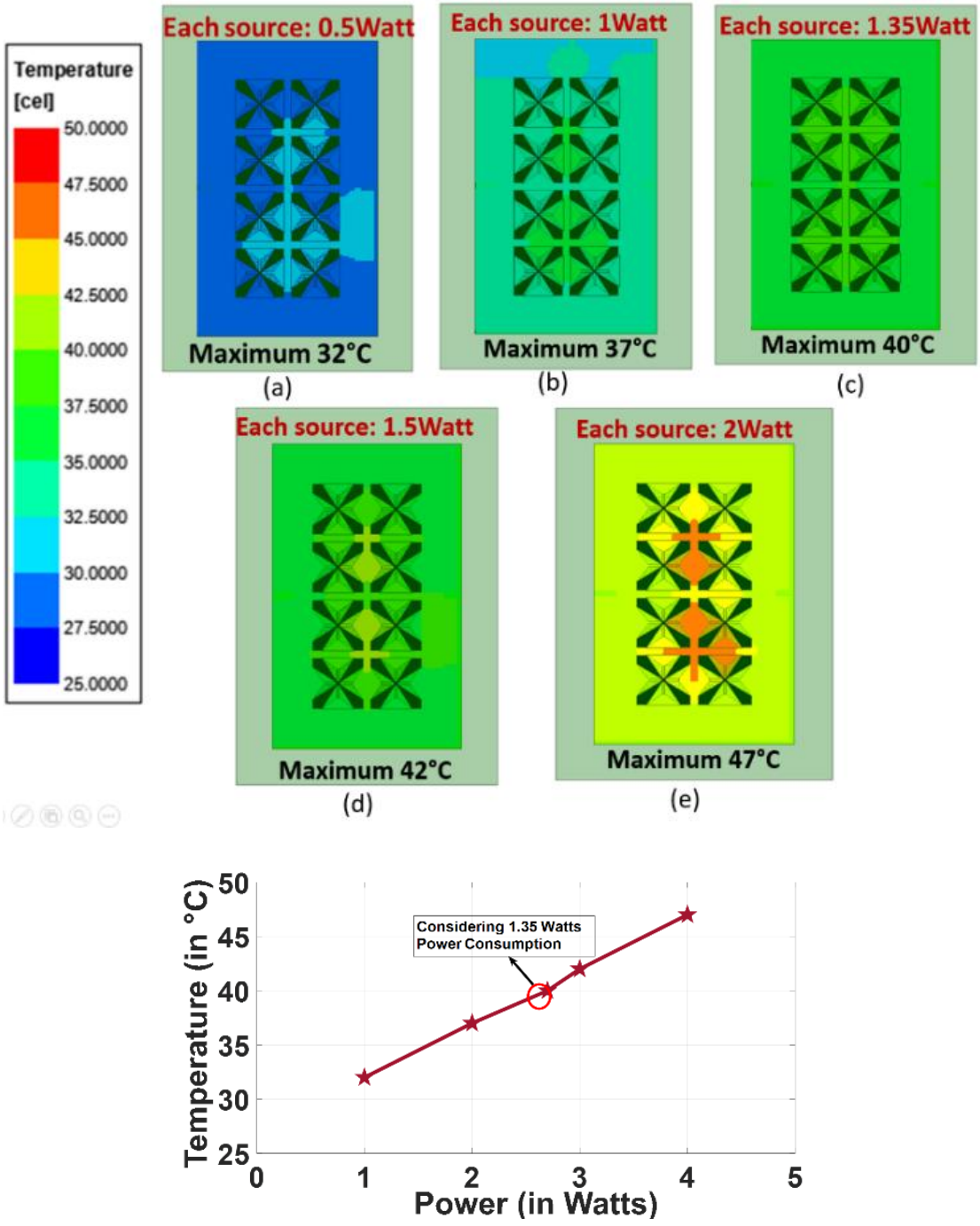

(f)

Fig.3.20. Temperature distribution of 4x2 array for the different input power consumptions (a) total 1 Watt, (b) total 2Watt, (c) total 2.7Watt, (d) total 3Watt, (e) total 4 Watt and (f) Input Power versus maximum temperature (the temperature when each chip has power consumption of 1.35 Watts is marked with a box in graph).

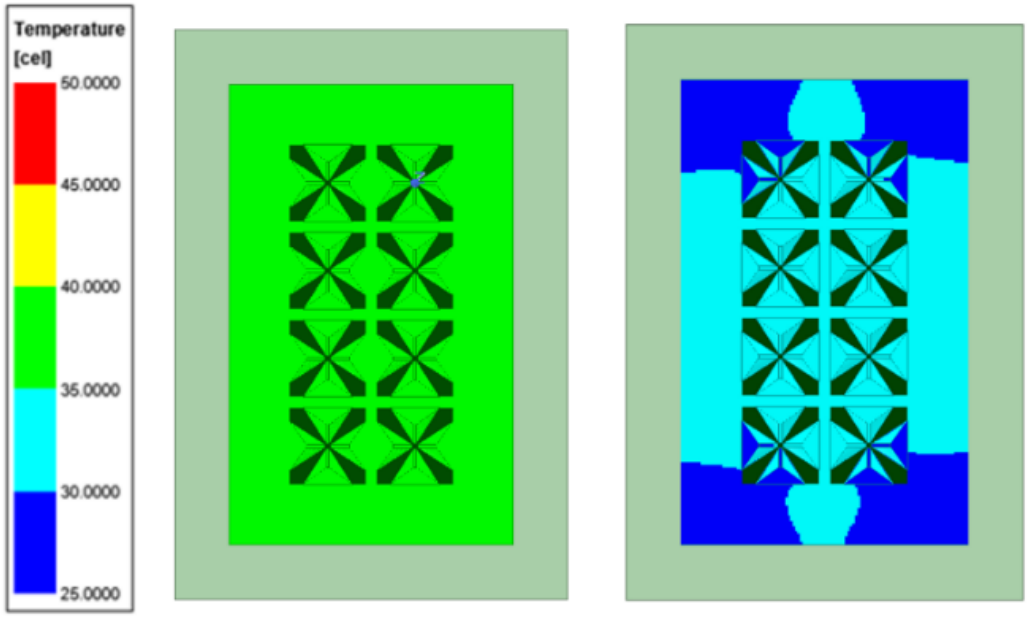

Fig. 3.21. Temperature distribution of 4x2 array for (a) Aluminum based structure, and (b) Copper based structure.

In Figs. 3.22(a) and 3.22(b), the comparison of the 4x2 antenna aperture is simulated with same simulation setup assuming each chip has power consumption of 1.35 Watts dissipating as heat, where no air flow is considered in Fig. 22(a) and 0.5 m^3/sec air flow is considered for Fig. 3.22(b). It is noticed that temperature of Fig. 22(a) is nearly 42°C whereas for Fig. 3.22(b) it ranges from 24-28°C. So, if some forced air flow can be arranged better heat sinking can be achieved with the same antenna structure. In most commercial applications, a fan is usually used to create air flow over heat sink, and in that case more temperature reduction can be achieved compared to that without any forced air flow depending on fan speed.

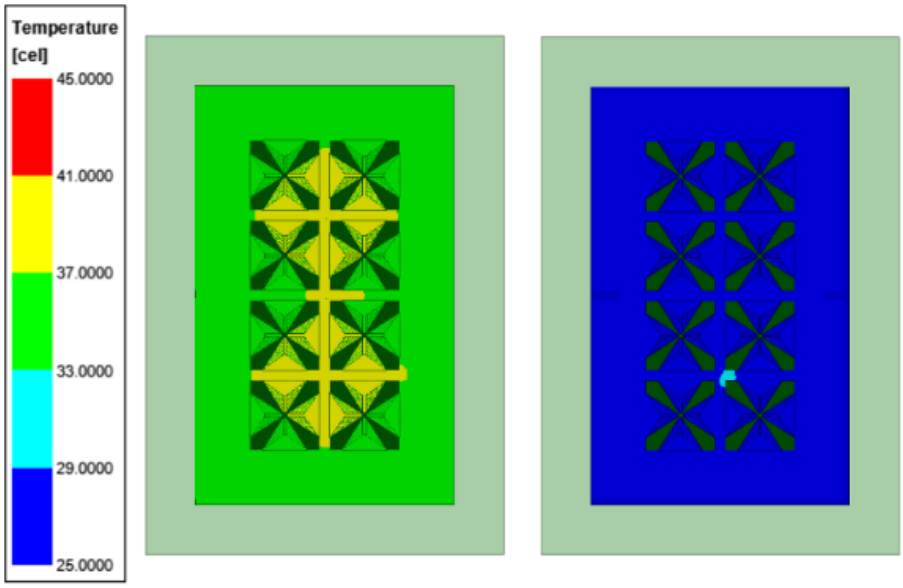

Fig. 3.22. Temperature distribution of the 4x2 array of aluminium alloy for (a) no air flow, and (b) $\mathbf{0.5}\ \boldsymbol{m^3/sec}$ air flow.

With the same simulation setup as in Fig. 3.20, a parametric study for temperature distribution for various heights of the radiators in 4x2 array is presented in Fig. 3.23. If we consider only convection (no forced airflow in horizontal direction), then the airflow is vertical, and hence increasing the height will diffuse more heat into air that is already heated up. Thus, from Fig. 3.23, we observe the maximum temperature of the 4x2 array comprised of 16 mm high radiators is 40°C whereas that of 32 mm high radiators is 30°C. Hence doubling the height can reduce temperature only by 10°C. Also, the maximum temperature is almost constant beyond 24mm high radiators. It is clear that the temperature reduction is very little with the increase of height beyond 24mm. Thus, it is evident that increasing the height beyond a particular height is not much helpful. However, we have to maintain height equal to half wavelength corresponding to center frequency of the operating band to get best performance as a radiator.

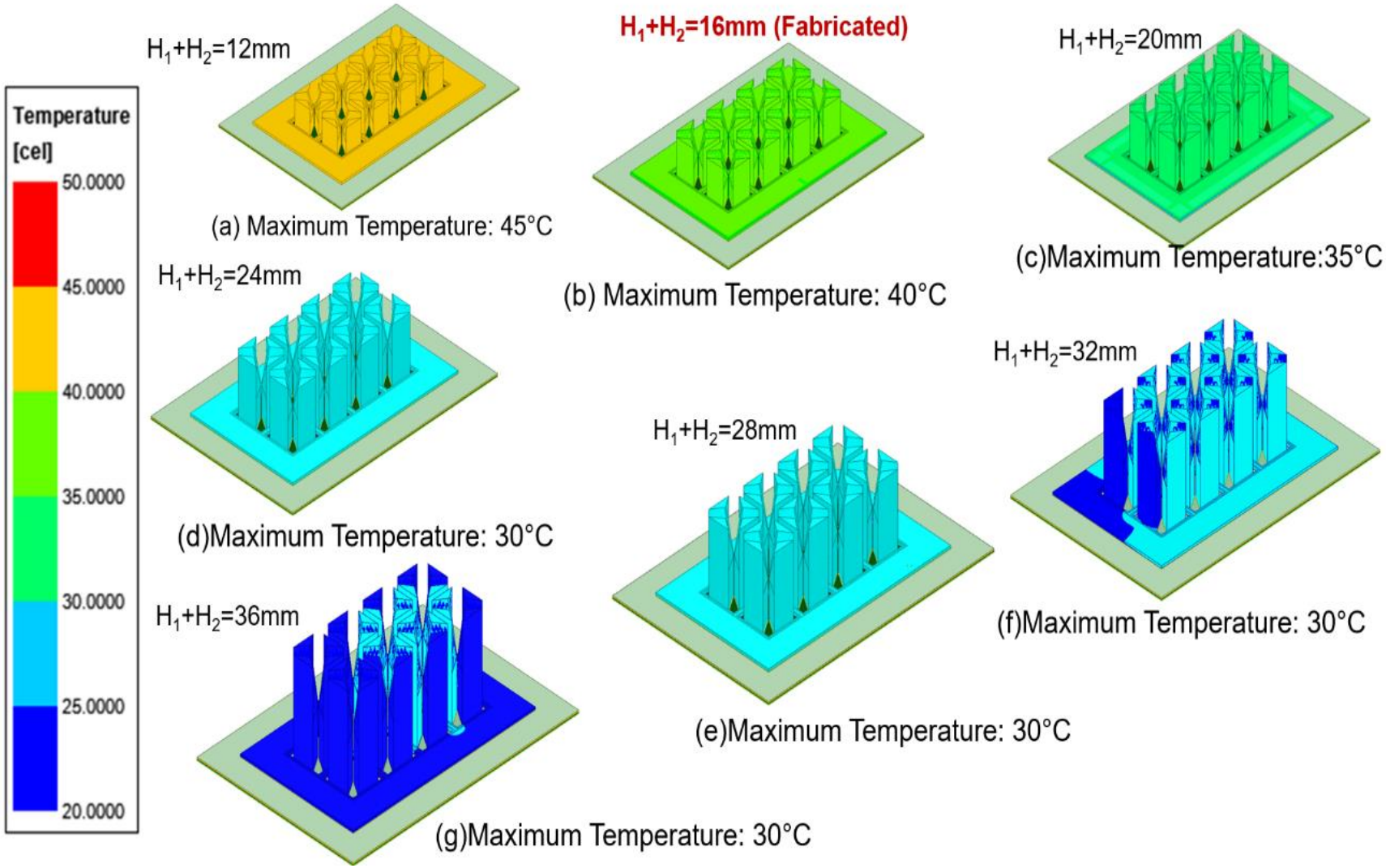

Fig. 3.23. Parametric study of temperature distribution for different heights.

Then we have considered 4x2 array comprised of hollow radiators made of metal sheet thickness of 1 mm. For any thickness more than skin depth, no change is expected in electromagnetic performance of the 4x2 antenna array. The temperature distribution of the 4x2 antenna array comprised of solid radiators and hollow radiators is shown in Figs. 3.24(a) and 3.24(b), respectively. The maximum temperature for solid radiators is 40°C, whereas for hollow radiators is 55°C. Also, we can see, in case of hollow radiators, heat is concentrated around the chip locations (55°C), and the temperature distribution is not even, which indicates the fact that hollow radiators are not as efficient as the solid ones in heat distribution and diffusion. So hollow radiators cannot be recommended as an effective heat sink.

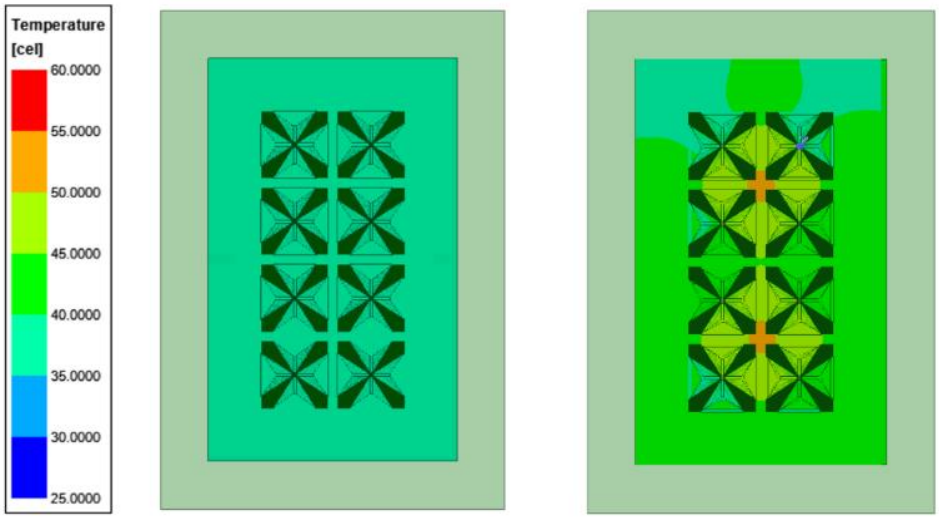

Fig.3.24. Temperature distribution of a 4x2 antenna array comprised (a) solid radiators and (b) hollow radiators.

Fig. 3.25 shows the temperature distribution of the 4x2 single polarized array. We can see the maximum temperature of the single polarized array is 45°C, which indicates the fact that the decrease in metal surface area causes increase in temperature. This is because of the fact that heat sink dissipates the heat to the air by increasing the working surface area of the device. So, if we design a dual polarized radiator then it should provide more surface area

compared to single polarized radiator, but on the other hand the radiators that resemble heat fins are now orthogonally placed, thereby, creating a box shaped disconnected air ways instead of a continuous one as in single polarized radiator. Hence, we have observed little difference in the temperature distribution between the single polarized (45°C) and dual polarized (40°C) arrays.

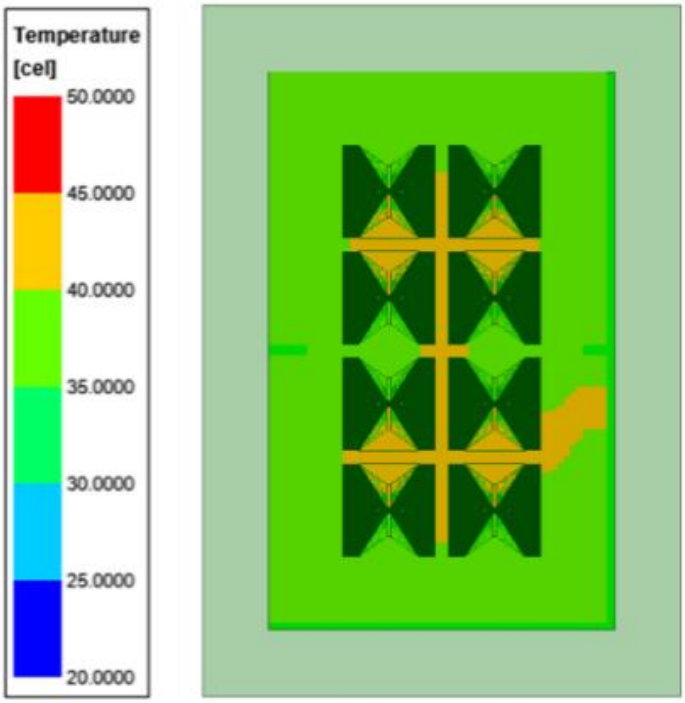

Fig. 3.25. Temperature distribution of the 4x2 single polarized array.

3.7.3. BFN layout and RFIC

In Fig. 3.26, the location of the two RFICs, position of the dual polarized antennas, and the antenna footprint in the BFN board layout is shown. Anokiwave RFICs (AWS-0101) [29] are used for the beamforming network. The AWS-0101 is a highly integrated silicon quad core IC which finds application in radar and phased arrays. Single chip supports four radiating elements, single beam transmit, and dual beam receive and provides all required beam steering controls for 6 bit phase and gain control. The 6-bit phase control implies each step

is of value $2\pi/2^6 = 5.625°$. The device provides 20 dB gain during transmit mode, 13 dBm output power during transmit, and 4.0 dB noise figure (NF) during receive. The device features electrostatic discharge (ESD) protection on all pins, operates from a +1.8V supply, and is packaged in a 56 lead 7x7 QFN for easy installation in planar phased array antennas. The chip footprint is approximately 6 mm x 6 mm. The multilayered beamforming board is fabricated and the antenna aperture is assembled with it. Direct Metal Laser Sintering (DMLS) 3D printing process is employed for the fabrication of the antenna aperture using aluminum alloy (*AlSi10Mg*, conductivity 600000 S/m).

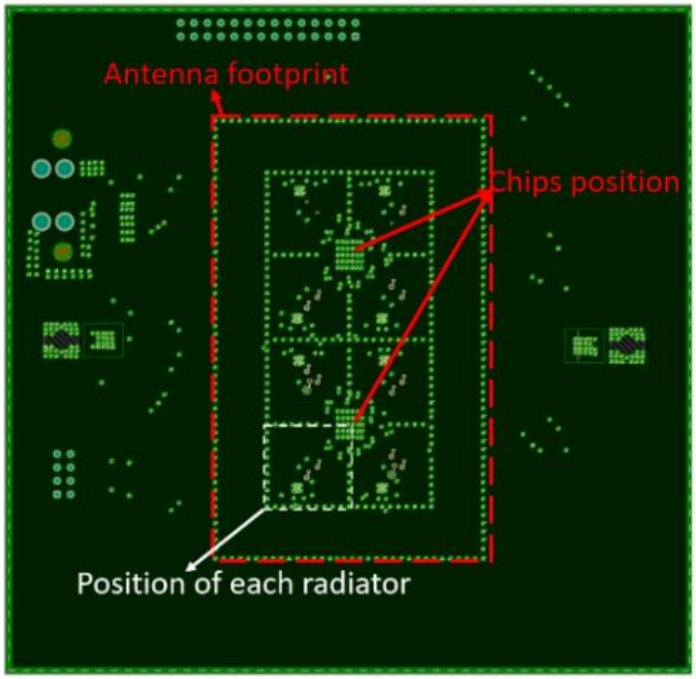

Fig.3.26. The beamforming board layout, showing the position of chips and antenna.

3.7.4. Beamforming algorithm

During the development of the graphical user interface (GUI) and beamforming algorithm, the mirror feed structure (for realizing low cross-polarization) is taken care of. The mirror ports must be excited with a 180° phase (as shown in Fig. 3.12(c)) to achieve in phase or

broadside radiation. We have employed uniform excitation in our measurements to demonstrate the performance although if only phased array performance is to be evaluated, we can apply non-uniform excitations also. The beamforming algorithm calculates the necessary phase of each of the channel, which is sent to the beamformer chip from the remote computer through the serial peripheral interface (SPI) controller. The current consumption of each chip is 870 mA at 1.8V which accounts to 1.56 Watts, however in our power experiments it drew only 750 mA, hence for our study we used 1.35 Watts throughout the work, as mentioned earlier.

3.7.5. Fabrication challenges and measurement results

Fig. 3.27(a) shows the fabricated antenna prototype and Fig. 3.37(b) shows the prototype in San Diego State University's Antenna and Microwave Laboratory (AML) inside far-field anechoic chamber that supports pattern measurements within 800 MHz to 40 GHz. Fig. 3.27(c) shows the comparison of the normalized measured and simulated radiation pattern for broadside, and -45° scan angle for Y-polarized array, respectively, along with the envelop of single element pattern for $\varphi=0^0$ plane at 11 GHz. We can observe that the scan performance is closely following the single element pattern, and the measured and simulated patterns have almost the same 3 dB gain-beamwidths for both scan angles. But we see the presence of a slight dip in the broadside measured pattern in addition to higher sidelobe level in measured patterns for both the scan positions. Considering the roughness of the 3D metal printed antenna structure, and the difference of thermal coefficient between the beamforming board and the 3D printed metal structure, fabrication of such an array is quite challenging. A superior assembly technique needs to be developed in future.

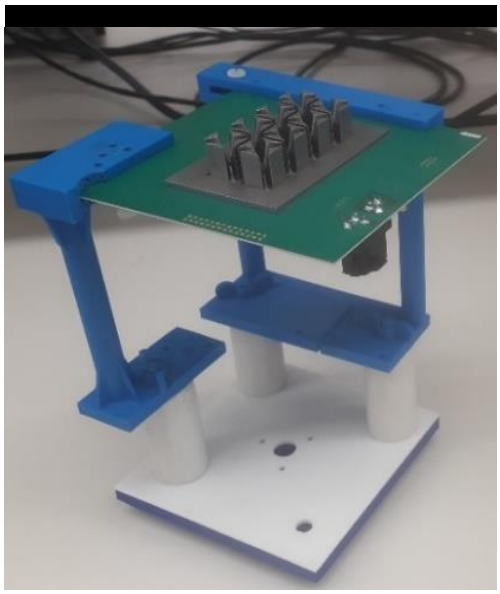

(a)

(b)

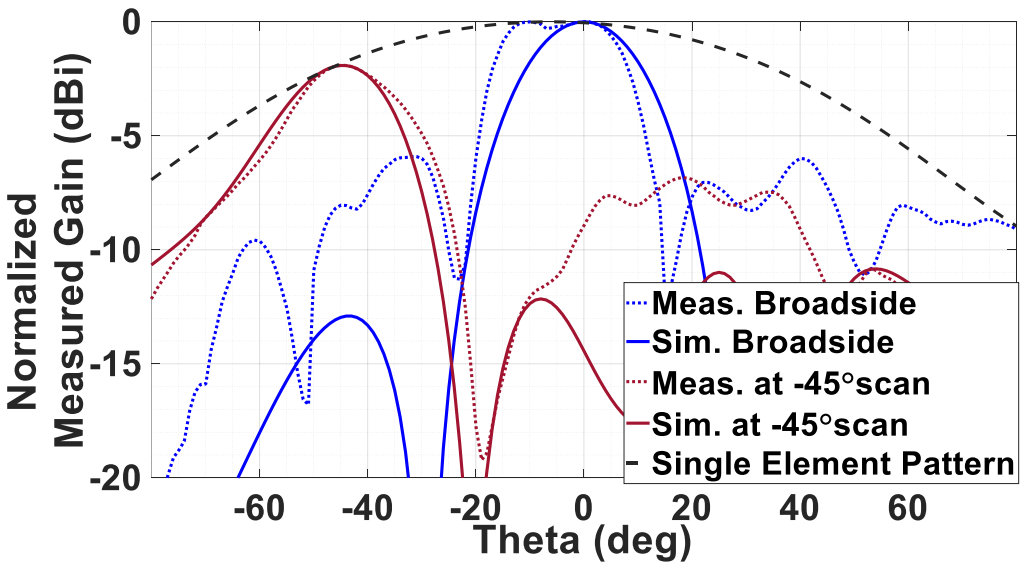
Normalized Measured Gain (dBi)
0
-5
-10
-15
-20
-60
-40
-20
0
20
40
60
Theta (deg)
Meas. Broadside
Sim. Broadside
Meas. at -45°scan
Sim. at -45°scan
Single Element Pattern

(c)

(d)

(e)

Fig. 3.27. (a) Fabricated antenna prototype (b) fabricated prototype in anechoic chamber, (c) Normalized simulated and measured radiation pattern at broadside, and -45° scan angle with single element pattern envelop for $\varphi=0^0$ plane at 11 GHz for X-polarized array, and the temperature distribution of the fabricated antenna array measured by IR camera, and (e) The temperature distribution of the antenna's BFN side (Backside) measured by IR camera.

Fig. 3.26(d) shows the temperature distribution of the fabricated array measured using an infra-red (IR) camera. We can see the measured maximum temperature of the antenna is nearly 41°C, whereas the maximum temperature distribution ranges from 40-41°C in the simulated result (Fig. 3.18). Therefore, in case of the thermal analysis, measured results are in good agreement with the simulated results. We can also see the temperature of the PCB from backside in Fig. 3.37 (e). In Fig. 3.37(e), it is seen that each chip is nearly 60°C, which agrees with that observed in Fig. 3.19(c). Thus, we can infer that the measured heat sink results are in good agreement with the simulated ones.

3.8 Dual beam scanning in the 4x2 array

Fig. 3.27 shows the generation of dual beam in the array, when both X- and Y-polarizations are excited and a progressive phase shift of Δø is provided in X-polarized antenna array, whereas a progressive phase shift of the (-Δø) is provided for Y-polarized antenna array. We can observe that X-polarized array is scanning at around 35° whereas Y- polarized array is scanning at -35° simultaneously. It is interesting to note that, dual beam is possible for this radiator, provided the chip has the capability of exciting both X- and Y-polarized antenna arrays simultaneously with different progressive phase shifts, while the beamforming algorithm is taking care of this function of the chip.

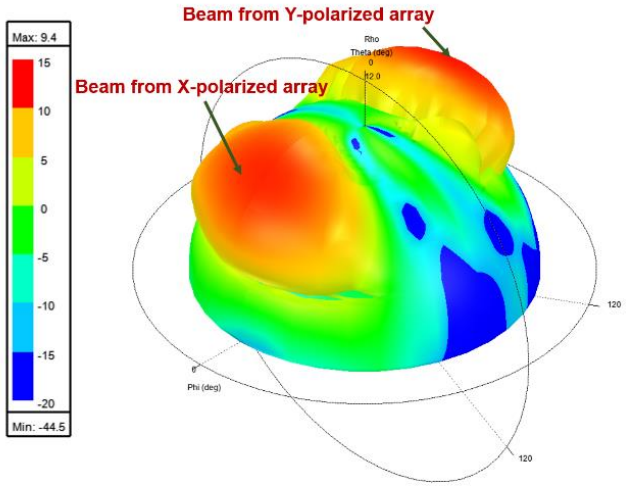

Fig. 3.28. Dual beam scanning when both X- and Y-polarizations are excited.

3.9. Conclusion

As far as we know, this is the first dual linear polarized all 3D metal printed phased array antenna integrated with RFICs based BFN where radiating elements are also serving as heat sink structures. The heat sink study has been validated with an IR camera. The antenna employs Anokiwave chips to generate dual linear polarization as well as achieve beam-steering performances. The mirror feed technique is applied to improve the cross-polarized fields. The antenna covers 8.5 GHz to 11 GHz with acceptable radiation patterns and low cross-polarized fields, and scans till ±50° in both X- and Y-polarizations. The maximum temperature on the antenna array is only 41°C, which indicates the fact that the antenna aperture is working as an efficient heat sink. We have achieved temperature reduction by 60°C with 4x2 antenna array heat sink structure when compared to temperature distribution of the BFN stack-up without the 4x2 array heat sink radiator. Though we have faced some fabrication challenges and cannot refabricate it again due to lack of funds, the measured patterns and temperature distribution prove that this dual linear polarized all metal antenna is working as heat sink also. Such an array antenna can be extended to other frequency bands and larger array sizes except that further maturity in fabrication and integration of a metal radiator with BFN board is needed.

Chapter 4

A 22- 28 GHz Polarization Reconfigurable Flat Panel 8x8 Tx/Rx Phased Array Antenna with Uniquely Arranged Novel Radiating Elements for CubeSat Communication

4.1. Introduction

The electronic scanning phased array antenna can provide high directivity with near-instantaneous beam steering capability [1], [2]. Recently, with the development in commercial beamforming chipsets, phased array antennas (PAAs) with integrated beamforming networks (BFNs) consisting of silicon radio frequency integrated circuits (RFICs) have attracted significant attention. Fully integrated chipsets replace the requirement for discrete transmit (Tx) or receive Rx) blocks and are typically comprised of a radio frequency switch, low noise amplifier in case of Rx channel, high power amplifier in case of Tx channel, phase shifters, and variable attenuators in a compact arrangement, thereby reducing overall size, cost, and RF losses. In [5], [6], [30]-[37], a number of polarization agile PAAs with RFIC based beamforming networks (BFN) are discussed elaborately. In [30], presents the advantages of the application of silicon RFICs for phased-array transmitters/receivers. In [5], [6], [31]-[37], the proposed phased arrays either work in Rx or in Tx modes, and the works presented in [5], [6], [31]-[37] emphasize the novelty from the system point of view, while a conventional stacked patch topology is employed as the basic radiating element. In other words, these papers focus more on the innovations in the RF system area rather than the radiating element and antenna aperture. In [13], a dual circular polarized Rx/Tx array for Ku-band and a dual slant linear polarized Rx/Tx array for Ka-band, are discussed. In [38], an elaborate discussion on silicon beamformers and state-of-the-art phased array antenna technology is discussed. In [39], a

flat panel 8x4 Tx/Rx PAA with the RFIC based BFN, and conventional stacked patch as radiating element, is used as a feed source for a reflector antenna. Recently, in [40], a novel 3D metal printed dual linear polarized RFIC-based 4x2 phased array antenna, with an emphasis on developing a novel radiator with heat sinking properties, is proposed.

On the other hand, polarization-reconfigurable antennas have attracted significant attention for advanced communication systems as multi-functional antennas for various applications, including cubesats. As cubesat missions proliferate, there is an increasing desire for higher gain dual circular polarized (CP) antenna systems to maintain reliable communication links. Different polarization-reconfigurable antennas have been reported in [41]–[45]. In [38], discussion about polarization-reconfigurable antennas are presented. In [46] and [47], polarization-reconfigurable phased array antennas (without RFIC-based integrated BFNs), are presented. In [48], an 8 ×8 dual linear/circular polarized passive PAA with a conventional stacked patch as its radiating element was discussed. In [49] a flat panel sequentially rotated dual circular polarized 8x8 phased array, with a circularly polarized stacked patch as its radiating element, is proposed.

The application of the work presented in this project is based on requirements derived from a National Aeronautics and Space Administration (NASA) Glenn Research Center (GRC) mission concept for an orbiting lunar relay providing persistent connectivity to the lunar south pole. The communications links supported by this relay include Tx/Rx links to the lunar surface, to Lunar Gateway, and direct-to-earth. These requirements are met or exceeded through the use of multiple dual circular polarized 16x32 (512-element) arrays that cover ±10° in the lunar surface link, ±15° in the gateway link, and ±2° in the direct-to-earth link with a minimum G/T of 0 dB/K and EIRP of 36 dBW, as shown in Fig. 4.1. However, in this work, we have explored the 8x8 PAA as a building block of this 512-element array.

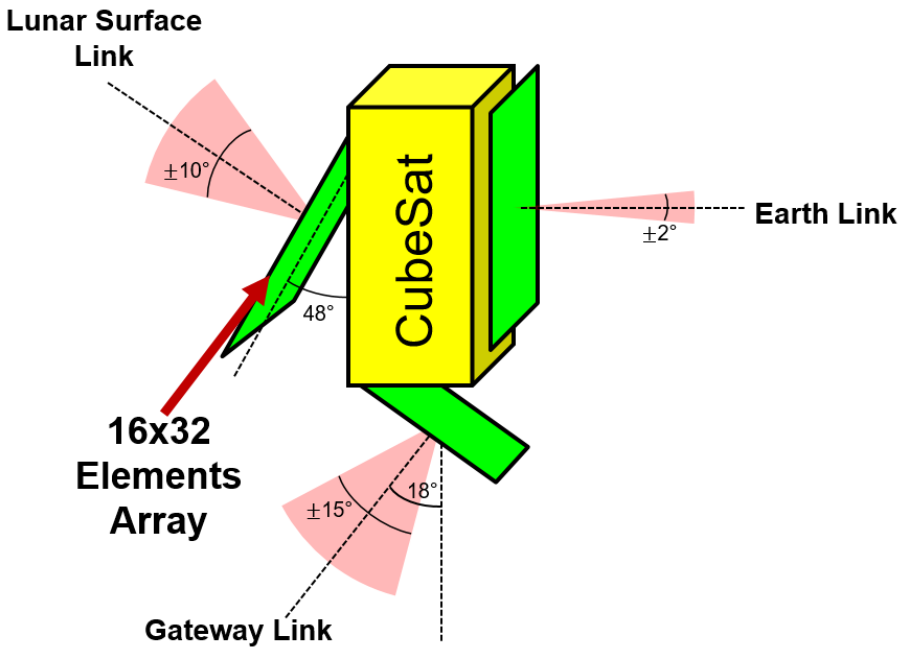

Fig. 4.1. Phased array antenna of 16x32 elements on cubesat chassis.

Here, a ±50° beam scanning, RFIC-based, polarization-reconfigurable Tx/Rx flat panel phased array antenna, comprised of uniquely arranged novel radiating elements, is proposed. The array covers 22-28 GHz bandwidth, offers low cross polarized fields when operating in dual linear polarizations, and maintains excellent axial ratio in dual CP cases over the entire bandwidth and for all scan angles up to 3dB gain drop/scan loss. According to the required specifications, the array should operate in two frequency bands: 22.55–23.55 GHz and 25.5–27.5 GHz, which covers part of the K- and Ka-bands. Since the individual bands are closely spaced, a single wideband antenna is designed. In view of the above, the novelty of the work presented herein are as follows: (i) a novel radiating element design that covers 22-28 GHz bandwidth, and resolves the poor isolation between two ports, thereby improving cross-polarized fields and providing axial ratio (AR) less than 3dB over the entire bandwidth, (ii) a unique arrangement of radiators to further improve cross-polarized fields and axial ratio, (iii) polarization reconfiguration (i.e., offering horizontal (X-), vertical (Y-), LHCP and RHCP), and (iv) the 8x8 array, integrated with an RFIC-based BFN, operates in both Tx/Rx modes, and provides excellent cross-polarized fields and AR below 3dB over the entire

bandwidth and for all scan angles up to the 3dB scan loss point (which is ±45°-±50°). In [50], brief results of the proposed novel polarization reconfigurable 64-elements phased array is discussed.

4.2. Single Radiating Element

A stacked microstrip patch antenna element is used for the basis of design as this topology is known to provide wide (10-20%) bandwidth [51]. The driven patch is configured with two orthogonal feed points to support dual polarization. Dual linear (horizontal, i.e., X- or vertical, i.e., Y-) polarization is achieved when any one of the two feed points of the driven patch is excited and the other one is matched terminated. When both feed points are equally excited and $\pm 90^{o}$ time phase is applied to any one feed point, then circular polarization (LHCP or RHCP) can be achieved. This single radiating element (Fig. 4.2) is analyzed along with the printed circuit board (PCB) stack-up layers used in the array BFN to predict the antenna performance.

In this work, dual linear/dual circular polarization is achieved by employing two feed points, however, this can result in poor isolation between the two feed ports leading to high cross-polarized fields and poor AR. Therefore, to achieve good isolation between two ports, in addition to good impedance matching over the desired bandwidth of 22 GHz to 28 GHz, three configurations of the stacked patch antenna (I, II, and III) are studied. The driven patch and parasitic patch geometry, along with feed point locations for configuration I, II, and III, are shown in Figs. 4.2(a), (b), and (c), respectively. Fig. 4.2(a) shows configuration I, which is a conventional stacked square patch. In configuration II (Fig. 4.2(b)), an L-shaped stub is placed in one corner of the driven patch in such a way that the stub lies adjacent to the two feed points to achieve improvement in isolation between them. Another L-shaped stub is placed in the opposite corner to maintain the symmetry of the patch. Fig. 4.2(c) presents configuration III, which is a modification of configuration II, where edge stubs are designed for all four edges on both the driven and parasitic patches. The stubs on the radiating edge is known to improve bandwidth [52]. Since the patch elements work in both dual linear and

dual circular polarizations, stubs are designed on all four edges of the square patch in configuration III to achieve bandwidth enhancement.

The performance of configurations I, II, and III are compared in terms of the reflection coefficient magnitude of port #1 (port #2 is identical) in Fig. 4.3(a); isolation between two ports in Fig. 4.3(b); AR (for circular polarization) in Fig. 4.3(c); and total antenna efficiency in Fig. 4.3(d). We can see that configuration I covers 22.5 to 27.5 GHz, and the isolation between the two ports degrades with frequency and increases to -10dB towards the higher end of the band. Configuration II offers improvement in isolation, but bandwidth is not improved, which is as expected from the previous discussion. Configuration III offers significant improvement in isolation in addition to bandwidth enhancement. Configuration III covers 22-28 GHz bandwidth and isolation below -15 dB over the entire bandwidth is achieved. In configuration III, the improvement in isolation leads to improvement in AR and total antenna efficiency, which can be seen from Figs. 4.3(c) and 4.3(d), respectively. The current distribution for the linear polarization condition (one port excited and other port match terminated) of the driven patch for configuration I and III are shown in Fig. 4.3(e), which shows that the L-shaped stub reduces the current flowing from the excited port to match terminated port by a significant amount in cases of configuration III when compared with the configuration I. Therefore, the L-shaped stub placed in one corner of the driven patch adjacent to the two feed points helps to achieve improvement in isolation between the two feed points, whereas another L-shaped stub is placed in the opposite corner to maintain the symmetry of the patch. The radiation pattern in the linear (vertically polarized) mode of configuration I and III at the center frequency (25 GHz) are compared in Figs. 4.4(a) and 4.4(b), respectively. High cross-polarized fields are a common problem in a conventional patch antenna with two feed points, which is evident from Fig. 4.4(a), however, cross-polarization is significantly improved in Fig. 4.4(b) with a sharp null at the broadside angle ($\Theta=0^{o}$). The slight asymmetry is noted in both Figs. 4.4(a) and (b), which is partly due to the ground via arrangement around the feed points in the BFN structure. The asymmetry in the radiation pattern in Fig. 4.4(b) is also partially due to the presence of the L-stubs, which is mitigated by the unique arrangement of radiators in the 2x2 sub-array of the target 8x8 array design. Thus, configuration III is employed as a single radiating element in the 8x8 array.

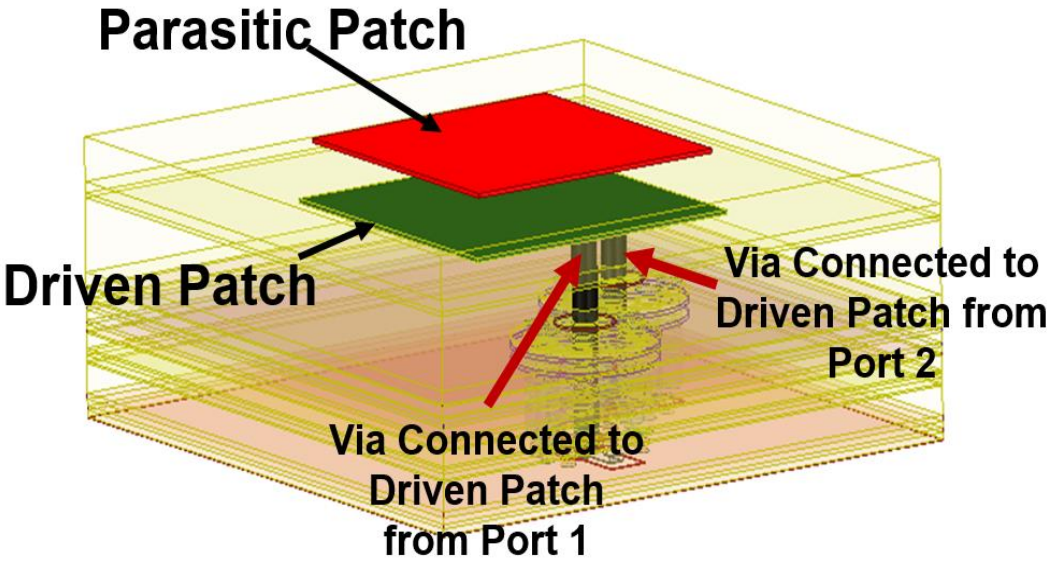
Parasitic Patch
Driven Patch
Via Connected to Driven Patch from Port 2
Via Connected to Driven Patch from Port 1

(a)

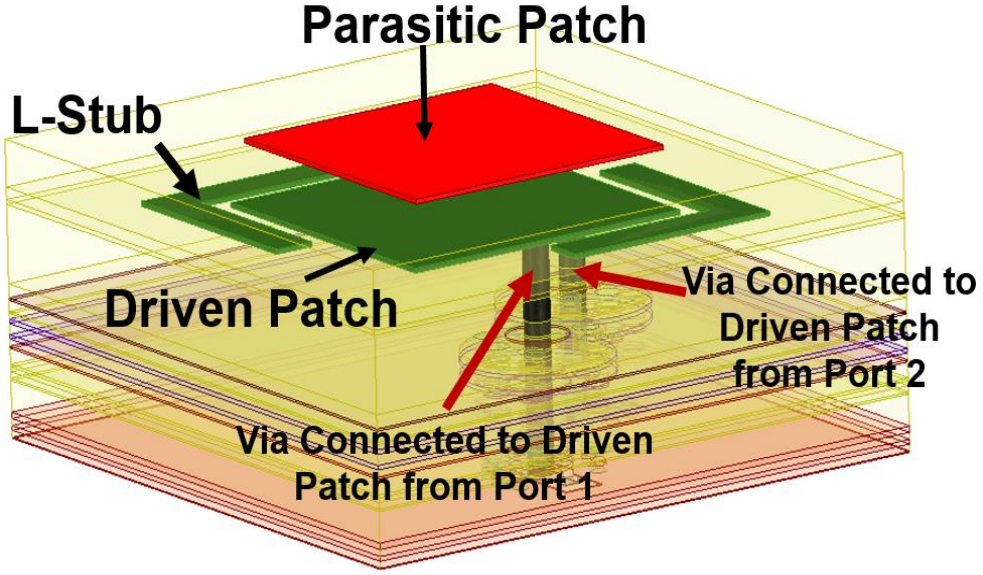
Parasitic Patch
L-Stub
Driven Patch
Via Connected to Driven Patch from Port 2
Via Connected to Driven Patch from Port 1

(b)

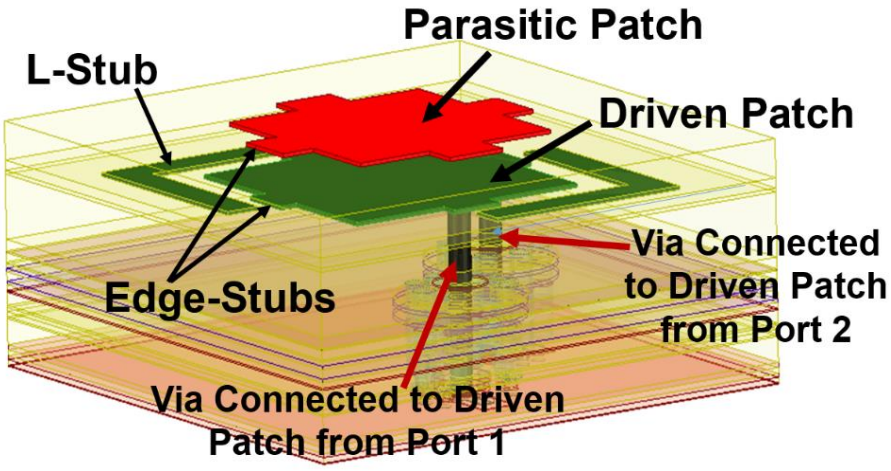

(c)

Fig 4.2. Isometric view of (a) configuration I, (b) configuration II, and (c) configuration III.

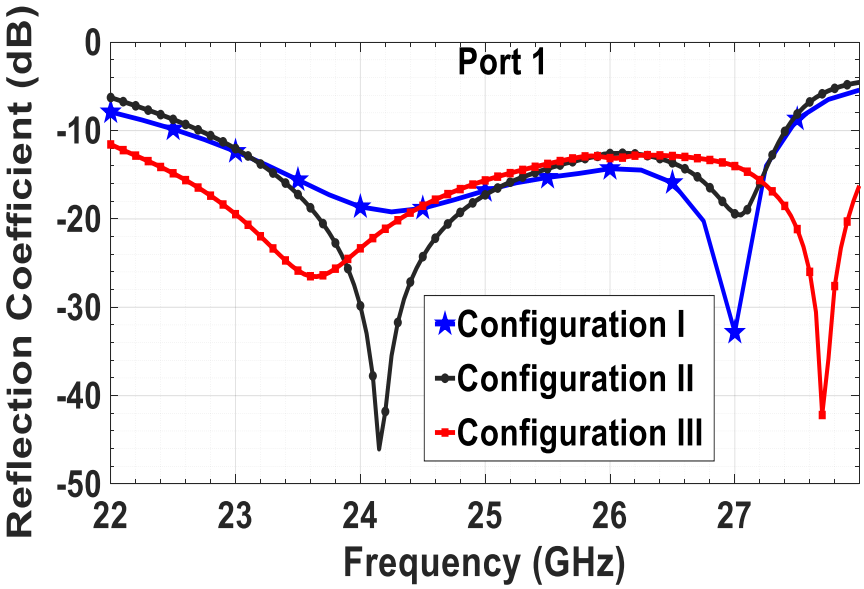

(a)

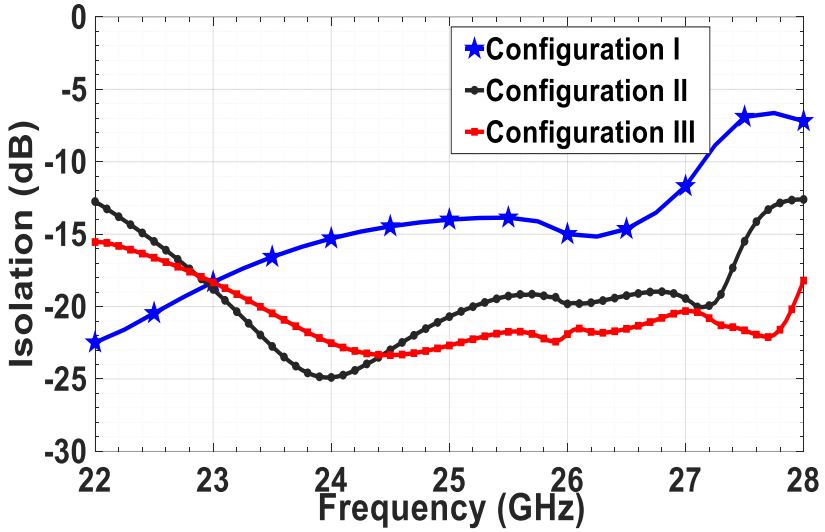
Configuration I
Configuration II
Configuration III
Isolation (dB)
0
-5
-10
-15
-20
-25
-30
22
23
24
25
26
27
28
Frequency (GHz)

(b)

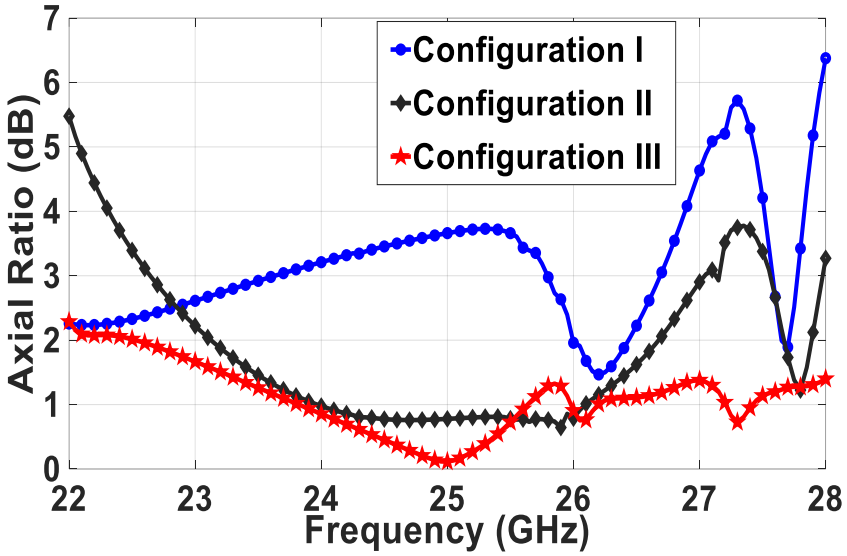
Configuration I
Configuration II
Configuration III
Axial Ratio (dB)
7
6
5
4
3
2
1
0
22
23
24
25
26
27
28
Frequency (GHz)

(c)

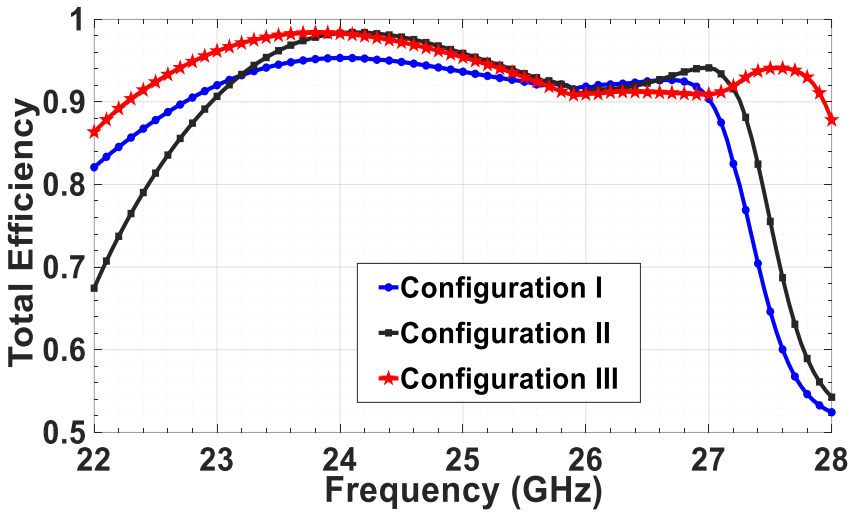

(d)

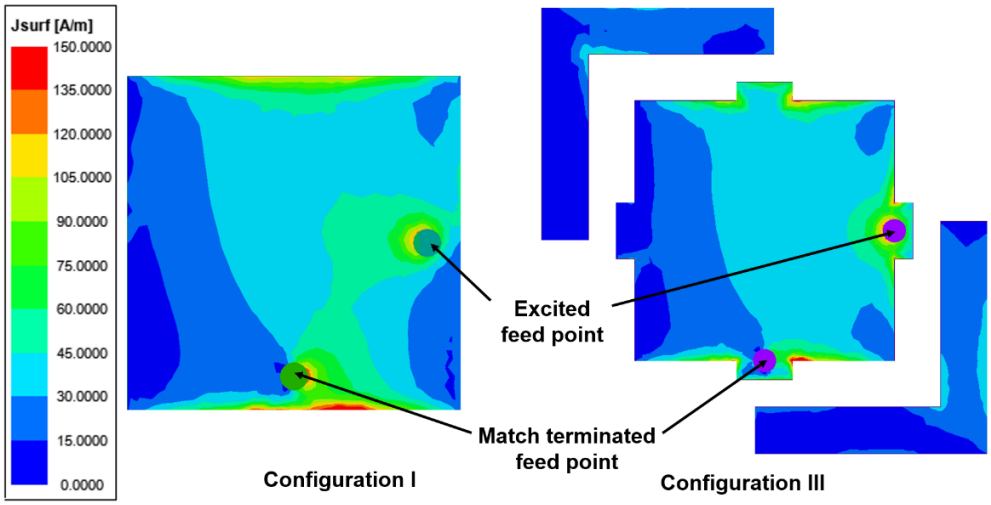

(e)

Fig. 4.3. For configurations I, II, and II: (a) Reflection coefficient magnitude of port 1, (b) isolation between two ports, (c) axial ratio, (d) total antenna efficiency, and (e) Current distribution of configuration I and III in linear polarization.

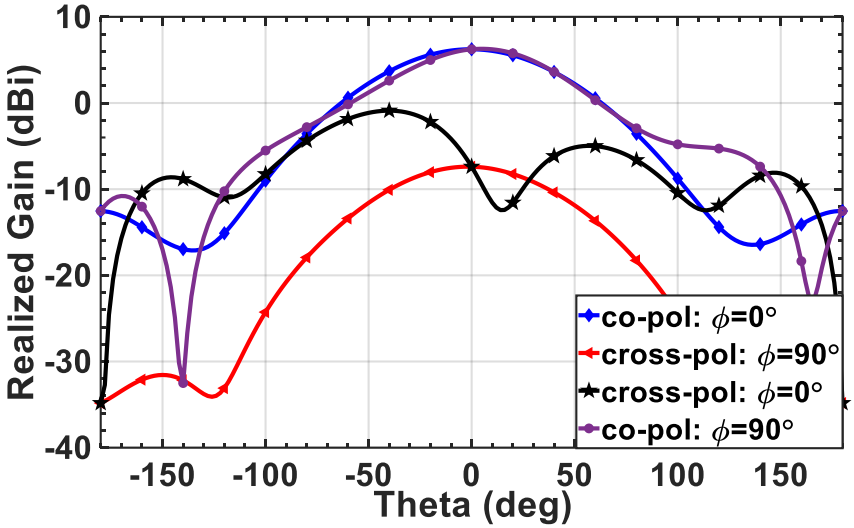

(a)

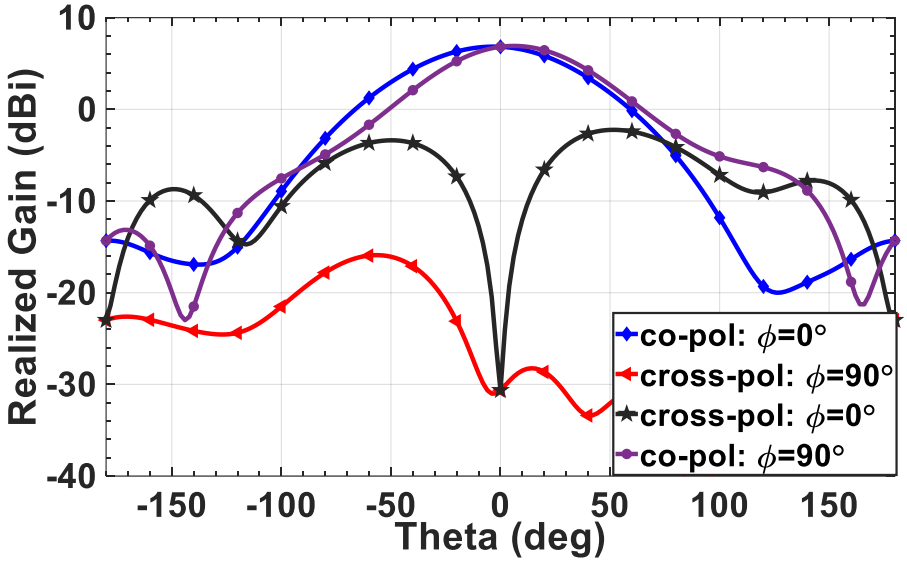

(b)

Fig. 4.4. Radiation pattern at 25GHz for (a) configuration I, and (b) configuration III in linear polarized mode.

4.3. Stack-up description of the PCB

Fig. 4.5(a) presents the top view of the driven and parasitic patches of configuration III. The patch dimension parameters, specified in Fig. 4.5(a), are as follows: $Lx_d \sim Ly_d \sim$ 2.8mm, $Lx_p \sim$

Ly_p ~ 2.6mm, d ~ 0.5mm, L_d ~ 0.5mm, lx ~ ly ~ 0.3mm, Lsx ~ Lsy ~ 2.5mm. Fig. 5(b) shows the bottom view of the coplanar waveguide (CPW) feed structure. Fig. 4.5(c) shows the side view of the radiating element along with the beamforming board stack-up. The driven patch is placed over h_1=30 mil thick substrate, whereas the driven and parasitic patches are separated by h_2=20 mil thick substrate. The overall thickness of the BFN stack-up is approximately 100 mils ($H+h_1+h_2$). Each driven patch is fed by two vias that are connected with a grounded CPW feed structure at the lowermost layer of the stack-up. Astra-MT77 of relative permittivity ε_r=3 is used as the core material whereas Tachyon of ε_r=3.02 is used as prepreg material in the BFN stack up. Astra-MT77 possesses a stable dielectric constant (Dk) between -40°C and +140°C at up to W-band frequencies [53], which makes it suitable for advanced commercial radio frequency printed circuit designs.

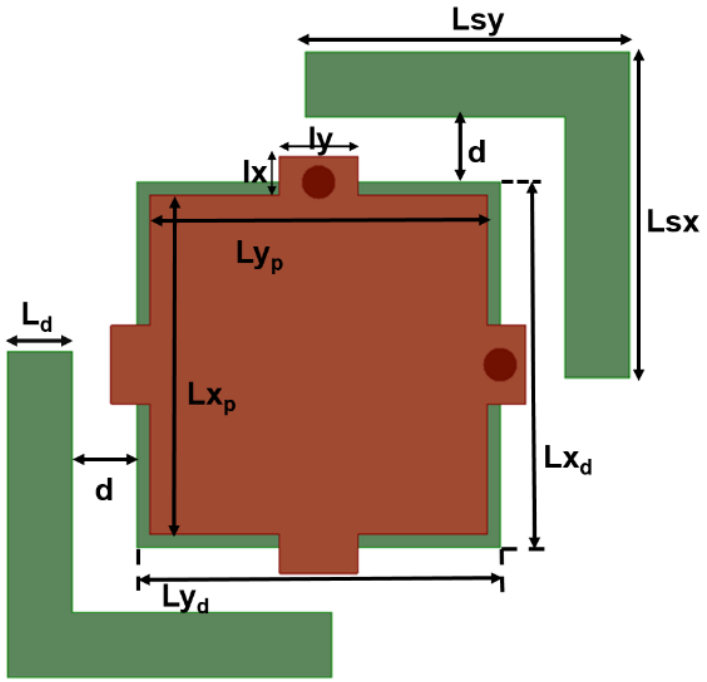

(b)

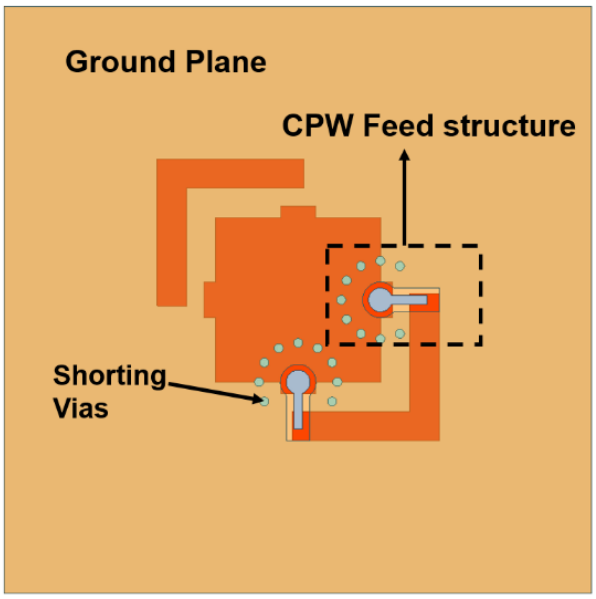

(b)

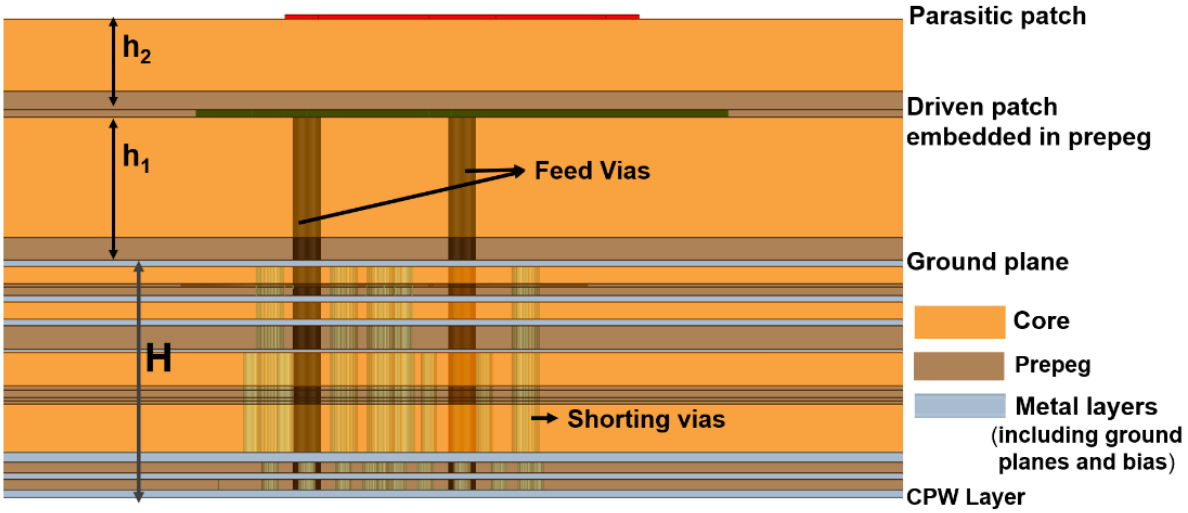

(c)

Fig. 4.5. (a) Top view of the driven and parasitic patch, (b) bottom view of the single element with CPW feed structure, and (c) BFN stack-up layers.

4.4. 2x2 Sub-array configuration and performance

An active PAA can be designed with an active device at each element, or with active devices at various sub-array levels such as in columns, rows, or groupings of elements. In this work, we have employed Anokiwave RFICs (AWMF-0165) [54] to control the amplitude and phase of the array elements. Each Anokiwave chip can work in both Tx and Rx modes and it is a dual-polarization RFIC with two common ports, each for one polarization (horizontal or vertical), and eight element ports, four of which correspond to one common polarization port and the remaining four corresponding to the other common polarization port of the chip. Each output of the chip can be controlled independently and externally through a serial peripheral interface (SPI) to provide the required phase and amplitude to each port of each radiating element. Therefore, each chip can feed four dual linear or dual CP antennas when the two common ports are combined using an external splitter. Each radiating element of the 2x2 sub-array has two orthogonally located feed points which can be controlled independently through the chip to achieve all of the four above-mentioned polarization in each radiating element. To achieve circular polarization (LHCP or RHCP), all eight outputs of the chip are used with half the ports applying a ±90° phase shift to one of the linear polarized element feeds to create circular polarization in each single element of the 2x2 sub-array.

In this work, the PAA is designed for 22-28 GHz and an inter-element spacing of half the free space wavelength ($\lambda_o/2$) corresponding to 25 GHz was chosen, which is $0.44\lambda_o$ at 22 GHz, and $0.56\lambda_o$ at 28 GHz. This allows grating lobe-free radiation patterns within 22-28 GHz considering 3dB scan loss in addition to the array factor benefits such as enhanced directivity (which is desired from the proposed PAA) without increasing the size of the array.

The bottom view and top view of a 2x2 conventional sub-array with an inter-element spacing of $0.5\lambda_o$ at 25 GHz are shown in Figs. 4.6(a) and 4.6(b), respectively. To achieve further improvement in the cross-polarization level in dual linear polarizations, the element mirroring is performed in both the horizontal and vertical planes [55], which can be seen in the bottom view and top view in Figs. 4.6(c) and 4.6(d), respectively. The 2x2 sub-array along with the chip footprint at the center underneath the BFN is shown in Fig. 4.6(e). The arrangement of feed points of the 2x2 sub-array with mirrored elements is shown in Fig.

4.6(f), where unit cell 2 is the mirror image of the unit cell 1 along the vertical plane, the unit cell 3 is the mirror image of the unit cell 1 along the horizontal plane, and unit cell 4 is a mirror image of the unit cell 1 along the horizontal and vertical planes. When the array is operating in dual linear polarization, for instance horizontal (X-) polarization, then the vertical (Y-) polarized ports are matched terminated. The adjacent elements along the X-direction (for instance, unit cell 2 and unit cell 4) are provided with a 180° phase shift in the ports along the X-axis to get a broadside pattern due to the mirror configuration (Fig. 4.6(g)). The amplitude and phase distribution of the array operating in vertical (Y-) polarization is also shown in Fig. 4.6(h)). In [55], it is explained how the cross-polarized fields are significantly reduced due to this mirror effect and we show its result in Fig. 4.7.

When the array operates in dual circular polarization (RHCP or LHCP), then both the ports of each radiating element are excited, and ±90° phase shift is applied to one port corresponding to the selected polarization of each radiator to generate CP. Selecting unit cell 1 as the reference element, each element adjacent to that reference element is provided with a 180° phase for mirrored ports (both ports are excited when operating in circular polarization). Now if we observe the phase distribution for the RHCP case (Fig. 4.6(i)), it appears as if unit cell 3 is rotated physically by 90° and provided with a 90° phase to both ports with respect to unit cell 1. Similarly, the unit cell 4 is physically rotated by 180° and provided with 180° phase to both ports with respect to unit cell 1, and unit cell 2 is physically rotated by 270° and provided with 270° phase to both ports with respect to unit cell 1. Therefore, in the 2x2 sub-array, each element is sequentially rotated in comparison with the reference element in a clockwise manner (the bottom view is shown in Fig. 4.6(i)). In [56], the sequential rotation technique is presented, and it is proved mathematically that CP performance can be improved by a significant amount. Therefore, when the sub-array works in CP, then it is comprised of sequentially rotated elements, which in turn helps to improve AR significantly. Thus, we can summarize that the unique arrangement of elements provides element mirror benefits in the case of dual linear polarizations and sequential rotation benefits in the case of dual CP. The phase distribution for the LHCP and RHCP cases are shown in Figs. 4.6(i) and 4.6(j), respectively. It is worth mentioning here that, by utilizing phase shifts from the Anokiwave RFICs (AWMF-0165) employed in BFN, we can generate

the time phase required for both dual linear polarization and dual circular polarization in this unique arrangement. Table 4.1. presents a tabular version of phase distribution of the 2x2 sub-array for all the four polarizations.

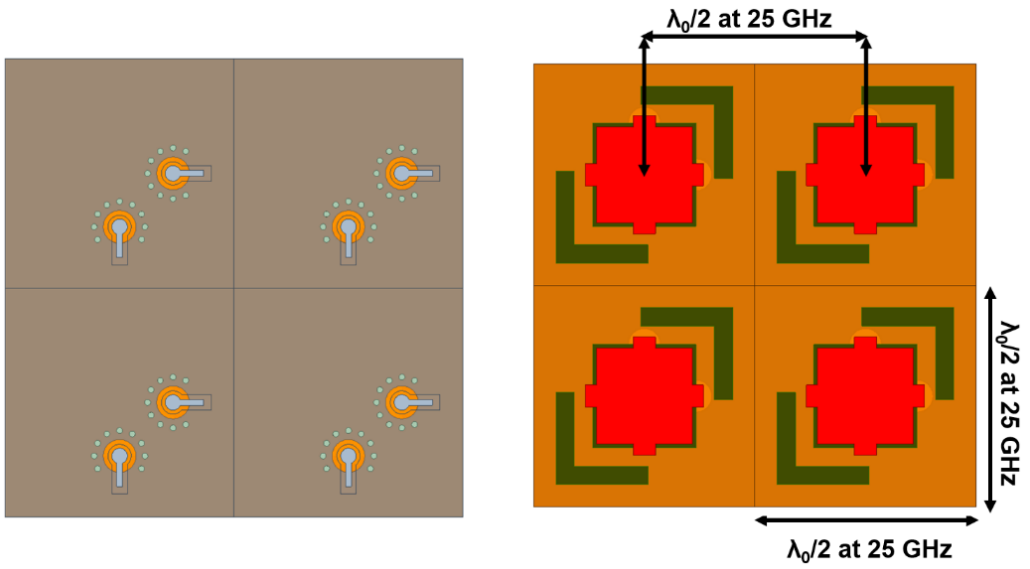

(a)

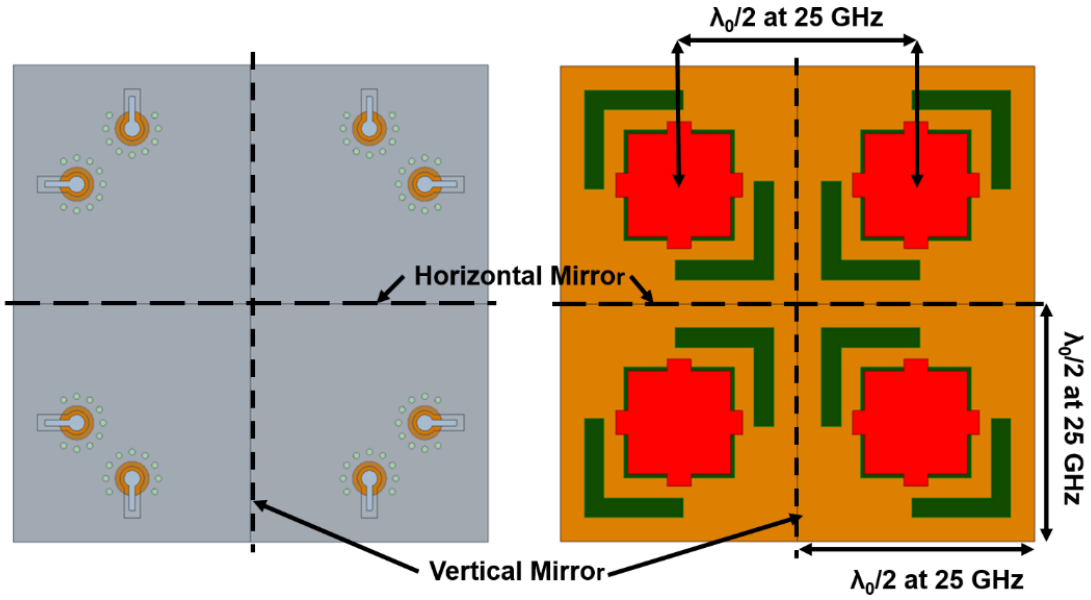

(b)

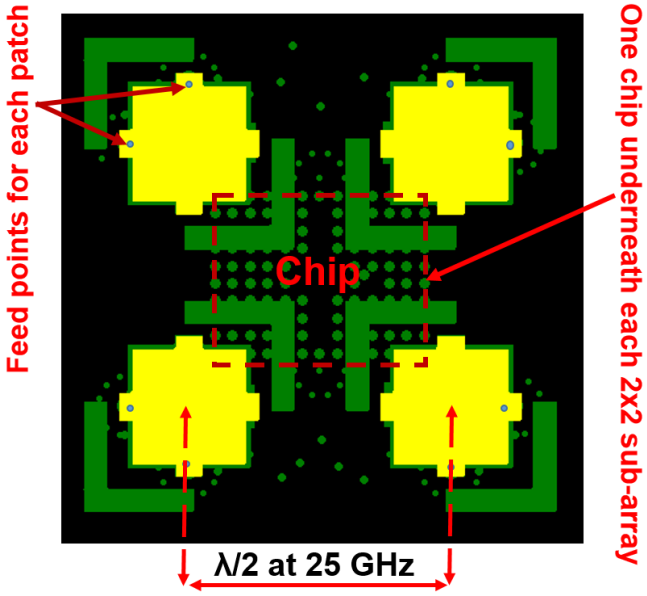
Feed points for each patch
One chip underneath each 2x2 sub-array
Chip
λ/2 at 25 GHz

(c)

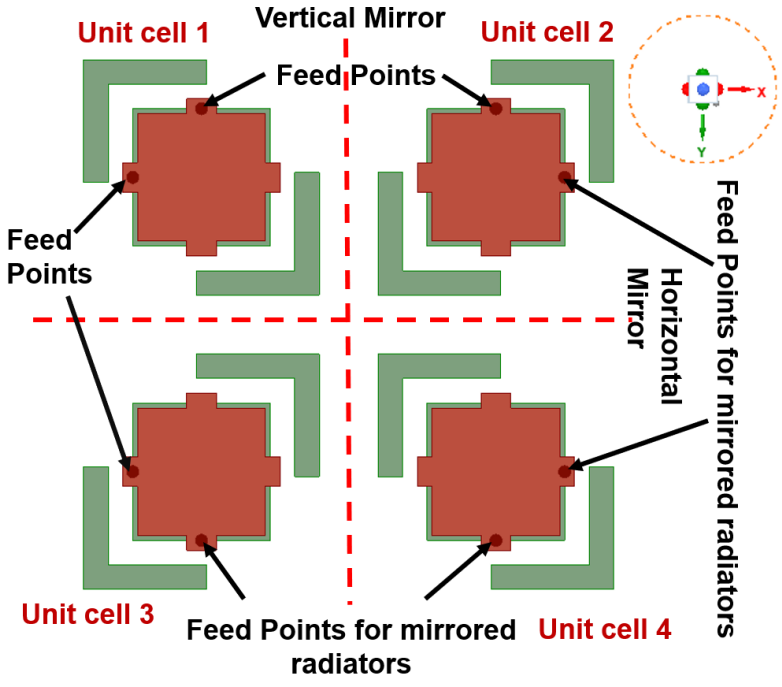
Unit cell 1
Vertical Mirror
Unit cell 2
Feed Points
Feed Points
Horizontal Mirror
Feed Points for mirrored radiators
Unit cell 3
Feed Points for mirrored radiators
Unit cell 4

(d)

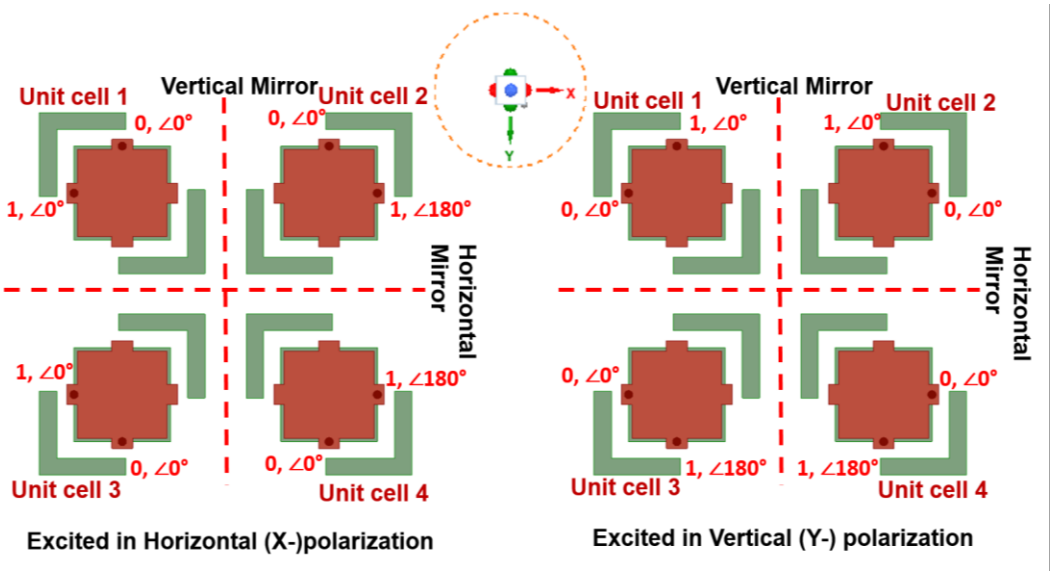

(e)

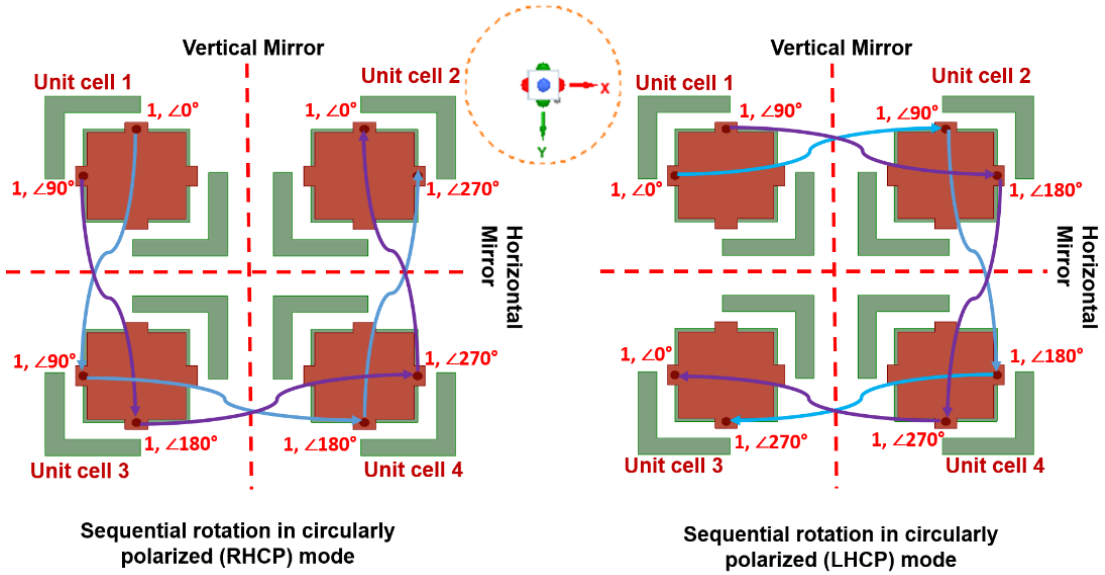

(f)

Fig. 4.6. (a) Bottom, and (b) top view of the conventionally arranged sub-array, (c) Bottom, and (d) top view of the proposed uniquely arranged sub-array, (e) chip footprint underneath the BFN, (f) feed configuration of the proposed uniquely arranged sub-array, and phase distribution of the (g) horizontally polarized, (h) vertically polarized, (i) LHCP, and (j) RHCP for 2x2 sub-array.

Table. 4.1: Phase distribution for different polarizations

Unit cell1		**Unit cell 2**		**Unit cell 3**		**Unit cell 4**		**Array Pol**
X-pol	**Y-pol**	**X-pol**	**Y-pol**	**X-pol**	**Y-pol**	**X-pol**	**Y-pol**	
1, 0°	0, 0°	1, 180°	0, 0°	1, 0°	0, 0°	1, 180°	0, 0°	H-pol
0, 0°	1, 0°	0, 0°	1, 0°	0, 0°	1, 180°	0, 0°	1, 180°	V-pol
1, 90°	1, 0°	1, 270°	1, 0°	1, 90°	1, 180°	1, 270°	1, 180°	RHCP
1, 0°	1, 90°	1, 180°	1, 90°	1, 0°	1, 270°	1, 180°	1, 270°	LHCP

The radiation pattern of the conventional and proposed uniquely arranged sub-array (with mirror effect) for the horizontal (X-) polarization at 25 GHz are shown in Figs. 4.7(a), 4.7(b), respectively. In the conventional array approach the separation between co- to cross-polarized fields is nearly 20dB, whereas the co-/cross- separation is more than 50dB (cross-polarized field is not visible till -40dB) in this uniquely arranged sub-array. Fig. 4.7(c) shows the vertical polarization radiation pattern of the proposed uniquely arranged sub-array at 25 GHz. In Figs. 4.7(d) and 4.7(e), the LHCP radiation pattern of the conventional sub-array is compared with that of the proposed sub-array. We can see the excellent null at the broadside for the LHCP pattern in the proposed sub-array case, which indicates a difference of more than 50 dB between the LHCP and RHCP patterns at $\theta=0°$. Fig. 4.7(f) shows the RHCP

pattern for the proposed sub-array. The AR at the broadside angle of both the conventional and proposed sub-arrays are compared in Fig. 4.7(g). We can notice a significant improvement in AR for the proposed arrangement. Thus, we can conclude that significant improvement in cross-polarized fields in addition to an excellent AR is achieved by employing this unique arrangement (Figs. 4.6(c)-(d)).

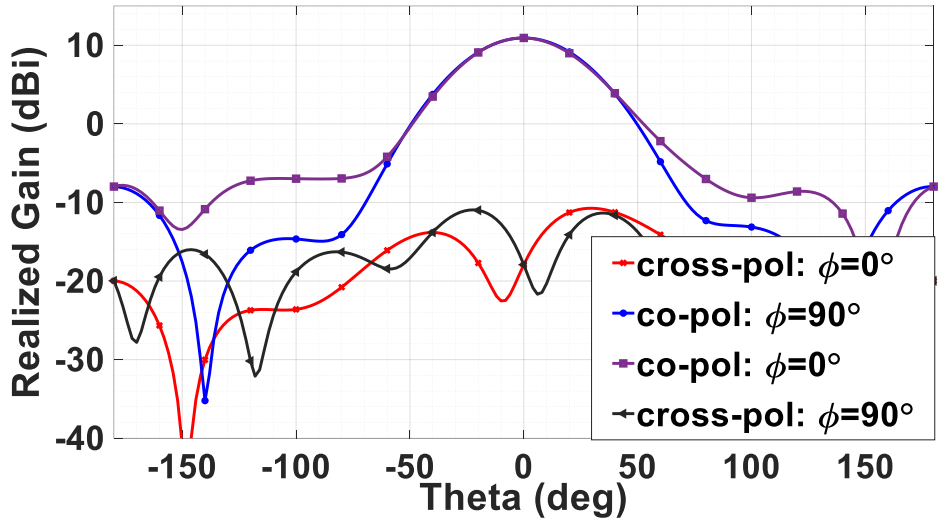

(a)

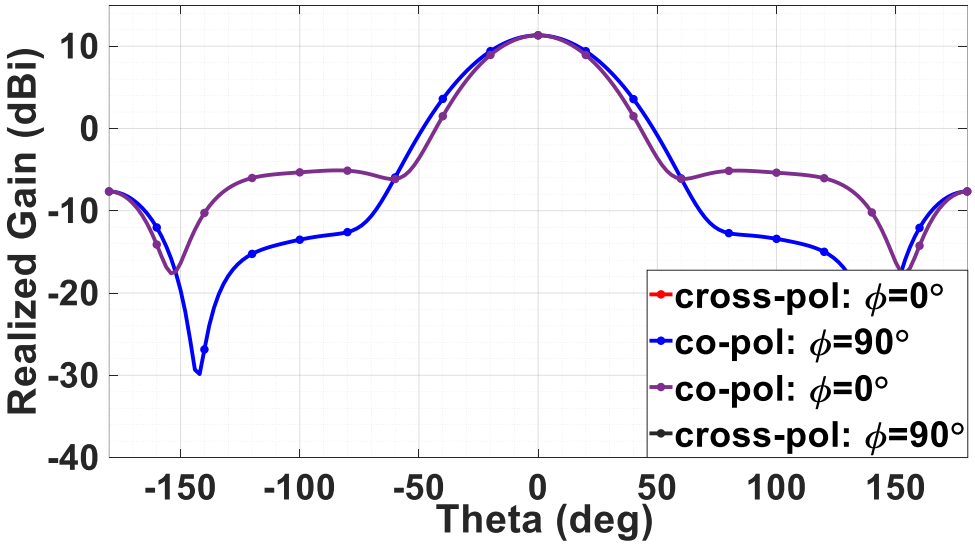

(b)

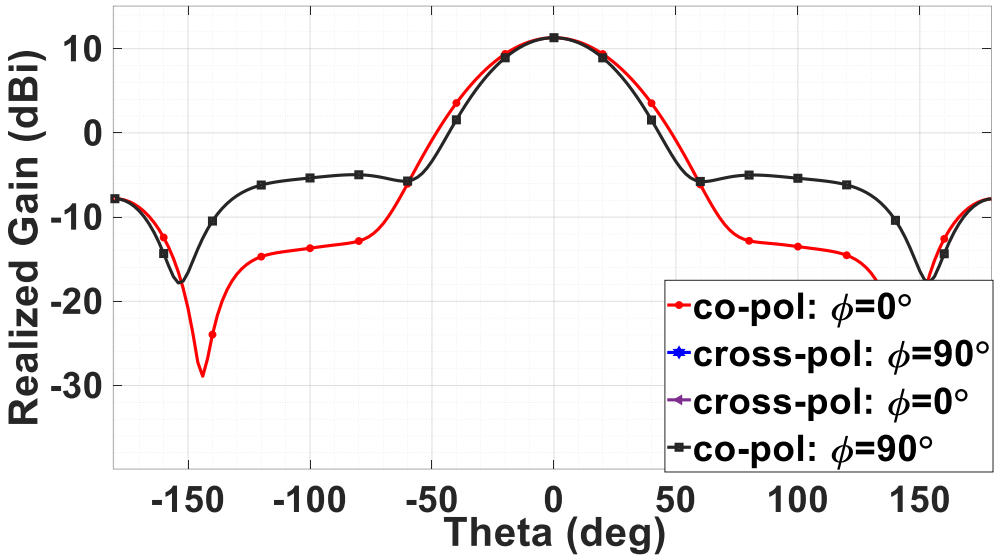
Realized Gain (dBi)
10
0
-10
-20
-30
-150
-100
-50
0
50
100
150
Theta (deg)
co-pol: ϕ=0°
cross-pol: ϕ=90°
cross-pol: ϕ=0°
co-pol: ϕ=90°

(c)

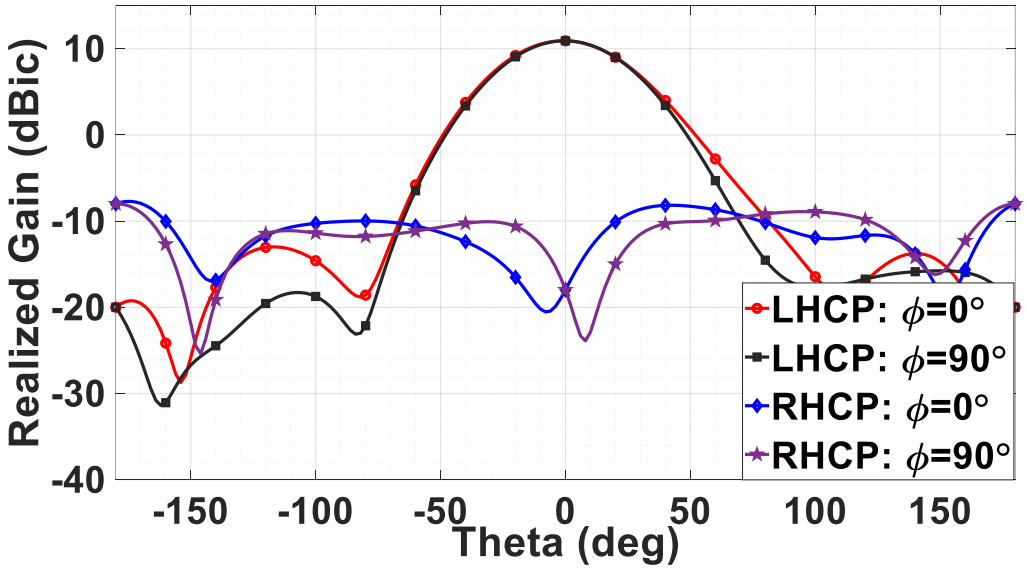
Realized Gain (dBic)
10
0
-10
-20
-30
-40
-150
-100
-50
0
50
100
150
Theta (deg)
LHCP: ϕ=0°
LHCP: ϕ=90°
RHCP: ϕ=0°
RHCP: ϕ=90°

(d)

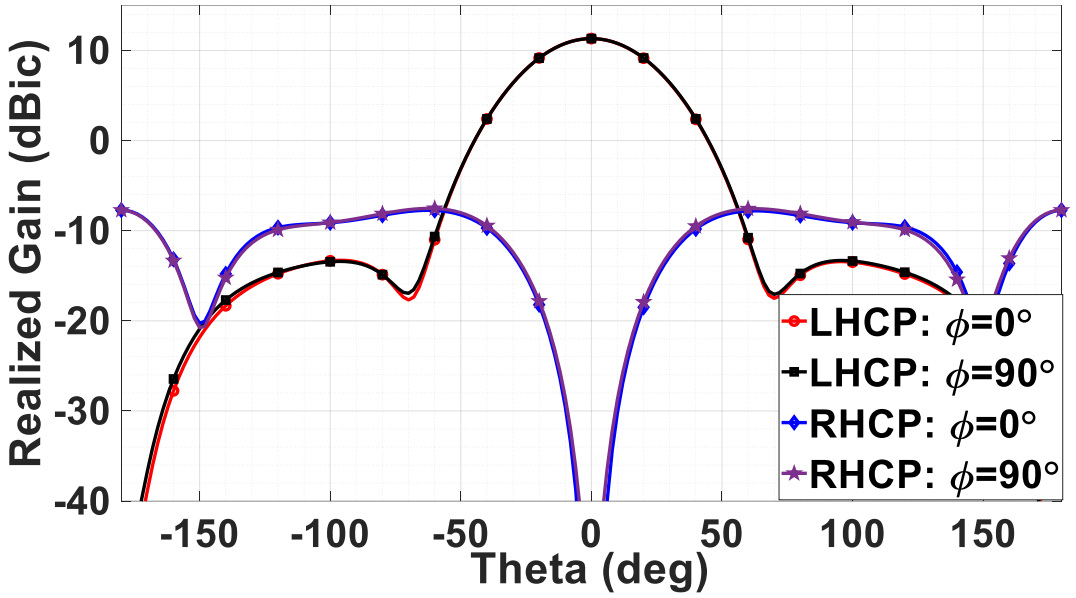
Realized Gain (dBic)
10
0
-10
-20
-30
-40
-150
-100
-50
0
50
100
150
Theta (deg)
LHCP: ϕ=0°
LHCP: ϕ=90°
RHCP: ϕ=0°
RHCP: ϕ=90°

(e)

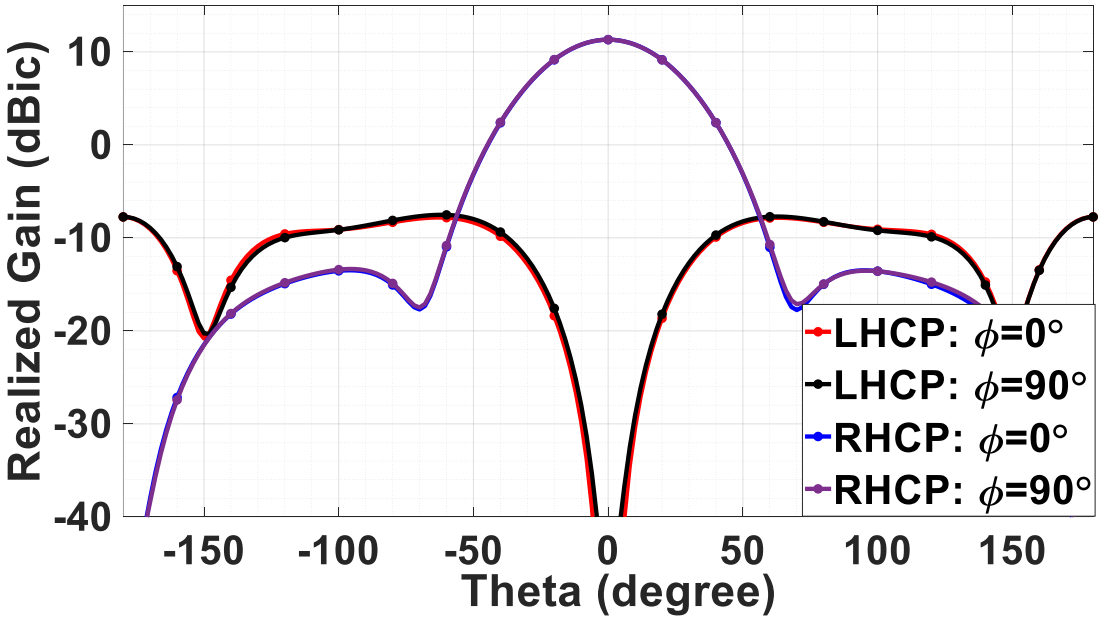
Realized Gain (dBic)
10
0
-10
-20
-30
-40
-150
-100
-50
0
50
100
150
Theta (degree)
LHCP: ϕ=0°
LHCP: ϕ=90°
RHCP: ϕ=0°
RHCP: ϕ=90°

(f)

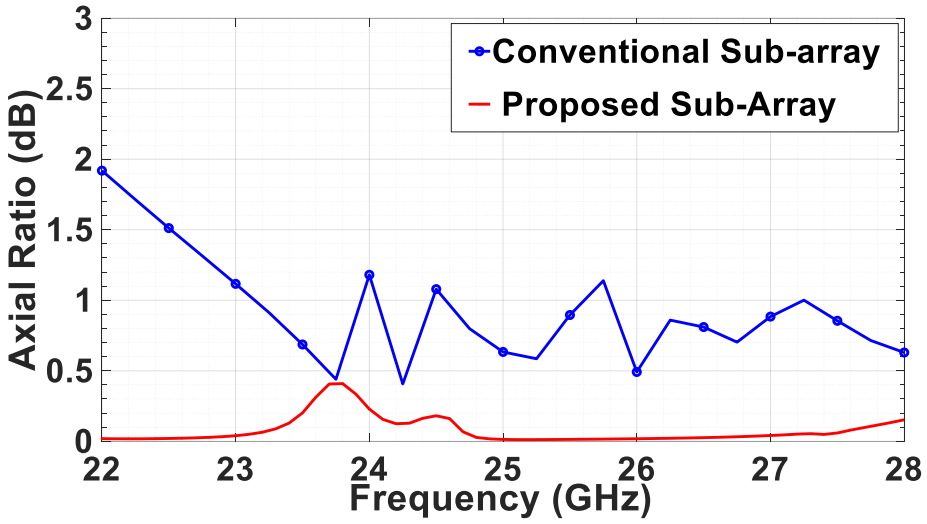

(g)

Fig. 4.7. Radiation pattern at 25 GHz for the horizontal (X-) polarization of the (a) conventional and (b) proposed sub-array, (c) for the vertical (Y-) polarization of the proposed sub-array (Note: for (b) and (c) cross-pol is lower than -40dB and hence out of scale), LHCP for the (d) conventional and (e) proposed sub-array, (f) for the RHCP of the proposed sub-array, and (g) AR vs frequency for the conventional and proposed (sequentially rotated 2x2 sub-array) sub-array.

4.5. 8x8 Array configuration and performance

4.5.1. 8x8 Array Configuration and Beamforming Algorithm

The 8x8 phased array is employing the proposed 2x2 uniquely arranged sub-array (Fig. 4.6(c-d)). The 8x8 array is simulated using the domain decomposition technique (DDM) with non-identical unit cells and an inter-element spacing of $0.5\lambda_o$ at 25 GHz along both horizontal (X-) and vertical (Y-) directions. The isometric view of the DDM model along with the unit cell arrangement of the 8x8 array is shown in Fig. 4.8(a). The arrangement of mirrored/sequentially rotated unit cells in DDM model of the 8x8 array is shown in Fig. 4.8(b), where Unit cell 2 is a mirror image of Unit cell 1 along vertical plane, Unit cell 3 is a

mirror image of Unit cell 1 along horizontal plane and unit cell 4 is a mirror image of Unit cell 1 along horizontal and vertical plane. If we consider circular polarization modes, then Unit cell 2 is 90° rotated compared to Unit cell1, Unit cell 4 is 180° rotated compared to Unit cell1, and Unit cell 3 is 270° rotated compared to Unit cell. The top view of the array is shown in Fig. 4.8(c), where the array dimensions, including the overall board dimension, are specified. The arrangement of chips along with the power splitter employed to feed the 4x4 chips (each chip in turn feeds four dual linearly/circularly polarized elements) are shown in Fig. 4.8(d).

When the array operates in dual linear polarization, progressive phase shifts are applied along the φ=0° direction to scan in the φ=0° plane or along the φ=90° direction to scan in the φ=90° plane to the X-polarized (or Y-polarized) feed points while Y-polarized feed points (or X-polarized feed points) are matched terminated, respectively, to achieve the desired beam scan performance. The CP beam scan patterns are achieved in the following way:

(i) By applying a 90° phase to either Y-polarized or X-polarized feed points, LHCP or RHCP are generated, respectively.

(ii) Progressive phase shifts are applied to both the X-polarized and Y-polarized feed points along the φ=0° direction to scan in the φ=0° plane or along the φ=90° direction to scan in the φ=90° plane.

The 180° phase is provided to each alternate (mirrored) port of the mirrored elements along both the horizontal and vertical directions to achieve in-phase radiation in the case of both dual linear and dual circular polarizations.

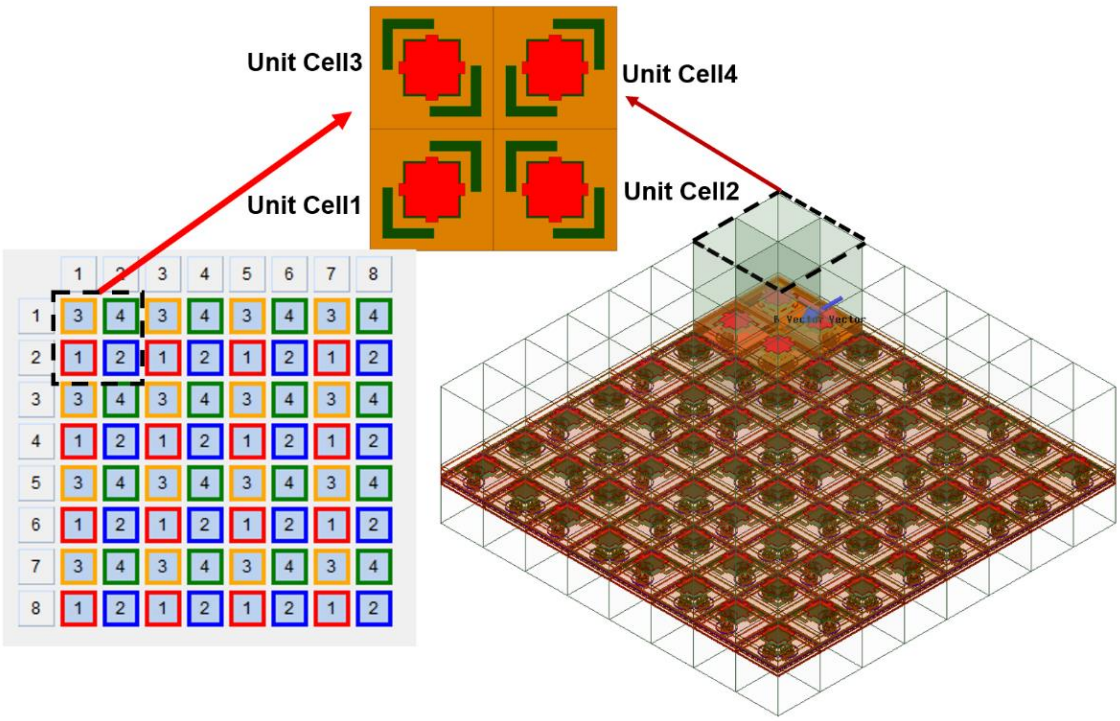
Unit Cell3
Unit Cell4
Unit Cell1
Unit Cell2

(a)

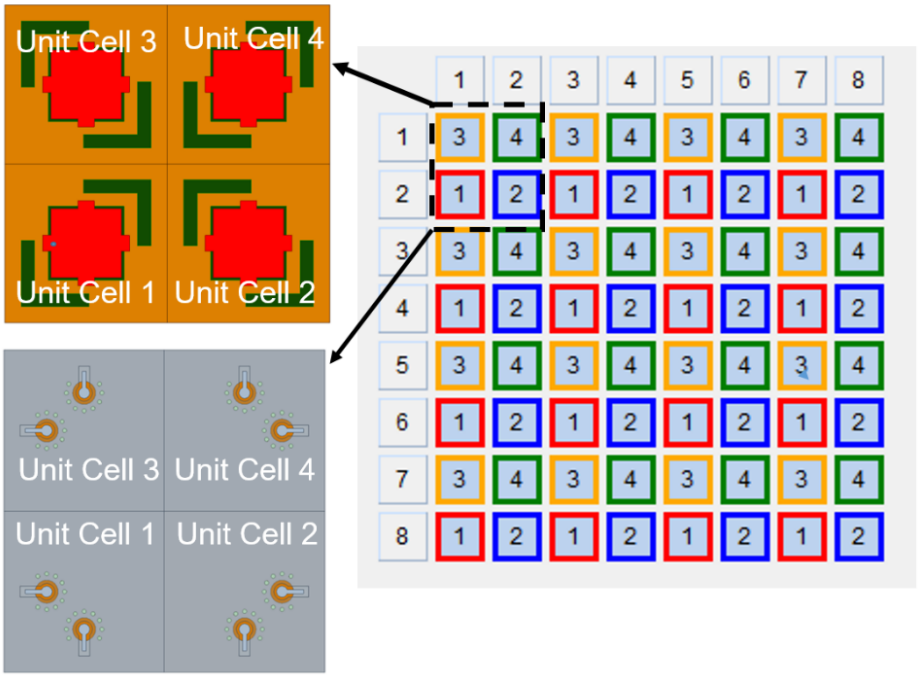
Unit Cell 3
Unit Cell 4
Unit Cell 1
Unit Cell 2
Unit Cell 3
Unit Cell 4
Unit Cell 1
Unit Cell 2

(b)

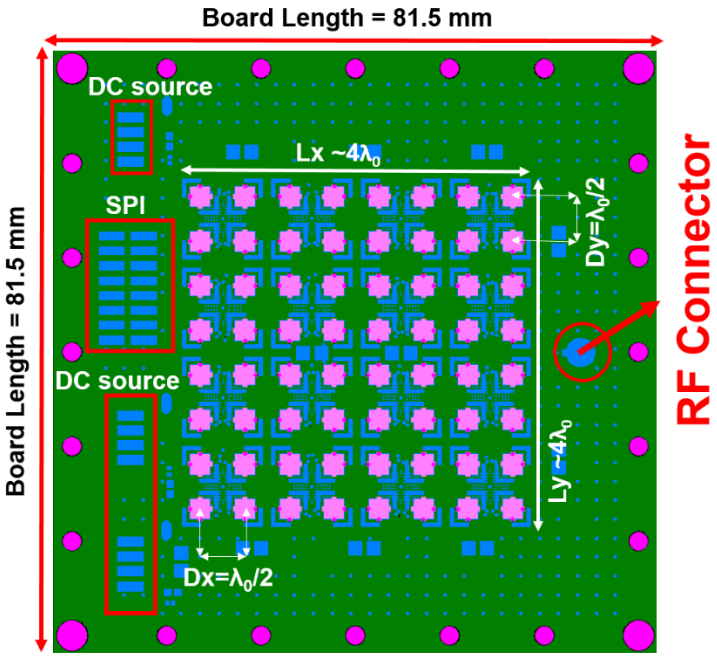

(c)

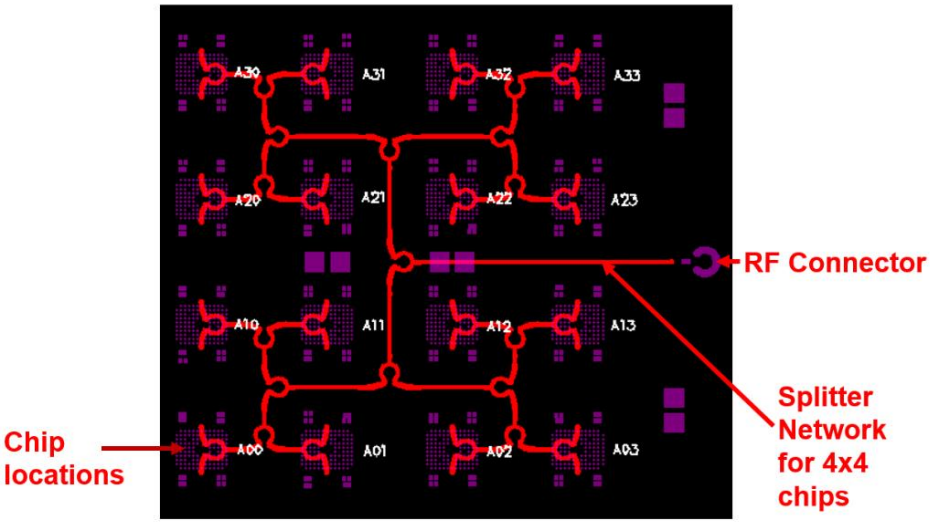

(d)

Fig. 4.8. Top view of the DDM model of the 8x8 array with non-identical unit-cells, (b) the arrangement of mirrored/sequentially rotated unit cells in DDM model, (c) top view of the 8x8 antenna aperture with BFN, and (d) arrangement of chips along with the power splitter underneath the array aperture.

4.5.2. Active Element Pattern (AEP) based Analytical Analysis and Simulated Results for the 8x8 array

The array pattern of the active element pattern (AEP) based 8x8 phased array can be analytically studied using the eqn. (4.1):

$$E^{array}(\theta,\varphi) = \sum_{n=1}^{N}\left[\left[\sum_{m=1}^{M} E_{mn}^{element}(\theta,\varphi)\, e^{j(m-1)(kd_x sin\theta cos\varphi+\beta_x}\right] e^{j(n-1)(kd_y sin\theta sin\varphi+\beta_y}\right] \quad (4.1)$$

Here, in eqn. (4.1), $M = N = 8$ refers to the number of elements along the X- or Y- directions, $d_x = d_y = 0.5\lambda_o$ at 25 GHz, and β_x and β_y are progressive phase shifts along the X- and Y-directions, respectively. $E_{mn}^{element}$ is the radiation pattern of the $(m,n)^{th}$ element in the 8x8 array which can be obtained from the active element pattern (AEP). The AEP of an array is the radiation pattern of the center element when only the center element is excited but all other array elements are matched terminated [57]. The AEP is the combination of the isolated element pattern and a space factor that includes the effects of the other coupled elements. However, with an even number of elements and elements in each 2x2 sub-array that are uniquely arranged, we will not be able to predict the scan performance accurately if we pick up the AEP of one element of the centrally located 2x2 sub-array. Therefore, we have computed an average AEP for the centrally located 2x2 sub-array. The average AEP is computed from AEPs of each element of the centrally located 2x2 sub-array, as shown in Fig. 4.9 (a) for linear polarization and Fig. 4.10 (a) for circular polarization. The average AEP is multiplied with the array factor (AF), as in eqn. (4.1), to compute the AEP-based scan performance.

In Fig. 4.9(a) the AEP of each element in the centrally located 2x2 sub-array (unit cells at (4,4), (4,5). (5,4) and (5,5) [see Fig. 4.8(b)] and the average AEP for the horizontally polarized element is shown for φ=0° plane at 25 GHz. The average AEP is computed from AEPs of each element of the centrally located 2x2 sub-array which are extracted from the simulated array

in HFSS when only the corresponding array element is excited and others matched terminated. The individual AEP looks asymmetric, mainly due to the fact that the element has unequal number of elements on both sides of the element in the even array, and also partially due to the presence of L-stubs and due to the ground via arrangement of the BFN. But the average AEP looks symmetrical, and we can see the symmetric beam scan performance in simulated and measurement results (shown later), which indicates the averaging of AEP is more practical than considering individual AEP. In Fig. 4.9(b), the normalized average AEP envelope is compared with the HFSS simulated scan performance in the φ=90° plane and is shown for the vertically polarized array at 25GHz. For a vertically (Y-) polarized array, *E*-fields are along the φ=90° plane direction. We see that the 3dB gain drop/scan loss is around ±55° for an average AEP, thereby indicating the possibility of excellent scan performance. In Fig. 4.9(b), the AEP-based scan performance in the φ=90° direction (*E*-plane) computed in MATLAB is also compared. We observe the similarity in scan performance between the computed and the fully excited simulated array. It is worth mentioning here that in the case of linear polarization modes of a microstrip patch array, it is important to analyze the scan performance mainly in the *E*-plane due to stronger mutual coupling. Therefore, the scan performance in the *H*-plane is not shown for the sake of brevity.

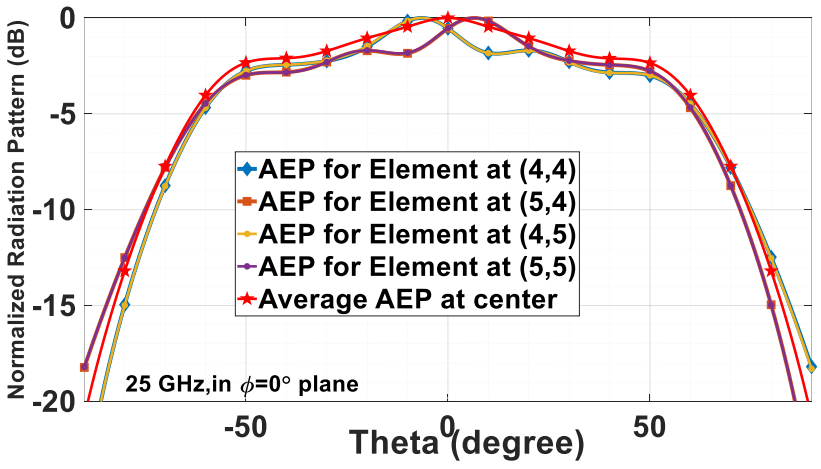

(a)

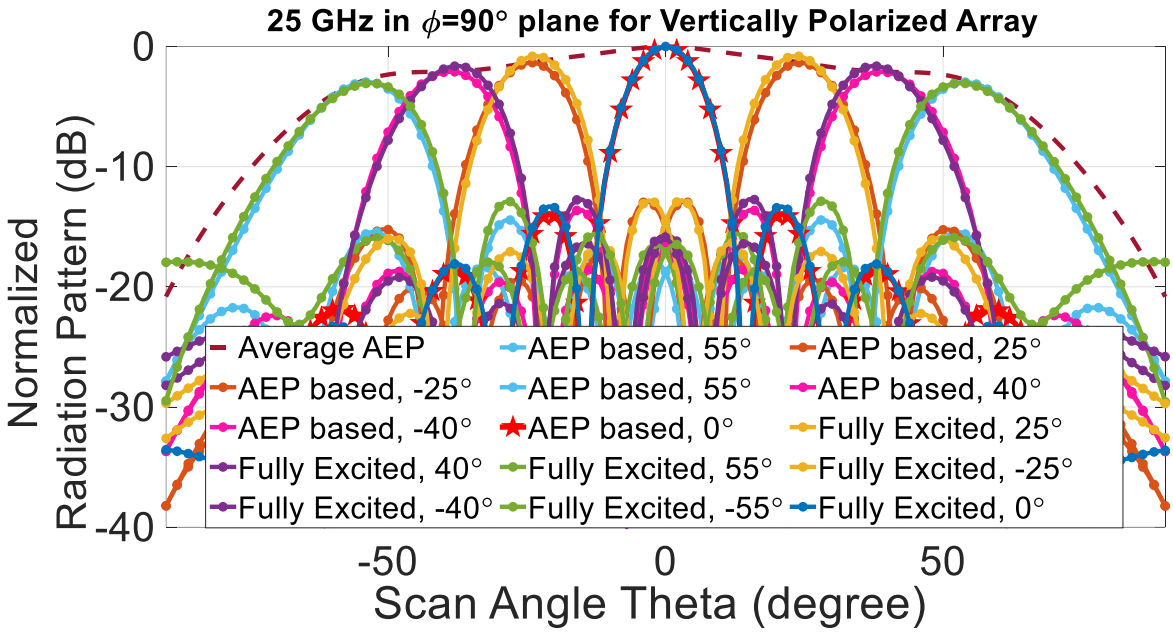

(b)

Fig. 4.9. (a) AEP and average AEP of the centrally located elements, and (b) comparison of AEP based scan and simulated scan performance of the horizontally polarized 8x8 array in E-plane at 25 GHz.

In Fig. 4.10(a) the AEP of each element in the centrally located 2x2 sub-array (unit cells at (4,4), (4,5). (5,4) and (5,5) [see Fig. 4.8(b)] and the average AEP for the left hand circularly polarized element is shown for φ=0° plane at 25 GHz. In Fig. 4.10(b), the normalized AEP-based scan performance of the LHCP array is compared with the normalized scan performance of the fully excited LHCP array simulated in HFSS in the φ=0° plane at 25 GHz, along with the normalized average AEP envelope. The scan performance between the computed and the fully excited simulated arrays is convincing with respect to the gain drop/scan loss profile. The scan performance in the other plane is identical, and hence not shown here.

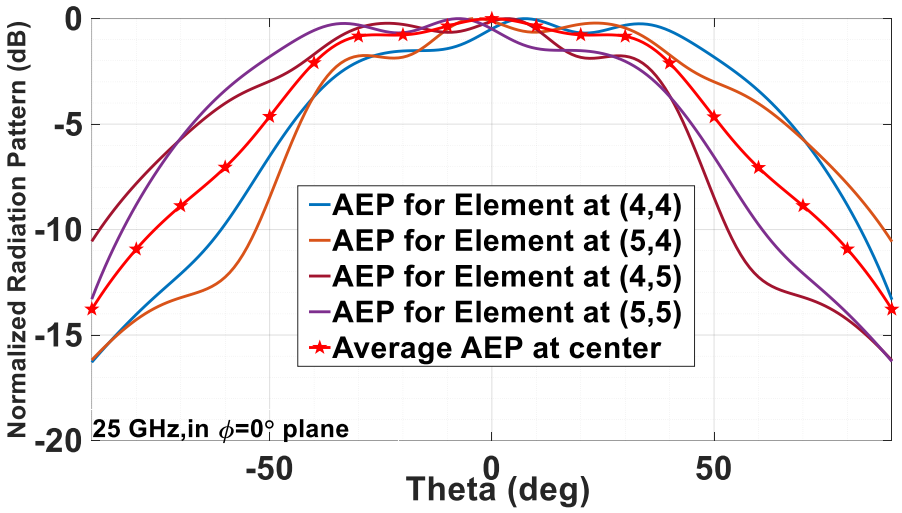

(a)

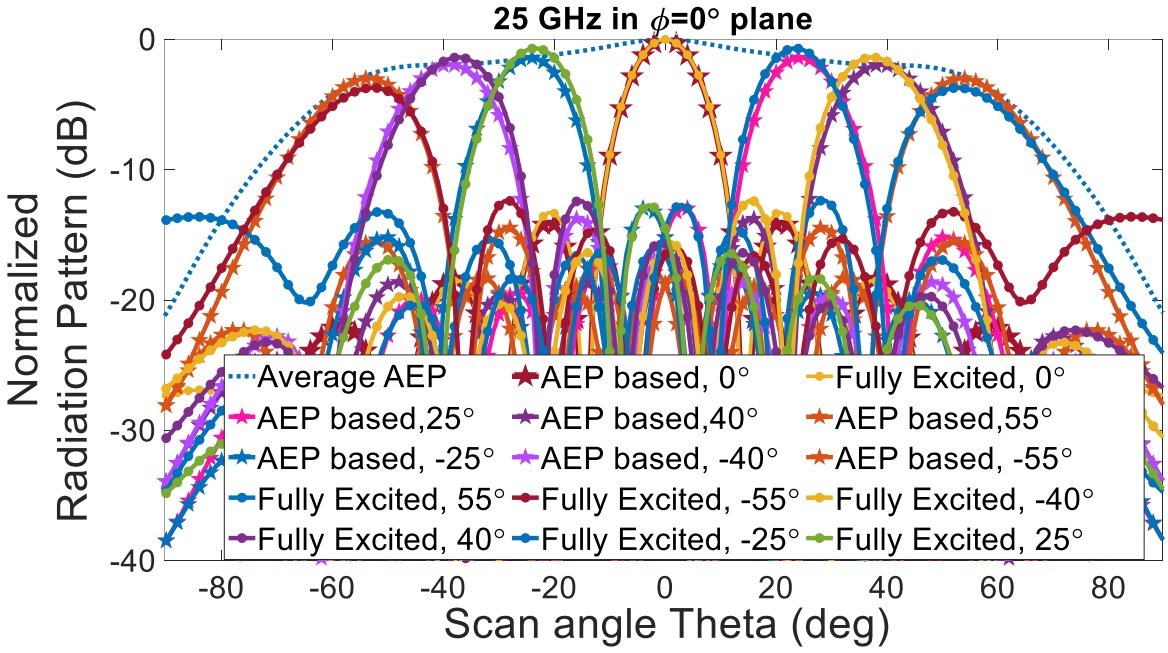

Fig. 4.10. (a) AEP and average AEP of the centrally located elements, and (b) comparison of AEP based scan and simulated scan performance of the LHCP 8x8 array in φ=0° plane at 25 GHz.

As mentioned earlier, the array should be working in two frequency bands: 22.55–23.55 GHz (center frequency: 23.05 GHz) and 25.5–27.5 GHz (center frequency: 26.5 GHz). But as individual bands are very closely spaced, we have designed a single wideband antenna. Here the broadside radiation pattern for vertical (Y-) polarization at 23 GHz, 25 GHz, and 26.5 GHz are shown in Figs. 4.11(a), (b), (c). We can observe that no cross-polarized fields are visible till -40dB and therefore, co-cross separation is more than 60dB in linear case. Thus, mirror arrangement has reduced the cross-polarized fields by a significant amount.

The Anokiwave chip employed in the BFN provides 6-bit phase and gain control for beam steering. The 6-bit phase control implies each step is of value $2\pi/2^6 = 5.625°$. Therefore, progressive phase shifts are limited to multiples of 5.625°. The linearly polarized beam scan performance in φ=0° and 90° directions at 23.5 GHz, 25 GHz and 26.5 GHz are shown in Figs. 4. 11(d)-(i). For the vertically polarized array, in Figs. 4.11(d) and (e), we can observe that the gain drop from approximately 22.3 dBi to approximately 19.6 dBi as beam scans from 0° to ±56° along φ=0° plane and approximately 22.3 dBi to approximately 19.1 dBi as beam scans from 0° to ±56° along φ=90° plane at 23.05 GHz. In Figs. 4.11(f) and (g), the gain drop from 23 dBi to 20.5 dBi as beam scans from 0 to ±51° along φ=0° plane and from 23 dBi to 19.3 dBi as beam scans from 0 to ±50° along φ=90° plane at 25 GHz. In Figs. 4.11(h) and (i), the gain drop from 23.5dBi to 20.5 dBi as beam scans from 0 to ±47° along φ=0° and 23.5dBi to 19.3 dBi as beam scans from 0 to ±42° along φ=90° plane at 26.5 GHz. Therefore, with respect to the scan performance employing linear polarization, we observe that as the beam scans, the realized gain in the *E*-plane drops faster than that in the *H*-plane, which is due to stronger mutual coupling between array elements in the *E*-plane.

The active *S*-parameter of the almost centrally located element (5,4) [see Fig.4.8(b)] is shown in Fig. 4.11(j) for the broadside, 25° scan and the maximum scan for the φ=0° and φ=90° planes. The active *S*-parameter is almost below (-10) dB over the entire bandwidth for both planes for the broadside, 25° scan, and the maximum scan. Here, it should be noted that we considered a scan out to approximately the 3dB gain drop point in both planes, but if this 3dB gain drop criteria is relaxed the array can scan further. The scanning performance for the horizontal and vertical polarizations is identical, with *E*-plane and *H*-planes

interchanged.

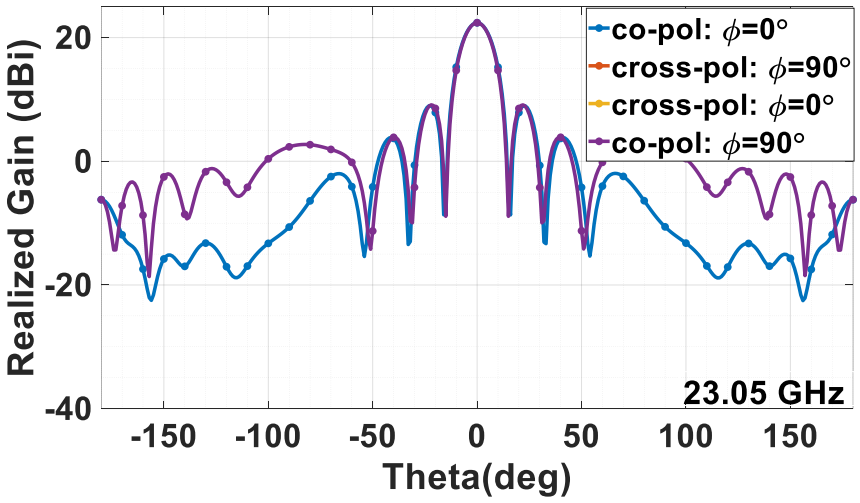

(a)

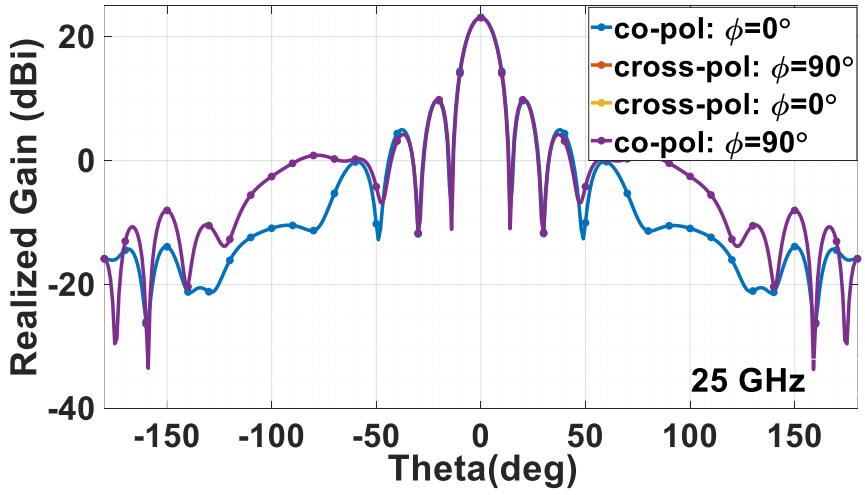

(b)

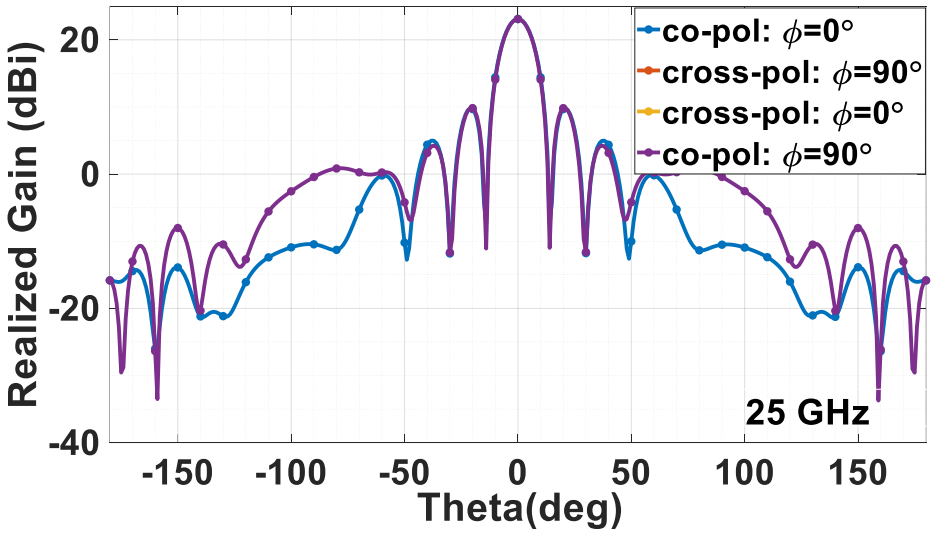
co-pol: ϕ=0°
cross-pol: ϕ=90°
cross-pol: ϕ=0°
co-pol: ϕ=90°
Realized Gain (dBi)
20
0
-20
-40
-150
-100
-50
0
50
100
150
Theta(deg)
25 GHz

(c)

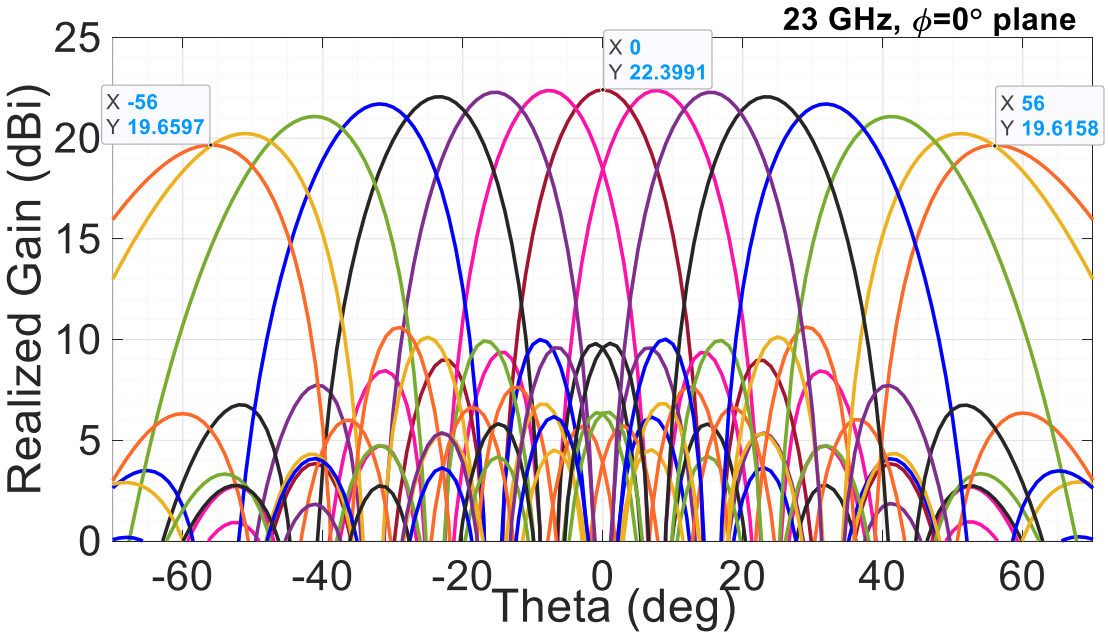
23 GHz, ϕ=0° plane
X 0
Y 22.3991
X -56
Y 19.6597
X 56
Y 19.6158
Realized Gain (dBi)
25
20
15
10
5
0
-60
-40
-20
0
20
40
60
Theta (deg)

(d)

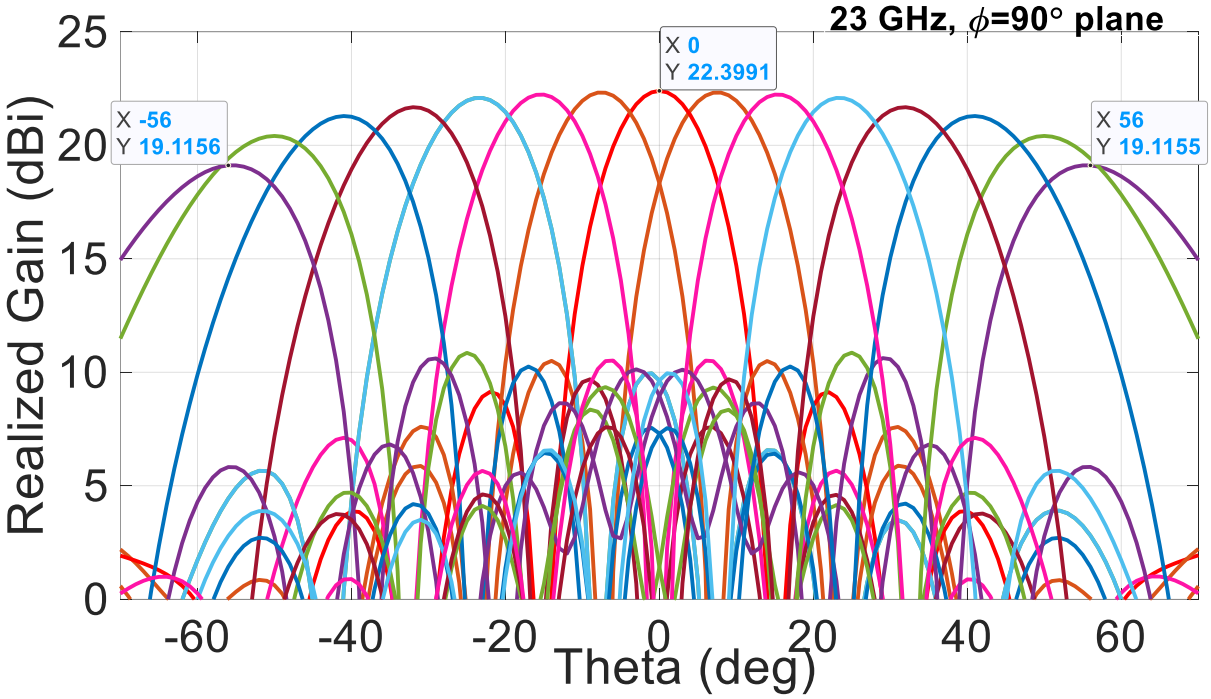
23 GHz, ϕ=90° plane
X 0
Y 22.3991
X -56
Y 19.1156
X 56
Y 19.1155
Realized Gain (dBi)
Theta (deg)
25
20
15
10
5
0
-60
-40
-20
0
20
40
60

(e)

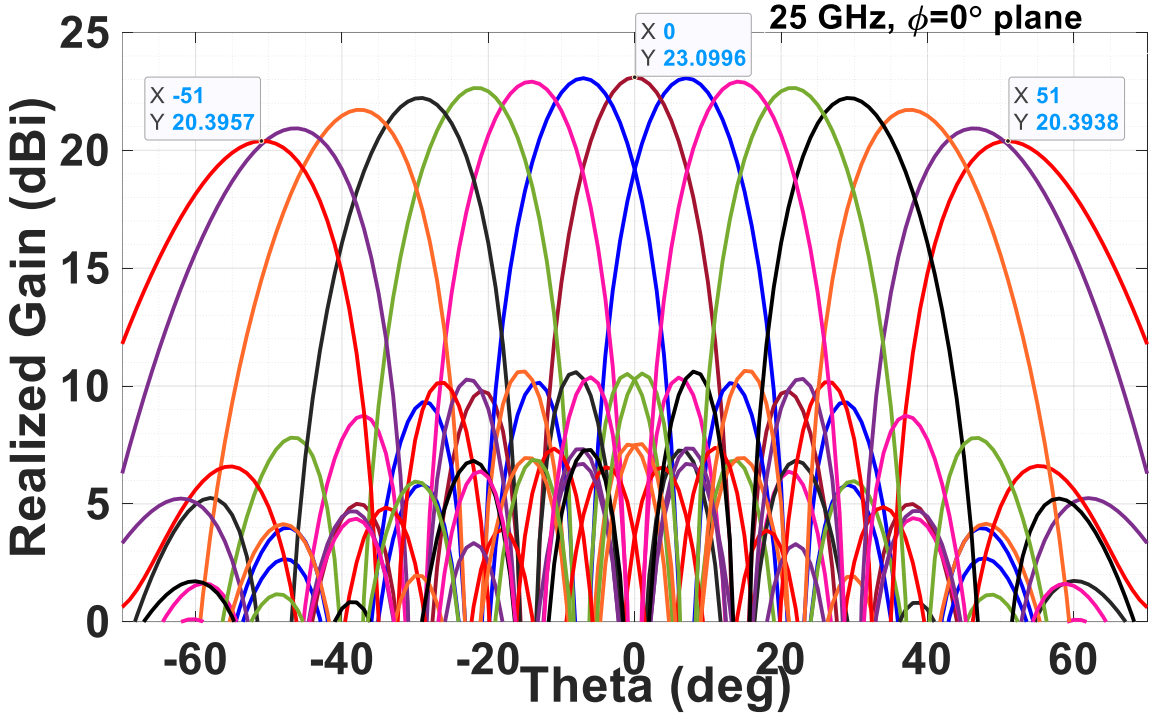
25 GHz, ϕ=0° plane
X 0
Y 23.0996
X -51
Y 20.3957
X 51
Y 20.3938
Realized Gain (dBi)
Theta (deg)
25
20
15
10
5
0
-60
-40
-20
0
20
40
60

(f)

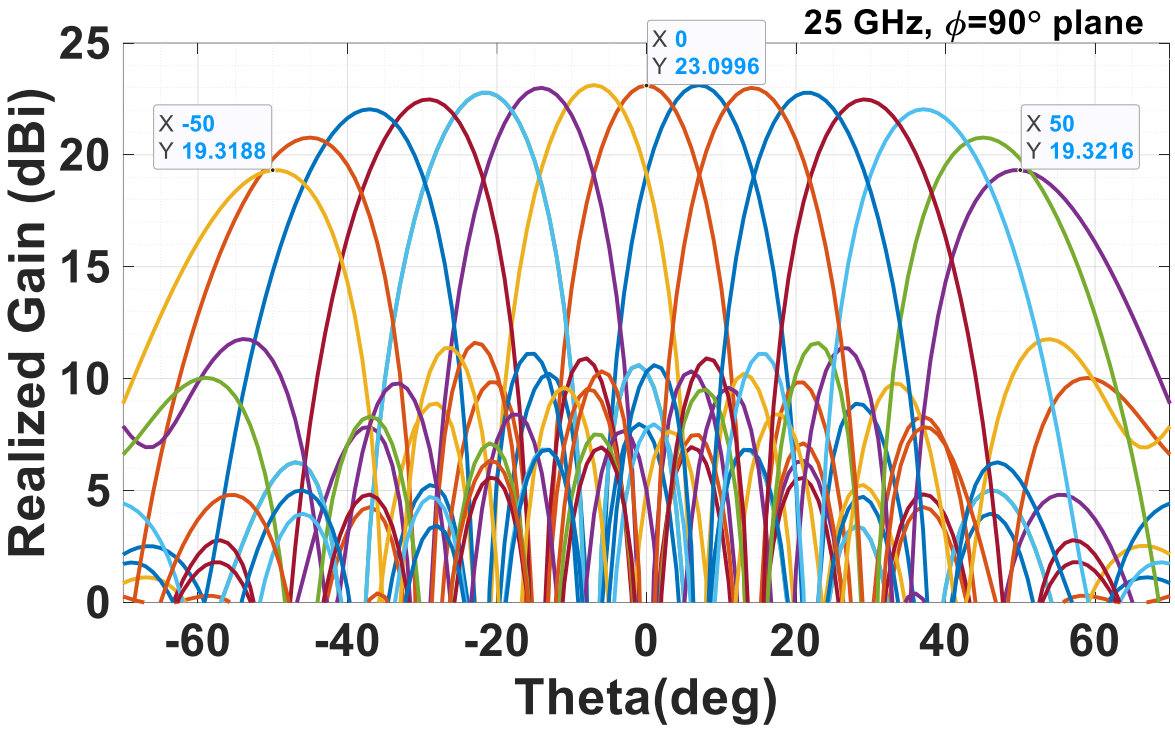
25 GHz, ϕ=90° plane
X 0
Y 23.0996
X -50
Y 19.3188
X 50
Y 19.3216
Realized Gain (dBi)
Theta(deg)
25
20
15
10
5
0
-60
-40
-20
0
20
40
60

(g)

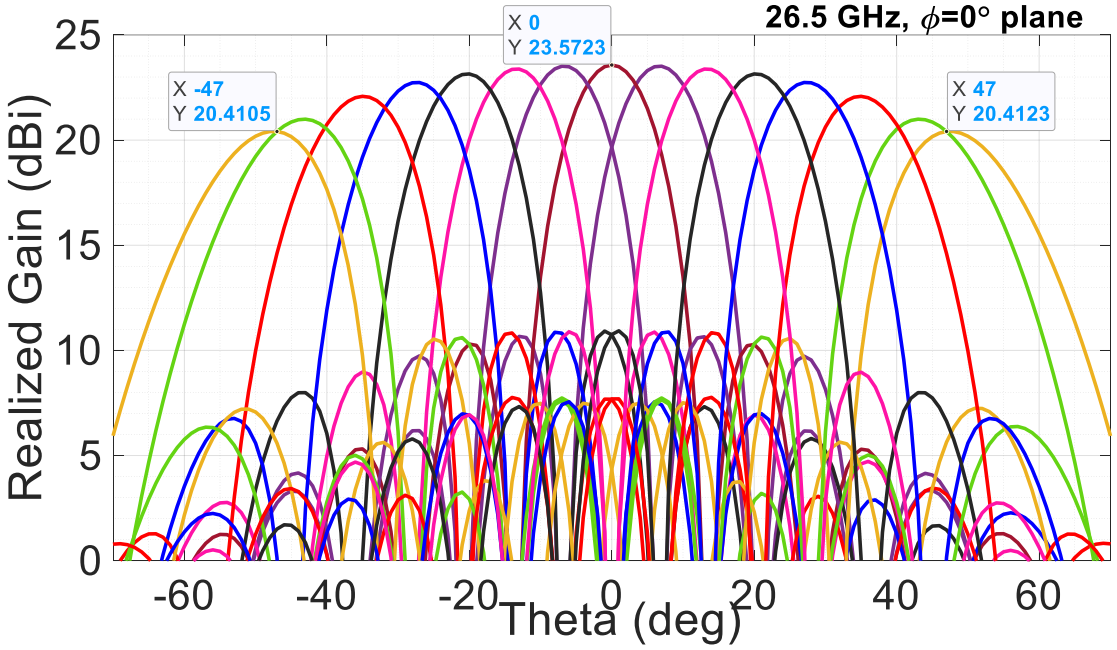
26.5 GHz, ϕ=0° plane
X 0
Y 23.5723
X -47
Y 20.4105
X 47
Y 20.4123
Realized Gain (dBi)
Theta (deg)
25
20
15
10
5
0
-60
-40
-20
0
20
40
60

(h)

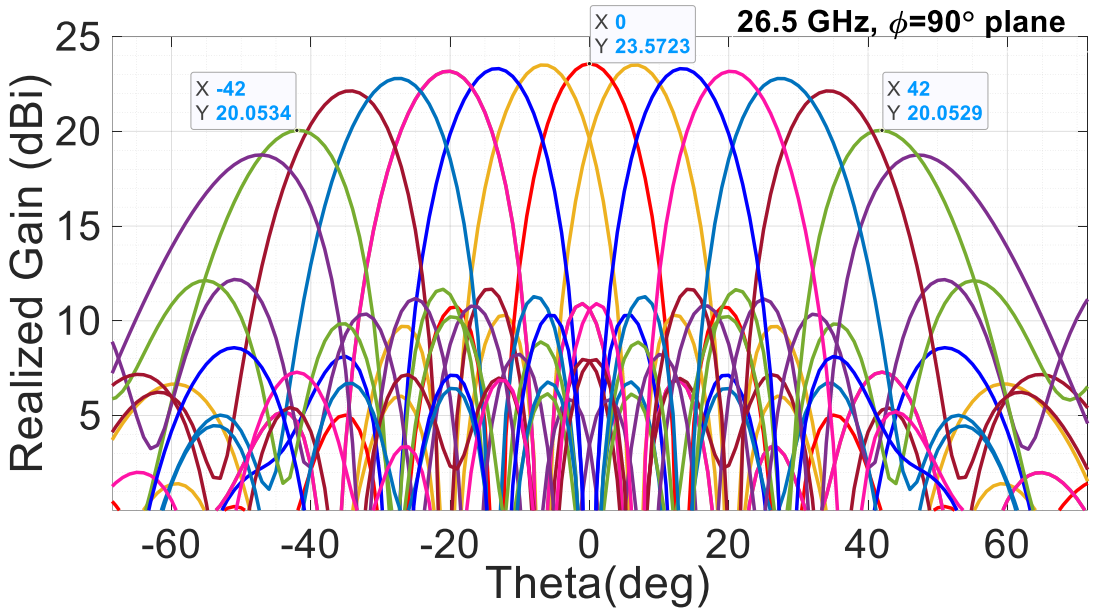

(i)

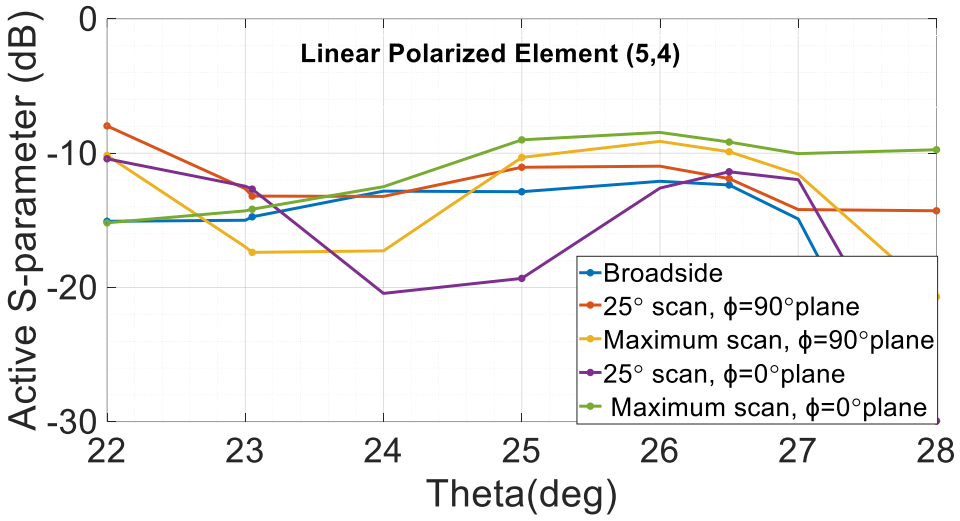

(j)

Fig. 4.11. Broadside radiation pattern at (a) 23 GHz, (b) 25 GHz, and (c) 26.5 GHz for vertically polarized 8x8 array in φ=0° and φ=90° plane at 25 GHz, the linearly polarized beam scan performance in (d) φ=0° and (e) φ=90° planes at 23GHz, (f) φ=0° and (g) φ=90° directions at 25 GHz, and (h) φ=0° and (i) φ=90° directions at 26.5 GHz, (j) active *S*-parameter for the element (5, 4), for the broadside, 25° scan and the maximum scan for φ=0° and φ=90° planes.

The broadside left hand circular polarized (LHCP) radiation pattern at 23 GHz, 25 GHz, and 26.5 GHz are shown in Figs. 4.12(a), (b) and (c), respectively. We can observe that the separation between LHCP (approximately 22-23 dBic) and RHCP (cross-polarized fields) is more than 60dB at θ= 0° position. Thus, the sequential arrangement has improved the axial ratio by a huge amount. LHCP beam scan performance in the φ=0° and φ=90° planes at 23 GHz, 25 GHz and 26.5 GHz are shown in Figs. 4.12(d)-(i). In Fig. 4.12(d) and 4.12(e), we observe that the gain drops from 22.4 dBic to 19.3 dBic as the beam scans from 0° to ±56° along both the φ=0° plane and the φ=90° plane at 23GHz. In Figs. 14(f) and (g), we observe that the gain drops from approximately 23.1 dBi to approximately 20.8 dBi as beam scans from 0° to ±46° along both φ=0° plane and φ=90° plane at 25 GHz. Figs. 4.12(h) and 4.12(i) show that the gain drops from 23.5 dBic to 20.5 dBic as the beam scans from 0° to ±42° along both the φ=0° plane and φ=90° plane at 26.5 GHz. In the case of circular polarization, the scan performance in both the φ=0° plane and the φ=90° plane are identical, which is as expected. The active *S*-parameter of the element (5, 4) [see Fig. 4.8(b)] is shown in Fig. 4.12(j) for the broadside, Θ=25° scan, and the maximum scan angle for both the φ=0° and φ=90° planes. In CP, the active *S*-parameter is almost below (-10) dB over the entire bandwidth for both planes (similar to the linear case), and for both ports (both ports are excited in the case of CP) for broadside, Θ=25° scan, and the maximum scan. Scanning performances in both LHCP and RHCP are identical, therefore only one polarization results are shown for the sake of brevity.

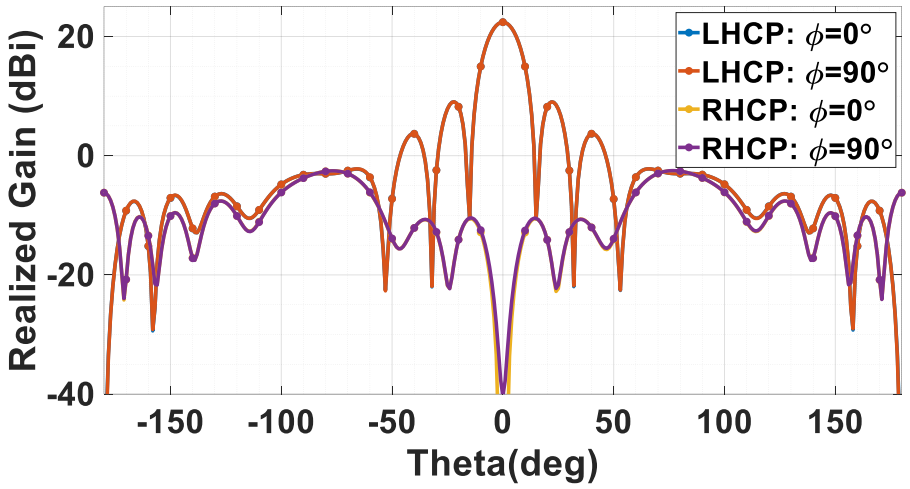
LHCP: ϕ=0°
LHCP: ϕ=90°
RHCP: ϕ=0°
RHCP: ϕ=90°
Realized Gain (dBi)
20
0
-20
-40
-150
-100
-50
0
50
100
150
Theta(deg)

(a)

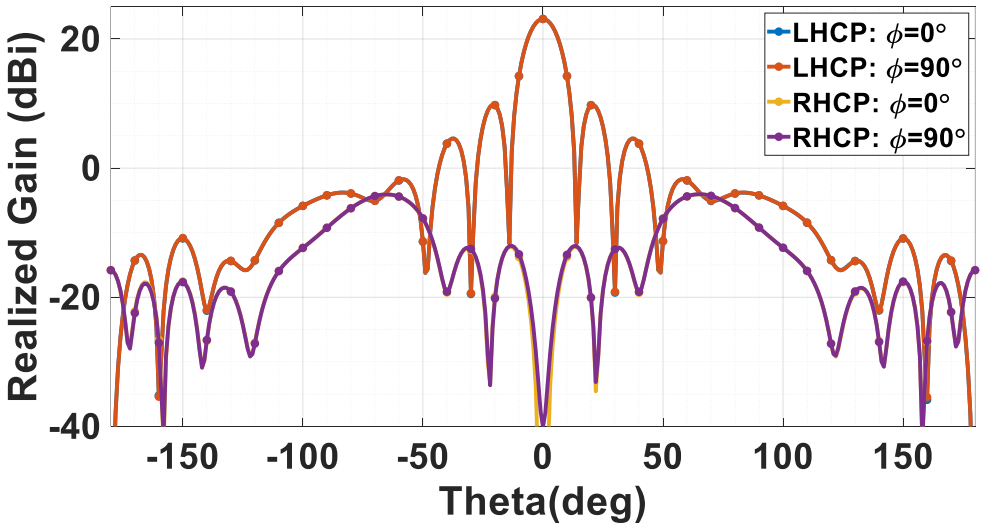
LHCP: ϕ=0°
LHCP: ϕ=90°
RHCP: ϕ=0°
RHCP: ϕ=90°
Realized Gain (dBi)
20
0
-20
-40
-150
-100
-50
0
50
100
150
Theta(deg)

(b)

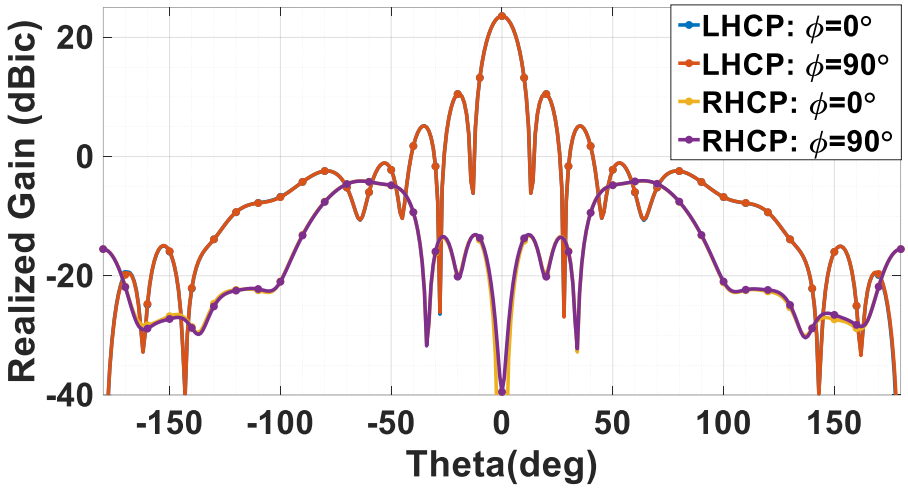
LHCP: ϕ=0°
LHCP: ϕ=90°
RHCP: ϕ=0°
RHCP: ϕ=90°
Realized Gain (dBic)
20
0
-20
-40
-150
-100
-50
0
50
100
150
Theta(deg)

(c)

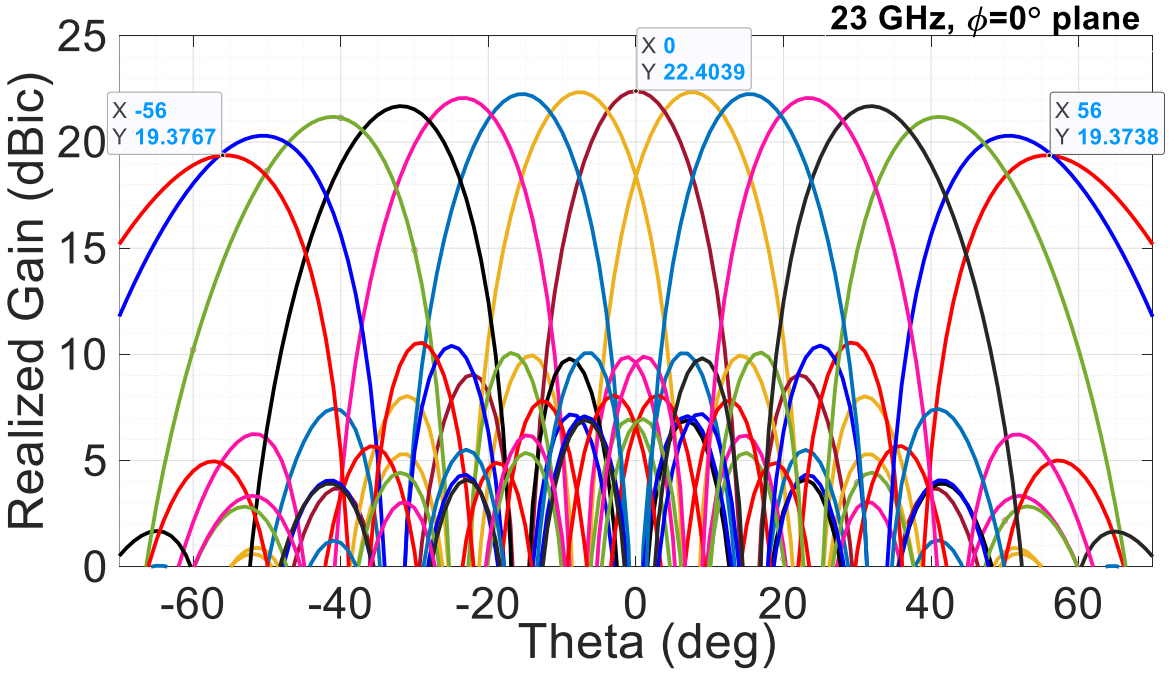
23 GHz, ϕ=0° plane
X 0
Y 22.4039
X -56
Y 19.3767
X 56
Y 19.3738
Realized Gain (dBic)
25
20
15
10
5
0
-60
-40
-20
0
20
40
60
Theta (deg)

(d)

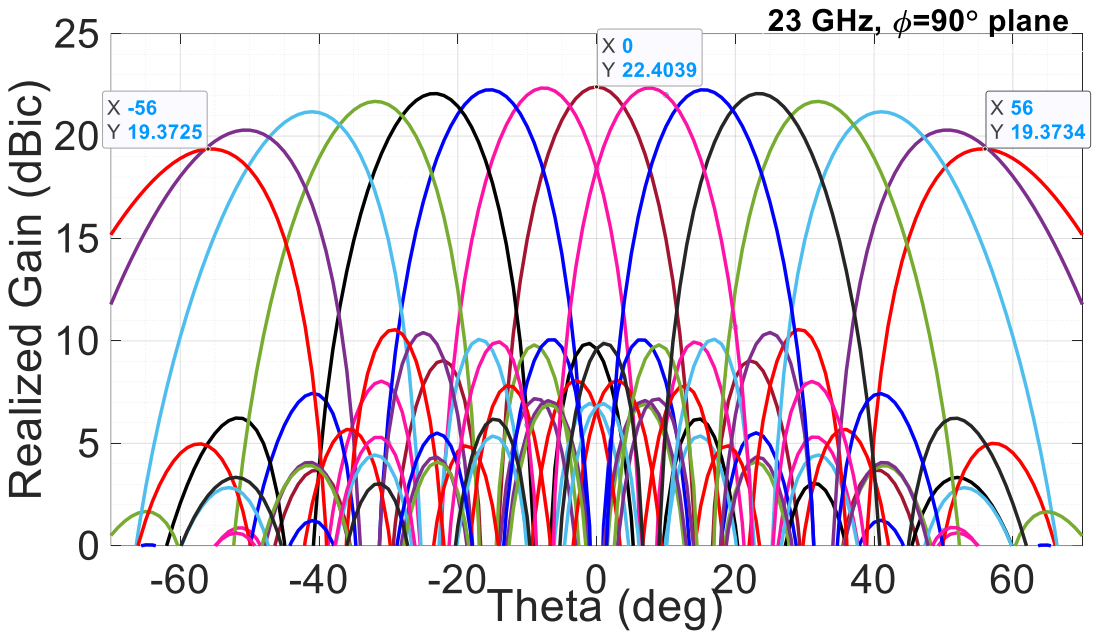
23 GHz, ϕ=90° plane
X 0
Y 22.4039
X -56
Y 19.3725
X 56
Y 19.3734
Realized Gain (dBic)
Theta (deg)
25
20
15
10
5
0
-60
-40
-20
0
20
40
60

(e)

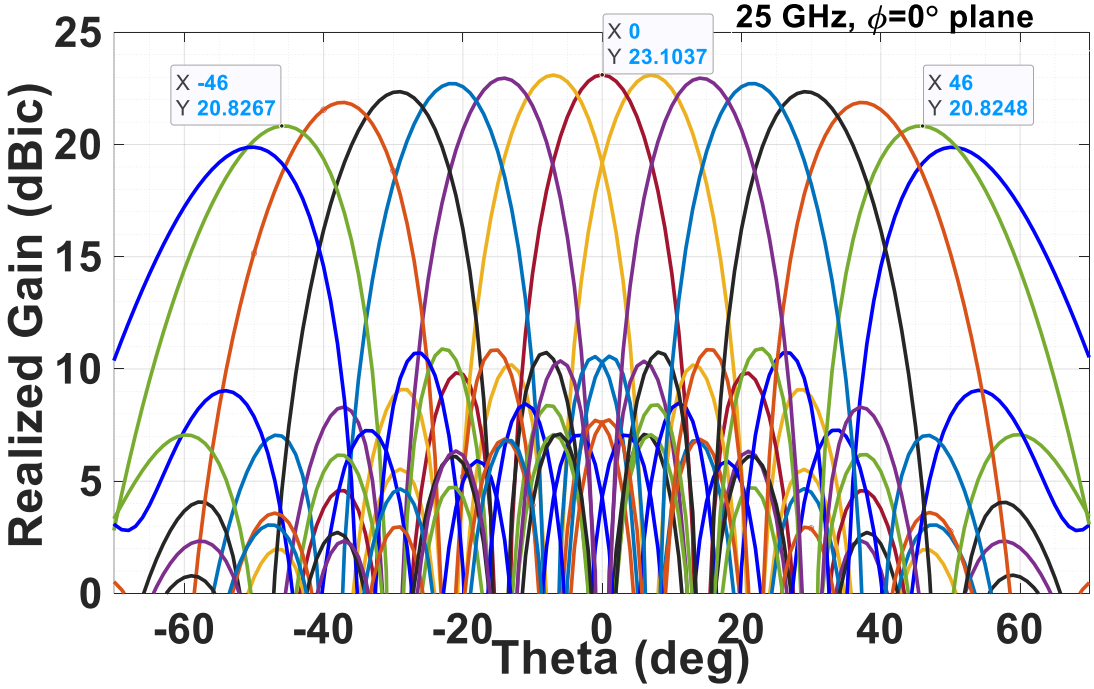
25 GHz, ϕ=0° plane
X 0
Y 23.1037
X -46
Y 20.8267
X 46
Y 20.8248
Realized Gain (dBic)
Theta (deg)
25
20
15
10
5
0
-60
-40
-20
0
20
40
60

(f)

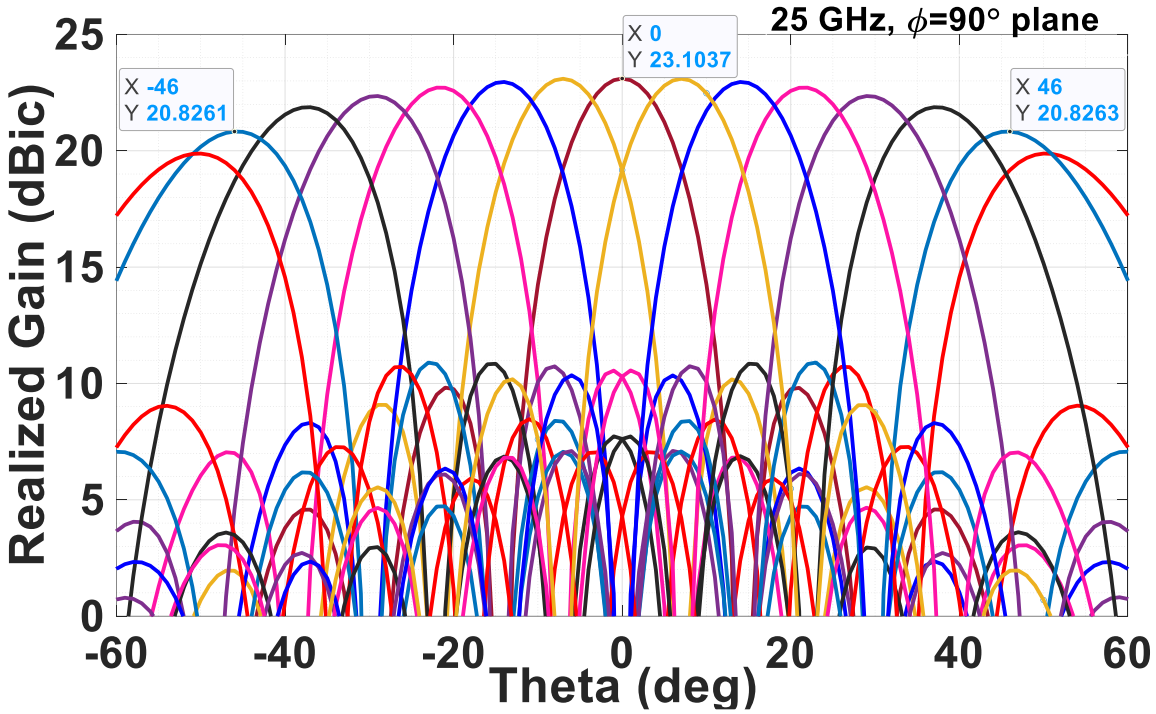
25 GHz, ϕ=90° plane
X 0
Y 23.1037
X -46
Y 20.8261
X 46
Y 20.8263
Realized Gain (dBic)
Theta (deg)
25
20
15
10
5
0
-60
-40
-20
0
20
40
60

(g)

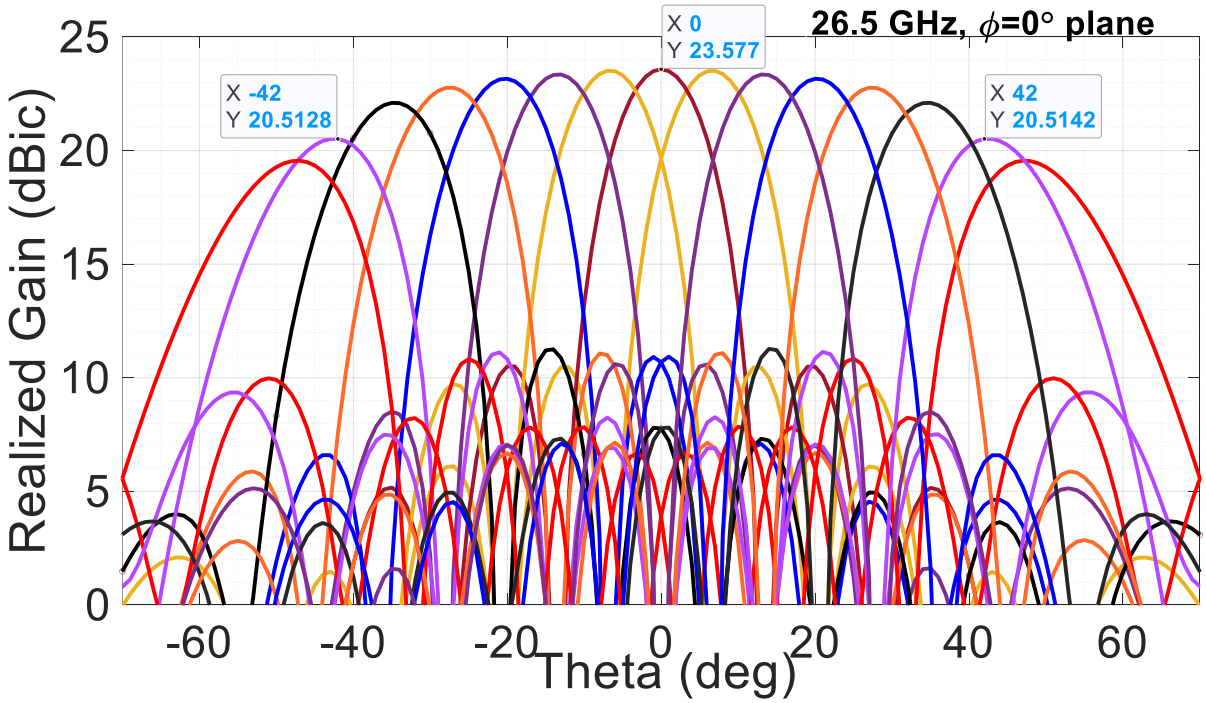
26.5 GHz, ϕ=0° plane
X 0
Y 23.577
X -42
Y 20.5128
X 42
Y 20.5142
Realized Gain (dBic)
Theta (deg)
25
20
15
10
5
0
-60
-40
-20
0
20
40
60

(h)

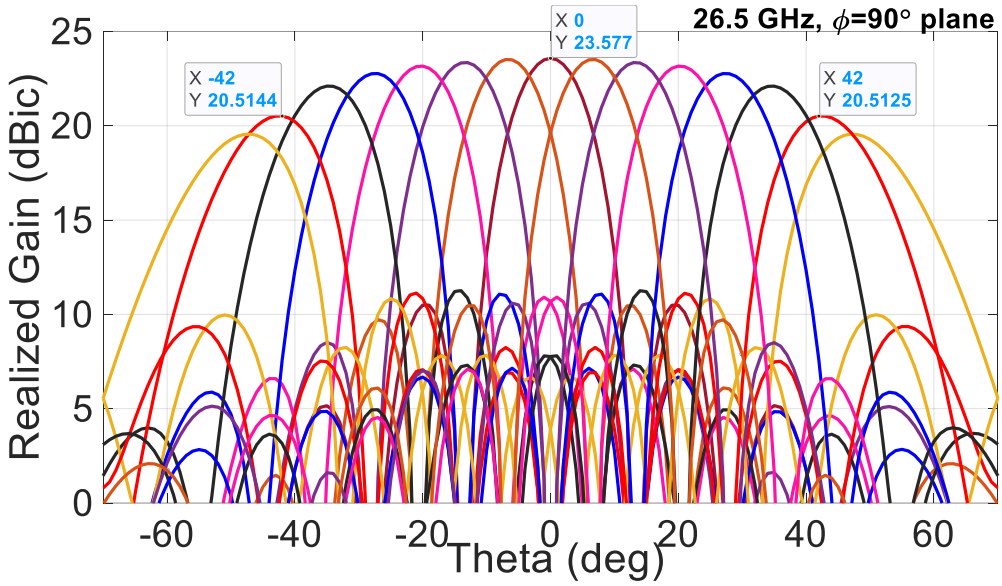

(i)

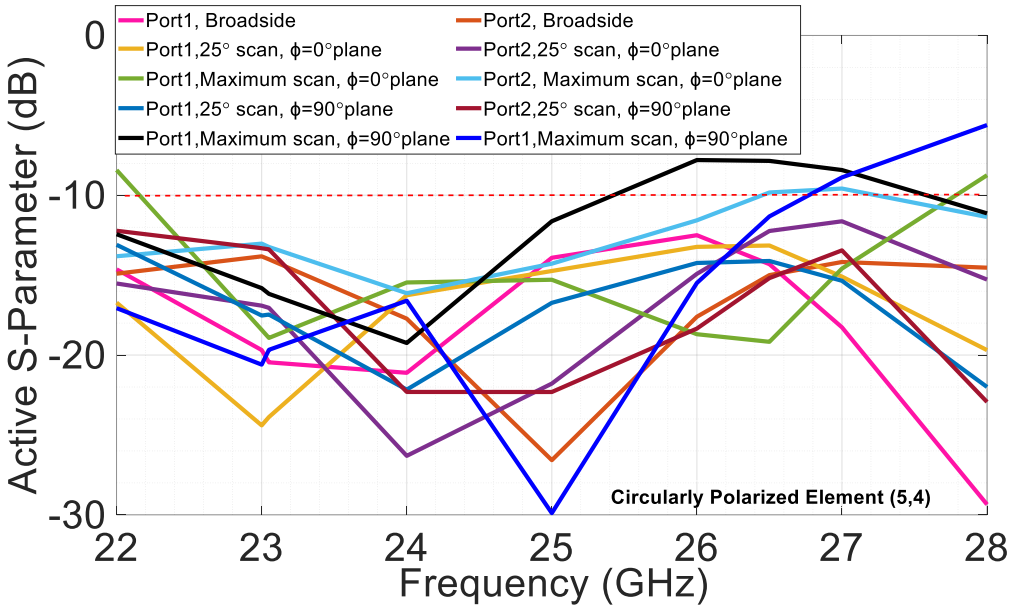

(j)

Fig. 4.12. Broadside radiation pattern at (a) 23 GHz, (b) 25 GHz, and (c) 26.5 GHz for LHCP 8x8 array in φ=0° and φ=90° plane at 25 GHz, LHCP beam scan performance in (d) φ=0° and (e) φ=90° directions at 23 GHz, (f) φ=0° and (g) φ=90° directions at 25 GHz and (h) φ=0° and (i) φ=90° directions at 26.5 GHz, and (j) active S-parameter for element (5, 4) for broadside, around 25° scan and maximum scan for φ=0° and φ=90° planes.

Figs. 4.13(a), (b) and (c) show the contour plot for broadside axial ratio at 23 GHz, 25 GHz and 26.5 GHz. We can observe excellent axial ratio is maintained over all the φ –planes in broadside direction. Figs. 14.13(d) and (e) shows the contour plot of axial ratio for maximum scan along φ=0° plane in positive θ direction at 23 GHz and 26.5 GHz, where observe excellent axial ratio is maintained for maximum scan also. The performance is identical along φ=90° plane also, and hence not shown here. Figs. 4.13(a) and 4.13(b) show the AR versus scan angle and realized gain versus scan angle for 23GHz, 25 GHz, and 26.5 GHz for the φ=0° and φ=90° planes. It can be observed that AR degrades and realized gain drops faster with the increase in frequency. However, AR is significantly below 3dB over the entire bandwidth and within the scan range up to the 3dB gain drop point.

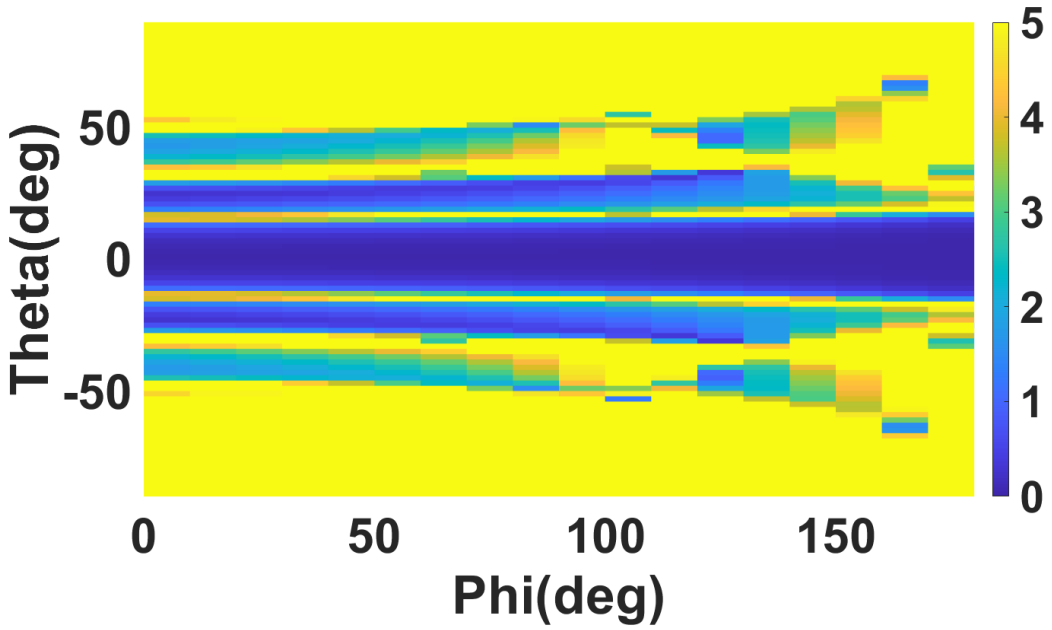

(a)

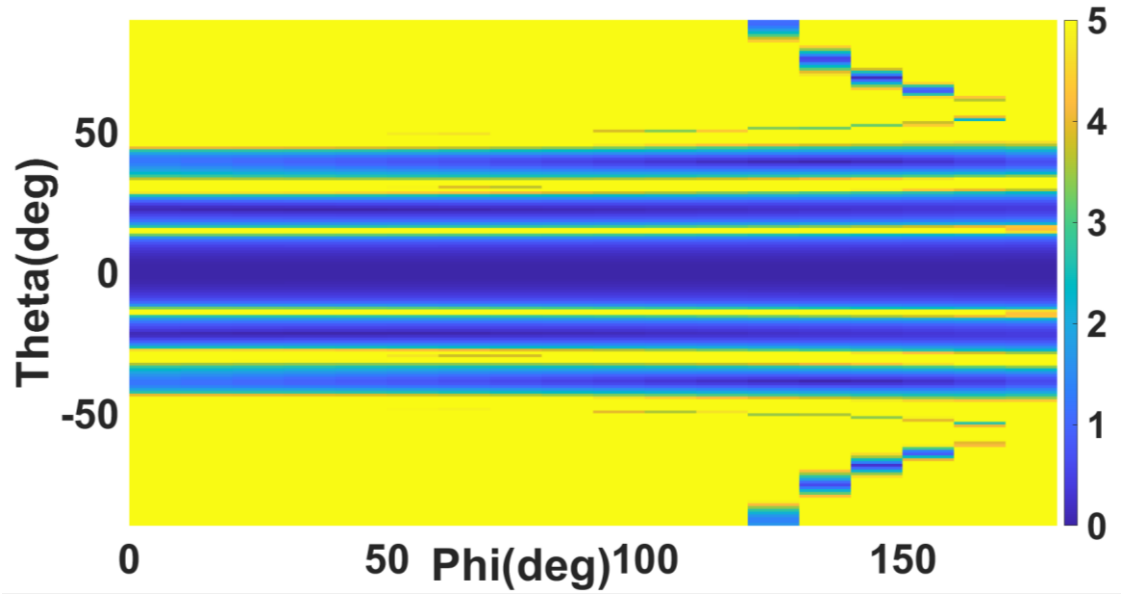
Theta(deg)
50
0
-50
0
50
Phi(deg)
100
150
5
4
3
2
1
0

(b)

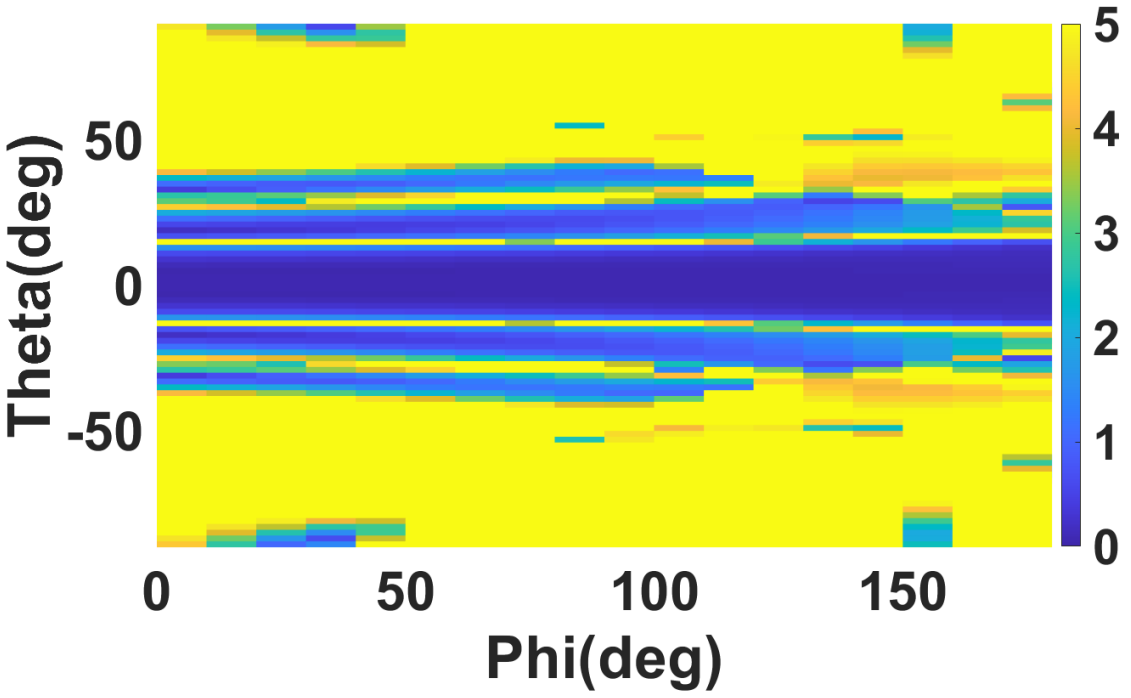
Theta(deg)
50
0
-50
0
50
100
150
Phi(deg)
5
4
3
2
1
0

(c)

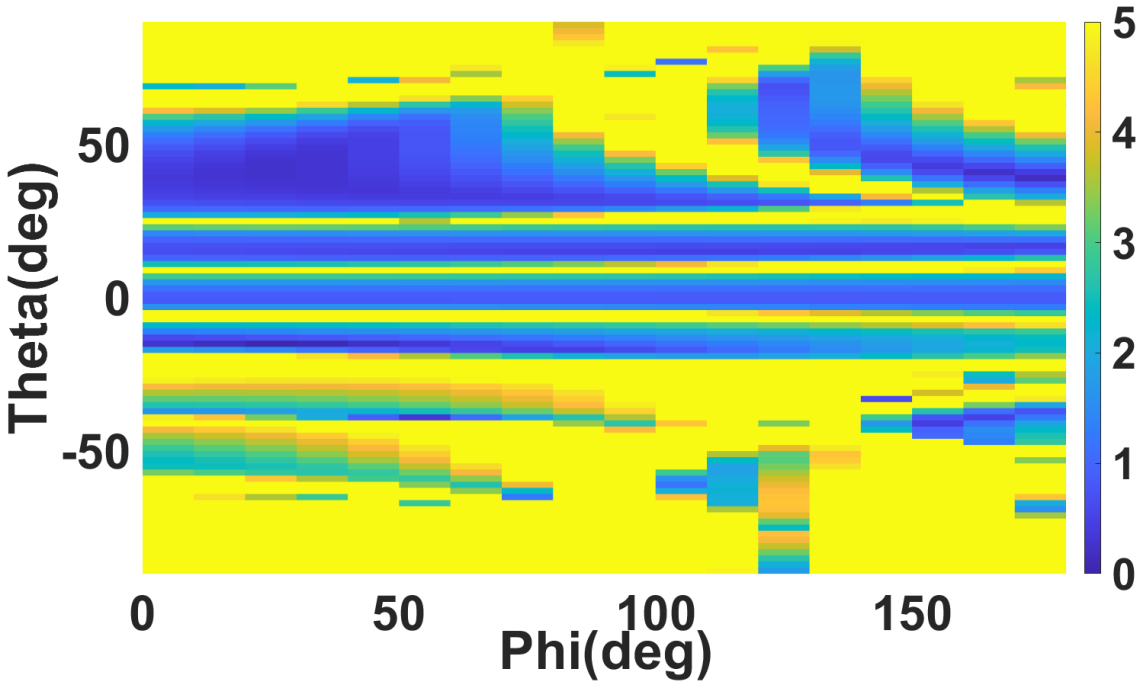
Theta(deg)
50
0
-50
0
50
100
150
Phi(deg)
5
4
3
2
1
0

(d)

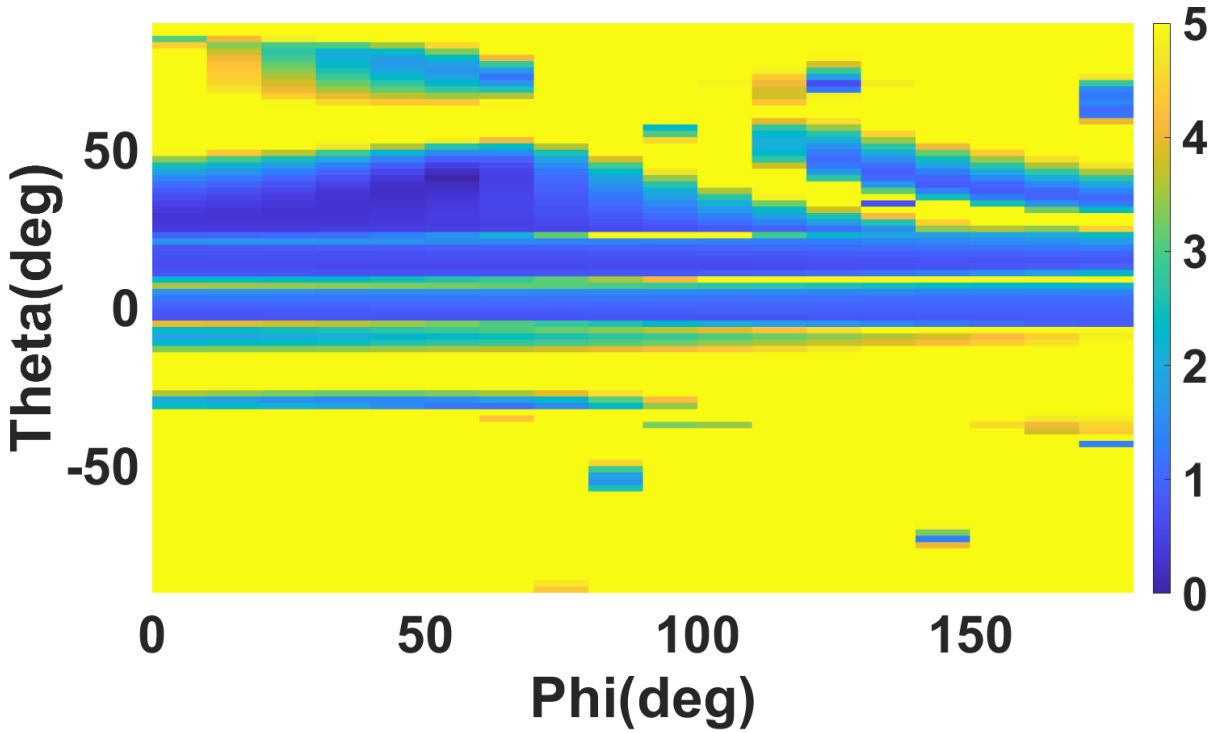
Theta(deg)
50
0
-50
0
50
100
150
Phi(deg)
5
4
3
2
1
0

(e)

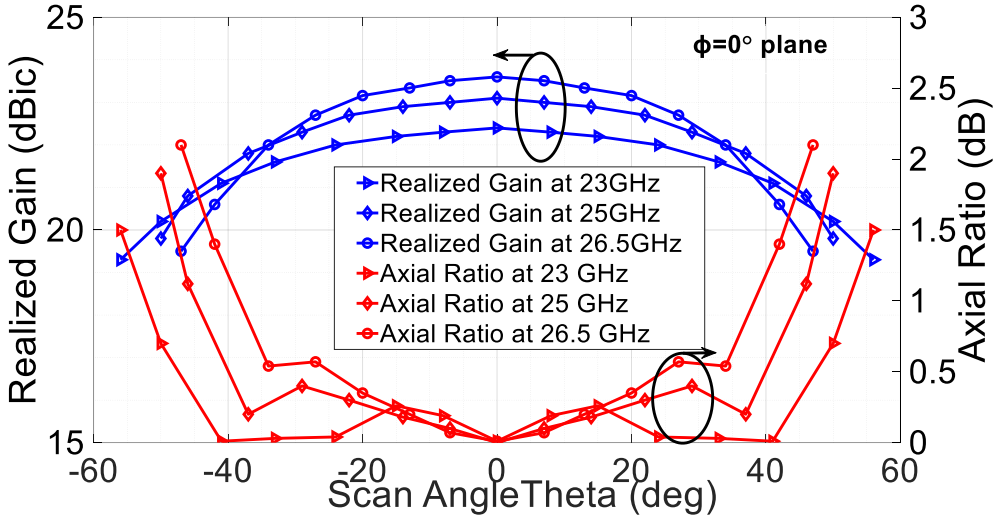

(f)

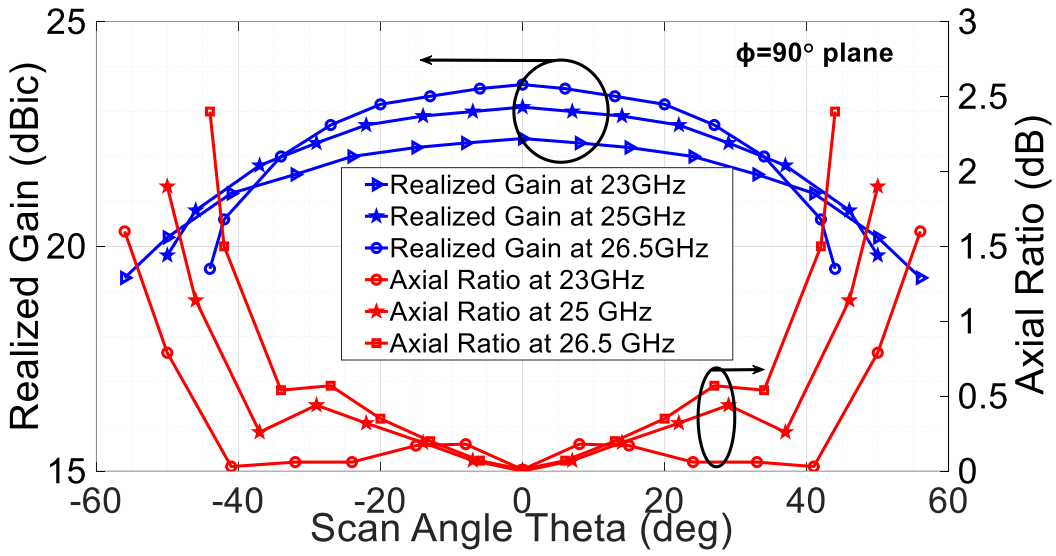

(g)

Fig. 4.13: The broadside axial ratio contour plot for (a) 23GHz, (b) 25 GHz, and (c) 26.5 GHz, the axial ratio contour plot for maximum scan for (d) 23 GHz, and (e) 26.5 GHz, axial ratio versus scan angle and realized gain versus scan angle for 23GHz, 25 GHz and 26.5 GHz for (e) φ=0° and (f) φ=90° planes.

4.6. Co-simulation with chips and splitter output

The schematic diagram of the beamforming chip (AWMF-0165) is shown in Fig. 4.14(a). The chip has two common Tx/Rx inputs, designated as port A and port B, respectively, each for one polarization (horizontal or vertical), and there are eight output ports referred to as element ports, four of which correspond to Tx/Rx common port A and remaining four correspond to Tx/Rx common port B. Each chip has a low noise amplifier, 6 bits phase shifter, and 5-bit gain control in the receive path and a high power amplifier, 6 bits phase shifter, and 5-bit gain control in transmit path. A switch is employed to select transmit or receive path and the switch is controlled externally by the serial peripheral interface (SPI). Also, the phase shifter, gain control and therefore each output of the chip can be controlled externally through SPI. The chip is half-duplex, and therefore the array either works in receive mode or works in transmit mode at a time.

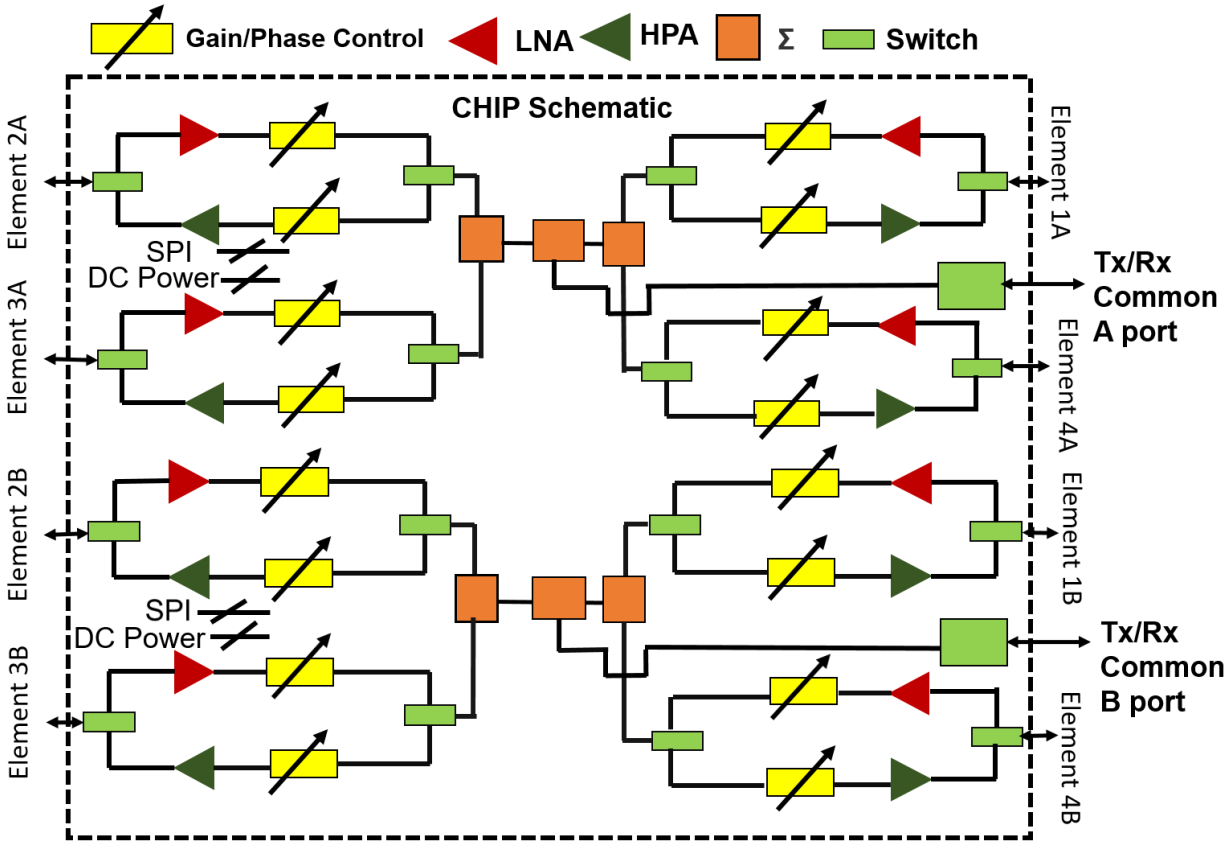

(a)

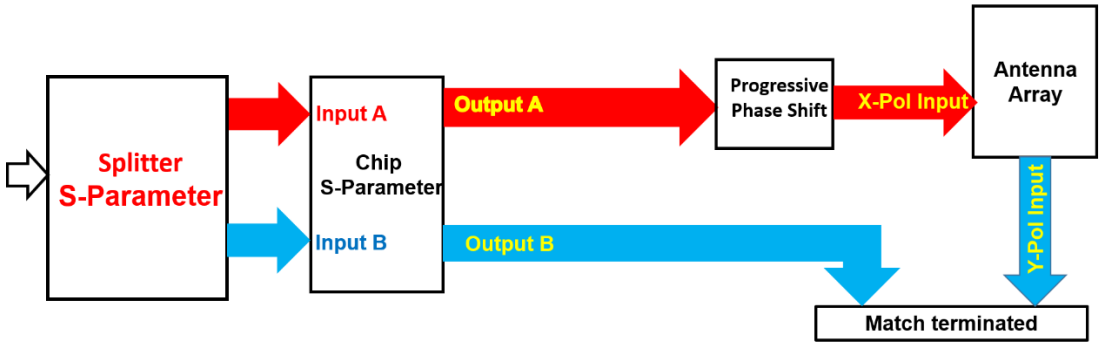

(b)

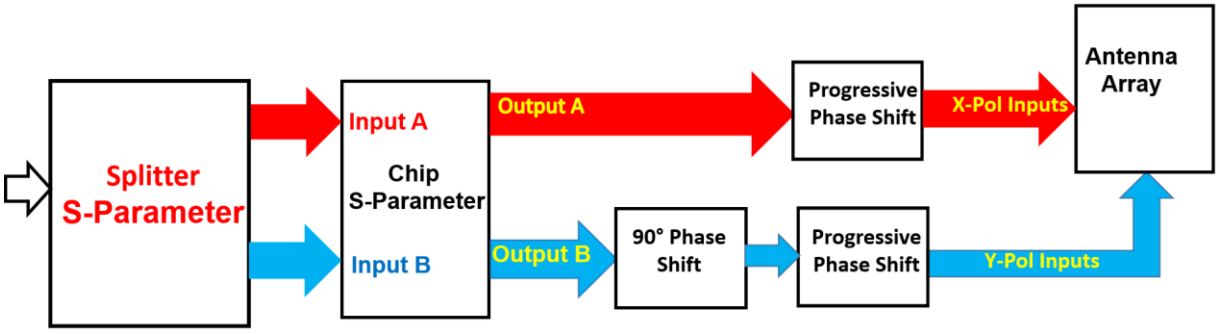

(c)

Fig. 4.14: (a) Schematic diagram of the Anokiwave chip, and Schematic diagram of the co-simulation in (b) linear polarization, and in (c) circularly polarization.

The effect of incorporating RFICs (AWMF-0165) in the passive array was simulated to determine if non-ideal responses from the chip lead to different amplitude and phase responses which can impact both linear and circular polarization. Circular polarization is expected to be more impacted because it employs both vertical and horizontal ports where

a phase mismatch is more deleterious. Fig. 4.14(b) shows the schematic diagram of the co-simulation when the array operates in linear polarization whereas Fig. 4.14(c) is the schematic diagram for co-simulation when the array operates in circular polarization.

Fig. 4.15(a) shows how a single chip with two inputs is placed at the center of a dual linear polarized 2x2 array underneath the beamforming board and connected to two feed points in each driven patch of the 2x2 sub-array (only driven patches are shown and L stubs are hidden so that feed points, chip position and chip inputs can be clearly seen). Initially, a 1x2 splitter is designed to feed a chip with two inputs. The performance of the splitter was simulated along with the RFIC to understand the performance implications to the 2x2 antenna system. The array is co-simulated with the 1x2 power splitter and chip *S*-parameter files using Ansys Electronics Circuit. Since the RFIC *S*-parameters data was only available down to 23.75 GHz, we have studied the array co-simulation response for 23.75 GHz and 26.5 GHz. The 1x2 splitter performance is shown in Fig. 4.15(b). It is evident from Fig. 4.15(b) that the power at the two inputs of each chip is the same, and isolation between the chip inputs is also better than (-20) dB over the entire bandwidth. Thus, the splitter is not incurring any mismatch between the horizontal and vertical polarizations of the chip. The radiation pattern at 25 GHz for linear polarization and circular polarization is shown in Figs. 4.15(c) and (d), respectively. The axial ratio versus frequency for the case without chip and with chip is shown in Fig. 4.15(e). We can observe the polarization purity and axial ratio has deteriorated when the array is co-simulated with chip output, but the axial ratio is still much below 3dB and polarization purity is also acceptable.

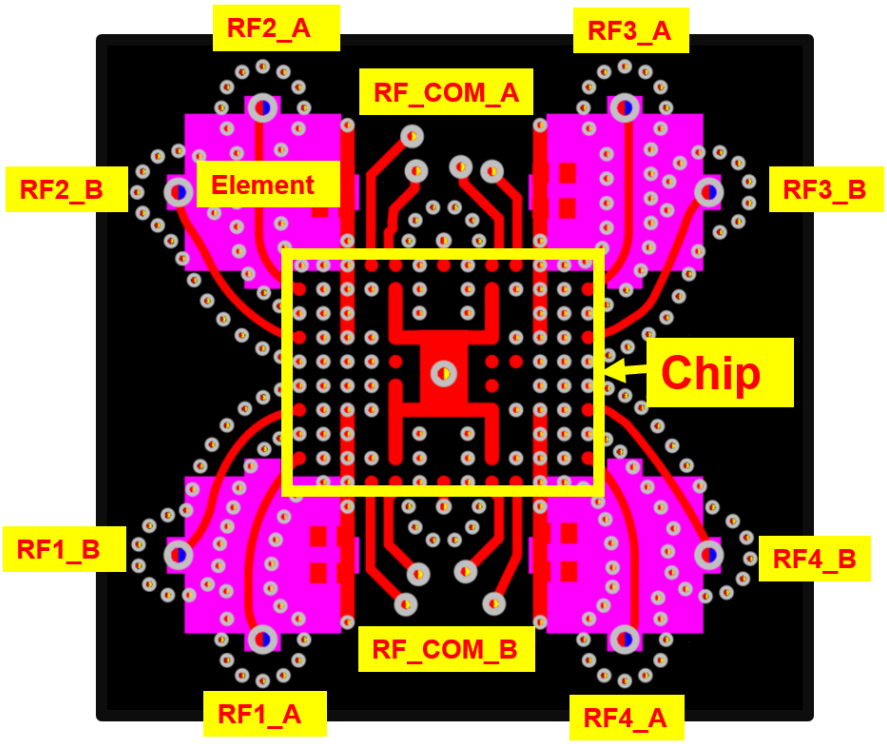
RF2_A
RF3_A
RF_COM_A
RF2_B
Element
RF3_B
Chip
RF1_B
RF4_B
RF_COM_B
RF1_A
RF4_A

(a)

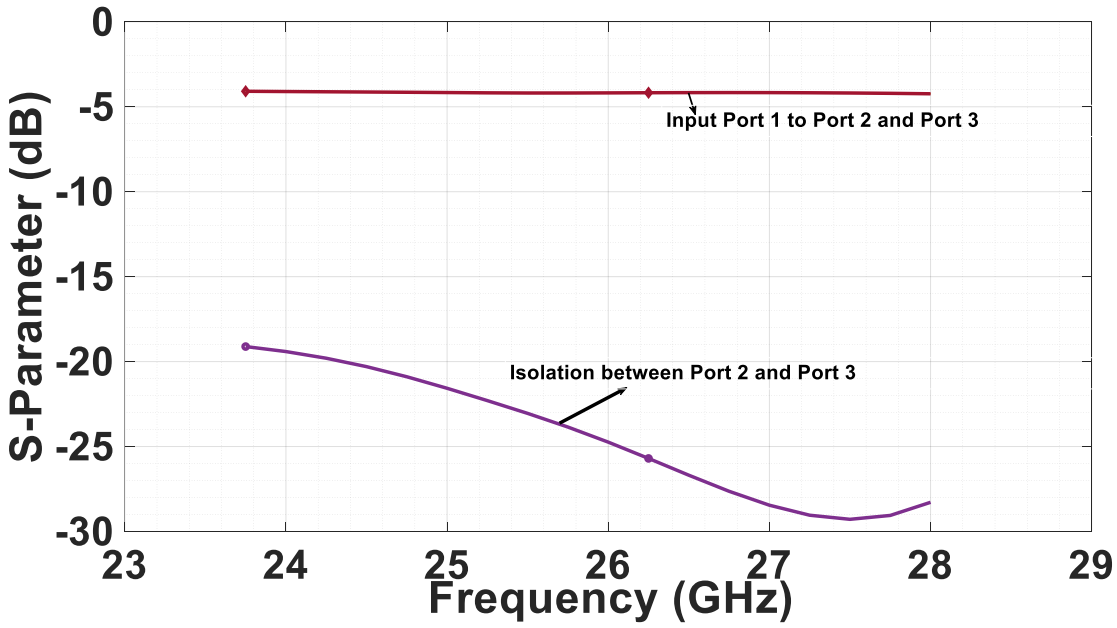
S-Parameter (dB)
0
-5
-10
-15
-20
-25
-30
23
24
25
26
27
28
29
Frequency (GHz)
Input Port 1 to Port 2 and Port 3
Isolation between Port 2 and Port 3

(b)

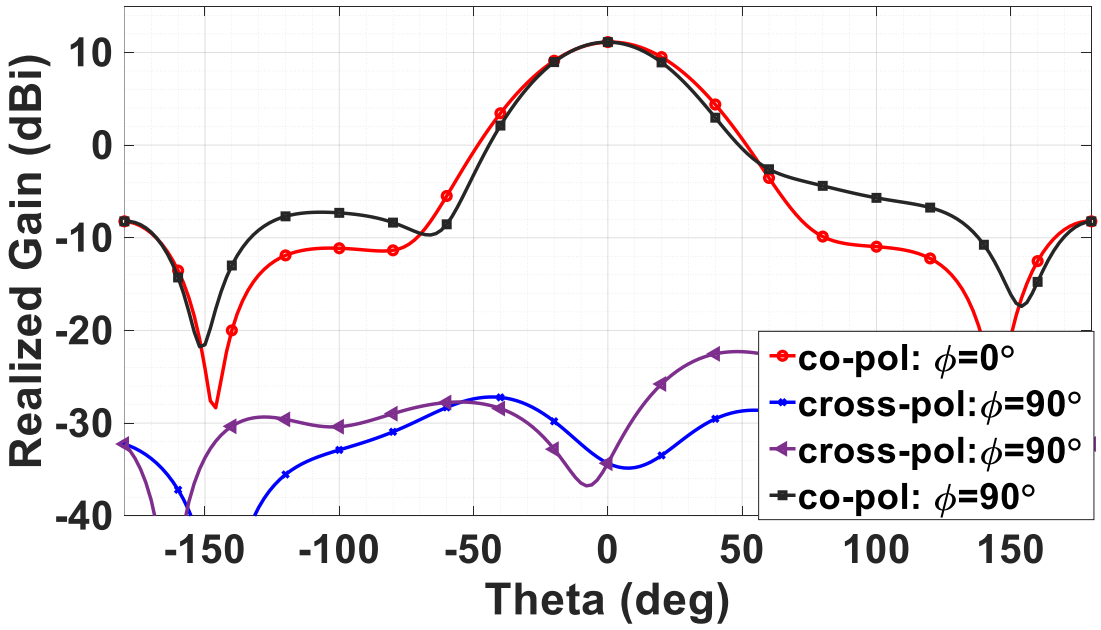
Realized Gain (dBi)
10
0
-10
-20
-30
-40
-150
-100
-50
0
50
100
150
Theta (deg)
co-pol: ϕ=0°
cross-pol:ϕ=90°
cross-pol:ϕ=90°
co-pol: ϕ=90°

(c)

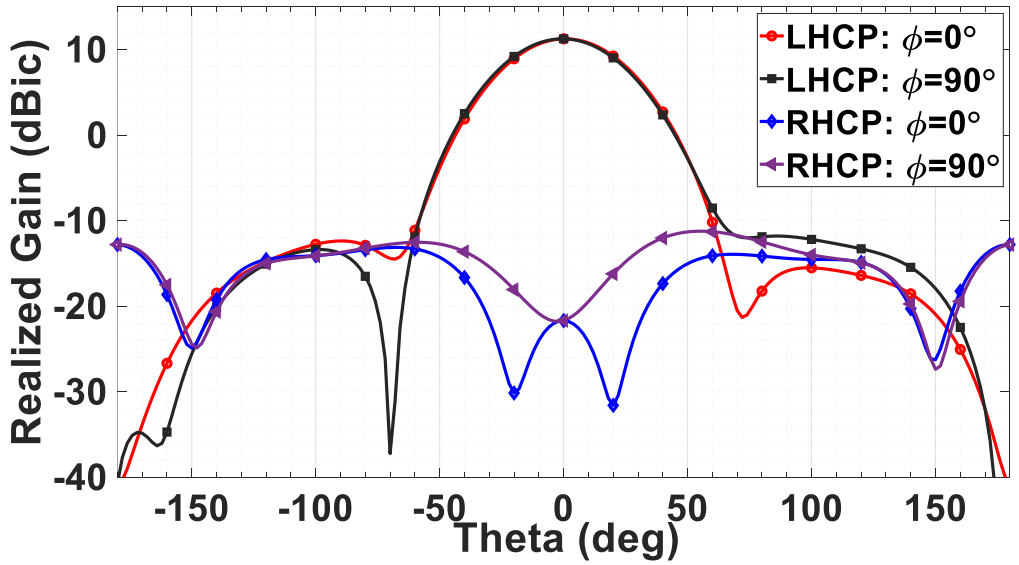
Realized Gain (dBic)
10
0
-10
-20
-30
-40
-150
-100
-50
0
50
100
150
Theta (deg)
LHCP: ϕ=0°
LHCP: ϕ=90°
RHCP: ϕ=0°
RHCP: ϕ=90°

(d)

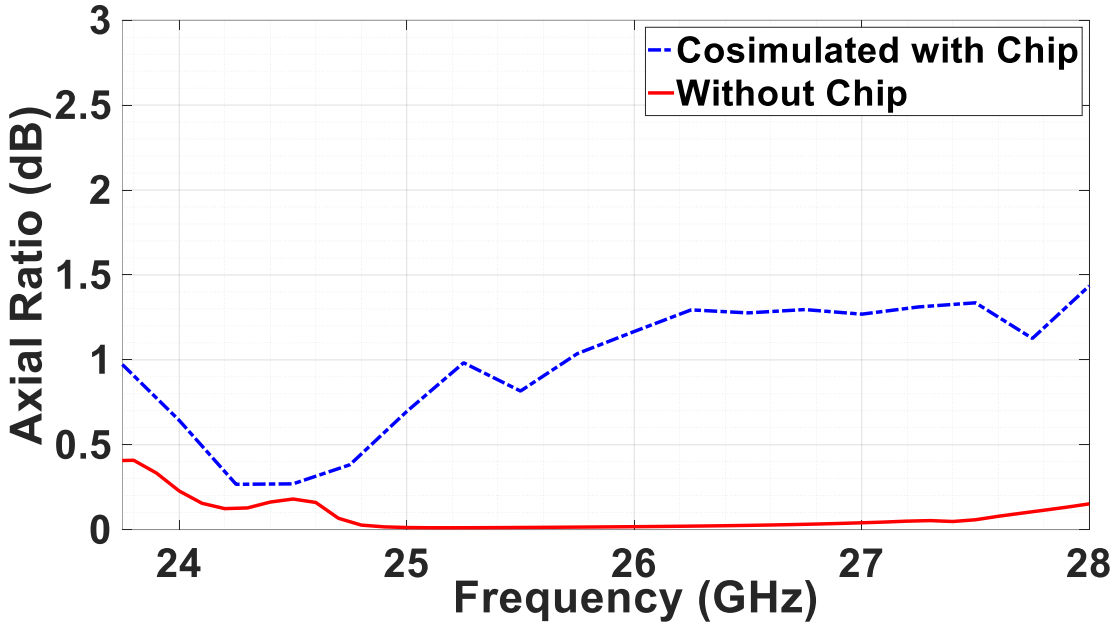

(e)

Fig. 4.15. (a) Schematic showing chip inputs, chip position and chip connection with the two feed points in each driven patch of a 2x2 sub-array (only driven patches are shown and L stubs are hidden so that feed points, chip position and chip inputs can be clearly seen), (b) 1x2 splitter performance, radiation pattern at 25 GHz (c) for linearly polarized array, (d) for circularly polarized array, and (d) axial ratio versus frequency for with and without chip.

In the next step, a 1x32 power splitter was designed to feed the 16 (4x4) chips, each chip with two inputs. The performance of the splitter was simulated along with the RFIC to understand the performance implications to the antenna system. The 1x32 splitter performance is shown in Fig. 4.16(a). Fig. 4.16(c), and 4.16(d), show the beam scan performance of the vertically (Y-) polarized array in the *E*-plane at 23.75 GHz, and 26.5 GHz. In Fig. 4.16(b), we can see that the gain drops from 22.4 dBi to 19.6 dBi as the beam scans from $\Theta = 0°$ to $\pm 48°$ at 23.75 GHz. In Fig. 4.16(c) we can see that the gain drops from 23.1 dBi to 20 dBi as the beam scans from $\Theta = 0°$ to $\pm 38°$ at 26.5GHz. Thus, we can say that the scan volume decreases by nearly 5°- 8° in addition to 0.5dB of peak gain drop.

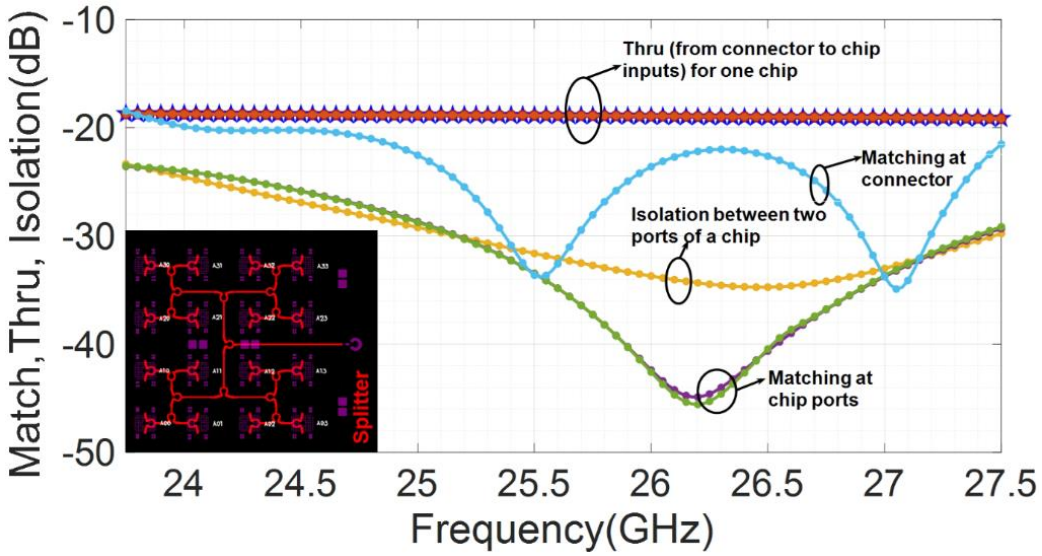
Thru (from connector to chip inputs) for one chip
Matching at connector
Isolation between two ports of a chip
Matching at chip ports
Splitter
Match,Thru, Isolation(dB)
Frequency(GHz)
-10
-20
-30
-40
-50
24
24.5
25
25.5
26
26.5
27
27.5

(a)

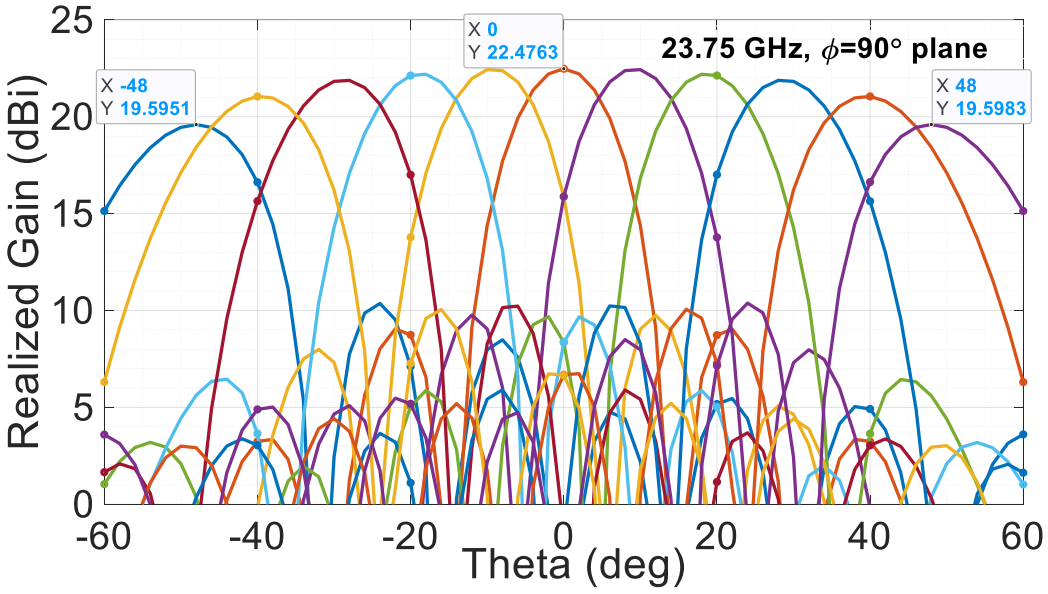
X 0
Y 22.4763
23.75 GHz, ϕ=90° plane
X -48
Y 19.5951
X 48
Y 19.5983
Realized Gain (dBi)
Theta (deg)
25
20
15
10
5
0
-60
-40
-20
0
20
40
60

(b)

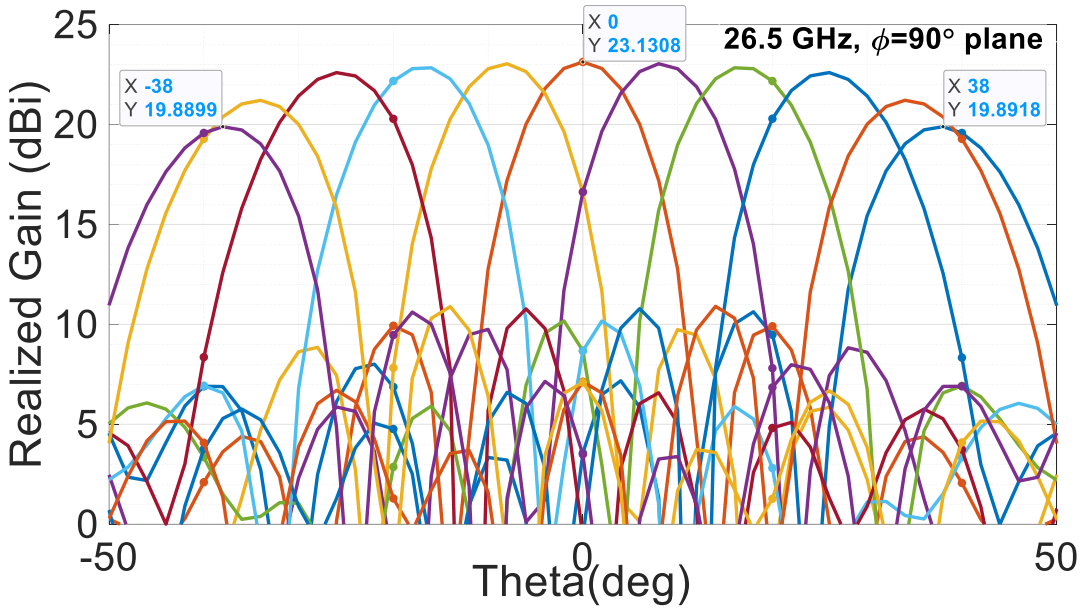
X 0
Y 23.1308
26.5 GHz, ϕ=90° plane
X -38
Y 19.8899
X 38
Y 19.8918
Realized Gain (dBi)
Theta(deg)
25
20
15
10
5
0
-50
0
50

(c)

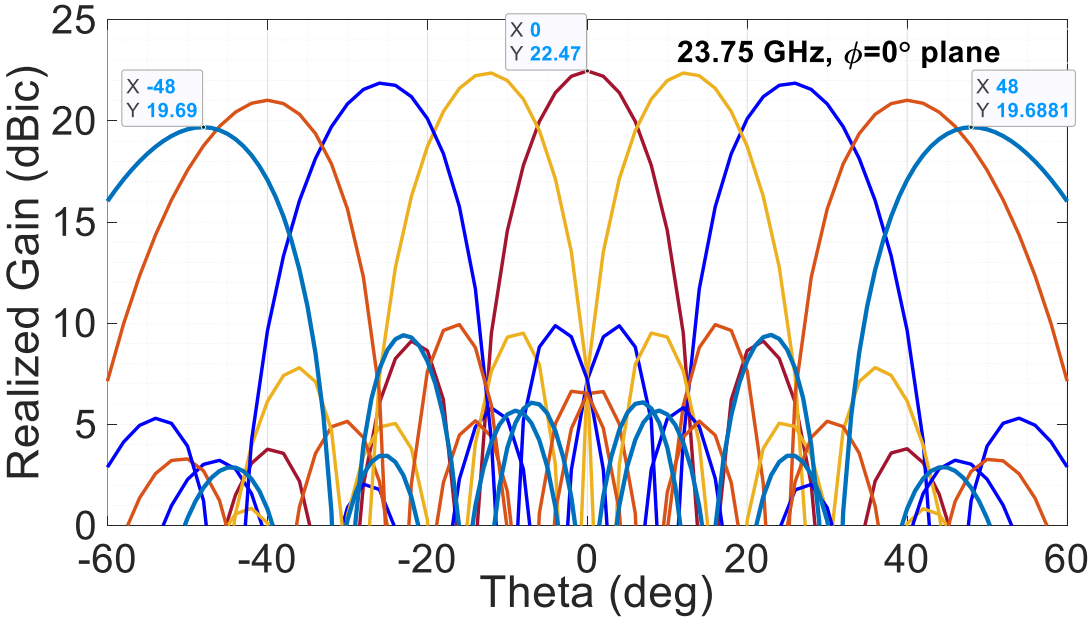
X 0
Y 22.47
23.75 GHz, ϕ=0° plane
X -48
Y 19.69
X 48
Y 19.6881
Realized Gain (dBic)
Theta (deg)
25
20
15
10
5
0
-60
-40
-20
0
20
40
60

(d)

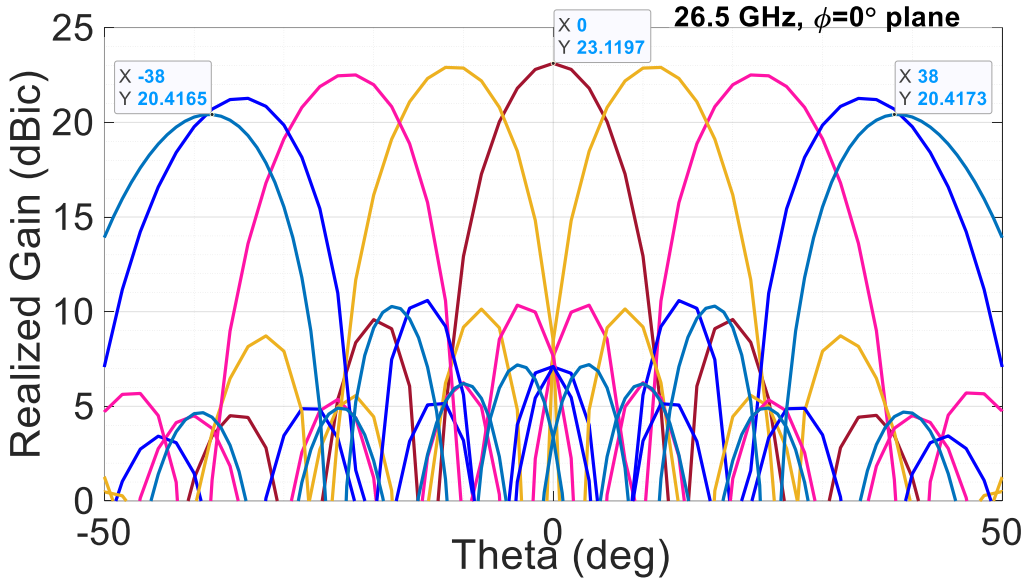

(e)

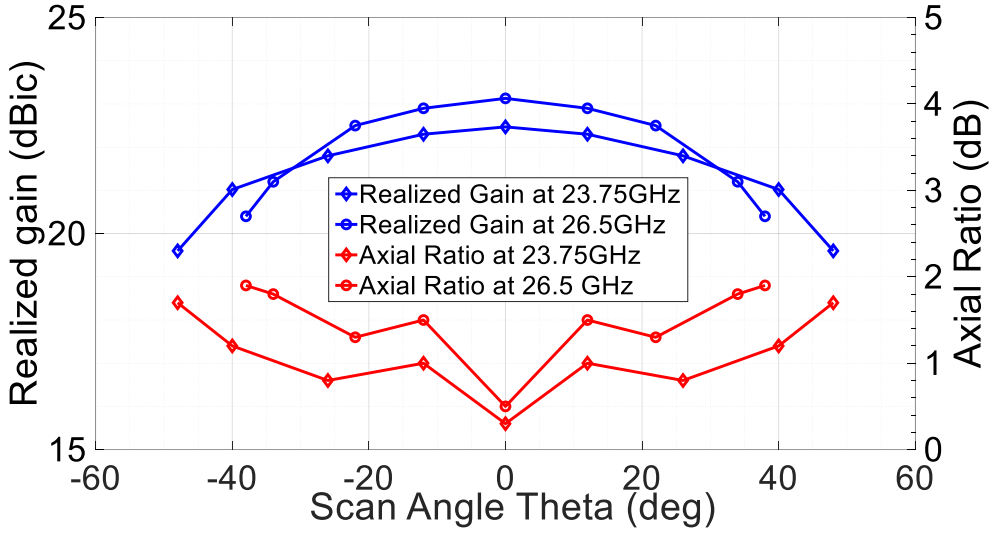

(f)

Fig. 4.16: (a) 1x32 Splitter performance for 4x4 =16 chips (each with two inputs), the beam scan performance in φ=90° directions (*E*-plane) at (b) 23.75 GHz, and (c) 26.5 GHz for the vertically polarized array, the LHCP beam scan performance in φ=0° plane at (d) 23.75 GHz, and (e) 26.5 GHz, and (f) AR and realized gain versus scan angles at 23.75 GHz and 26.5 GHz.

Figs. 4.16(d) and 4.17(e) show the beam scan performance for LHCP in the φ=0° plane at 23.75 GHz, and 26.5 GHz, respectively. We can see that the gain drops from 22.4 dBic to 19.6 dBic as the beam scans from Θ = 0° to ±48° at 23.75GHz, and from 23.1 dBic to 20.4 dBic as the beam scans from Θ = 0° to ±38° at 26.5GHz, respectively. We can also observe a decrease in scan volume by 5°- 8° in the CP case along with a 0.5 dB peak gain drop, which is similar to the linear polarization case. The performance in the φ=0° and φ=90° planes are identical in the CP case, and hence only the φ=0° plane is shown for the sake of brevity. Fig. 4.16(f) shows the AR and realized gain versus scan angles at 23.75 GHz, and 26.5 GHz for the φ=0° plane. We can notice degradation in AR also, but it is below 2 dB at the 3dB gain drop for both frequencies. It is worth mentioning that if significant degradation is observed in AR performance, then phase mismatch between the two sets of outputs (horizontal and vertical) of the chip should be compensated.

Here we have shown results based on the *S*-parameter files for the chip in Rx mode only, although the S-parameter files are available for both Rx and Tx modes.

4.7. Temperature Estimation of the array

Before we power up the 8x8 array, we should estimate the heat generation from the chip, and design a heat sink to assure that the chips are safe. To save computational time, and quickly predict the temperature of the array, we had simulated the 4x4 array (without any heat sink) in Ansys Icepak, with an assumption of 2x2 sources at the location of chips or in other words one source underneath the BFN at the center of each 2x2 sub-array, with a power of 6 Watts per source (chip) which is the maximum power of the chip when the array is working in CP mode. The temperature distribution of the 4x4 array with 2x2 sources underneath the BFN (without any heat sink) is shown in Fig. 4.17 (a). We can see the maximum temperature is approximately 170°C.

Then we have planned to use a 12.7 mm thick heat sink interface board with 20mm extensions on both sides of the array along horizontal plane, along with a 35mm thick finned heat sink, with fin width of 2mm and fin separation of 8mm, attached to that board, for the

heat sink purpose. The structure of the 4x4 array with the heat sink attached with the bottom side of the BFN and the temperature distribution of the 4x4 array with that heat sink is shown in Fig. 4.17(b). We can see the maximum temperature has decreased to 65°C to 70°C. According to chip specifications, chips are quite safe at this temperature. Though we have carried out the thermal analysis for 4x4 array, we can extrapolate the results for 8x8 array, because though number of chips increases in 8x8 array, but the surface area of the heat sink also increases which in turn helps to maintain the temperature.

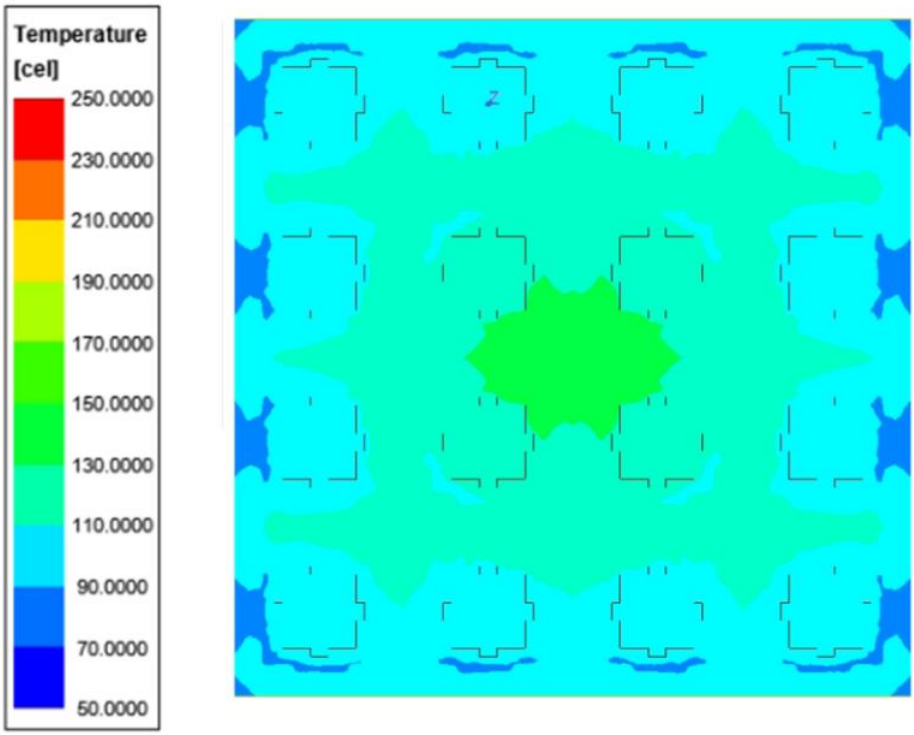

(a)

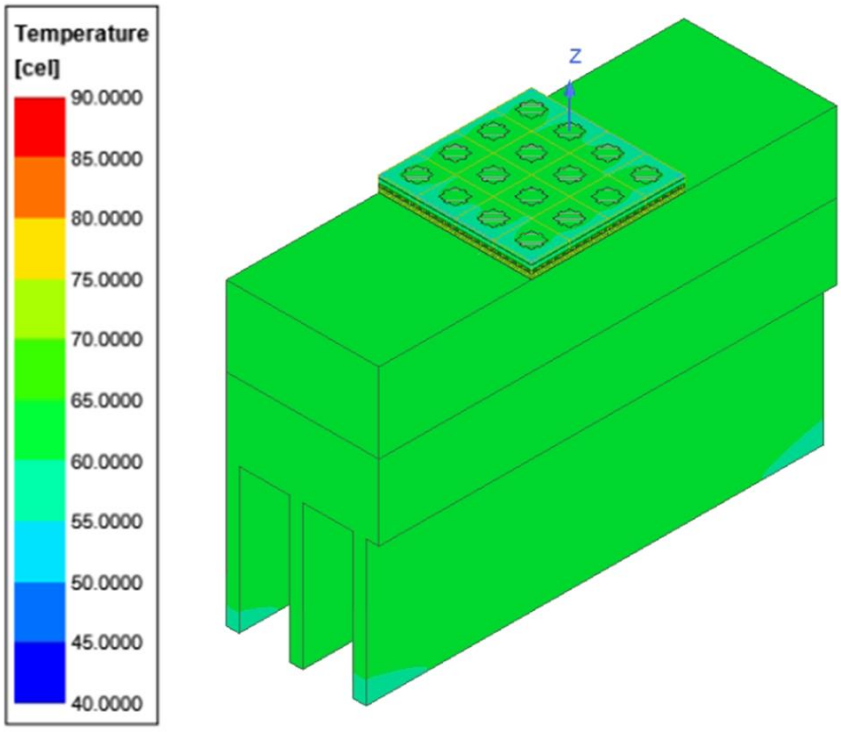

(b)

Fig. 4.17: Temperature distribution of 4x4 array with 2x2 sources of each 6 Watts power underneath BFN (a) without heat sink, and (b) with heat sink.

4.8. Fabrication and Measurement

Figs. 4.18(a) and 4.18(b) show the schematic diagram of the measurement setup and the fabricated antenna prototype, including the heat sink beneath the antenna, in the planar near-field chamber at NASA GRC, respectively. Fig. 4.18(a) explains how the phase and amplitude excitation are sent to the beamformer chip from the remote computer through the SPI controller. The beamforming algorithm accounts for the phase distribution of the unique 2x2 arrangement and is written in Python. Using the graphical user interface (GUI) created via Python, we can select the polarization (linear or CP) and steer the beam to the required scan positions. Fig. 4.18(c) shows the temperature distribution of the antenna in CP at the TX mode quiescent point as measured by an infrared (IR) camera. The maximum measured temperature of the array aperture is 42°C, considering an airflow of 18 cubic feet per minute at -15°C across heat sink fins.

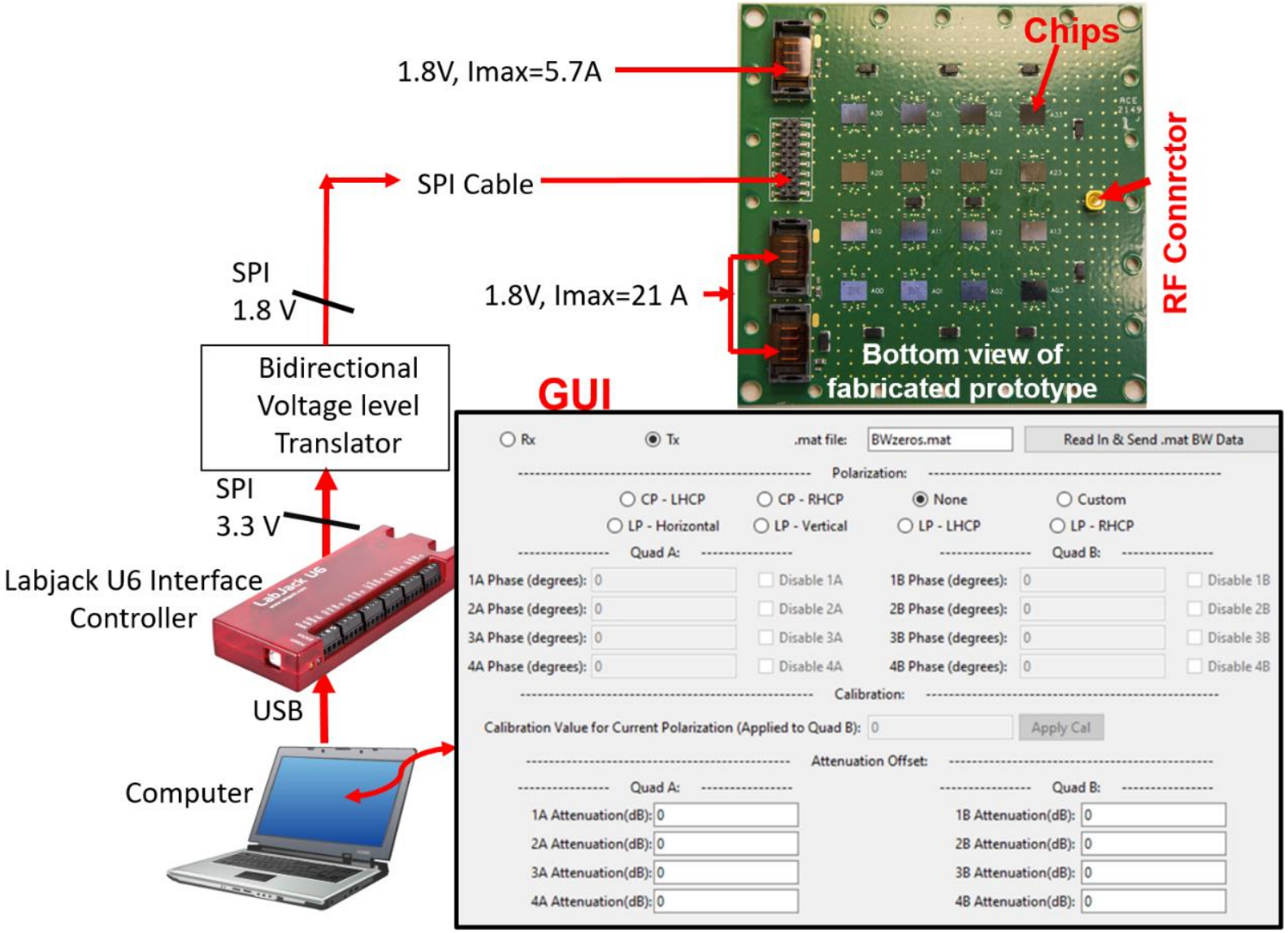
1.8V, Imax=5.7A
SPI Cable
SPI
1.8 V
1.8V, Imax=21 A
Bidirectional
Voltage level
Translator
SPI
3.3 V
Labjack U6 Interface
Controller
USB
Computer
Chips
RF Conrctor
Bottom view of
fabricated prototype
GUI
Rx
Tx
.mat file:
BWzeros.mat
Read In & Send .mat BW Data
Polarization:
CP - LHCP
CP - RHCP
None
Custom
LP - Horizontal
LP - Vertical
LP - LHCP
LP - RHCP
Quad A:
Quad B:
1A Phase (degrees):
Disable 1A
1B Phase (degrees):
Disable 1B
2A Phase (degrees):
Disable 2A
2B Phase (degrees):
Disable 2B
3A Phase (degrees):
Disable 3A
3B Phase (degrees):
Disable 3B
4A Phase (degrees):
Disable 4A
4B Phase (degrees):
Disable 4B
Calibration:
Calibration Value for Current Polarization (Applied to Quad B):
Apply Cal
Attenuation Offset:
Quad A:
Quad B:
1A Attenuation(dB):
1B Attenuation(dB):
2A Attenuation(dB):
2B Attenuation(dB):
3A Attenuation(dB):
3B Attenuation(dB):
4A Attenuation(dB):
4B Attenuation(dB):

(a)

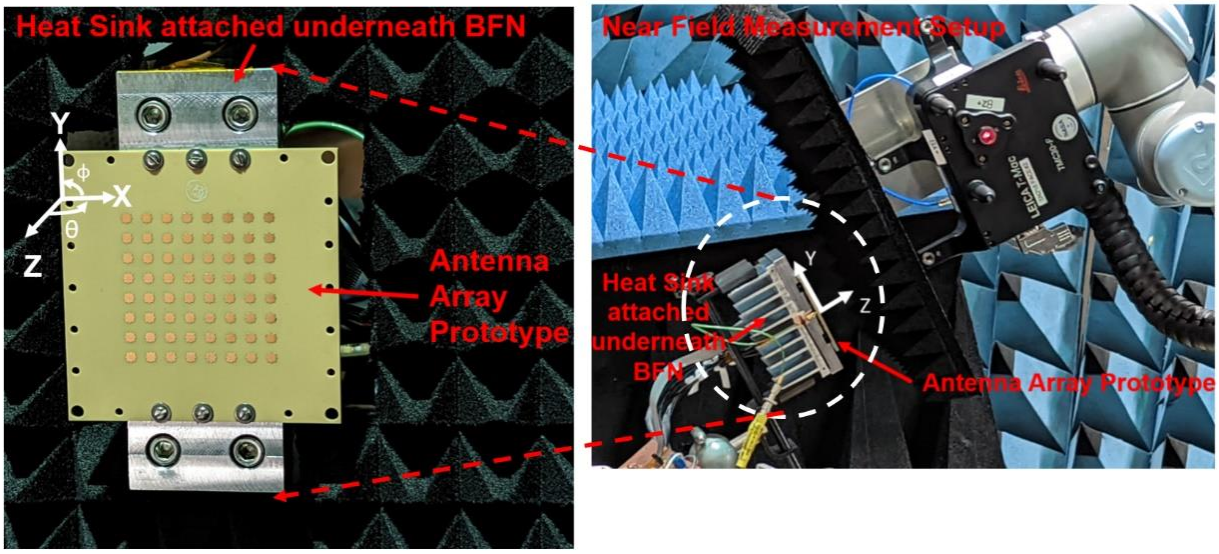

(b)

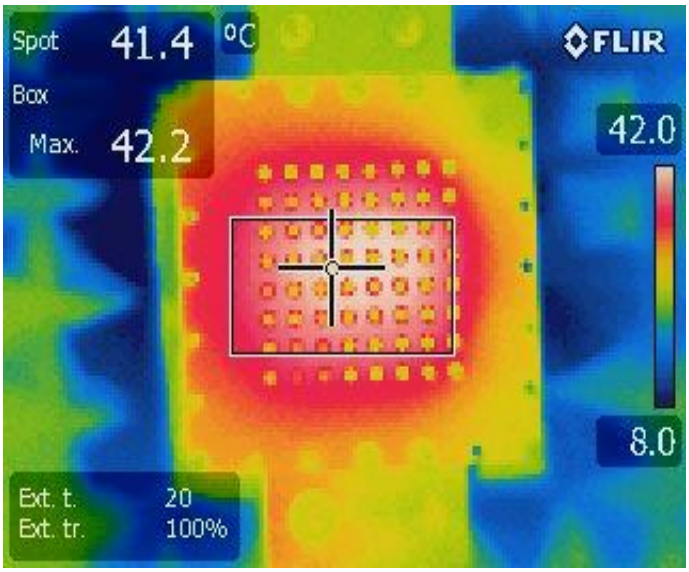

(c)

Fig. 4.18: (a) Schematic diagram of the measurement setup, (b) Fabricated prototype in the spherical near-field chamber, and (c) Temperature distribution of the CP array measured at the Tx mode quiescent point using an infra-red (IR) camera.

In Fig. 4.19(a), we have shown the normalized measured and simulated broadside radiation pattern for vertical (Y-) polarization at 26.5 GHz. We can observe that the simulated and measured 3dB gain-beamwidth is approximately 12° in both planes (which corresponds to the directivity is 23.6 dBi as in simulation), and the cross-polarized fields are not visible until -40 dB in the measured pattern, whereas the simulated cross-polarized field is not visible even at -40 dB. Thus, it is shown that the 2x2 mirror arrangement has reduced the cross-polarized fields by a significant amount and validated by measurements. Figs. 4.19(b) and (c) show the measured normalized gain magnitude plot versus azimuth and elevation angles for the broadside radiation pattern at 26.5 GHz and horizontal polarization. The directivity is 23.6 dBi for horizontal polarization also with very low cross-polarized fields.

Figs. 4.19(d)-(k) show the beam scan performance of the horizontally polarized array at around a 30° scan position. It is worth mentioning that the beam scans farther at lower frequency for the same progressive phase shift. Therefore, when our intended direction for the beam scan is around 30° at 25 GHz, in Figs. 4.19(d)-(k), we can observe that the beam scans that for φ=0°, 90°, 180° and 270° planes, the beam scans at 28.3° with a directivity of 22.8 dB, -28.7° with a directivity of 22.8 dB, -26.9° with a directivity of 22.9 dB and 28.3° with a directivity of 22.6 dB respectively. The measured scan loss/gain drop (23.6 dBi to around 22.8 dBi) is in very good agreement with the simulated data (23.6 dBi to 22.8 dBi at 28°).

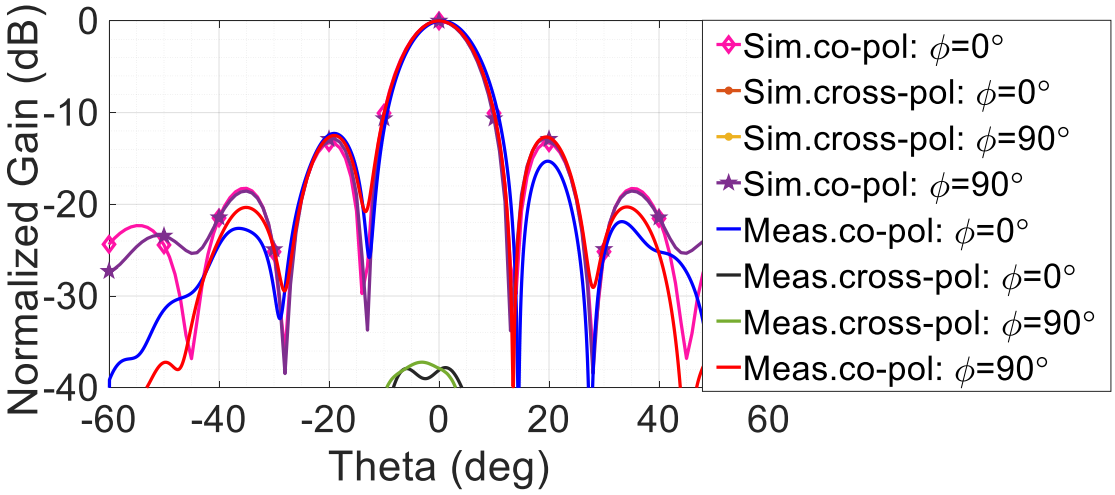

(a)

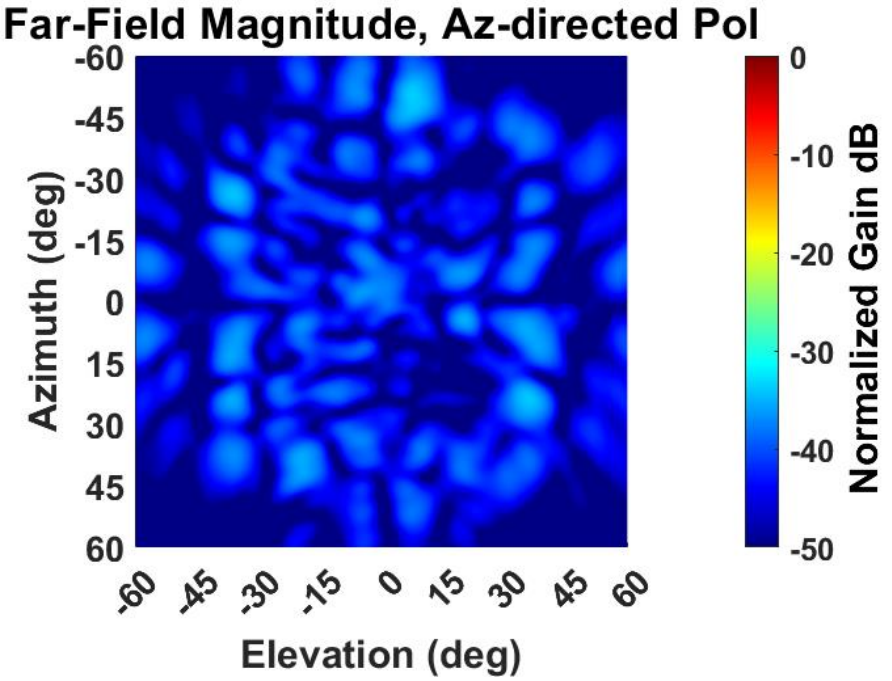
Far-Field Magnitude, Az-directed Pol
Azimuth (deg)
-60
-45
-30
-15
0
15
30
45
60
Elevation (deg)
-60
-45
-30
-15
0
15
30
45
60
Normalized Gain dB
0
-10
-20
-30
-40
-50

(b)

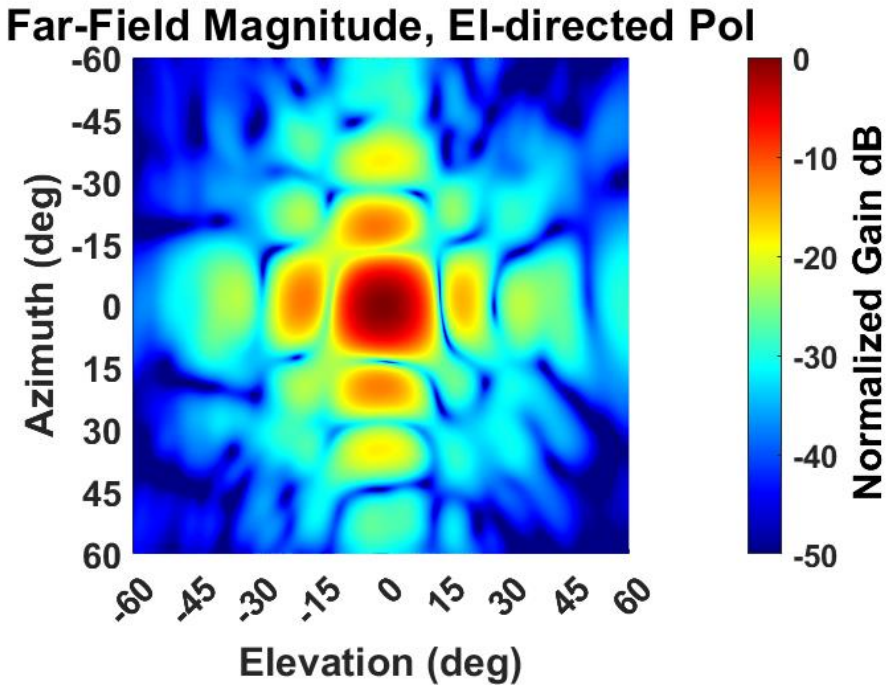
Far-Field Magnitude, El-directed Pol
Azimuth (deg)
-60
-45
-30
-15
0
15
30
45
60
Elevation (deg)
-60
-45
-30
-15
0
15
30
45
60
Normalized Gain dB
0
-10
-20
-30
-40
-50

(c)

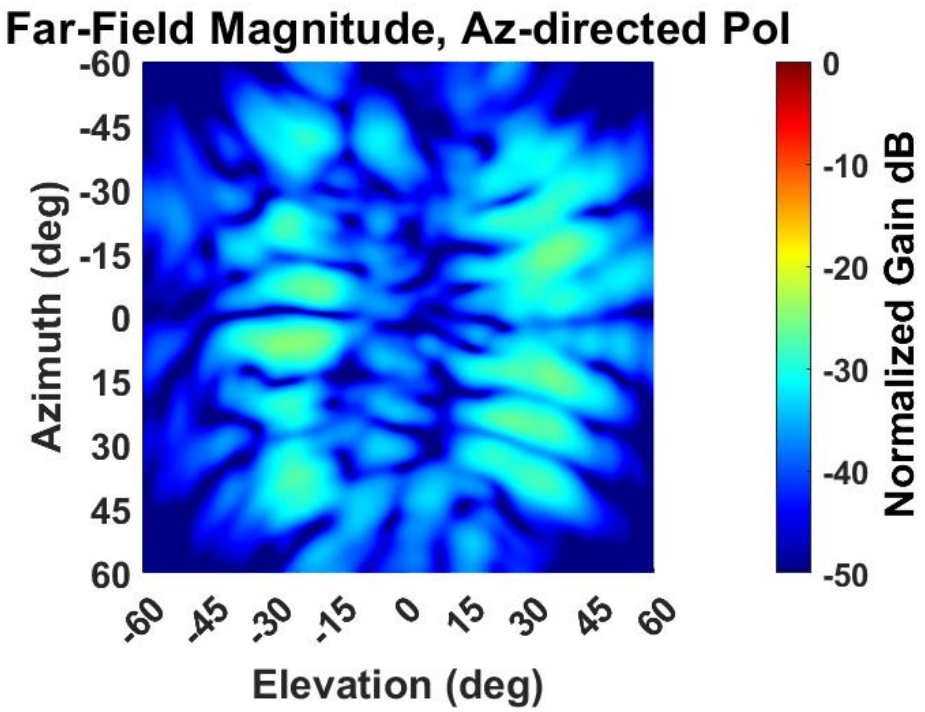
Far-Field Magnitude, Az-directed Pol
Azimuth (deg)
-60
-45
-30
-15
0
15
30
45
60
Elevation (deg)
-60
-45
-30
-15
0
15
30
45
60
Normalized Gain dB
0
-10
-20
-30
-40
-50

(d)

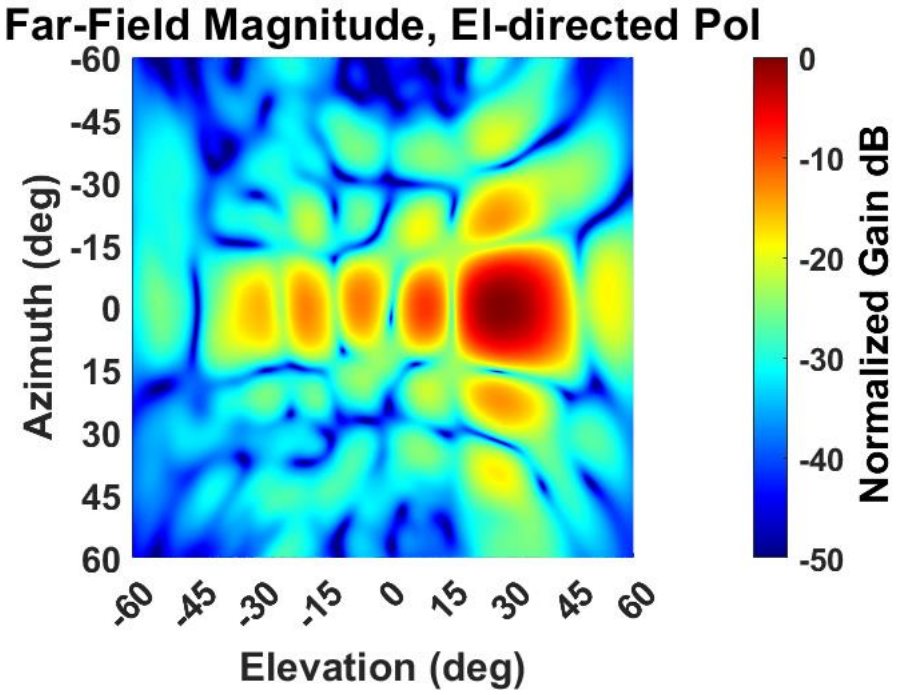
Far-Field Magnitude, El-directed Pol
Azimuth (deg)
-60
-45
-30
-15
0
15
30
45
60
Elevation (deg)
-60
-45
-30
-15
0
15
30
45
60
Normalized Gain dB
0
-10
-20
-30
-40
-50

(e)

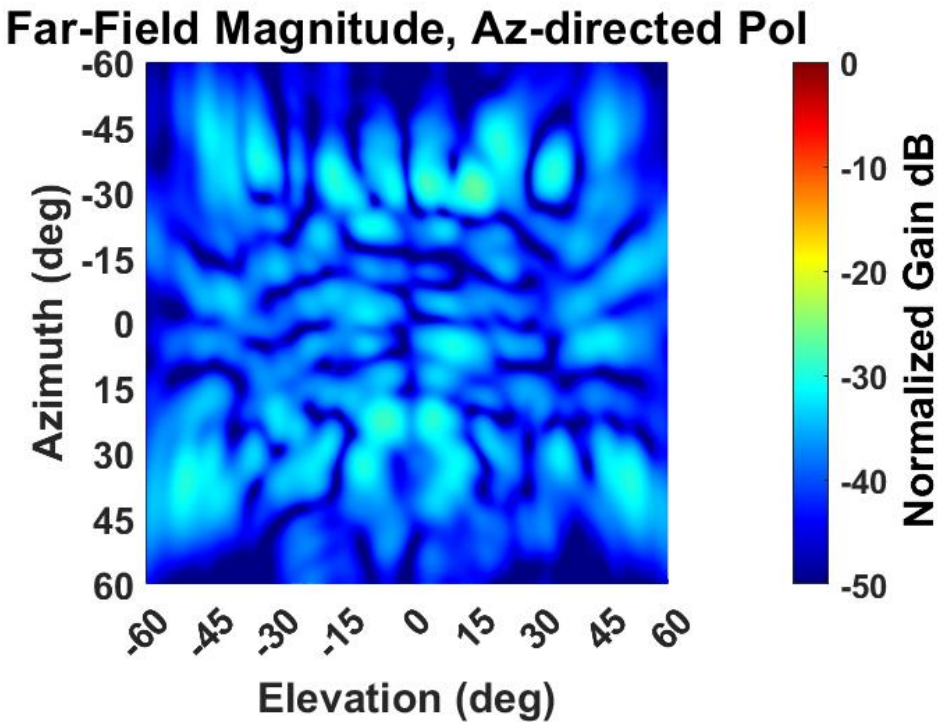
Far-Field Magnitude, Az-directed Pol
Azimuth (deg)
-60
-45
-30
-15
0
15
30
45
60
Elevation (deg)
-60
-45
-30
-15
0
15
30
45
60
Normalized Gain dB
0
-10
-20
-30
-40
-50

(f)

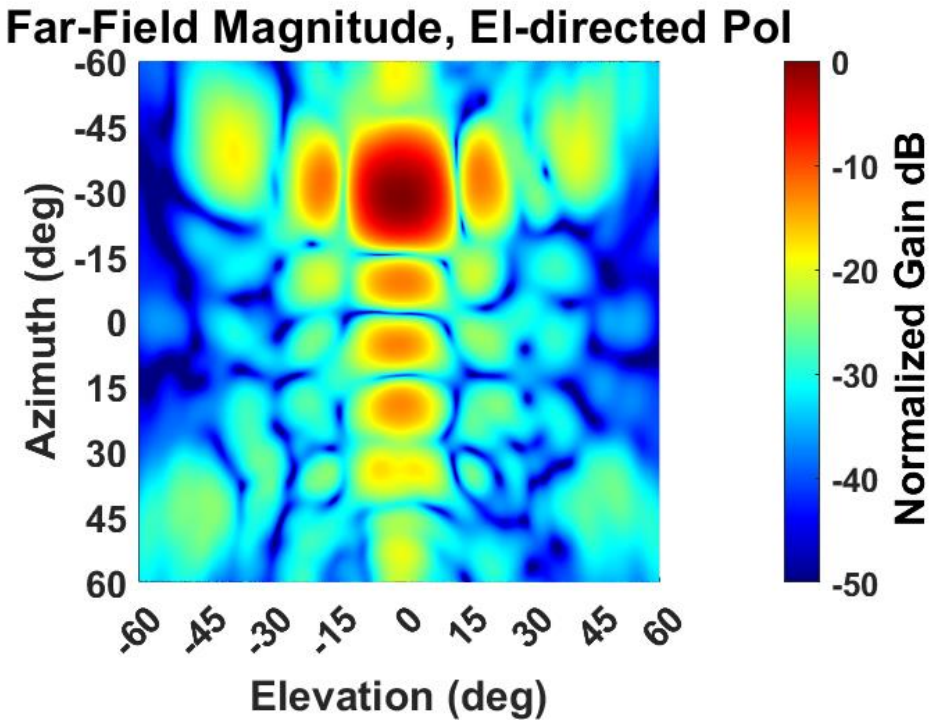
Far-Field Magnitude, El-directed Pol
Azimuth (deg)
-60
-45
-30
-15
0
15
30
45
60
Elevation (deg)
-60
-45
-30
-15
0
15
30
45
60
Normalized Gain dB
0
-10
-20
-30
-40
-50

(g)

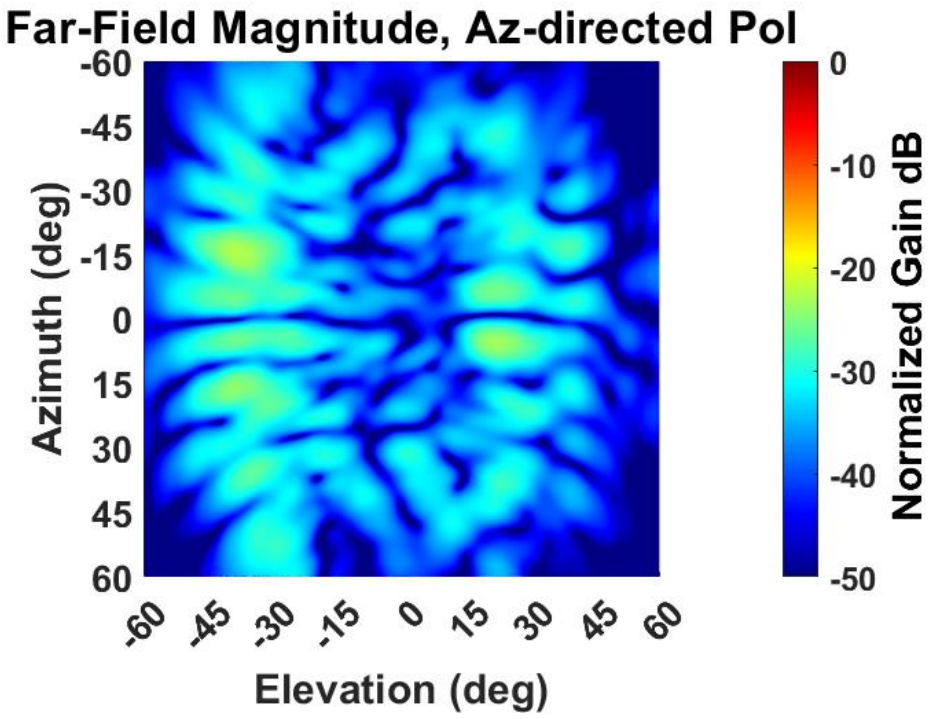
Far-Field Magnitude, Az-directed Pol
Azimuth (deg)
-60
-45
-30
-15
0
15
30
45
60
Elevation (deg)
-60
-45
-30
-15
0
15
30
45
60
Normalized Gain dB
0
-10
-20
-30
-40
-50

(h)

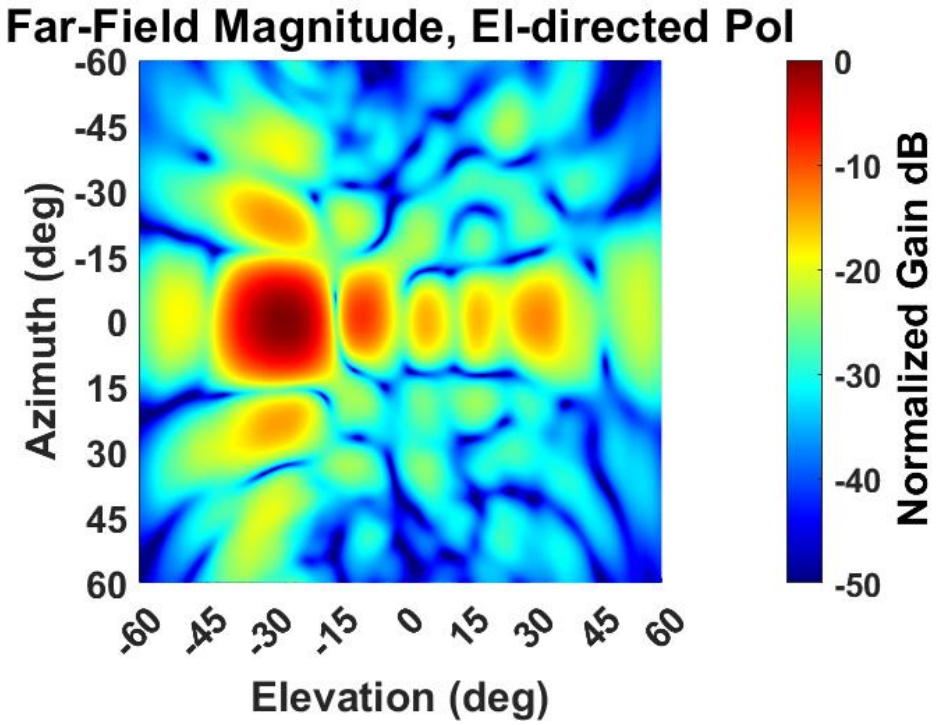
Far-Field Magnitude, El-directed Pol
Azimuth (deg)
-60
-45
-30
-15
0
15
30
45
60
Elevation (deg)
-60
-45
-30
-15
0
15
30
45
60
Normalized Gain dB
0
-10
-20
-30
-40
-50

(i)

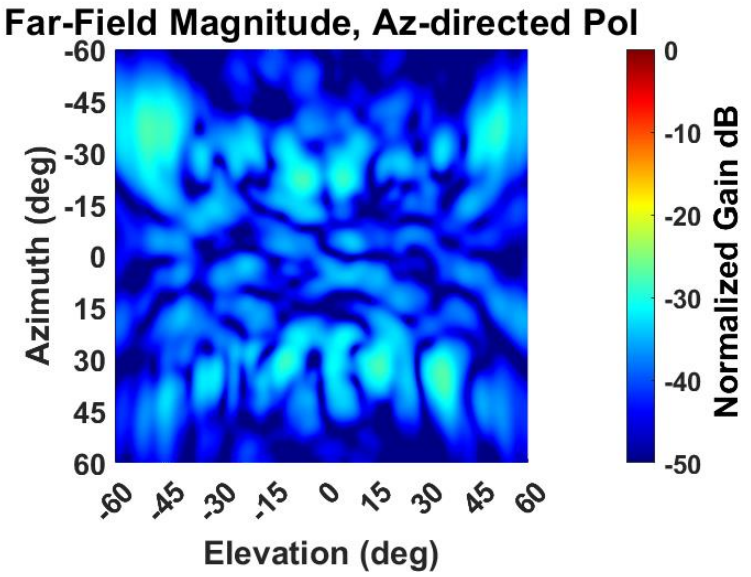

(j)

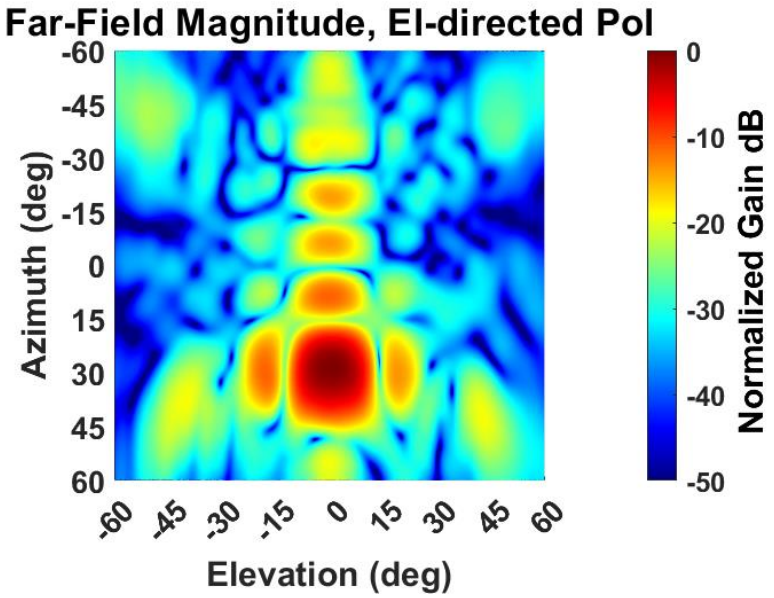

(k)

Fig. 4.19: Dual linear (a) measured (Meas.) and simulated (Sim.) broadside radiation pattern for vertical polarization, magnitude plots (versus azimuth and elevation angles) for the measured horizontal polarization, broadside in (b) and (c), and around 30^{o} beam scan cases for φ=0° in (d) and (e), φ=90° in (f) and (g), φ=180° in (h) and (i), and φ=270° planes in (j) and (k).

The simulated and measured normalized broadside LHCP radiation patterns at 23 GHz and 26.5 GHz are shown in Figs. 4.20(a) and 4.20(b), respectively. At 23 GHz, we can observe that the simulated and measured 3 dB gain-beamwidth is approximately 13° in both planes. The calculated broadside AR is 0.7 dB with a directivity of 22.6 dBic. At 26.5 GHz, we can observe the measured and simulated 3 dB gain-beamwidth of approximately 12° and the separation between the LHCP and RHCP (cross-polarized fields) is more than 40dB at the θ = 0° position. Thus, the sequential arrangement has improved the AR by a significant amount, which is validated by measurements. The calculated broadside AR is 0.26 dB and the directivity is 23.6 dBic.

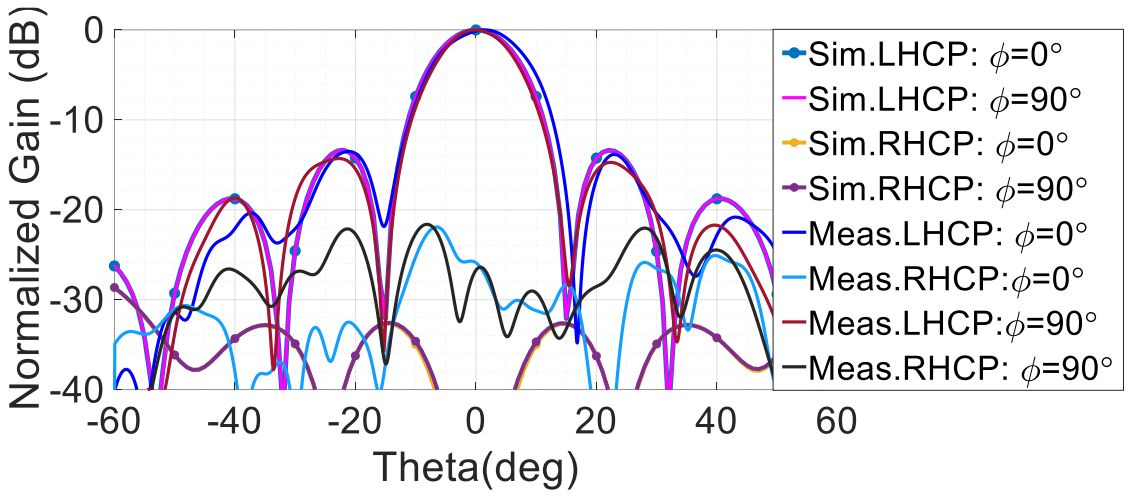

(a)

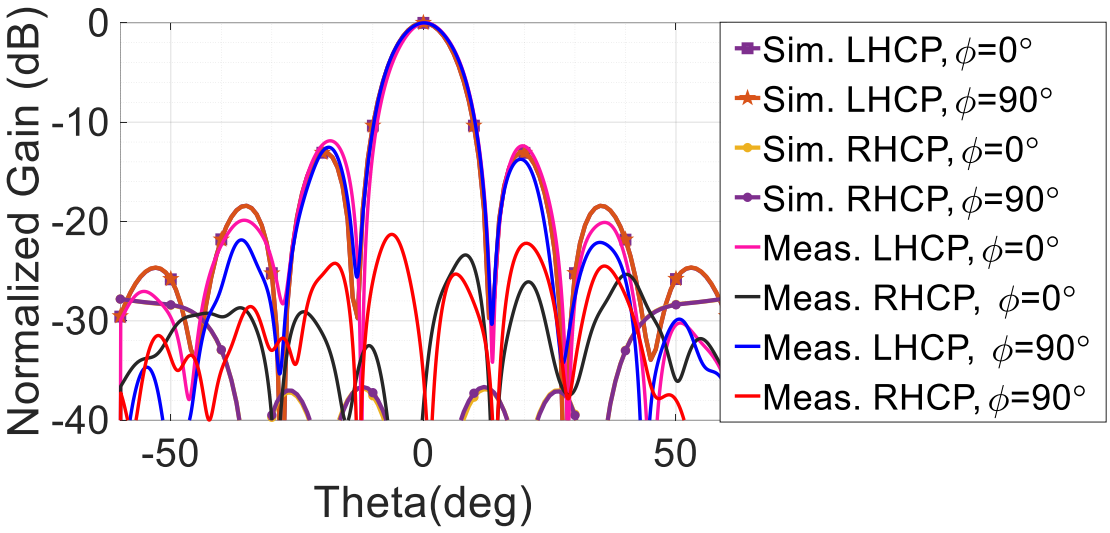

(b)

Fig. 4.20: LHCP measured (Meas.) and simulated (Sim.) broadside radiation patterns (a) 23 GHz, and (b) 26.5 GHz.

Figs. 4.21(a), and 4.21(b) show the LHCP scan performance for φ=0° (left side of the figure) and φ=90° (right side of the figure) at 23 GHz and 26.5 GHz, respectively. For both the φ=0° and φ=90° planes, the scan to Θ=42° and Θ=35° are shown for 23 GHz and 26.5 GHz, respectively. We can observe the first sidelobe level for the maximum scan is worse in the φ=90° plane compared to the φ=0° plane, but a minimum 6dB separation between the peak gain and sidelobe is maintained. Fig. 21(c) shows the measured scan loss and AR versus scan angle for φ=0° (left side of the figure) and φ=90° (right side of the figure) at 23 GHz, and 26.5 GHz, respectively. We can observe that the AR is almost below 3dB to Θ=42° scan range at 23 GHz, whereas, from the co-simulation, the 3dB scan loss/gain drop was to Θ=48° at 23.75 GHz (Fig. 4.17). Although RFIC (AWMF-0165) *S*-parameters data sheet provides data only down to 23.75 GHz, the results at 23 GHz are still acceptable. At 26.5 GHz, we can observe that the AR is almost below 3dB to Θ=35° scan range whereas, per the co-simulation study, the 3dB gain drop occurs at Θ=38° (Fig. 4.17). Calibration of the RFIC and finite array element imbalances is expected to improve polarization and sidelobe level performance.

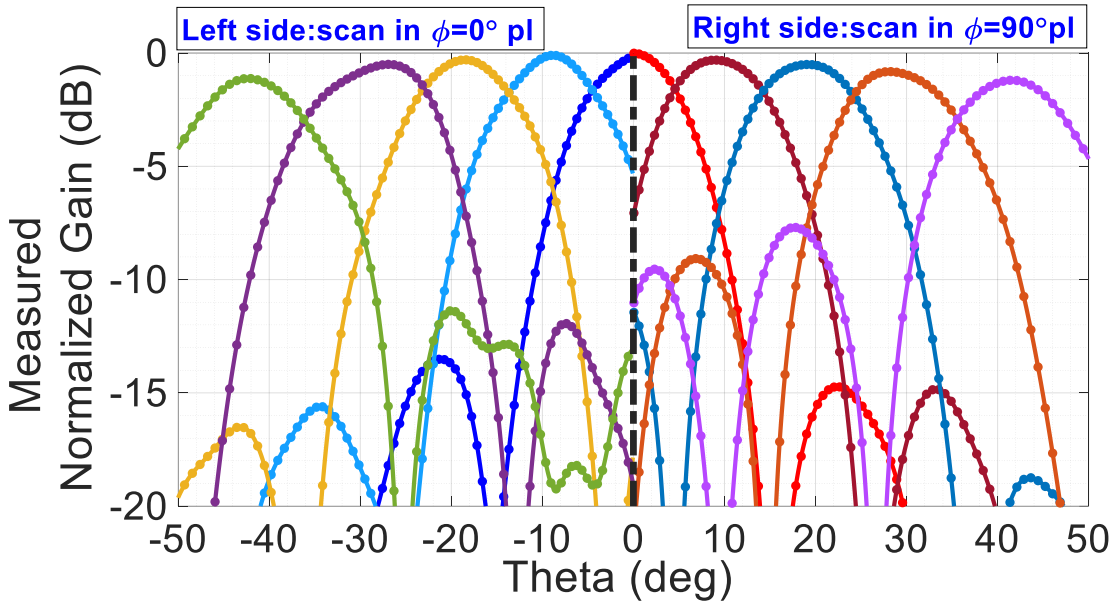
Left side:scan in ϕ=0° pl
Right side:scan in ϕ=90°pl
Measured
Normalized Gain (dB)
0
-5
-10
-15
-20
-50
-40
-30
-20
-10
0
10
20
30
40
50
Theta (deg)

(a)

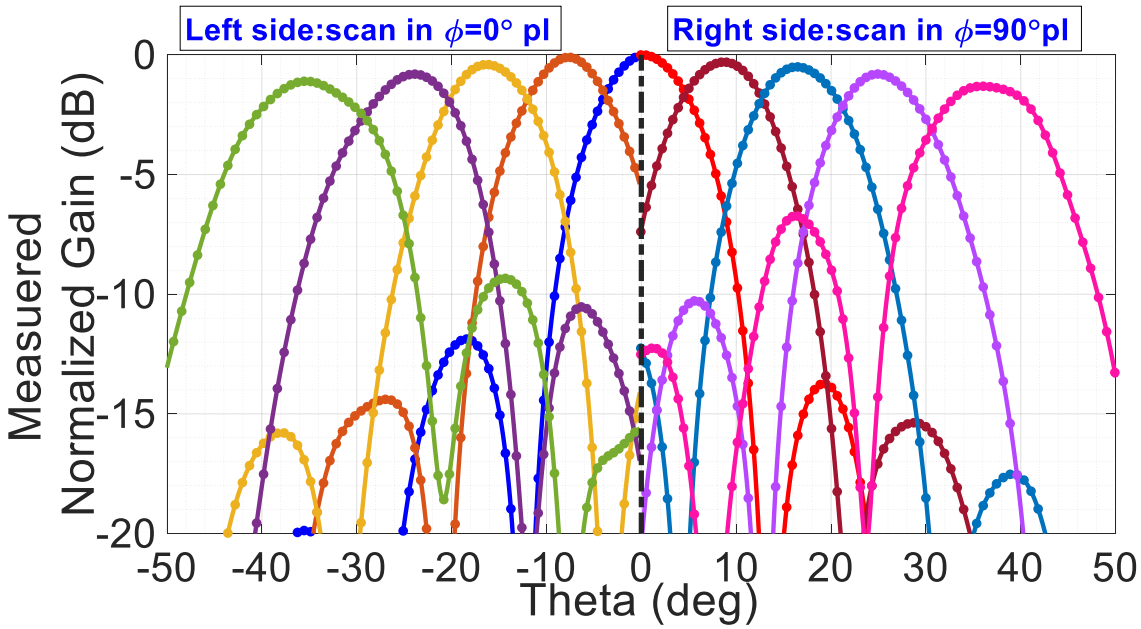
Left side:scan in ϕ=0° pl
Right side:scan in ϕ=90°pl
Measuered
Normalized Gain (dB)
0
-5
-10
-15
-20
-50
-40
-30
-20
-10
0
10
20
30
40
50
Theta (deg)

(b)

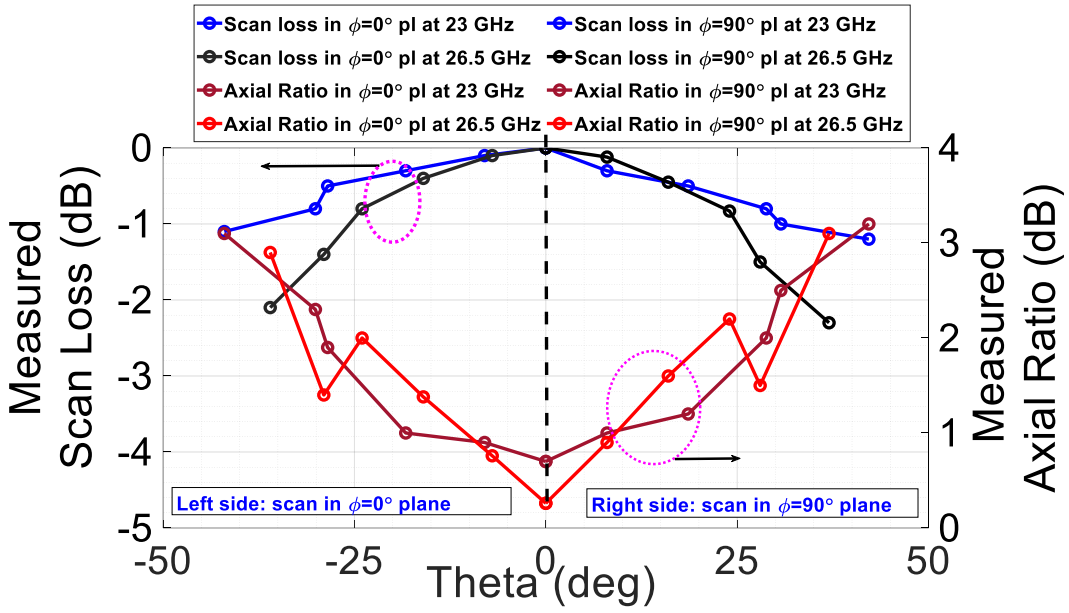

(c)

Fig. 4.21: Scan performance in φ=0° (left side of the figure), and φ=90° (right side of the figure) planes for (a) 23GHz, and (b) 26.5 GHz, and (c) scan loss and axial ratio versus scan angle at 23 GHz and 26.5 GHz in LHCP.

Figs. 4.22(a) and 4.22(b) show measured broadside magnitude plots for RHCP and LHCP (cross-pol) patterns for 26.5 GHz. The directivity is 23.6 dBic and the AR is 0.3 dB. Figs. 4.22(c) and 4.22(d) show patterns at 30° scan angle in the φ=0° plane with a directivity of 22.2 dBic and with an AR of 1.4 dB. The RHCP is found to be similar to the LHCP case, and hence not shown in detail for the sake of brevity.

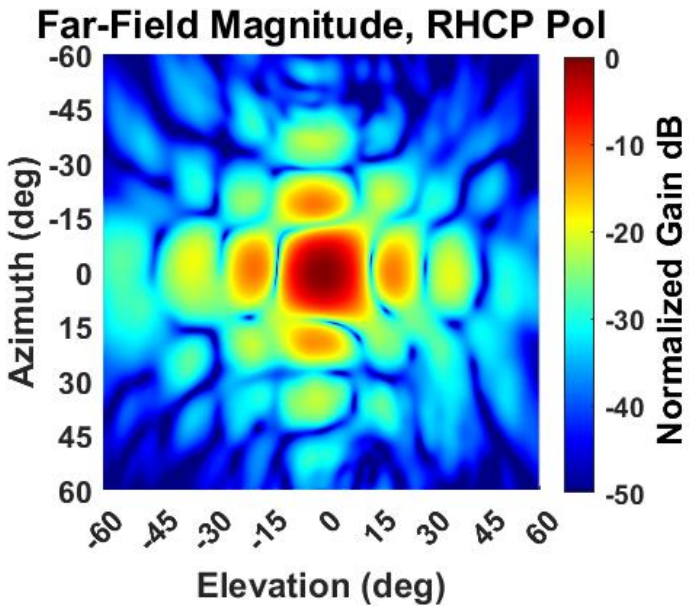
Far-Field Magnitude, RHCP Pol
Azimuth (deg)
-60
-45
-30
-15
0
15
30
45
60
Elevation (deg)
-60
-45
-30
-15
0
15
30
45
60
Normalized Gain dB
0
-10
-20
-30
-40
-50

(a)

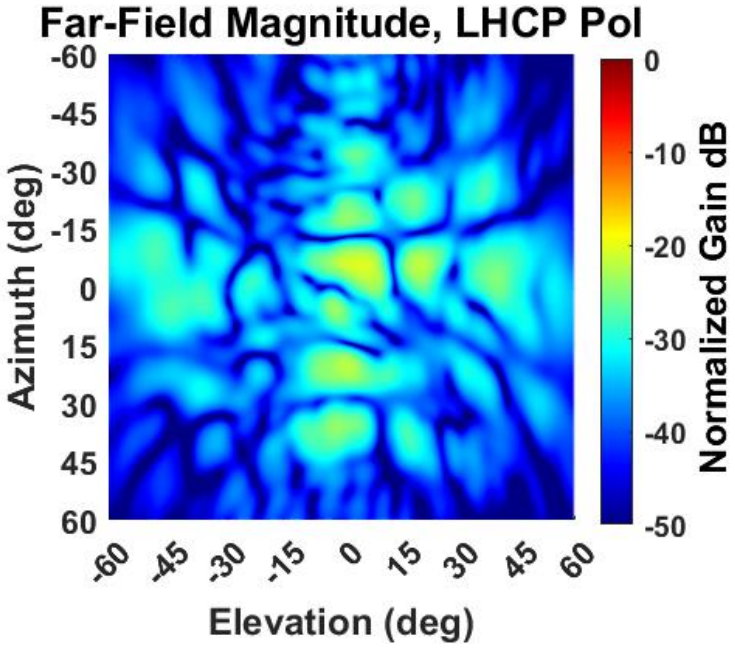
Far-Field Magnitude, LHCP Pol
Azimuth (deg)
-60
-45
-30
-15
0
15
30
45
60
Elevation (deg)
-60
-45
-30
-15
0
15
30
45
60
Normalized Gain dB
0
-10
-20
-30
-40
-50

(b)

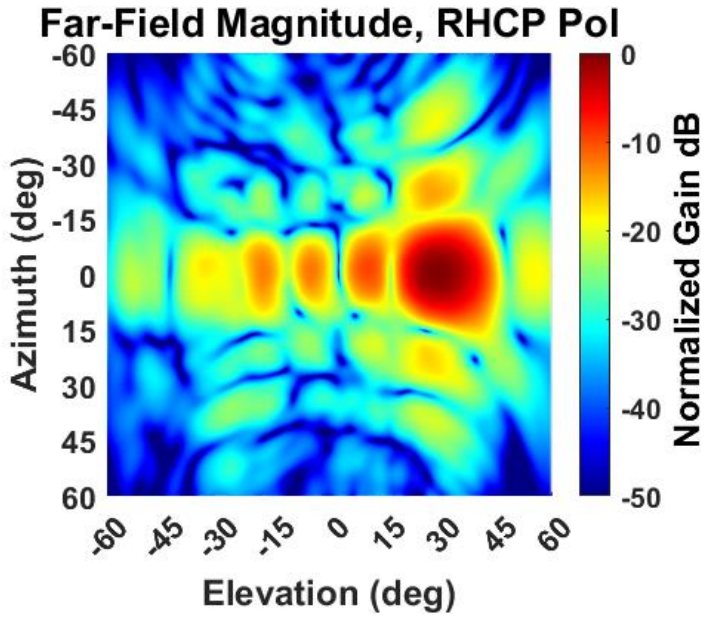

(c)

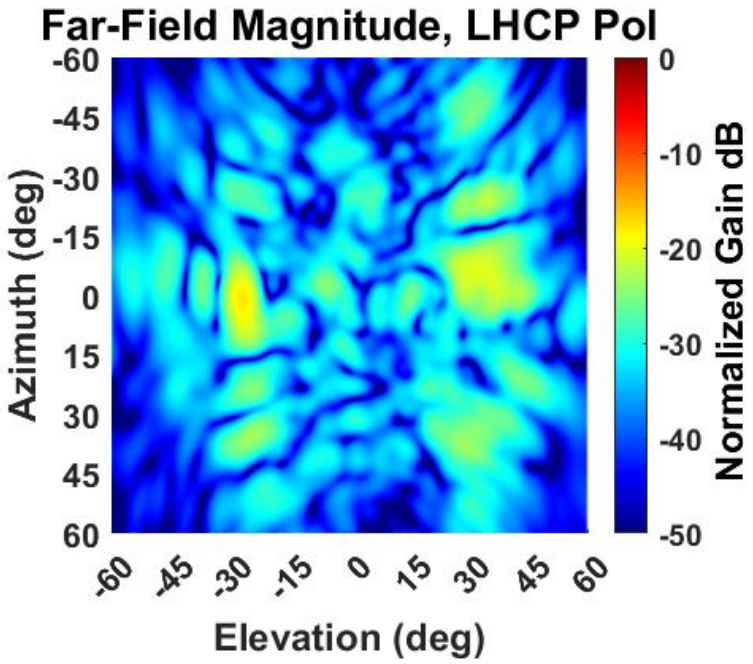

(d)

Fig. 4.22: Magnitude plot at 26.5 GHz in RHCP (a) and (b) broadside, and (c) and (d) 30° scan angle in φ=0° plane.

4.9. G/T and EIRP evaluation and measured results

The brief calculation for the gain over noise temperature of the array (G/T) is as follows:

The system noise temperature of the array is calculated as:

$$T_{system} = T_s + T_{a'} \tag{4.2}$$

$$T_{a'} = \eta_{ant} T_a + T_0(1 - \eta_{ant}) = 269.67+31.9=301.57 \tag{4.3}$$

Scene temperature, $T_a = 303\ K$

Room temperature, $T_0 = 290K$

$$\eta_{ant} = 10^{\frac{-L_{ant}}{10}} = 0.89 \tag{4.4}$$

$L_{ant} = 0.5\ dB$ is Antenna loss that can be found from simulation

$$T_s = T_0(F_s - 1) = 290 * 1.238 = 359.02K \tag{4.5}$$

Noise Figure of the chip is 3.5 dB in Rx mode.

$$F_s = 10^{3.5/10} = 2.238 \tag{4.6}$$

Thus, $T_s = 301.57 + 359.02 = 660.59K$

The gain over noise in LHCP at 26.5 GHz is given as:

$$\frac{G}{T} = G_{ant} - 10\ log_{10}^{(T_{system})} = 23\text{-}28.199 \approx \text{-}5.2\ \text{dB/K} \tag{4.7}$$

Thus, the computed gain over noise temperature (G/T) of the array at 26.5 GHz is $-5.2 dB/K$. The G/T of the array versus frequency for LHCP, shown in Fig. 4.23(a), was measured using the cold-source method [58]. The array was configured for LHCP with a uniform illuminated boresight beam. System gain was estimated using an OEWG probe in the far field and a WR34 standard gain horn. Complex vertical (V) and horizontal (H) measurements using the probe were combined to synthesize CP using $(H \pm jV)/\sqrt{2}$. The gain to temperature (G/T) was calculated to be -6.7 dB/K at 23 GHz and -5.3 dB/K at 26.5 GHz when observing a 303 K scene temperature. It is to be noted that there is an outlier at 25 GHz in measurement results which appeared due to the PNA band change. Therefore, we observe that the measured G/T for LHCP at 26.5 GHz is in good agreement with the calculated results.

The effective-isotropic-radiated-power EIRP of the array per polarization is given by [2]:

$$EIRP_{perPol,P1dB} = 20log_{10}^{(N)} + G_{element} + P_{element,P1dB} \tag{4.8}$$

Where $P_{element,P1dB}$ is the input power for each radiating element per polarization.

The EIRP of the array for circular polarization is given by:

$$EIRP_{LHCP,P1dB} = 20log_{10}^{(N)} + G_{element} + P_{element,P1dB} + 3dB \tag{4.9}$$

$P_{element,P1dB} \approx P_{channel,P1dB} = 9.7dBm$ at 26.5 GHz

Where, $P_{channel,P1dB}$ is the output chip power per channel at P1dB at 26.5 GHz.

$G_{element} = 4.5\ dBi$ is the peak realized gain obtained from the active element pattern of the 8x8 array at 26.5 GHz.

Therefore,

$$EIRP_{LHCP,P1dB} = 20log_{10}^{(N)} + G_{element} + P_{element,P1dB} + 3dB$$

$$= 36dB + 4.5\ dB + 9.7dBm + 3dB = 53.2dBm \qquad (4.9)$$

Therefore, the calculated EIRP at 26.5 GHz is 53.2dBm. Fig. 4.23(b) shows the input DC power versus effective-isotropic-radiated-power (EIRP) and the array gain (normalized to small signal) versus LHCP EIRP in transmit mode. For this test, an open-ended waveguide probe (OEWG) is placed in the far-field with power meters used to measure the input and output levels of the antenna system. A signal generator is used to vary the input signal to the array under CW excitation. We can observe the phased array offers an EIRP of 57.9 dBm and 52.4 dBm at P1dB at 23 GHz and 26.5 GHz, respectively. Therefore, the measured EIRP for LHCP at 26.5 GHz is in good agreement with the calculated results. The slight difference between the measured and calculated EIRPs is due to the loss in transmission lines from the chip output to the antenna input and the adhesive thermal gap filler material employed to attach the aluminum heat sink with the array (Fig. 4.18(b)) to mitigate the heat generated by the chips. We can also observe in Fig. 4.23(b) that the DC power consumption of the array is 55Watts when EIRP is 52.4dB (P1dB) at 26.5 GHz.

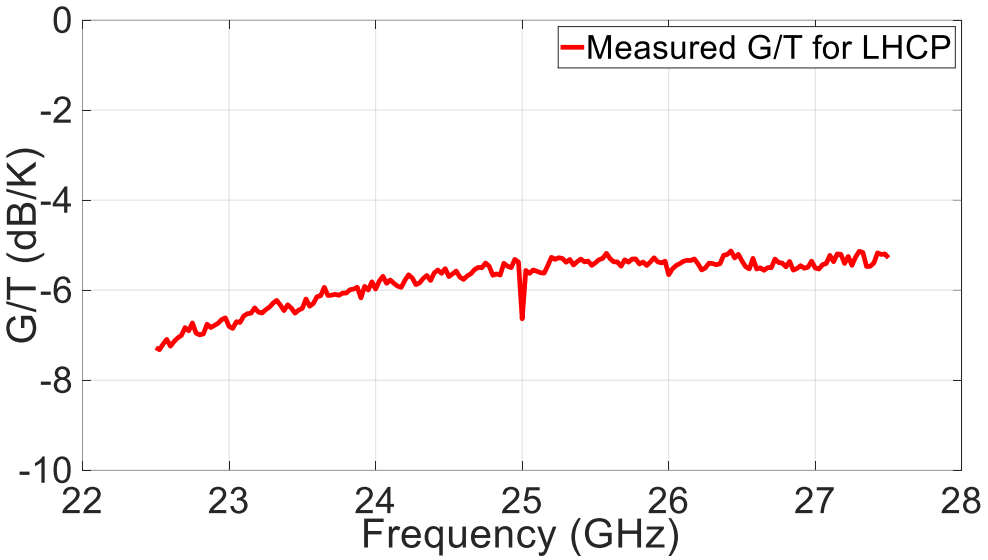

(a)

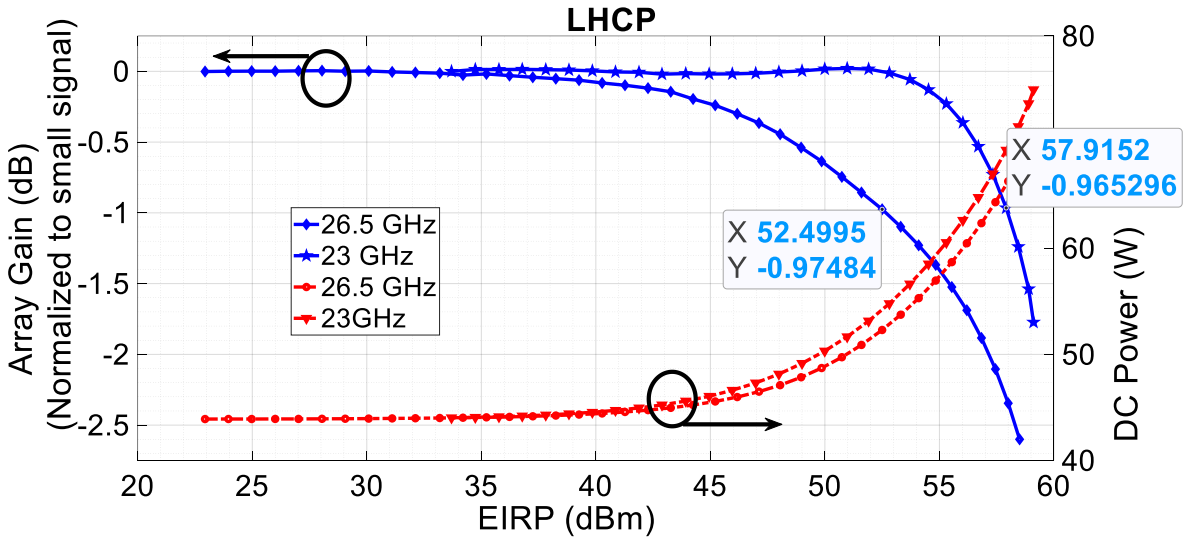

(b)

Fig. 4.23: (a) G/T versus frequency for LHCP, and (b) Measured normalized compression gain versus EIRP and DC input power versus EIRP.

4.10. Beam squint in wideband arrays

Beam squint is an important aspect to discuss in case of a wideband array. Fig. 4.24 presents the measured patterns at 23 GHz, 25 GHz, and 27 GHz, with a progressive phase shift adjusted to scan at -28^0 for 25 GHz. We can see that the beam scans at -30^0 for 23 GHz and -25^0 at 27 GHz for same progressive phase shift. The squint angle θ at frequency f is predicted from the following formula.

$$\sin(\theta) = \frac{f_0}{f}\sin(\theta_s) \tag{4.10}$$

where θ_s is the phased-array scan angle at f_0.

Therefore, as the peak radiation angle changes with frequency, phased array without time-delay correction at the element or subarray levels, has the inherent issue of beam squint.

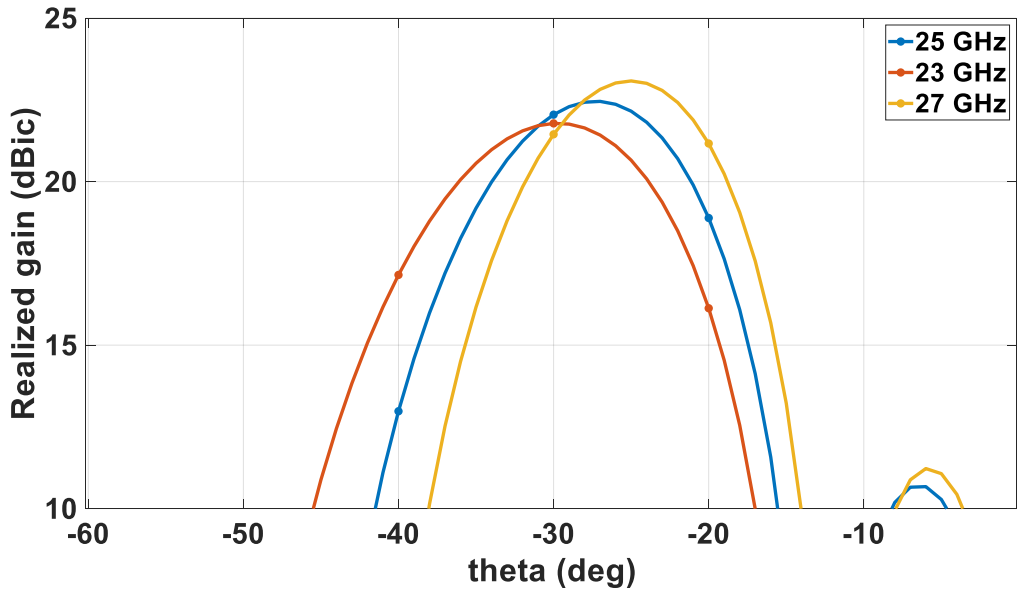

Fig. 4.24. Beam squint in wideband array.

But *K/Ka*-band SATCOM channel bandwidth do not exceed 400 MHz while centered at different frequency at a time, and the beam squint in a 400 MHZ range is not significant.

4.11. Conclusion and Future Study

A wideband (22-28 GHz), flat panel, polarization reconfigurable Tx/Rx phased array antenna with uniquely arranged novel radiating elements is explored which can find applications in CubeSat and 5G communications. The array is comprised of novel radiators that provide excellent isolation between the two ports, and the array has utilized the 6-bit phase control capability of the beamforming chip extensively to offer multiple benefits like polarization reconfiguration, mirror arrangement in the dual linear case and, sequential arrangement in the dual CP case. In the simulation study, the array scans to Θ=±56° at the lower end of the band and to Θ=±42° at the upper end of the band for all four polarizations, considering 3dB scan loss/gain drop. Low cross-polarized fields and AR below 3dB is achieved over the entire bandwidth and for all the scan angles to the 3dB gain drop point. The array can scan further if the 3dB gain drop criteria is relaxed, although we limited our study considering 3dB gain drop and 3dB AR criteria. The simulated analysis performance is validated using a planar near-field measurement for all four polarizations over the bandwidth, including radiation patterns, and AR performance. Also, the *G/T* in receive mode and EIRP in transmit mode is presented. Though we have presented the uniform excitation cases only, the 5-bit gain control capability of the chip can be employed for non-uniform excitation applications as well. The array can be scaled to other frequencies and chips can be selected accordingly. Thus, undoubtedly, this array is versatile and highly applicable to advanced communication systems.

Chapter 5

Dual Circular Polarized (RHCP/LHCP) Dual (Ku/K-) Band Shared Aperture Feed Source with Common Phase Center for an Offset Reflector Antenna

5.1. Introduction

SATCOM employs reflector antennas with circularly polarized feed sources at their terminals for high directivity and relatively low cost [59]-[61]. SATCOM requires two independent far-off bands for the transmit (Tx) and receive (Rx) applications. Therefore, if a feed can be designed in such a way that the field strength at the edge of a reflector relative to that at the vertex due to the radiation pattern of the feed is same for two widely separated frequency bands, a same reflector can serve for transmitting and receiving in SATCOM applications. In [8] a linear polarized metallic EBG dual-band antenna with higher frequency 1.5 times of the lower frequency, suitable as a feed of a reflector with a focal-length-to-diameter (f/d) ratio of 1.2, is proposed for spatial applications. In [62], a dual-band dual-polarized feed for a symmetrical single-reflector antenna is proposed where reflector has a focal length to diameter ratio of 0.25.

The basic principles of Fabry-Perot cavity (FPC) antenna, comprised of a partially reflective surface (PRS) placed at a predetermined height above the primary radiator, was elaborately explained in [63]-[66]. Fig.5.1 shows the flow chart of parametric study of the PRS structure [66]. This work [66] presents a detailed parametric study for PRS height, thickness and dimensions, and proposed a lucid guideline for the PRS selection through the given flow chart. FPC antenna is explained as a leaky wave antenna in [67] and [68]. FPC based dual-linear polarized sparse array was proposed in [7], where the inter-element spacing for the sparse array is computed from the element pattern minimum for the element in FPC.

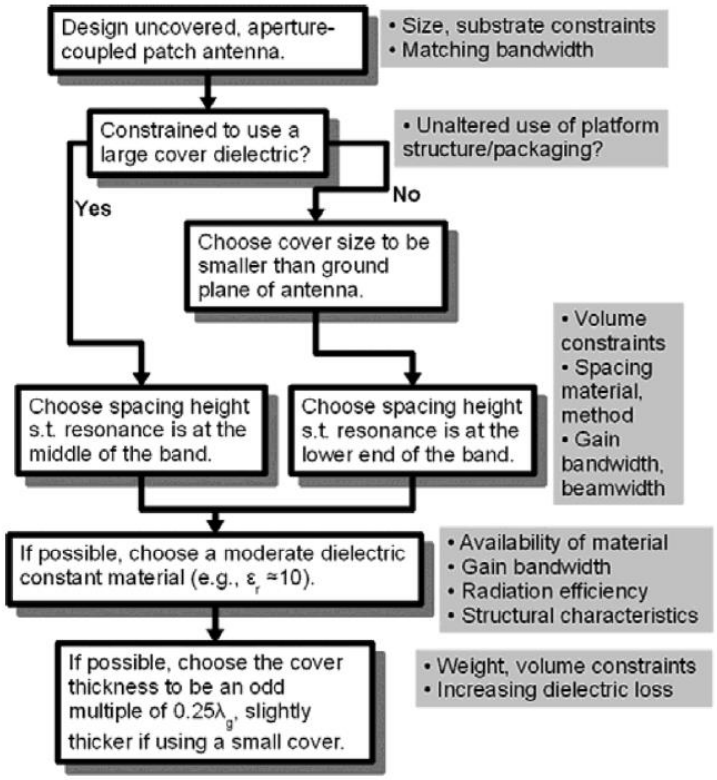

Fig. 5.1. A flow chart for parametric study of PRS structure [66].

Based on the concept of array thinning proposed in [7], here, a right hand circular polarized (RHCP) 2x2 sparse array is designed inside a Fabry-Perot cavity (FPC) for Ku- (14.2-14.8 GHz, with center frequency f_L=14.5GHz) band with a single layer PRS as a superstrate. A conventional left hand circular polarized (LHCP) 2x2 K- (25-26 GHz with center frequency f_H=25.5 GHz) band array is designed on the same substrate layer with same phase center as the Ku-band array, as shown in Fig. 1. The single element for both frequency bands is microstrip line fed corner truncated circular polarized patch antenna derived from opposite corner truncations of a square patch [1]. The well-known technique of sequential rotation [56] is applied to achieve a considerable axial ratio (AR) bandwidth at both Ku- and K-bands. The dual band (f_L:f_H=1:1.8) arrays with overlapping apertures is designed in such a way that the feed is suitable for an offset parabolic reflector of f/d ratio of 1.5. Preliminary study results of the dual band dual circular polarized feed for a parabolic reflector is presented in [69].

Ideally in case of a purely circularly polarized feed, the offset parabolic reflector is not supposed to depolarize the signal, rather a beam squint is observed in plane perpendicular to the offset plane [59]-[61]. But the cross-polarized fields of the feed within the -10dB beamwidth of the radiation pattern for both the bands has to be minimized to get best performance, the reflector f/d being selected considering 10dB gain drop from the vertex till the edge of the reflector for both bands. Different types of defected ground structures have been explored as an effective way to mitigate high cross-polarization in [70]-[72]. Further, a cross-shaped defected ground structure (CSDGS) is incorporated in both Ku- and K-band structures for improvement of cross-polarized fields [see Fig. 5.1].

Therefore, the novelty of this work is in the technique of designing a RHCP/LHCP dual band feed for two far-off bands (f_L:f_H=1:1.8) with same phase center and controlled cross-polarized fields and sidelobes while the half edge illumination beamwidths (usually -10dB beamwidth) for both the bands remain similar.

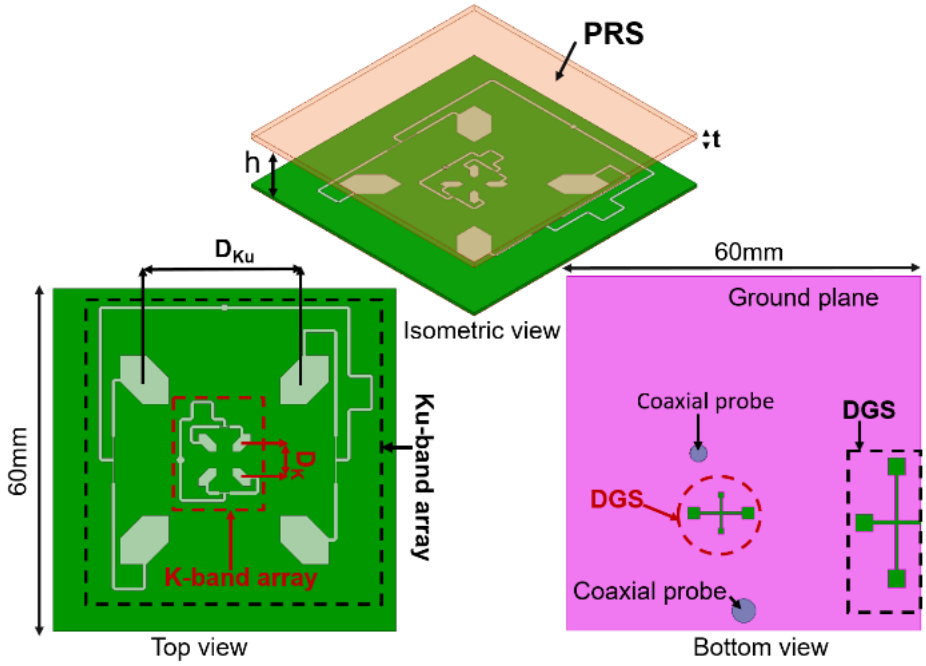

(a)

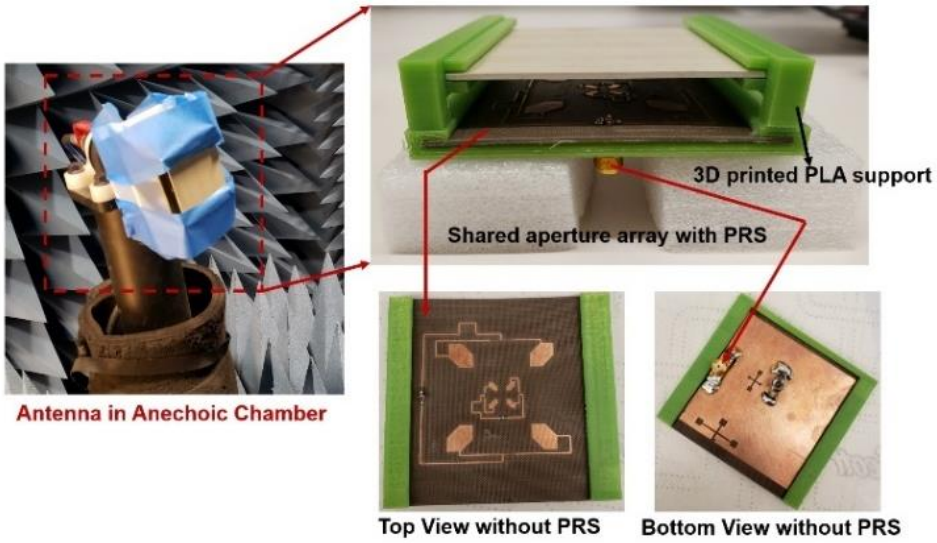

(b)

Fig. 5.2. (a) Configuration of the two shared-aperture arrays at Ku- and K-band with overlapping apertures inside FPC, and (b) Fabricated prototype in anechoic chamber.

5.2. Design Principle

The FPC height is approximately determined by $h = n\lambda/2$, where n is an integer, and λ is the free space wavelength at the resonant frequency of the primary radiator [63]. Therefore, the same height of the PRS is applicable for a primary radiator at Ku-band (say, 14 GHz) when n=1, and a primary radiator at Ka-band (say, 28 GHz) when n=2.

For a fixed beam broadside array [2], the grating lobes appears at $\theta = \pm 90^0$ when interelement spacing (D) approaches unity, and sidelobe level (SLL) increases. The position of the first grating lobes of the array factor for a fixed beam broadside array is given by $sin\,\theta_{GL} = \lambda/D$. Grating lobes can be reduced significantly if the D is chosen in such a way that θ_{GL} occurs at element pattern minimum. Since $sin\,\theta_{GL}$ is an increasing function, larger D can be chosen if the first null beamwidth of the element pattern can be decreased which in turn indicates increase in directivity. Therefore, the PRS helps in directivity enhancement [65]

which offers the flexibility to choose *D* comparable to or more than a wavelength to design a 2x2 sparse array at Ku-band, as shown in Fig. 5.1.

The most important parameter for a reflector antenna is the f/d which is usually governed by the -10dB half edge illumination of the feed source. Therefore, the dual band feed has to be designed in such a way that the field strength at the edge of a reflector relative to that at the vertex due to the feed radiation pattern is same for both the bands. Approximately same -10dB beamwidth can be achieved only when the directivity is identical for both bands. But if we choose 14-15 GHz bandwidth for n=1 ($h = n\lambda/2$) for FPC, n=2 happens at 28-30 GHz range which provides higher directivity and reduced beamwidth. Therefore, we have selected a frequency range of 25-26 GHz (K-band) which provides similar directivity profile as 14-15GHz range in the FPC. Thus, we choose approximately f_L:f_H= 14.5: 25.5 =1:1.8 for best performances.

Theoretically, the thickness of PRS should be odd multiple of $0.25\lambda_g$ for best performance, where λ_g is the wavelength in the dielectric [61]. But here, the thickness is selected such that almost same directivity profile can be obtained for both the bands and must be an available thickness in data sheet of the chosen material.

This concept can be utilized for any two far-off ($\approx 1:n$, since $h = n\lambda/2$, where n is any integer) bands for Tx and Rx purpose in SATCOM applications, subject to judicious choice of PRS height (h), material and thickness. It can be noted that, though this concept is valid for $n \geq 2$, but it may be more challenging to choose proper f/d when $n > 2$. Moreover, best performance can be achieved if Tx and Rx bands are in 1: 1.8 (f_L:f_H=1:1.8) ratio instead of 1:2.

5.3. Single Element Radiation Pattern

The normalized radiation pattern of a microstrip line fed circular polarized corner truncated patch antenna at Ku-band with and without superstrate is shown in Fig. 5.2. The substrate is a 30mil thick Arlon 250A of permittivity ε_r =2.5, and Rogers TMM10 (ε_r =9.2) of thickness

1.27 mm is chosen as a PRS material (discussed in next section with reference to Fig. 5.5). In FPC, the element pattern null is at 68^0 at 14 GHz, and the corresponding D is found to be approximately 23.2 mm which is almost 1.1 times the free space wavelength at 14 GHz. But in order to achieve same phase center for both the arrays, we have chosen D = 25 mm to accommodate the K-band array at the center of the Ku-band array, as shown in Fig. 1. D could be further increased by choosing a PRS material of higher permittivity or increasing the number of layers [69].

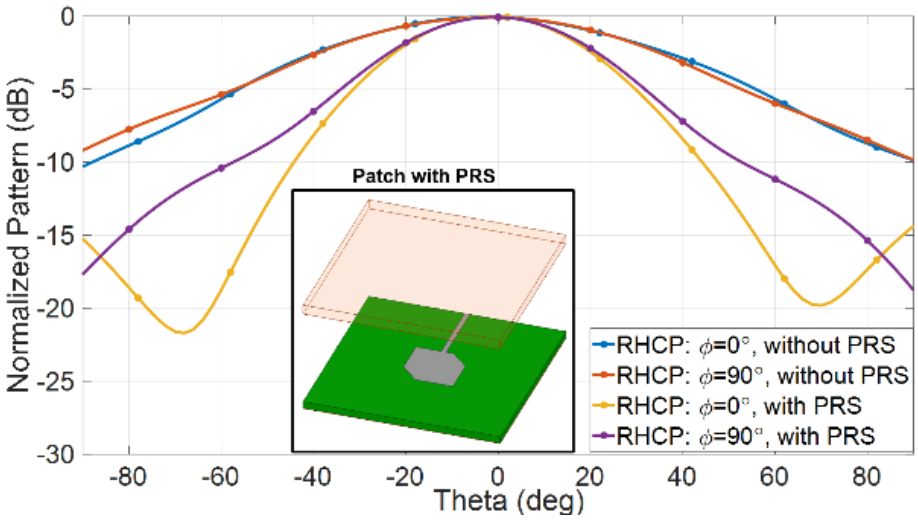

Fig. 5.3. Single element normalized radiation pattern of a circular polarized corner truncated patch antenna at Ku-band with and without PRS.

5.4. Shared Aperture Arrays

In the next step, FPC based sequentially rotated RHCP 2x2 sparse array with interelement spacing, D_{Ku}=25 mm [see Fig. 5.3] is designed at Ku-band and a sequentially rotated 2x2 K-band LHCP conventional array with interelement spacing of D_K=6 mm (half free space wavelength at 25 GHz) is designed on the same substrate at the center of the Ku-band array. Therefore, it is clear that the Ku-band array and the K-band array has overlapping apertures

or in other words they have shared apertures with a same phase center. Fig. 5.3(a) shows the reflection coefficient magnitude for Ku- and K-bands. Figs. 5.3(b) and (c) shows the axial ratio and gain versus frequency for Ku- and K-bands. Considering impedance mating equal or below -10dB along with the 3dB axial ratio criteria, the array offers a bandwidth of 14.1-14.8 GHz in Ku-band and 25.4-26 GHz in K-band. The normalized radiation pattern of the Ku-band (14.5GHz) and K-band (25.5 GHz) arrays are shown in Figs. 5.3(c) and (d), respectively, and we can observe that separation between co- to cross-polarized fields is not better than 10dB in both the cases, which is mainly due to the extensive feed structure. The cross-polarized fields are more prominent and asymmetrical in K-band. As discussed earlier, cross-polarized fields should be significantly low within -10dB beamwidth of the feed source for reflector applications. Therefore, we have introduced a CSDGS, as shown in Fig. 5.1, which helps to improve cross-polarized fields by a significant amount.

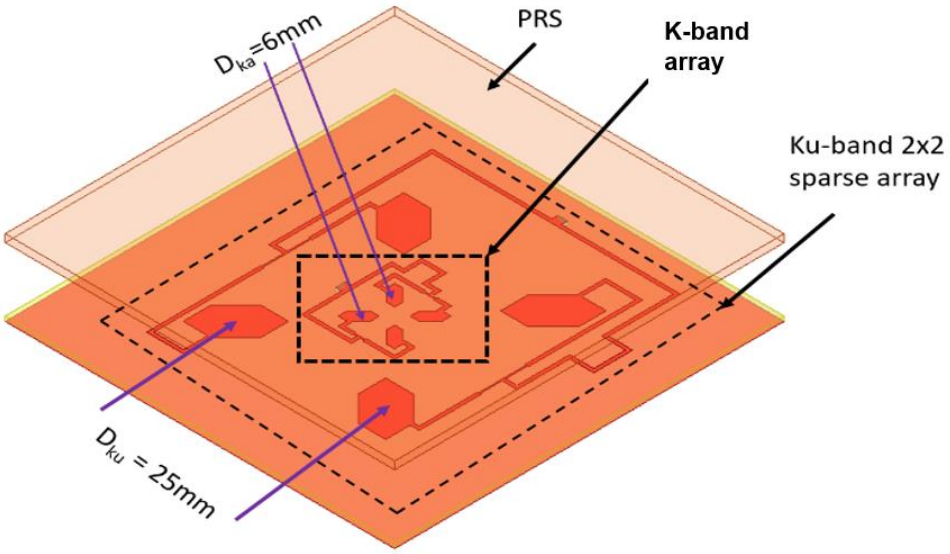

(a)

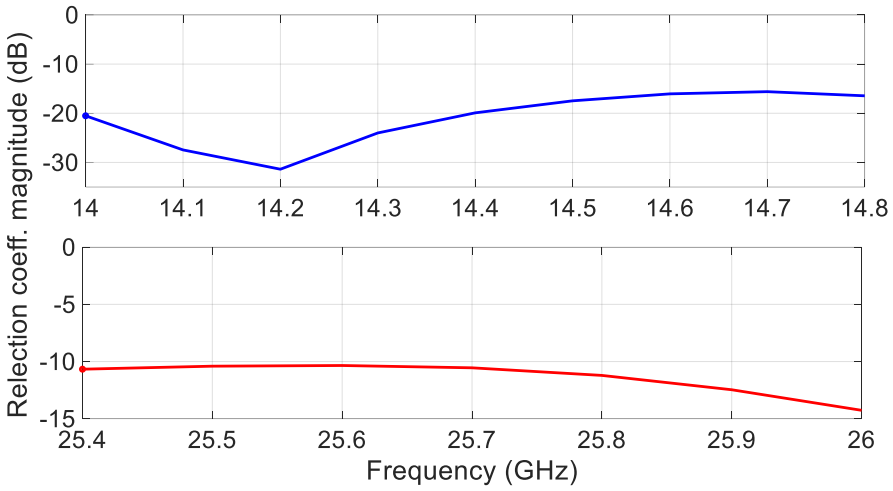
Relection coeff. magnitude (dB)
0
-10
-20
-30
14
14.1
14.2
14.3
14.4
14.5
14.6
14.7
14.8
0
-5
-10
-15
25.4
25.5
25.6
25.7
25.8
25.9
26
Frequency (GHz)

(b)

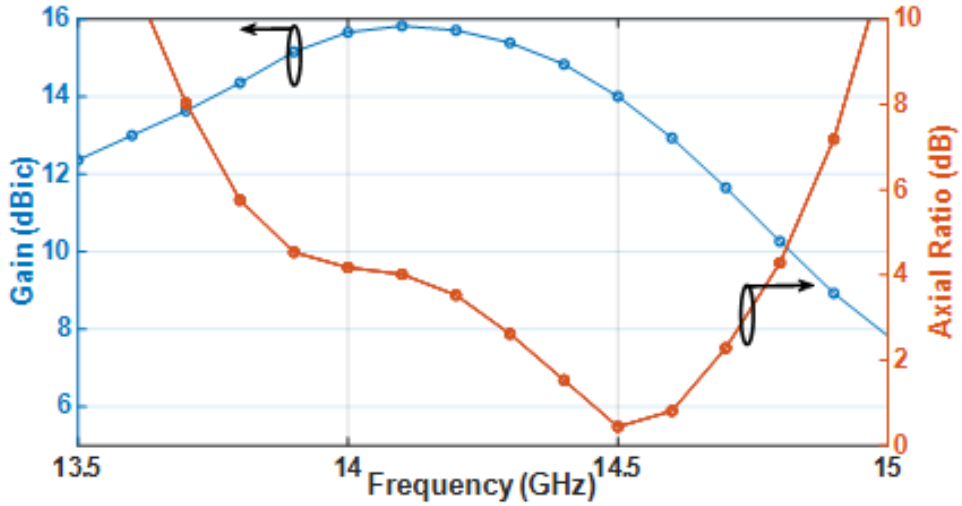
Gain (dBic)
Axial Ratio (dB)
16
14
12
10
8
6
10
8
6
4
2
0
13.5
14
14.5
15
Frequency (GHz)

(c)

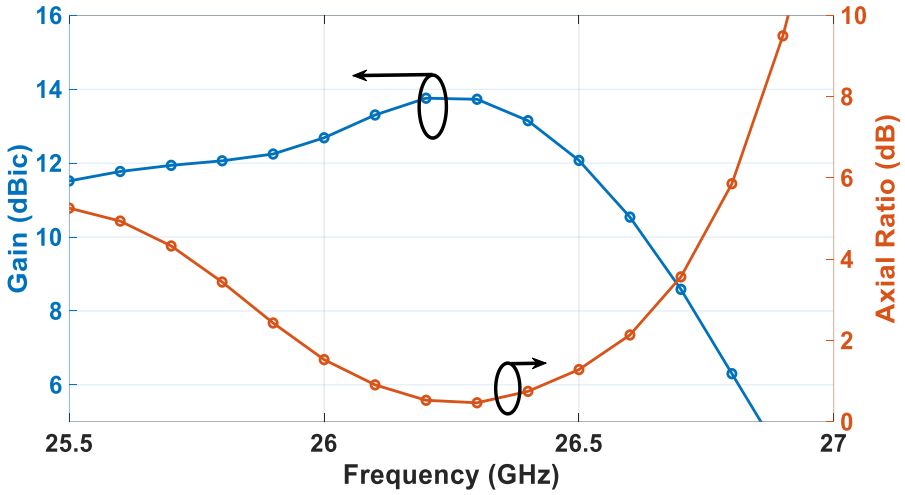
Gain (dBic)
Axial Ratio (dB)
Frequency (GHz)
16
14
12
10
8
6
10
8
6
4
2
0
25.5
26
26.5
27

(d)

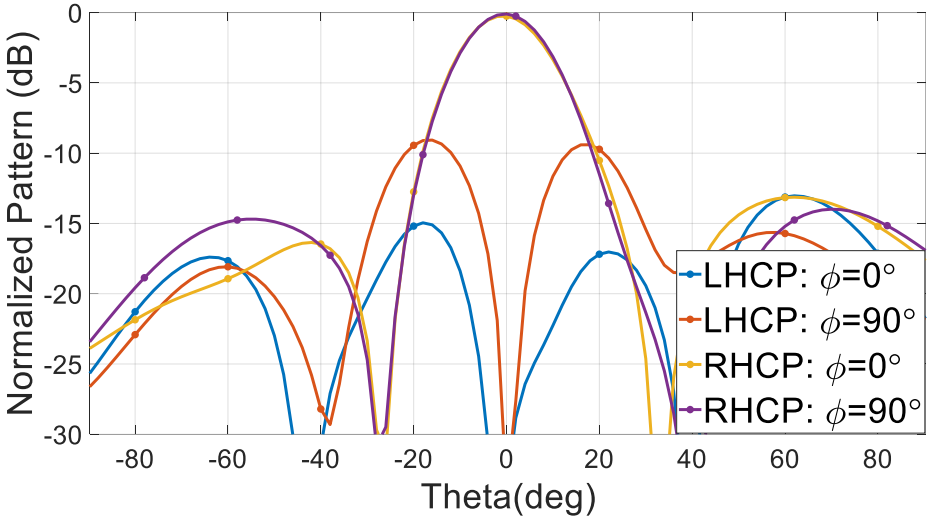
Normalized Pattern (dB)
Theta(deg)
0
-5
-10
-15
-20
-25
-30
-80
-60
-40
-20
0
20
40
60
80
LHCP: ϕ=0°
LHCP: ϕ=90°
RHCP: ϕ=0°
RHCP: ϕ=90°

(e)

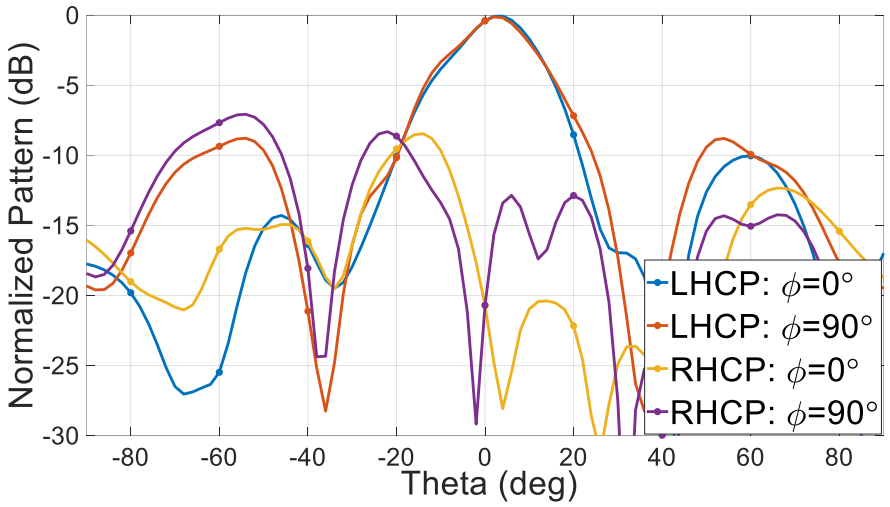

(f)

Fig. 5.4. (a) Configuration of the shared aperture array, (b) Magnitude of reflection coefficient, broadside gain and AR for (c) Ku-band array, (d) Ka-band array, and broadside radiation pattern at (e) 14.5 GHz, and (f) 25.5 GHz.

5.5. Shared aperture arrays with CSDGS

A CSDGS is introduced for both Ku- and K-band arrays as shown in Fig. 5.1. The optimized dimensions of the CSDGS at Ku- and K-bands are shown in Fig. 5.4(a), where, L_{Ku1}=16 mm, L_{Ku2}=8 mm, L_{K1}=7.2mm, L_{K2}=5.2 mm, w_{Ku1}=0.6 mm, w_{Ku2}=0.6 mm, w_{K1}=0.6 mm, w_{K2}=0.5 mm, a_{Ku1}=3 mm, a_{Ku2}=3 mm, a_{K1}=2 mm, a_{K2}=1 mm, b_{Ku1}=3 mm, b_{Ku2}= 3 mm, b_{K1}=2 mm, and b_{K2}=1 mm. The optimized dimensions of the corner truncated patches are shown in Fig. 5.4(b), where L_{ku}=8.6 mm, L_k=3.2 mm, l_{ku}=4.6 mm, and l_k=1.3 mm. Rogers TMM10 (ε_r =9.2) is chosen as a PRS material and a parametric study for directivity versus frequency for different available thickness (t in Fig.5.1(a)) is presented in Fig. 5.5. It is evident that directivity varies from 13-15dBic for both the bands for a PRS thickness of 1.27mm. The fabricated prototype in anechoic chamber along with the top and bottom view of the shared aperture array

without PRS and side view with PRS is shown in Fig. 5.1(b). The overall dimension of the structure is 60 mm x 60 mm x10.7 *(h)* mm. During the fabrication of the structure, we had taken the substrate dimension slightly larger than the ground plane (GP) to accommodate a 3D printed support made of PLA to hold the substrate and superstrate at the predetermined separation and integrate the two pieces, as shown in Fig.5.1(b). We have verified the simulation results considering the PLA structure and found that the PLA support has no mention worthy effects on the antenna performance.

The simulated and measured magnitude of input reflection coefficients, and AR for both Ku- and K-band arrays is shown in Figs. 5.6(a) and (b) respectively. We can see that, considering the 3dB AR criteria, the array covers a 14.2-14.8 GHz in Ku-band and 25.1-26 GHz in K-band. The measured and simulated normalized radiation patterns at 14.5 GHz and 25.5 GHz are shown in Figs. 5.6(c) and (d), respectively. The Ku-band array is designed to work in RHCP and K-band array is designed to work in LHCP. The separation between co-to cross polarized fields has improved to 20dB after the use of CSDGS and SLL is better than -15dB.

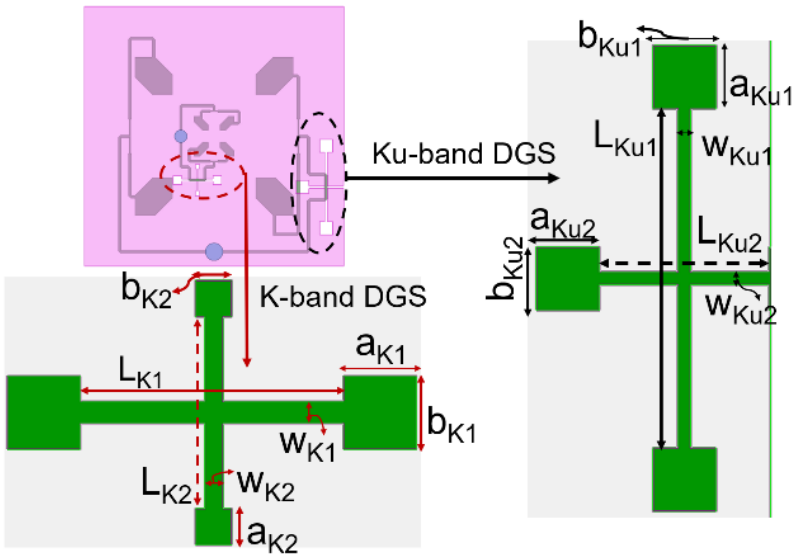

(a)

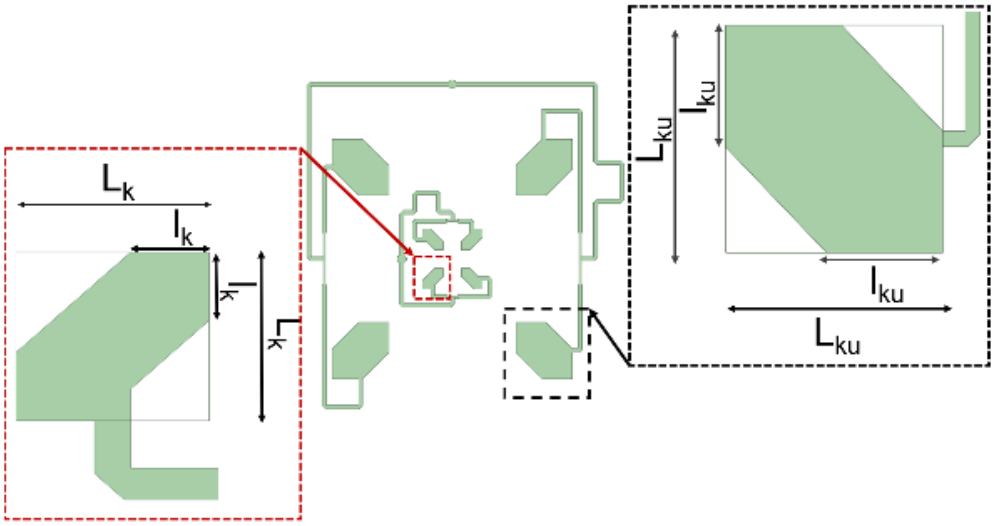

(b)

Fig. 5.5. (a) Bottom view of the GP with zoom in view of the CSDGS along with dimensions, and (b) the top view of the Ku- and Ka-band arrays with zoom in view of the truncated patches at Ku- and Ka-band along with patch dimensions.

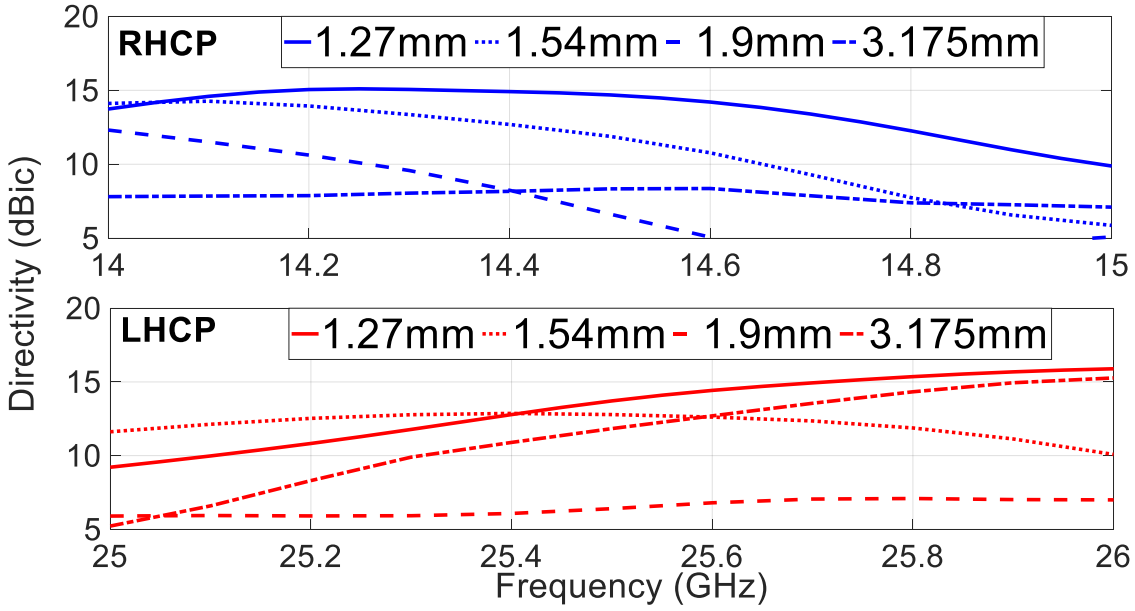

Fig. 5.6. Directivity versus frequency for different values of PRS thickness '*t*' for Ku- and K-band.

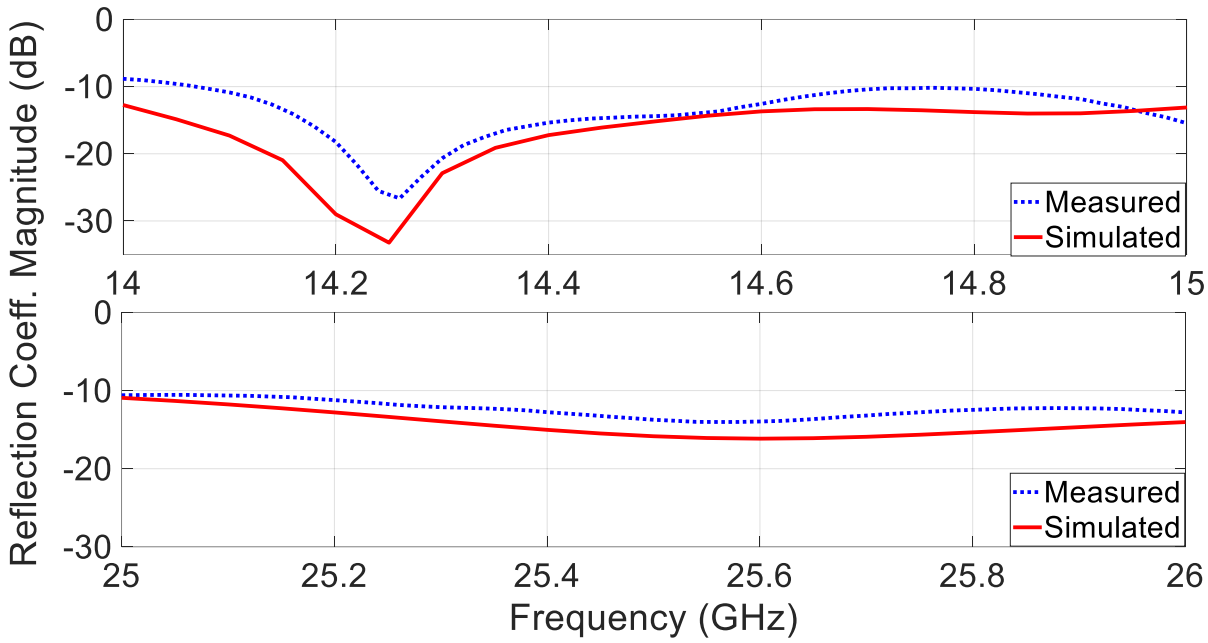
Reflection Coeff. Magnitude (dB)
0
-10
-20
-30
14
14.2
14.4
14.6
14.8
15
Measured
Simulated
0
-10
-20
-30
25
25.2
25.4
25.6
25.8
26
Measured
Simulated
Frequency (GHz)

(a)

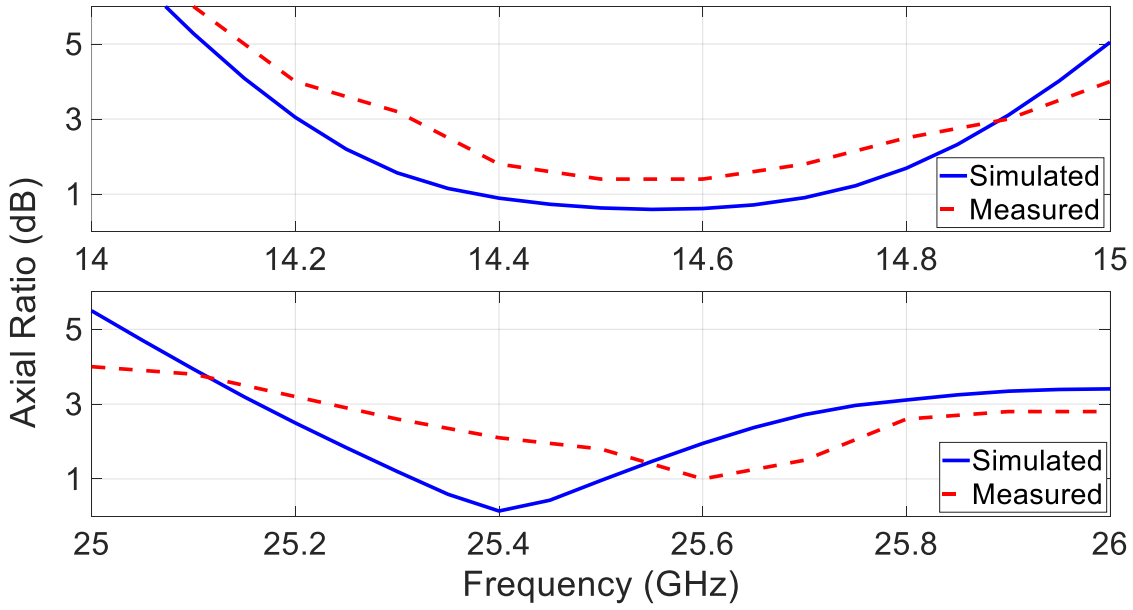
Axial Ratio (dB)
5
3
1
14
14.2
14.4
14.6
14.8
15
Simulated
Measured
5
3
1
25
25.2
25.4
25.6
25.8
26
Simulated
Measured
Frequency (GHz)

(b)

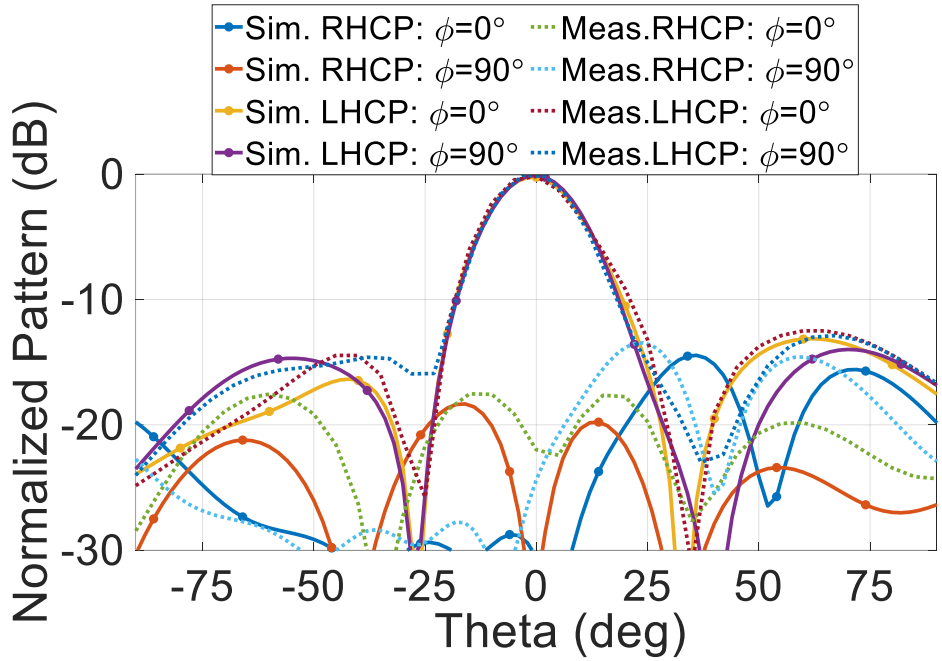

(c)

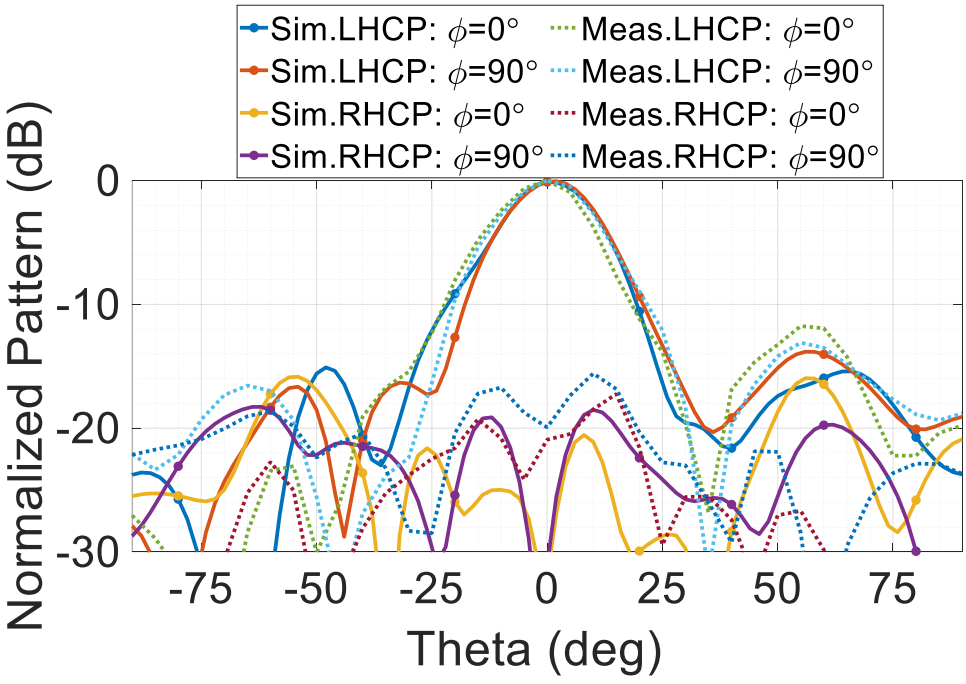

(d)

Fig. 5.7. Simulated and measured (a) Magnitude of reflection coefficient at Ku-band and Ka-band, (b) AR versus frequency at Ku-band and K-band, and radiation patterns at (c) 14.5 GHz, and (d) 25.5 GHz.

The physical insight of the cross-polarization mitigation by deploying a CSDGS can be explained from the comparison of the vector current distribution of the GP shown in Fig. 5.7 for K-band structure at 25.5 GHz with and without CSDGS. In the case of the GP without CSDGS, it is observed that along with LHCP, less strong RHCP is developed which is the source of cross-polarized fields. When the CSDGS is introduced, the RHCP is weakened by a significant amount which reduced cross-polar field. The same explanation applies for Ku-band as well, but not shown here for the sake of brevity.

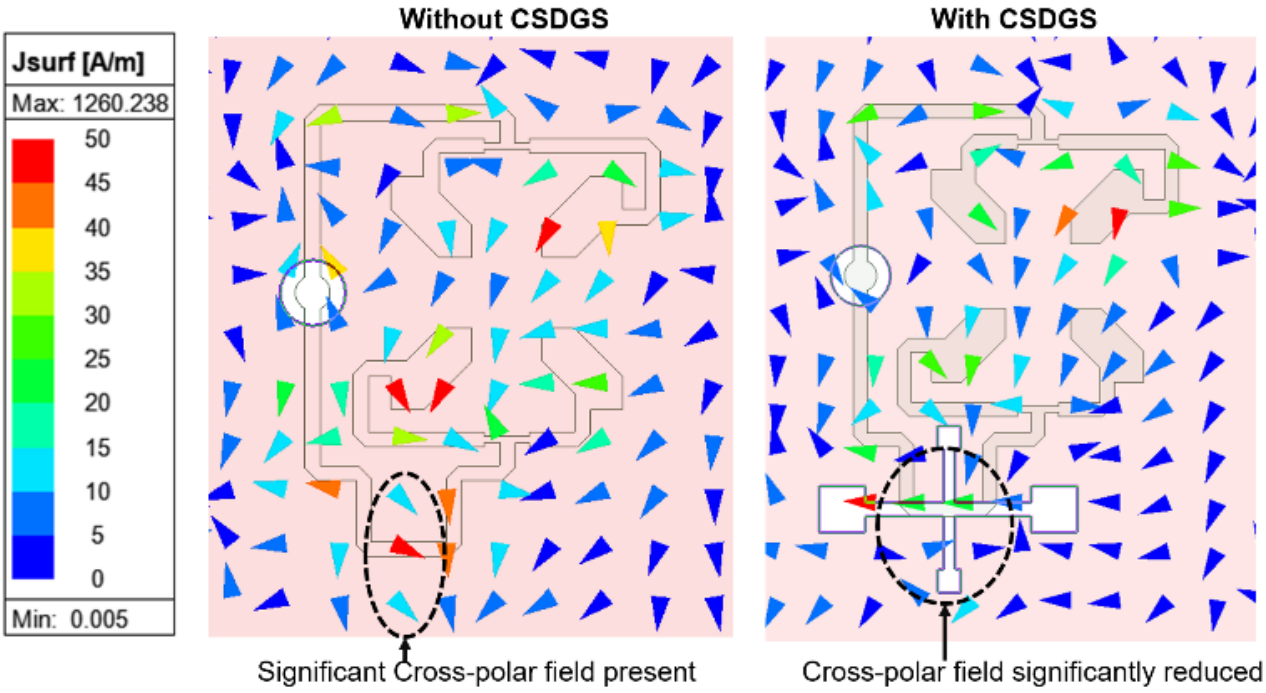

Fig. 5.8. Comparison of current distribution of the GP for with and without CSDGS for Ka-band array (bottom view).

Cross polarization may be further improved by designing the feeding network on a substrate below the ground plane and feeding the patches by vias, but that will cause back radiation which will show up as spill over in reflector pattern. A multi-layered stripline based feed structure with ground vias and feed vias can provide significant performance improvement, but the structure will be complicated for fabrication.

5.6. Shared aperture array as a feed of an offset parabolic reflector

We can observe from Figs. 5.6(c) and (d) that the 10dB beamwidth at both Ku- and K-band arrays is approximately $\varphi_0 = 18^0$ which is suitable as a feed source for an offset parabolic reflector of f/d=1.5 as calculated from the equation for offset parabolic reflector given in [12]. Also, the feed source has to be directed toward the center of the offset reflector from the focal axis by an angle of approximately $\varphi_f = 18^0$ as calculated from [12]. We have chosen a reflector with d=50cm which is almost 24λ at 14GHz and 42λ at 25 GHz. The beam squint calculated from [1] is only 0.03^0 and 0.02^0 at Ku- and K-band respectively. The configuration of offset parabolic reflector along with the feed source is shown in Fig. 5.8(a). A f/d versus beamwidth and feed angle versus beamwidth for an offset parabolic reflector is shown in Fig. 5.8(b). Figs. 5.8(c) and (d) show the radiation patterns at 14.5 GHz, and 25.5 GHz, respectively, for the shared aperture arrays placed at the focal point of the offset parabolic reflector.

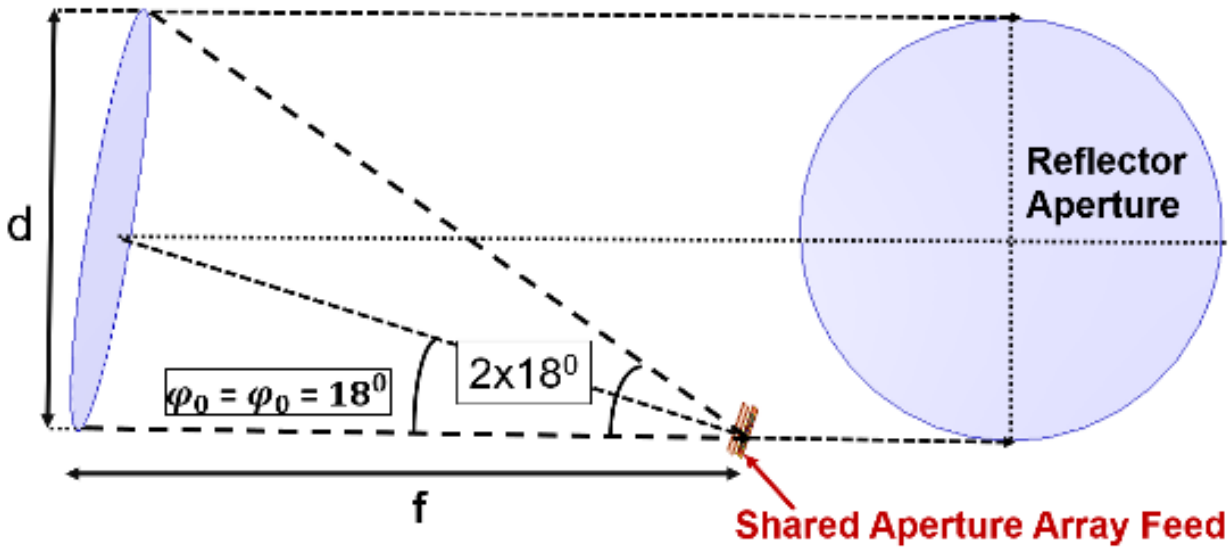
d
Reflector
Aperture
$\varphi_0 = \varphi_0 = 18^0$
2x18^0
f
Shared Aperture Array Feed

(a)

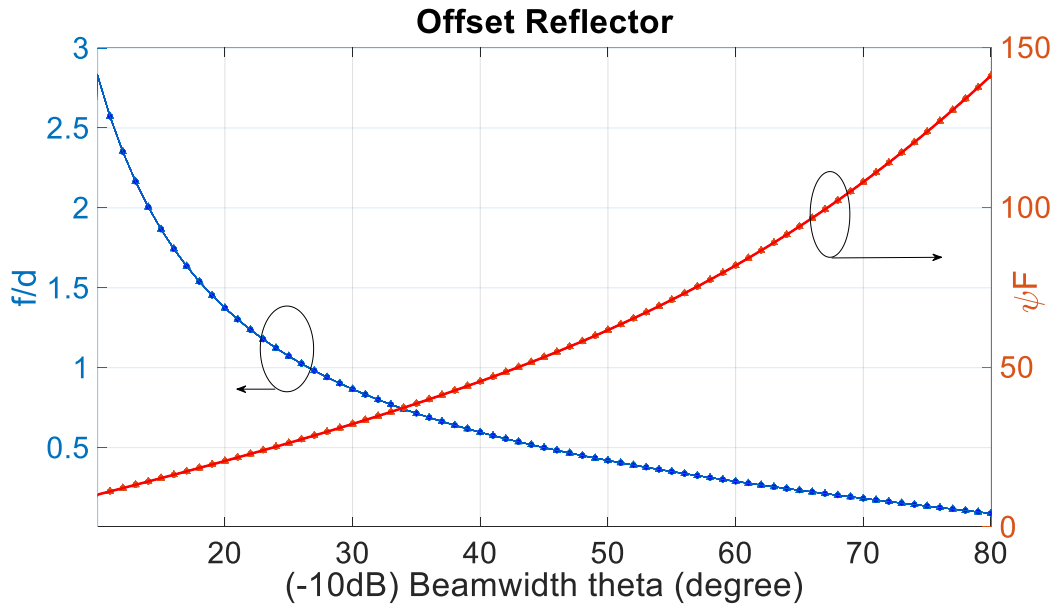
Offset Reflector
f/d
ψF
(-10dB) Beamwidth theta (degree)
3
2.5
2
1.5
1
0.5
150
100
50
0
20
30
40
50
60
70
80

(b)

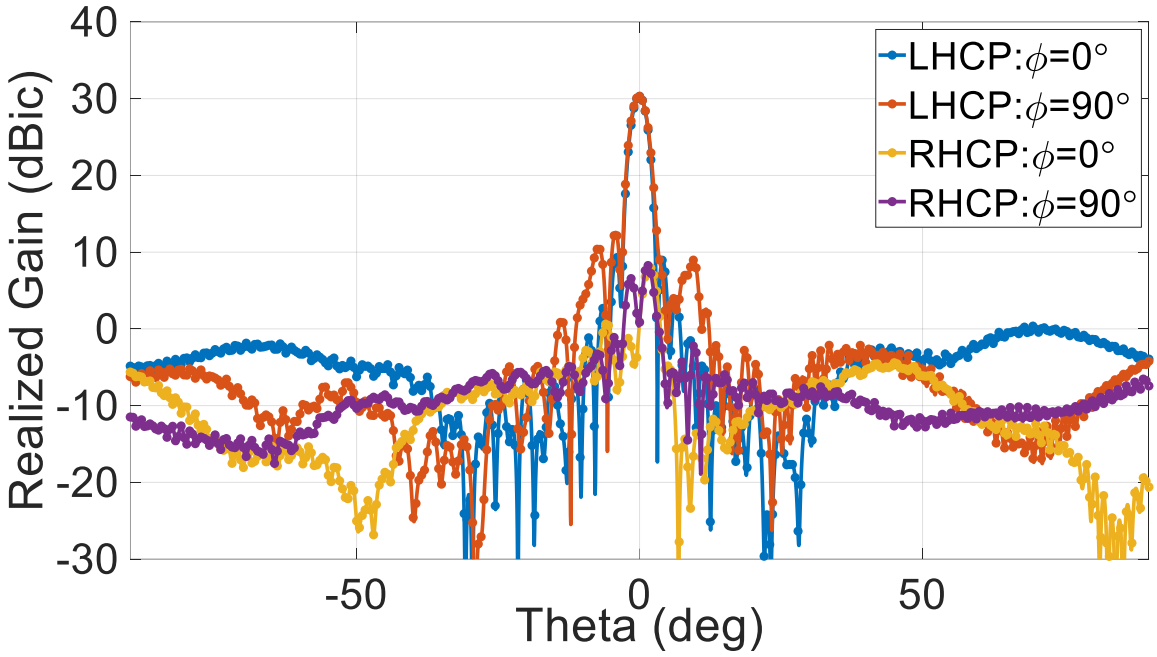

(c)

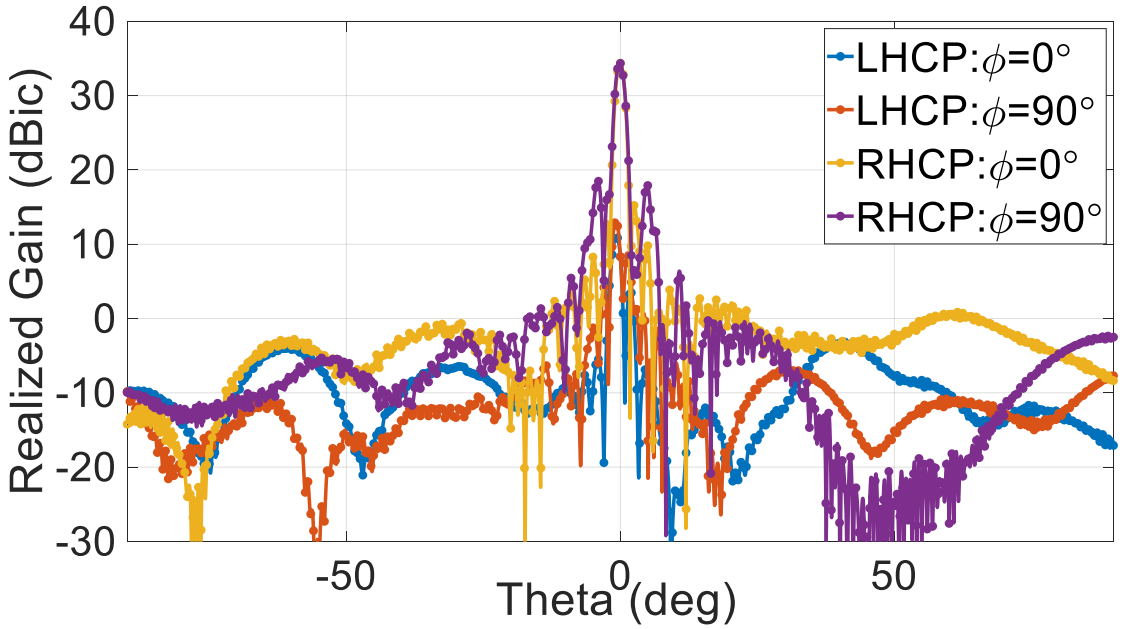

(d)

Fig.5.9. (a) Configuration of the offset reflector with shared aperture array at focal point, (b) f/d and feed angle versus frequency, and radiation pattern at (a) 14.5GHz, and (d)25.5 GHz.

We have achieved a peak gain of 30 dBic at 14.5 GHz, and 35 dBic at 25.5 GHz, with peak co-cross polarization separation being better than 20dB and SLL level almost -20dB below the peak gain for both bands. It is worth mentioning that reflector reverses the sense of rotation, and hence we can observe LHCP at Ku- and RHCP at K-band.

5.8. Conclusion

Here, a dual band (f_L:f_H =1:1.8) circular polarized feed design for reflector (with f/d=1.5) planned for SATCOM applications, is proposed. Grating lobes has been suppressed by element pattern minimum and the arrayed elements are located at a distance larger than the free space wavelength in FPC at Ku-band. The K-band is chosen as the higher band instead of Ka-band so that the half edge illumination is same for both the bands. The K-band array with interelement spacing of half wavelength is designed on the same substrate so that both Ku- and K-band arrays have same phase center. A CSDGS is employed at both the bands to improve cross-polarized fields. The feed structure is fabricated and tested for its impedance matching and radiation pattern. The concept can be applicable for any two far-off (= 1: 1.8) bands for Tx and Rx purpose, subject to proper choice of PRS height, material, and thickness.

Chapter 6

Conclusion and Future Work

7.1. Conclusion

For satellite communications (SATCOM), battlefield applications, 5G communications and different other developing technological applications, the phased array antennas (PAAs) are preferred over mechanical scanning antennas. PAA can radiate ample amount of microwave power in an intended direction to accomplish system link requirements and the beam can be electronically scanned instantaneously. The recent developments of commercial silicon beamforming chipsets has increased the flexibility of phased array antennas. The fully integrated chipset discards the need for discrete transceiver blocks and employs a transmit/receive (T/R) switch, low noise amplifier, power amplifier, phase shifters, and variable attenuators. Moreover, the fully integrated chipset reduces overall size, cost, and RF losses. This doctoral research presents the design and development of two different wideband dual linear/dual circular polarized Phased Array Antennas with integrated beamforming network using 5G Silicon RFICs for two different applications.

In the first research project, a 4x2 wideband, dual linear polarized phased array antenna, comprised of intuitively shaped all metallic radiators with an overall cross-section of $\lambda/2 \times \lambda/2$ and height nearly equal to $\lambda/2$ corresponding to the center frequency (9.5 GHz), working also as heat sink, is presented for X-band (8.5-11.5 GHz) applications. The peak broadside gain is varying between 11-14 dBi over the bandwidth. Peak gain varies from 12.8-12.5 dBi at 9.50 GHz as beam scans till ±45° in $\varphi=0^0$ plane and ±30° in $\varphi=90^0$ plane. The 4x2 antenna aperture is 3D metal printed, and the beamforming network, consisting of Anokiwave RFICs, is integrated with the antenna aperture. The temperature reduction of 60°C is obtained using this heat sink antenna structure, which is also validated with an infrared (IR) camera.

This second project is based on requirements derived from a National Aeronautics and Space Administration (NASA) Glenn Research Center (GRC) mission concept for an orbiting lunar relay providing persistent connectivity to the lunar south pole. A flat panel 8x8 phased array with radio frequency integrated chips (RFIC) based beamforming network, is proposed. The array works in dual linear in addition to dual circular polarizations over a bandwidth of 22-28 GHz, with a realized gain of 23 dBi/dBic in the broadside direction. The array scans till ±50° within 3dB scan loss point, and offers axial ratio (AR) below 3dB over the entire bandwidth within the entire scan range. The array consists of novel radiating elements arranged exclusively in 2x2 sub-array level, thereby improving cross-polarized fields and axial ratio. The measurement results of the scan loss and axial ratio for different scan angles of the array is in good agreement with simulated results, and the G/T in receive mode and EIRP in transmit mode are also measured. Though the array is designed for NASA lunar project, the array is versatile and can find application in various advanced 5G communication systems.

Reflector antennas with circularly polarized feed sources find applications in SATCOM for high directivity and relatively low cost. SATCOM requires two independent widely separated bands for the transmit (Tx) and receive (Rx) purpose. In the third project, a Fabry-Perot cavity based shared aperture for two circularly polarized 2x2 arrays, one working at Ku-band and other at Ka-band, both having same phase center, is designed as a dual band feed of an offset parabolic reflector. The technique of sequential rotation is employed to achieve circular polarization at both Ku- and Ka-bands. A peak gain of 32 dBic is achieved at Ku-band and 35 dBic is achieved at Ka-band with axial ratio bandwidth of 500MHz at Ku-band and 1 GHz at Ka band.

7.2. Future Study

In the first project, presented in Chapter 3, the heat sink array antenna can be extended to other frequency bands and larger array sizes except that better technology for integration of the metal radiator with BFN board is to be investigated. A conducting adhesive called silver epoxy can be employed to adhere the metal structure with the board and avoid the bimetallic strip effects. Due to the roughness of the 3D metal printed antenna structure, and the

difference of thermal coefficient between the beamforming board and the 3D printed metal structure, fabrication of such an array is quite challenging. An improved assembly technique is required to be developed in future.

For the second project, presented in Chapter 4, the array is versatile, and can be scaled to any even number of elements, for instance it can be scaled to a 16x16, 32x32 or 64x64 array and so forth. According to the NASA requirements, the array will be scaled to a 16x32 = 512 elements array. When the array will be placed in a cubesat, a shooting bouncing ray analysis of the array along with the cubesat should be completed to consider the practical situation. Apart from NASA application, the array can be excited with various amplitude tapers to reduce side lobe level and study the performances. A monopulse or difference pattern can be obtained by first setting the phases on the elements for a certain scan angle and then adding a 180° phase shift to half of the array, thereby generating a null at the scan angle. Any rotated linear polarizations can be obtained if the horizontal and vertical polarizations are excited in phase or out of phase such that $\varphi = \tan^{-1}\frac{|V|}{|H|}$, and φ can be 30^0, 45^0, 60^0, and so forth. The error vector magnitude for digitally modulated signal can be studied as a potential topic of interest. Also, the EIRP at P1dB for different scan angles can be measured. The array can be designed for any frequency range to meet different applications, provided the chip has to be selected accordingly. The array may need a radome for protection, and analysis with radome is required in that case. The phased array can be employed as a feed source for a cylindrical parabolic reflector.

The third project, which is presented in chapter 5, is based on the design of a dual band feed source for a parabolic reflector antenna. We have built the feed source and tested it for impedance matching and radiation pattern for validation, and showed the simulated results only in case of reflector performance. The reflector and the array will be simulated with a strut and the setup will be built and tested for validation. Also, the feed can be designed and simulated for different frequency pairs in 1:1.8 ratio for different applications.

References

1. Constantine A. Balanis, "*Antenna Theory: Analysis and Design*", 4th Edition, John Wiley, Feb 2016.
2. R. J. Mailloux, "*Phased Array Antenna Handbook*", 2nd ed., Artech House, 2005.
3. S. M. Duffy, G. A. Brigham, K. B. Newman and J. S. Herd, "Stepped notch antenna array used as a low thermal resistance heat sink", *2013 IEEE Antennas and Propagation Society International Symposium (APSURSI)*, pp. 622-623, 2013.
4. Jiawei Qian , Min Tang , Yao-Ping Zhang, and Junfa Mao, "Heatsink Antenna Array for Millimeter-Wave Applications", *IEEE Transactions on Antennas and Propagation,* vol. 68, no. 11, November 2020.
5. A. H. Aljuhani, T. Kanar, S. Zihir and G. M. Rebeiz, "A 256-Element Ku-Band Polarization Agile SATCOM Receive Phased Array With Wide-Angle Scanning and High Polarization Purity," in *IEEE Transactions on Microwave Theory and Techniques*, vol. 69, no. 5, pp. 2609-2628, May 2021, doi: 10.1109/TMTT.2021.3056439.
6. A. H. Aljuhani, T. Kanar, S. Zihir and G. M. Rebeiz, "A 256-Element Ku-Band Polarization Agile SATCOM Transmit Phased Array With Wide-Scan Angles, Low Cross Polarization, Deep Nulls, and 36.5-dBW EIRP per Polarization," in *IEEE Transactions on Microwave Theory and Techniques*, vol. 69, no. 5, pp. 2594-2608, May 2021, doi: 10.1109/TMTT.2021.3053293.
7. R. Gardelli, M. Albani and F. Capolino, "Array thinning by using antennas in a Fabry–Perot cavity for gain enhancement," IEEE Transactions on Antennas and Propagation, vol. 54, no. 7, pp. 1979- 1990, July 2006, doi: 10.1109/TAP.2006.877172.
8. A. Kanso, R. Chantalat, M. Thevenot, E. Arnaud and T. Monediere, "Offset Parabolic Reflector Antenna Fed by EBG Dual-Band Focal Feed for Space Application," in *IEEE Antennas and Wireless Propagation Letters*, vol. 9, pp. 854-858, 2010, doi: 10.1109/LAWP.2010.2070055.
9. G. Mishra, S. K. Sharma, J. -C. S. Chieh and R. B. Olsen, "Ku-Band Dual Linear-Polarized 1-D Beam Steering Antenna Using Parabolic-Cylindrical Reflector Fed by a Phased

Array Antenna," in *IEEE Open Journal of Antennas and Propagation*, vol. 1, pp. 57-70, 2020, doi: 10.1109/OJAP.2020.2977876.

10. https://athena.ecs.csus.edu/~milica/EEE212/HAND/HFSSintro.pdf
11. Liu ZG. Fabry-Perot resonator antenna. Journal of Infrared, Millimeter, and Terahertz Waves. 2010 Apr;31:391-403.
12. T. A. Milligan, "Reflector antennas," in *Modern Antenna Design*. Hoboken, NJ, USA: Wiley, 2005, p. 580.
13. Jia-Chi S. Chieh, Everly Yeo, Raif farkouh, Alejandro Castro, Maxwell Kerber, Randall B. Olsen , Emmanuel J. Merulla , and Satish K. Sharma, "Development of Flat Panel Active Phased Array Antennas Using 5G Silicon RFICs at Ku- and Ka-Bands", *IEEE Access*, volume 8, 2020, pp. 192669- 192681.
14. Satish K Sharma and Jia-Chi S. Chieh, "*Multifunctional Antennas and Arrays for Wireless Communication Systems*", IEEE Press/Wiley, May 2021.
15. Wang, Yan & Wang, Congsi & Lian, Peiyuan & Xue, Song & Liu, Jing & Gao, Wei & Shi, Yu & Wang, Zhihai & Yu, Kunpeng & Peng, Xuelin & Du, Biao & Xiao, Song. (2020), "Effect of Temperature on Electromagnetic Performance of Active Phased Array", Antenna. Electronics. 9. 1211. 10.3390/electronics9081211.
16. C. F. Lee, K. Li, S. Y. Poh, R. T. Shin, and J. A. Kong, "Electromagnetic radiation from a VLSI package and heatsink configuration," *Proc. IEEE Int. Symp. Electromagn. Compat.,* Jul. 1991, pp. 393–398.
17. C. E. Brench, "Heatsink radiation as a function of geometry," *Proc. IEEE Symp. Electromagn. Compat.*, Aug. 1994, pp. 105–109.
18. P. Qu, M. K. Iyer, and Y. Qiu, "Radiated emission from pin-fin heat sink mounted on an EBGA package," *Proc. IEEE 8th Topical Meeting Electr. Perform. Electron. Packag.,* 1999, pp. 199–202.
19. K. Li, C. F. Lee, S. Y. Poh, R. T. Shin, and J. A. Kong, "Application of FDTD method to analysis of electromagnetic radiation from VLSI heatsink configurations," *IEEE Trans. Electromagn. Compat.,* vol. 35, no. 2, pp. 204–214, May 1993.
20. X. He, and T. H. Hubing, "Mitigation of unintentional radiated emissions from tall VLSI heatsinks using ground posts*," IEEE Trans. Electromagn. Compat.*, vol. 55, no. 6, pp.

1271–1276, Dec. 2013.

21. L. Covert, and J. Lin, “Simulation and measurement of a heatsink antenna: A dual-function structure,” *IEEE Trans. Antennas Propag.,* vol. 54, no. 4, pp. 1342–1345, Apr. 2006.
22. J. J. Casanova, J. A. Taylor, and J. Lin, “Design of a 3-D fractal heatsink antenna,” *IEEE Antennas Wireless Propag. Lett.,* vol. 9, pp. 1061–1064, Nov. 2010.
23. https://repository.tudelft.nl/islandora/object/uuid:13bcfb5c-34ad-400c-ad65-54e51db9d2d3/datastream/OBJ/download
24. Y. Aslan, J. Puskely, J. H. J. Janssen, M. Geurts, A. Roederer and A. Yarovoy, "Thermal-Aware Synthesis of 5G Base Station Antenna Arrays: An Overview and a Sparsity-Based Approach," in *IEEE Access*, vol. 6, pp. 58868-58882, 2018, doi: 10.1109/ACCESS.2018.2873977.
25. Rudraishwarya Banerjee, Satish K. Sharma, Philip Nguyen, Jia-Chi S. Chieh, Randall Olsen, “Investigations of All Metal Heat Sink Dual Linear Polarized Phased Array Antenna for Ku-Band Applications”, *2020 International Applied Computational Electromagnetics Society Symposium (ACES)*.
26. Ansys Icepak help [https://www.ansys.com]
27. https://rogerscorp.com/advanced-electronics-solutions//ro4000-series-laminates/ro4350b-laminates
28. Kim Woelders, and Johan Granholm, “Cross-Polarization and Sidelobe Suppression in Dual Linear Polarization Antenna Arrays”, *IEEE Transactions on Antennas and Propagation*, vol. 45, no. 12, December 1997.
29. https://www.anokiwave.com/products/aws-0101/index.html
30. G. M. Rebeiz and K. -j. Koh, "Silicon RFICs for phased arrays," in *IEEE Microwave Magazine*, vol. 10, no. 3, pp. 96-103, May 2009, doi: 10.1109/MMM.2009.932078.
31. S. Shahramian, M. J. Holyoak, and Y. Baeyens, ‘‘A 16-element W-band phased-array transceiver chipset with flip-chip PCB integrated antennas for multi-gigabit wireless data links,’’ *IEEE Transactions on Microwave Theory and Techniques* IEEE, vol. 66, no. 7, pp. 3389–3402, Jul. 2018.
32. G. Gültepe, T. Kanar, S. Zihir and G. M. Rebeiz, "A 1024-element ku-band SATCOM phased-array transmitter with 45-dBW single-polarization EIRP," *IEEE Transactions*

on Microwave Theory and Techniques, vol. 69, no. 9, pp. 4157-4168, Sept. 2021, doi: 10.1109/TMTT.2021.3075678.

33. G. Gültepe and G. M. Rebeiz, "A 256-element dual-beam polarization-agile SATCOM ku-Band phased-array with 5-dB/K G/T," *IEEE Transactions on Microwave Theory and Techniques*, vol. 69, no. 11, pp. 4986-4994, Nov. 2021, doi: 10.1109/TMTT.2021.3097075.
34. G. Gultepe, K. Low, Q. Ma and G. M. Rebeiz, "A 1024-Element K-band Commercial SATCOM User Terminal with a G/T of 10.2 dB/K and Two Simultaneous Beams," *2022 IEEE International Symposium on Phased Array Systems & Technology (PAST)*, Waltham, MA, USA, 2022, pp. 01-04, doi: 10.1109/PAST49659.2022.9974984.
35. Y. Yin, Q. Ma and G. M. Rebeiz, "A 14-17.2 GHz Dual-Polarized 256-Element Transmit Phased-Array with 40 dBW EIRP," *2022 IEEE International Symposium on Phased Array Systems & Technology (PAST)*, Waltham, MA, USA, 2022, pp. 01-04, doi: 10.1109/PAST49659.2022.9974988.
36. K. K. W. Low, S. Zihir, T. Kanar and G. M. Rebeiz, "A 27–31-GHz 1024-element ka-Band SATCOM phased-array transmitter with 49.5-dBW peak EIRP, 1-dB AR, and ±70° Beam Scanning," *IEEE Transactions on Microwave Theory and Techniques*, vol. 70, no. 3, pp. 1757-1768, March 2022, doi: 10.1109/TMTT.2021.3139911.
37. K. K. W. Low, T. Kanar, S. Zihir and G. M. Rebeiz, " A 17.7–20.2-GHz 1024-element k-band SATCOM phased-array receiver with 8.1-dB/K G/T, ±70° beam scanning, and high transmit isolation," *IEEE Transactions on Microwave Theory and Techniques*, vol. 70, no. 3, pp. 1769-1778, March 2022, doi: 10.1109/TMTT.2022.3142275.
38. S. K. Sharma and J.-C. S. Chieh, "*Multifunctional Antennas and Arrays for Wireless Communication Systems*", Piscataway, NJ, USA, Wiley-IEEE Press, May 2021.
39. G. Mishra, S. K. Sharma, J. -C. S. Chieh and R. B. Olsen, "Ku-Band Dual linear-polarized 1-D beam steering antenna using parabolic-cylindrical reflector fed by a phased array antenna," in *IEEE Open Journal of Antennas and Propagation*, vol. 1, pp. 57-70, 2020, doi: 10.1109/OJAP.2020.2977876.
40. R. Banerjee, S. K. Sharma, J. -C. S. Chieh and R. Farkouh, "Investigations of heat sink property of a novel dual linear polarized low cross-polarization X-Band phased array antenna employing silicon RFICs-based beamforming network," in *IEEE Open Journal*

of Antennas and Propagation, vol. 3, pp. 523-537, 2022, doi: 10.1109/OJAP.2022.3170791.

41. J. M. Kovitz, H. Rajagopalan, and Y. Rahmat-Samii, "Design and implementation of broadband MEMS RHCP/LHCP reconfigurable arrays using rotated E-shaped patch elements," *IEEE Trans. Antennas Propag.*, vol. 63, no. 6, pp. 2497–2507, Jun. 2015.
42. J.-S. Row and J.-F. Wu, "Aperture-coupled microstrip antennas with switchable polarization," *IEEE Trans. Antennas Propag.*, vol. 54, no. 9, pp. 2686–2691, Sep. 2006.
43. D. Seo and Y. Sung, "Reconfigurable square ring antenna for switchable circular polarization," *Electron. Lett.*, vol. 51, no. 6, pp. 438–440, Mar. 2015.
44. J.-B. Yan, R. D. Hale, A. Mahmood, F. Rodriguez-Morales, C. J. Leuschen, and S. Gogineni, "A polarization reconfigurable low profile ultrawideband VHF/UHF airborne array for fine-resolution sounding of polar ice sheets," *IEEE Trans. Antennas Propag.*, vol. 63, no. 10, pp . 4334–4341, Oct. 2015.
45. K. M.-J. Ho and G. M. Rebeiz, "A 0.9–1.5 GHz microstrip antenna with full polarization diversity and frequency agility," *IEEE Trans. Antennas Propag.*, vol. 62, no. 5, pp. 2398–2406, May 2014.
46. B. Babakhani, S. K. Sharma and N. R. Labadie, "A Frequency agile microstrip patch phased array antenna with polarization reconfiguration," *IEEE Transactions on Antennas and Propagation*, vol. 64, no. 10, pp. 4316-4327, Oct. 2016, doi: 10.1109/TAP.2016.2598156.
47. G. Mishra and S. K. Sharma, "A Multifunctional full-polarization reconfigurable 28 GHz staggered butterfly 1-D-Beam steering antenna," *IEEE Transactions on Antennas and Propagation*, vol. 69, no. 10, pp. 6468-6479, Oct. 2021, doi: 10.1109/TAP.2021.3070226.
48. R. Banerjee, S. K. Sharma and S. Das, "Design of dual circular polarized wideband stacked patch flat panel phased array antenna using ka-band 5G silicon RFICs in beamforming network," *2021 IEEE 19th International Symposium on Antenna Technology and Applied Electromagnetics (ANTEM)*, 2021, pp. 1-2, doi: 10.1109/ANTEM51107.2021.9519083.
49. Sanghamitro Das, Satish K. Sharma, Seth W. Waldstein, James M. Downey, Bryan L. Schoenholz, Sarah M. Dever, James A. Nessel, and Rudraishwarya Banerjee, "A flat-

panel 8×8 wideband K–/Ka–band dual circularly polarized phased array antenna for cubeSat communications", *IEEE Transactions on Antennas and Propagation*, (*submitted for consideration*)

50. Rudraishwarya Banerjee, Satish K. Sharma, Waldstein Seth, Downey James,Schoenholz L. Bryan, Sarah M. Dever, James A. Nessel, Sanghamitro Das, "A Dual linear/circular polarized 64-elements phased array antenna for SATCOM applications", National Radio Science Meeting, 2023, Jan 10-Jan 14, 2023.
51. R. Garg, P. Bhartia, I. Bahl, and A. Ittipiboon, Microstrip Antenna Design Handbook. Norwood, MA, USA: Artech House, 2001.
52. M. Du Plessis and J. Cloete, "Tuning stubs for microstrip-patch antennas," *IEEE Antennas and Propagation Magazine*, vol. 36, no. 6, pp. 52-56, Dec. 1994, doi: 10.1109/74.370523.
53. Isola, Astra MT77, https://www.isola-group.com/pcb-laminates-prepreg/astra-mt77-laminate-and-prepreg/
54. Anokiwave.com,https://www.anokiwave.com/products/awmf-0165/index.html
55. J. Huang, "Dual-polarized microstrip array with high isolation and low cross-polarization", *Microwave Opt. Technol. Lett.*, vol. 4, no. 3, pp. 99-103, Feb. 1991.
56. P. S. Hall, "Application of sequential feeding to wide bandwidth, circularly polarised microstrip patch arrays," *IEE Proc. H (Microw.,Antennas Propag.)*, vol. 136, no. 5, pp. 390–398, Oct. 1989.
57. D. M. Pozar, "The active element pattern," *IEEE Transactions on Antennas and Propagation*, vol. 42, no. 8, pp. 1176-1178, Aug. 1994, doi: 10.1109/8.310010.
58. J. Dunsmore, "OTA G/T measurements of active phased array antenna noise using a vector network analyzer," *94th ARFTG Microwave Measurement Symposium (ARFTG)*, 2020.
59. S. K. Sharma, L. Shafai and S. Rao, "Handbook of Reflector Antennas and Feed Systems, Volume I: Theory and Design of Reflectors", Norwood, MA, USA:Artech House, Jume 2013.
60. L. Shafai, S. K. Sharma and S. Rao, "Handbook of Reflector Antennas and Feed Systems, Volume II: Feed Systems", Norwood, MA, USA:Artech House, June 2013.

61. G. Mishra, S. K. Sharma and J. -C. S. Chieh, "A Circular Polarized Feed Horn With Inbuilt Polarizer for Offset Reflector Antenna for W -Band CubeSat Applications," in *IEEE Transactions on Antennas and Propagation*, vol. 67, no. 3, pp. 1904-1909, March 2019, doi: 10.1109/TAP.2018.2886704
62. A. N. Plastikov, V. A. Vasiliev and S. E. Chadov, "Dual-band dual-polarized log-periodic feed for reflector antenna," *2013 IX Internatioal Conference on Antenna Theory and Techniques*, Odessa, Ukraine, 2013, pp. 455-457, doi: 10.1109/ICATT.2013.6650810.
63. G. V. Trentini, "Partially reflecting sheet arrays," in *IRE Transactions on Antennas and Propagation*, vol. 4, no. 4, pp. 666-671, October 1956, doi: 10.1109/TAP.1956.1144455.
64. N. Alexopoulos and D. Jackson, "Fundamental superstrate (cover) effects on printed circuit antennas," in *IEEE Transactions on Antennas and Propagation*, vol. 32, no. 8, pp. 807-816, August 1984, doi: 10.1109/TAP.1984.1143433.
65. D. Jackson and N. Alexopoulos, "Gain enhancement methods for printed circuit antennas," in *IEEE Transactions on Antennas and Propagation*, vol. 33, no. 9, pp. 976-987, September 1985, doi: 10.1109/TAP.1985.1143709.
66. C. Meagher and S. K. Sharma, "A Wideband Aperture-Coupled Microstrip Patch Antenna Employing Spaced Dielectric Cover for Enhanced Gain Performance", IEEE Transactions on Antennas & Propagation, Vol. 58, No. 9, September, 2010, pp. 2802-2810.
67. D. R. Jackson and A. A. Oliner, "A leaky-wave analysis of the high-gain printed antenna configuration," in *IEEE Transactions on Antennas and Propagation*, vol. 36, no. 7, pp. 905-910, July 1988, doi: 10.1109/8.7194.
68. D. R. Jackson and A. A. Oliner, "Leaky-Wave Antennas: Chapter 7, Modern Antenna Handbook", Wiley, November 2007.
69. R. Banerjee, S. K. Sharma and F. Capolino, "A Shared Aperture Ku-/Ka-Band Feed Source for a High Gain Fixed Beam Offset Reflector Antenna," *2022 IEEE Conference on Antenna Measurements and Applications (CAMA)*, Guangzhou, China, 2022, pp. 1-3, doi: 10.1109/CAMA56352.2022.10002441.

70. D. Guha, M. Biswas and Y. M. M. Antar, "Microstrip Patch Antenna With Defected Ground Structure for Cross Polarization Suppression," in *IEEE Antennas and Wireless Propagation Letters*, vol. 4, pp. 455-458, 2005, doi: 10.1109/LAWP.2005.860211.
71. D. Guha, C. Kumar and S. Pal, "Improved Cross-Polarization Characteristics of Circular Microstrip Antenna Employing Arc-Shaped Defected Ground Structure (DGS)," in *IEEE Antennas and Wireless Propagation Letters*, vol. 8, pp. 1367-1369, 2009, doi: 10.1109/LAWP.2009.2039462.
72. D. Guha, S. Biswas, and Y. Antar, "Defected ground structure for microstrip antennas," in *Microstrip and Printed Antennas*, D. Guha and Y. Antar, Ed. Chichester, U. K.: Wiley, 2011.
73. Amr Elsakka , Amirashkan Farsaei , A. J. van den Biggelaar , Adrianus Cornelis Franciscus Reniers , Martin N. Johansson , Rob Maaskant, Ulf Johannsen, Oleg A. Iupikov, A. Bart Smolders and Marianna V. Ivashina , "A mm-Wave Phased-Array Fed Torus Reflector Antenna With ±30° Scan Range for Massive-MIMO Base-Station Applications," in *IEEE Transactions on Antennas and Propagation*, vol. 70, no. 5, pp. 3398-3410, May 2022, doi: 10.1109/TAP.2021.3138450.
74. Rudraishwarya Banerjee, Satish K. Sharma, Seth W. Waldstein, James M. Downey, Bryan L. Shoenholz, Sarah M. Dever, James A. Nessel, and Sanghamitro Das, "A 22 GHz -28 GHz Polarization Reconfigurable Flat Panel 8x8 Tx/Rx Phased Array Antenna with Uniquely Arranged Novel Radiating Elements for CubeSat Communication," in *IEEE Transactions on Antennas and Propagation,* vol. 71, no. 5, pp. 4138-4152, May 2023, doi: 10.1109/TAP.2023.3249820.
75. Rudraishwarya Banerjee, Satish K. Sharma, Seth W. Waldstein, James M. Downey, Bryan L. Shoenholz, Sarah M. Dever, James A. Nessel, and Sanghamitro Das, "A Wideband Dual Linear/Circular Polarized 64-Element Phased Array Antenna for SATCOM Applications," *2023 United States National Committee of URSI National Radio Science Meeting (USNC-URSI NRSM)*, Boulder, CO, USA, 2023, pp. 60-61, doi: 10.23919/USNC-URSINRSM57470.2023.10043128.